UNIVERSITY OF SOUTHAMPTON

Holographic Lasers

David Ianto Hillier

Submitted for the degree of Doctor of Philosophy

Faculty of Engineering, Science and Mathematics
Optoelectronics Research Centre

September 2004

UNIVERSITY OF SOUTHAMPTON

ABSTRACT

Faculty of Engineering, Science and Mathematics
Optoelectronics Research Centre

Doctor of Philosophy

Holographic Lasers

By David Ianto Hillier

This thesis presents the development of CW adaptive solid state lasers which dynamically correct for phase distortions within their cavity by phase conjugation.

In these systems gain gratings are formed by spatial hole burning caused by interference of coherent beams in the laser amplifier and the subsequent modulation of the population inversion. The gain grating formation is used for phase conjugation by using the amplifier in a four-wave mixing geometry. The diffraction efficiency of these gain gratings is studied both experimentally and theoretically. Phase conjugate reflectivities of 100 times are achieved via four-wave mixing in a diode-bar side-pumped Nd:YVO_4 amplifier.

The gain grating four-wave mixing scheme is developed into a seeded resonator by using an input beam in a self intersecting loop geometry. The phase conjugate resonator is modeled and characterised experimentally achieving single spatial and longitudinal mode outputs of 2.5W (in a side loop geometry) and 8W (in a ring geometry). The seed laser is replaced by an output coupler forming a self-starting adaptive resonator achieving single spatial mode outputs of 7W.

The ability of the ring resonator to be power-scaled is investigated by the insertion of a power amplifier into its input/ouput arm. It is shown that a phase conjugate output of 6W can be scaled to 11.6 W by the insertion of the amplifier.

A fibre based four-wave mixing scheme is investigated but no experimental evidence of any phase conjugation is observed.

"Inconceivable!"

" You keep using that word. I do not think it means what you think it does"

from 'The Princess Bride' By S. Morgenstern
Abridged By William Golding

Declaration of Authorship

I, *David Ianto Hillier* declare that the thesis entitled

Holographic Lasers

and the work presented in it are my own. I confirm that:

- This work was done wholly while in candidature for a research degree at this university;
- The following part of this thesis has been previously submitted for a PhD at this university;
  - The work performed in chapter 4 on the ring resonator and in chapter 5 are included in the thesis of Dr Jason Hendricks, and we worked on these parts of the thesis together.
- where I have quoted from the work of others, the source is always given, With the exception of such quotations this thesis is entirely my own work;
- I have acknowledged all main sources of help;
- the following chapters of this thesis are based on work done by myself jointly with others;
  - I worked with Dr Jason Hendricks on both the holographic ring resonator described in chapter 4 and amplified resonator described in chapter 5.
  - The work described in chapter 6 was performed in conjunction with Dr Stephen Barrington, the postdoc on an EPSRC funded project.
- Parts of this work have been published as given in appendix D

David Hillier
September 2004

Acknowledgments

Where to begin, well obviously with Rob, without whom none of this would have been possible. His understanding, optimism, and belief kept both me and the project going; no one could ask for a better supervisor.

Then naturally comes Jason and Steve who I worked with on the project; Jason who taught me about meticulous lab work and Steve who showed me that the "Bits of random metal" drawer contained all of the really useful stuff. Thanks must also go to Dr Dave Shepherd, Dr Mike Damzen and Dr Ara Minassian for many helpful discussions.

The various people who made things for me: fibres from Dr Duncan Harwood and Dr Richard Williams, crystal fibres from Dr Michel Digonnett and Dr Laetitia Laversenne, Simon and Tim who managed to turn inexplicable drawings in to immensely useful bits of metal.

Then comes the people who made life more interesting: The office formerly known as 2071 and all who sailed in her over the last four years. The Rookery Road boys; Ethan, Al, John and Dom for helping me believe that it wasn't just happening to me. The fencing club and team for getting me out of the lab: S-division for taking me to foreign climes and getting me drunk, and the team for many hung over Thursday mornings.

I must also thank: Mr Blake a truly inspirational physics teacher, my parents for all of their support, and finally, Kate for putting up with me blathering on about phase conjugation, keeping me sane(ish), and generally being wonderful.

This project was funded by EPSRC grant number GR/R01545/01.

Contents

Glossary

A glossary of abbreviations and commonly used terms

AR Anti-reflection

ASE Amplified spontaneous emission

BP Backward pump

cc Complex conjugate

DFWM Degenerate four-wave mixing

FWM Four-wave mixing

FP Forward pump

HWP Half-wave plate

M^2 A measurement of beam quality

MOPA Master oscillator power amplifier

NRTE Non-reciprocal transmission element

PC Phase conjugate

PCM Phase conjugate mirror

SBS Stimulated Brillouin scattering

SLM Single longitudinal mode

SSSPG Small signal single pass gain

Chapter 1

Introduction

1.1 Overview

In the first section of this chapter the concept of phase conjugation is introduced, and described both qualitatively and analytically. Its use in distortion correction is discussed and compared with the behaviour of a plane mirror. Various common methods of achieving phase conjugation are introduced and a comparison is made between them.

In the second section diode pumped solid state lasers will be discussed. The advantages of diode pumping will be described with respect to the high brightness and output powers in the CW regime. The neodymium (Nd^{3+}) laser ion will be described for its use in a Nd:YVO_4 laser emitting at 1.06 μm . Heat deposition in solid state lasers due to the quantum defect and various up-conversions will be covered with respect to their effect on laser performance.

Existing methods of power scaling solid state lasers will then be described along with the use of phase conjugation to develop high power systems.

Finally an overview is presented of the work in this thesis summarising each of the chapters.

1.2 Phase conjugation

Phase conjugation was first observed by Zel'dovich [1] in 1972 but its roots can be traced back further to earlier work in static [2] and dynamic [3] holography. Zel'dovich passed a beam through an etched glass plate into a cell of compressed methane. He observed that the scattered beam exactly retraced the path of the incident beam through the glass plate cancelling out the phase distortions.

Two beams are considered to be phase conjugates of each other if they have the same wavefronts but the opposite propagation directions. This means that the k-vectors of the two beams have the opposite sign and that the amplitude functions of the beams are the complex conjugate of each other (which is where the name 'phase conjugate' comes from).

When a beam is incident on a conventional mirror, only the component of the k vector that is perpendicular to the plane of the mirror is reversed. If a divergent beam is incident on a plane mirror its reflection will diverge in the same manner (Figure 1.1a). Hence for a beam reflecting from a flat mirror located in the $x - y$ plane, reflection is given by

$$Ae^{i((k_x+k_y+k_z)\cdot r-\omega t)} \Rightarrow A'e^{i((k_x+k_y-k_z)\cdot r-\omega t)} \tag{1.1}$$

If however the beam is incident on a phase conjugate mirror then all three components of the k vector of any incident beam will be reversed with a reflection given by

$$Ae^{i((k_x+k_y+k_z)\cdot r-\omega t)} \Rightarrow A'e^{i(-(k_x+k_y+k_z)\cdot r-\omega t)} \tag{1.2}$$

This causes the reflected wavefront to exactly retrace the path of the inci-

dent beam regardless of the initial spatial structure of the beam. Figure 1.1b shows the reflection of a divergent beam by a phase conjugate mirror.

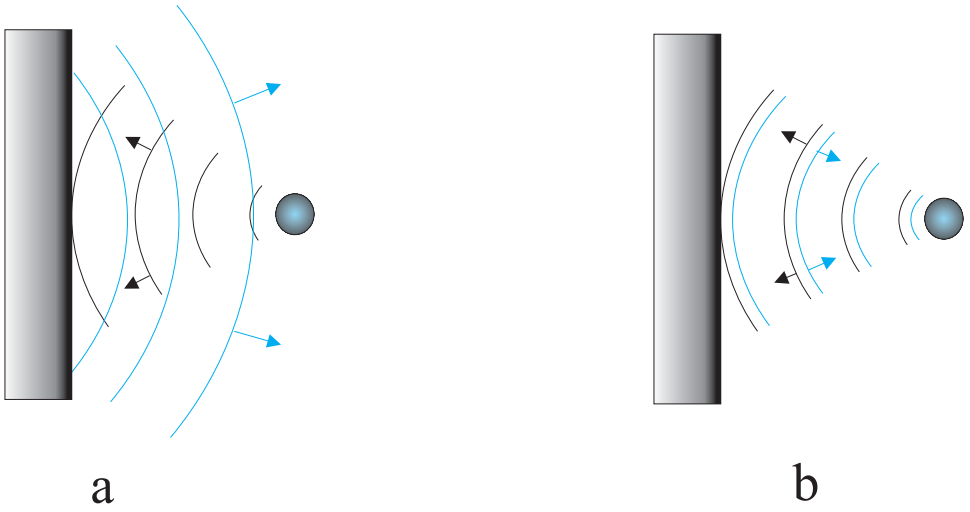

Figure 1.1: a, Reflection from a plane mirror. b, Reflection from a phase conjugate mirror.

1.2.1 Distortion correction theory

One of the main uses of phase conjugation is for distortion correction. When a beam with a flat wavefront is passed through a phase aberrator (an etched glass plate for example) its transmitted wavefront will be distorted. If this distorted beam is then reflected by a conventional mirror it will pass back though the aberration again with the wavefront of the beam being further distorted (Figure 1.2).

This can be considered analytically by taking an ideal plane wave of the form

$$E(x, y, z, t) = A_0(x, y, z)e^{i(kz-\omega t)} \tag{1.3}$$

where E is the optical field and A_0 its amplitude. The plane wave is then transmitted through the phase aberration to give

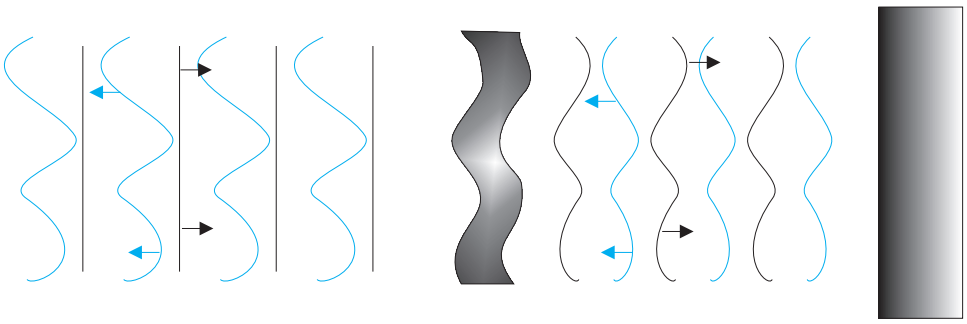

Figure 1.2: Reflection from a conventional mirror causing cumulative aberration.

$$E'(x,y,z,t) = A_0(x,y,z)e^{i(kz+\phi(x,y,z)-\omega t)} \tag{1.4}$$

where $\phi(x,y,z)$ describes the effect on the phase of the beam imposed by the phase aberration.

E' is then reflected by a plane mirror with an amplitude reflectivity r to give

$$E''(x,y,z,t) = rA_0(x,y,z)e^{i(-kz+\phi(x,y,z)-\omega t)} \tag{1.5}$$

Which, on transmission back through the aberrator gives a final field of

$$E'''(x,y,z,t) = rA_0(x,y,z)e^{i(-kz+2\phi(x,y,z)-\omega t)} \tag{1.6}$$

The beam has now been passed through the distortion twice, each time distorting its wavefront further.

If the distorted beam (E') is instead reflected by a phase conjugate mirror the wavefront of the beam will be maintained with the propagation direction reversed. When the phase conjugate beam passes back through the phase aberration the distortions on the beam will be undone, and the final

beam will have the same flat wavefront as the original beam (Figure 1.3).

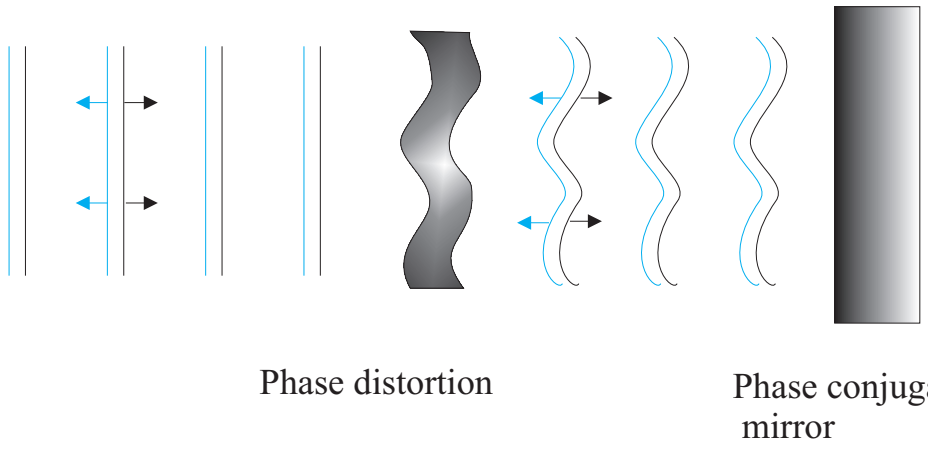

Figure 1.3: Reflection by a phase conjugate mirror cancels out any phase distortion.

This can be viewed analytically by taking the distorted beam E' (equation 1.4) with reflection via a phase conjugate mirror of reflectivity r_{pc} to give

$$E''(x,y,z,t) = r_{pc}A_0(x,y,z)e^{i(-kz-\phi(x,y,z)-\omega t)} \tag{1.7}$$

Which when transmitted back through the phase aberrator results in a final beam of the form

$$\begin{aligned} E'''(x,y,z,t) &= r_{pc}A_0(x,y,z)e^{i(-kz-\phi(x,y,z)+\phi(x,y,z)-\omega t)} \\ E'''(x,y,z,t) &= r_{pc}A_0(x,y,z)e^{i(-kz-\omega t)} \end{aligned} \tag{1.8}$$

The phase distortion that was imposed on the beam has been removed leaving an exact replica of the original beam travelling in the opposite direction.

It is also interesting to compare the expanded versions [1]of the initial and phase conjugated beams.

[1]Up to now it has been assumed that $\cos(kz-\omega t) = e^{-i(kz-\omega t)}$ rather than the full form $\cos(kz-\omega t) = (e^{-i(kz-\omega t)} + e^{i(kz-\omega t)})/2$.

$$\begin{aligned} E(x,y,z,t) &= A_0(x,y,z)(e^{i(kz-\omega t)} + e^{-i(kz-\omega t)}) \\ &= A_0(x,y,z)(e^{i(kz-\omega t)} + e^{i(-kz+\omega t)}) \\ E'''(x,y,z,t) &= r_{pc}A_0(x,y,z)(e^{i(-kz-\omega t)} + e^{-i(-kz-\omega t)}) \\ &= r_{pc}A_0(x,y,z)(e^{i(kz+\omega t)} + e^{i(-kz-\omega t)}) \end{aligned} \tag{1.9}$$

It can be seen that when written in this form the only difference between E''' and E is the sign of the time component (ωt) of the two beams and r_{pc}. This is why phase conjugate beams are sometimes referred to as being "time reversed". Obviously nothing is really travelling backwards in time but it helps to visualise how a phase conjugate exactly retraces the path of the original signal beam. This time reversal has been misunderstood in the past leading to pseudo scientific claims of 'magical' properties [4].

1.2.2 Methods of achieving phase conjugation

Phase conjugation can be achieved via a range of nonlinear optical effects. The most commonly used methods of achieving phase conjugate are described here.

1.2.2.1 Stimulated Brillouin Scattering

Stimulated Brillouin Scattering (SBS) was the mechanism used in the first observation of phase conjugation by Zel'dovich [1] and has been used in the generation of phase conjugate waves ever since [5] [6] [7]. SBS is achieved by focusing a beam into some material where a counter-propagating beam is generated through stimulated scattering.

Initially a beam is launched into the SBS cell and spontaneously scatters off localised variations in the material [2] (Figure 1.4a). The scattered beam

[2]This can include; temperature variations (which will in turn cause variations in the

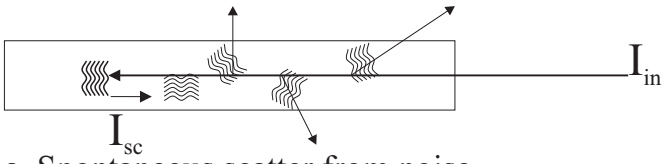

a. Spontaneous scatter from noise

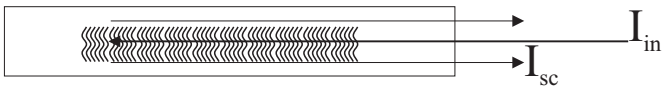

b. Interference between incident and scattered light

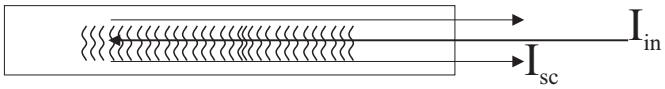

c. Amplification of sound wave by electrostriction

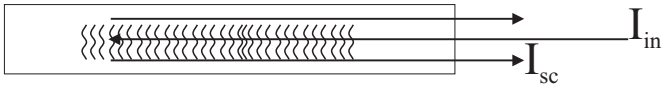

d. Increased scattering from the intensified sound wave

Figure 1.4: Schematic of the SBS process (adapted from figure 2.2 in *Phase Conjugate Laser Optics* [8])

which counter-propagates with respect to the initial beam overlaps with it forming an interference pattern (Figure 1.4b). This interference pattern then generates an acoustic wave via the electrostrictive effect [3] (Figure 1.4c). The initial beam scatters off the acoustic wave reinforcing the back scattering (Figure 1.4d) and building up the signal. Any reflectivity depends strongly on the length of the interference area causing the phase conjugated backscattered part to dominate. The acoustic compression wave travels through the medium causing a Doppler shift in the phase conjugate beam.

The sound wave has an angular frequency (Ω)and travels in the same direction as the k-vector of the initial beam. The Doppler shift imposed on the reflected beam is given by $\omega_{inc} - \omega_{ref} = \Omega$. This causes the interference between the incident and reflected beams to beat at a frequency of Ω which will reinforce the acoustic wave.

The threshold at which SBS occurs can be estimated from

$$P_{th} \simeq \frac{25 A_{eff}}{L_{eff} g} \tag{1.10}$$

where L_{eff} is the effective interaction length (which depends on the coherence length), and g is the Brillouin gain coefficient.

SBS has been observed in a wide range of substances (which tend to be highly toxic and/or require high pressures) but most of the recent work has been concentrated on solid state materials especially multimode silica fibres. Whilst these have lower SBS gains than the more traditional materials (Brillouin gains of 130 cm/GW with a threshold of 18 kW have been achieved in CS_2 [9] compared with 5.8 cm/GW with a 300 kW threshold [10] in silica) this is compensated for by the ability to produce far longer

refractive index), defects in crystals, pressure variations in gases, or any form of impurity in the medium.

[3] The presence of an optical field in a medium causes a stress which is proportional to the square of the field.

gain regions. SBS in multimode silica fibres has been used to achieve phase conjugate reflectivities of up to 90% [10]. Work is currently under way to try and bring SBS phase conjugation in fibres into the CW regime [11].

1.2.2.2 Four-wave mixing

Four-wave mixing is a form of dynamic holography where the hologram is simultaneously written and read by the same three beams [12]. Four-wave mixing has been achieved via a wide range of nonlinear effects; parametric amplification [13], photo-refractives [14], molecular reorientation effects in liquid crystals [15], saturable absorbers [16] and saturable gain [17]. In all of these cases the same fundamental mechanism applies.

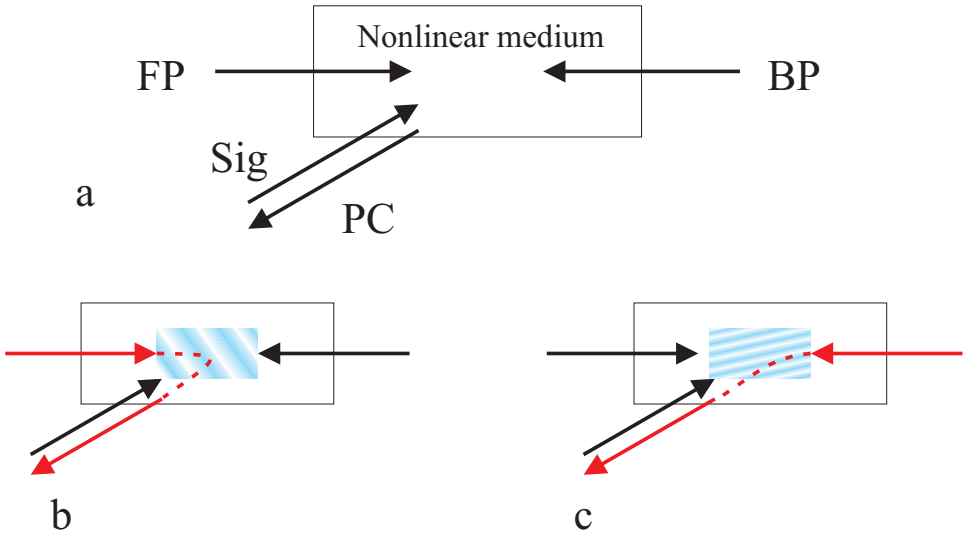

Figure 1.5: Four-wave mixing. a, a schematic of the beams. b, a reflection grating formed between the backward pump(BP) and signal (Sig) beams. c, a transmission grating formed between the forward pump(FP) and signal (Sig) beams.

In degenerate four-wave mixing three beams intersect in a nonlinear medium. Two of the beams (the backward and forward pump) are aligned such that they counter-propagate, while the third (the signal beam) intersects them at some angle (Figure 1.5a). Two interference patterns are formed [4]; one be-

[4]There are actually six interference patterns present but only two contribute to phase conjugation.

tween the signal beam and the backward pump beam, the other between the signal and forward pump beam . These interference patterns write gratings in the medium by one of the nonlinear process previously mentioned. The pump beam which was not involved in the writing of each grating then diffracts off it as a phase conjugate of the signal beam (Figures 1.5b and c). In non-degenerate four-wave mixing the angles which the beams meet are chosen such that Bragg matching occurs between the incident beams and their corresponding gratings.

1.2.2.3 Self pumped photo-refractives

Self pumped phase conjugation via the photo-refractive effect [18] [19] is used for a wide range for optical techniques due to its ease of use and need of only low power beams (phase conjugation has even been observed with microwatt beams [20]).

The photo-refractive effect is a change in the refractive index of a material due to an incident optical field. Figure 1.6 shows the process which is undergone in the formation of the refractive index grating generated by an interference pattern formed in a photo refractive material. Initially the two beams intersect forming an interference pattern (figure 1.6a). At the anti-nodes of the interference pattern the intensity is great enough to excite charge carriers in the crystal from the donor band to the conduction band (figure 1.6b). These charges migrate (via diffusion and the influence of any externally applied electric fields) to areas with a weaker field . A spatial periodic variation in charge has now been formed that exactly maps the original interference pattern (figure 1.6c). These areas of high and low charge in turn generate an electric field $\pi/2$ out of phase with the interference pattern (figure 1.6d). The refractive index of the medium is altered by the electric field via the electro-optic effect and forms a refractive index grating (figure 1.6e) which is also $\pi/2$ out of phase with the interference pattern.

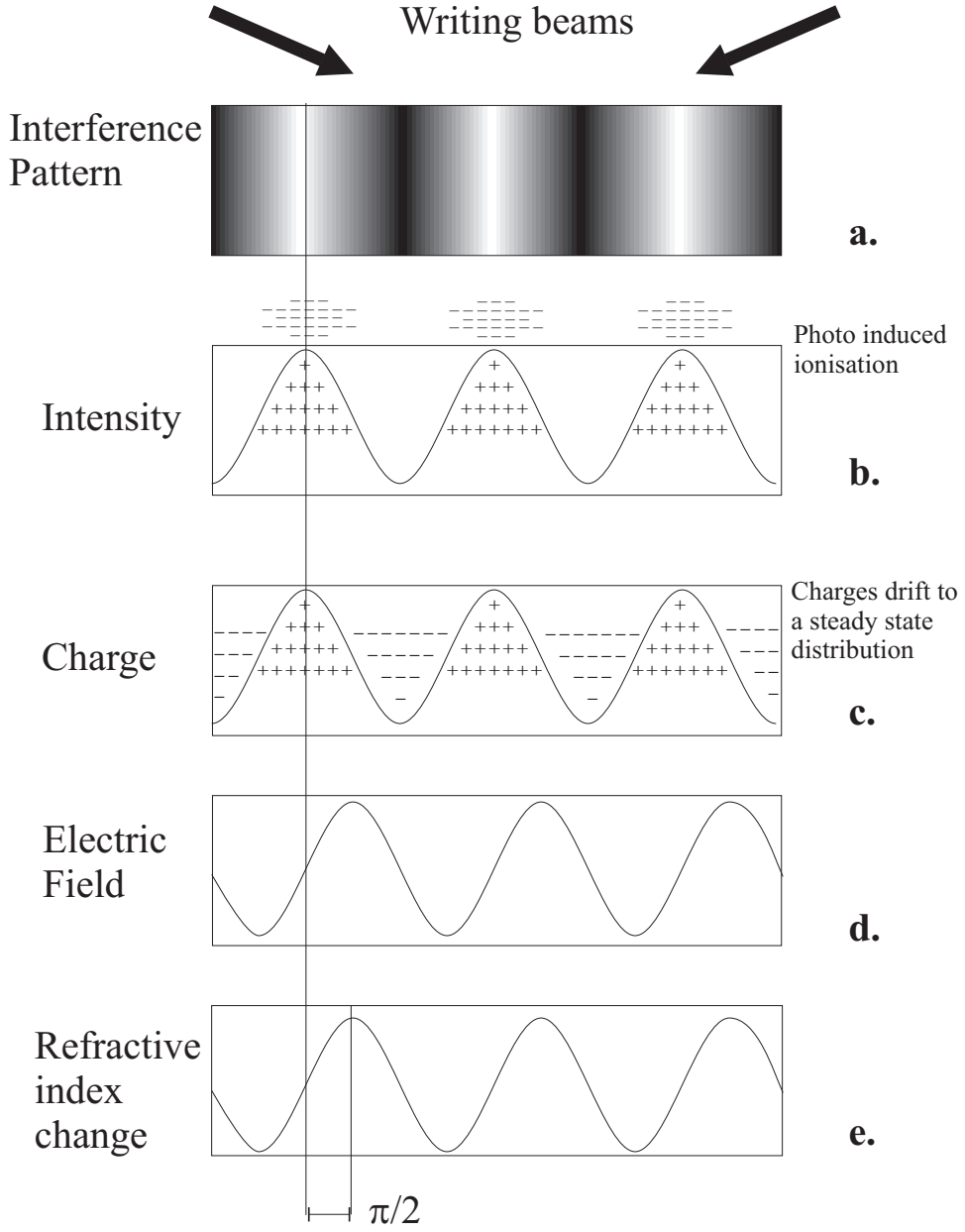

Figure 1.6: The photo-refractive mechanism (after [21])

The change in refractive index due to the incident field is given by

$$\triangle n = -\frac{1}{2} r_{eff} E n_0^3 \tag{1.11}$$

where r_{eff} is some linear combination of components of the electrooptic tensor element, E the electric field and n_0 the unperturbed refractive index.

Self pumped photo-refractive phase conjugators operate via four-wave mixing but in a very interesting way. The device used by Feinberg [22] consists of a beam launched into a single crystal of $BaTiO_3$. When the beam is launched into the crystal (perpendicular to the crystal's c-axis) it 'fans out' (due to the change in refractive index it induces via the photo-refractive effect) illuminating one of the edges of the crystal. This edge acts as a retro-reflector directing the light back towards the incident beam. Where two components of this beam counter-propagate (beams 2 and 2' in figure 1.7) they form a two counter-propagating loop of light. At point **b** (and indeed point **a**) beams 2 and 3 counter-propagate and intersect beam 1; this is a four-wave mixing geometry and as such generates a phase conjugate of beam 1.

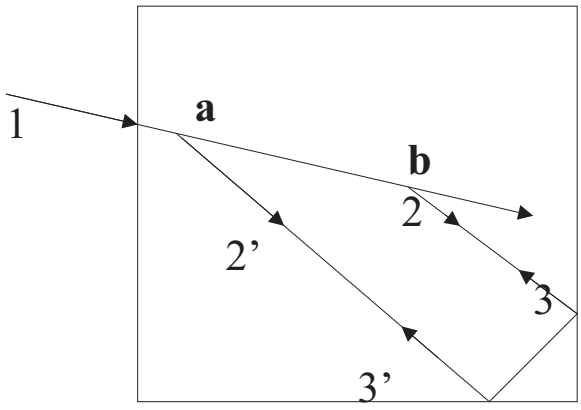

Figure 1.7: A self-pumped $BaTiO_3$ phase conjugator [22]

The main disadvantage of photo-refractive phase conjugators is the length of time that it takes the effect to build up, which ranges from microseconds

to some times many minutes. This build-up period is because the light induced refractive index change depends on the optical energy rather than the optical intensity of the incident beams [19].

1.2.2.4 Adaptive optics

Whilst the use of adaptive optics is not technically a form of phase conjugation it is used for distortion correction and will be covered here for completeness. Increasingly nowadays adaptive control is used to define the spatial properties of laser cavities in a similar manner to our use of phase conjugation.

Adaptive optics involves the use of deformable mirrors to control the shape of a wavefront [23], and are used in a range of imaging regimes, for example in astronomy to reduce distortions caused by atmospheric fluctuations and in high power lasers for mode selection. Recently the highest intensity of laser light ever achieved (8.5×10^{21}W/cm^2 in a 1.2J, 27fs pulse) was produced using adaptive optics to focus the beam into a spot less than 1µm across [24].

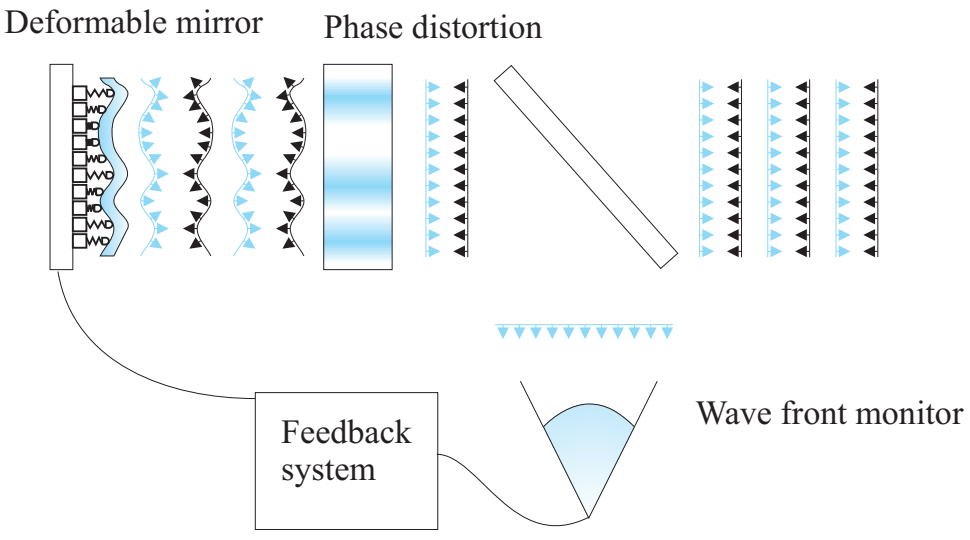

Figure 1.8: An adaptive optics system

A typical adaptive optical system involves a deformable mirror connected

to a computer controlled feedback system as shown in figure 1.8. Here a beam is passed through a phase distortion (such as a pumped amplifier) then reflected by the deformable mirror back through the distortion. The reflected beam is sampled and the mirror dynamically molded to achieve correction for the distortion. The fidelity of wavefront replication is limited by the density of actuators and maximum local radius of curvature of the mirror and accuracy of the feedback systems.

1.3 Diode pumped solid state lasers

The field of solid state lasers covers any laser whose host medium is a crystal, glass or ceramic. Solid state lasers have been the subject of a great deal of research since the creation of the first laser [25].

Early solid state lasers were mostly pumped with flashlamps which caused them to be bulky and inefficient. With the development of diode lasers came the first example of a diode pumped solid state laser [26] in 1964.

The development of high power diode lasers has revolutionised the field of solid state lasers. These devices produce high power, high brightness outputs yet are cheap and compact. Single emitter diodes have been built to achieve outputs of up to 10W [27] [28]. Many emitters can be combined into bars or stacks achieving outputs of, for diode bars 90W [29] and diode bar stacks of 1.3kW [30]. Diode lasers are ideally suited for pumping laser crystals due to their comparatively narrow bandwidth (compared with flashlamps), brightness and high power.

The high powers and intensities have opened up the possibility of building cheap and compact diffraction-limited lasers. However these high powers inevitably come with intense heating which leads to thermally-induced distortions.

1.3.1 Neodymium as a laser ion

The neodymium ion (Nd^{3+}) was the first trivalent rare earth ion to be used in a laser. It is most commonly used in host materials such as YAG, YVO_4, YLF and glass, but stimulated emission has been achieved in over 100 different host materials to date [31].

When pumped at 808nm the ion's outer electron is excited to the ${}^4F_{5/2}$/ ${}^2H_{9/2}$ manifold, from where it rapidly de-excites down to the metastable ${}^4F_{3/2}$ level.

Lasing occurs predominantly on the ${}^4F_{3/2} \rightarrow {}^4 I_{11/2}$ transition at around 1.06µm (depending on the host medium). Lasing is also possible on the ${}^4F_{3/2} \rightarrow {}^4 I_{9/2}$ and ${}^4F_{3/2} \rightarrow {}^4 I_{13/2}$ transitions with emission at around 0.9µm and 1.35µm respectively (again the exact emission wavelength is dependent upon the host medium).

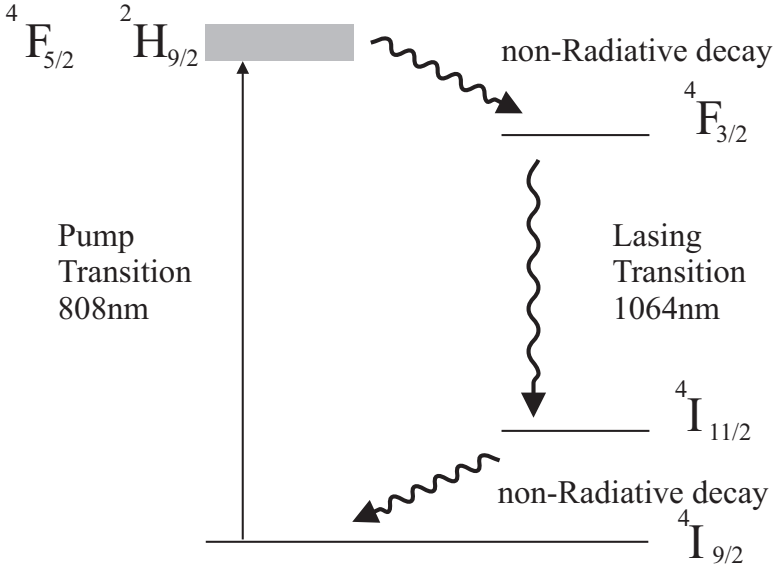

Figure 1.9: Nd^{3+} energy levels when pumped at 808nm emitting at 1064nm.

1.3.1.1 Nd:YVO_4

Nd:YVO_4 was first proposed for use as a laser material by O'Connor in 1966 [32] but it wasn't until 1987 [33] that crystals of suitable optical quality to build a viable system were available. Its high stimulated emission cross-section at the lasing wavelength (4.6 times greater than Nd:YAG [34]), short absorption length and wide absorption bandwidth (again compared with Nd:YAG) make it a very desirable laser crystal [35].

Nd:YVO_4 is a naturally birefringent uniaxial crystal. Its stimulated emission cross-section is three times higher along the a-axis than that along the b and c axes which leads to polarised laser output. This polarised output means that the thermally induced birefringence effects which Nd:YAG suffers from are avoided.

The material and lasing properties of 1.1%at doped Nd:YVO_4 are given in table A.1.

1.4 Heat deposition in solid state lasers

Heat deposition in solid state lasers is a problem which severely limits possible output powers and beam qualities. The major causes of heating are the quantum defect and up-conversion. Problems with absorptions to non-radiative states have decreased since the replacement of flashlamp pumped systems with narrower bandwidth diode based pumping. However, the high pump intensities achievable from diodes have themselves produced new problems.

1.4.1 The quantum defect

The quantum defect is the difference in energy between the lasing and pump photons. The emissions between the pump band and upper laser

level and the lower laser level and ground state are all non-radiative. The proportion of energy lost thermally can be calculated from

$$QD = \frac{E_{pump} - E_{lasing}}{E_{pump}} = 1 - \frac{\lambda_{lasing}}{\lambda_{pump}} \tag{1.12}$$

When pumped at 808nm and lasing at 1064nm Nd:YVO_4 loses 24% of the pump power to heat through this process.

1.4.2 Up-conversion

When Nd^{3+} lasers are pumped at 808nm several spectroscopic up-conversion processes impede efficient laser action. These processes include energy transfer (or Auger) upconversion [36] [37] [38], excited state absorption [39] and cross relaxation [37].

1.4.2.1 Energy transfer upconversion

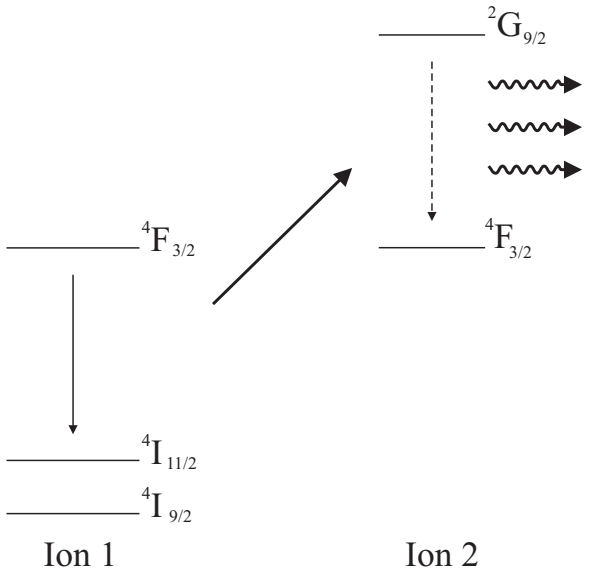

Figure 1.10: Energy transfer upconversion.

Energy transfer up-conversion occurs when two ions in the $^4F_{3/2}$ metastable level are in close proximity. One of the ions relaxes down to the $^4I_{11/2}$ level [38] transferring its energy to the second ion which is in turn promoted to a higher state ($^2G_{9/2}$). The excited ion relaxes down to the $^4F_{3/2}$ level non-radiatively (Figure 1.10).

1.4.2.2 Excited state absorption

A schematic of excited state absorption is shown in figure 1.11. A Nd^{3+} ion is excited by a pump photon to the $^4F_{5/2}$ level, and it then rapidly relaxes down to the metastable $^4F_{3/2}$ level. This is then followed by the absorption of another pump photon which excites it up to the $^2D_{5/2}$ level after which it decays non-radiatively to the $^4G_{7/2}$ level.

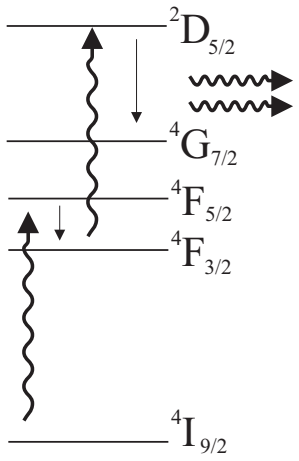

Figure 1.11: Excited state absorption.

1.4.2.3 Cross relaxation

Cross relaxation [37](also referred to as self quenching) occurs between an ion excited to the metastable $^4F_{3/2}$ level and an ion in its ground state. The excited ion relaxes down to the $^4I_{15/2}$ level transferring its energy to the other ion which is excited into the $^4I_{15/2}$ level. Both ions then relax down to the ground state non-radiatively (Figure 1.12).

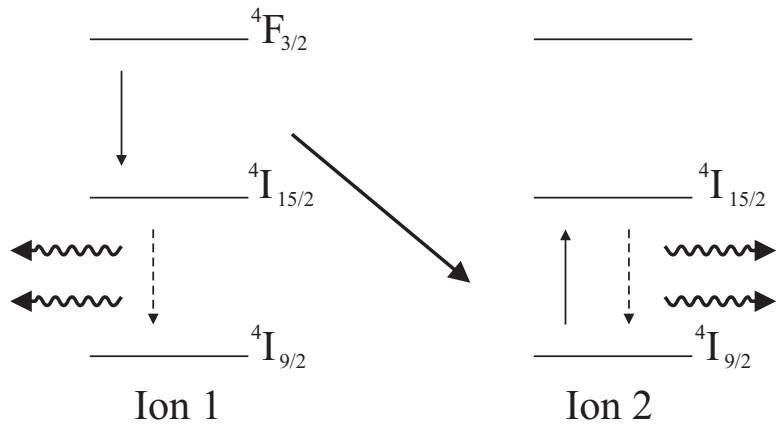

Figure 1.12: Cross relaxation.

1.5 Power scaling of lasers

One of the main uses of phase conjugation is in the power scaling of lasers. It is comparatively easy to build a low power laser which operates on a single spatial and longitudinal mode. Developing higher power systems is a much more complicated endeavour. Heating of the laser medium due to the quantum defect and parasitic spectroscopic processes cause changes in refractive index, thermal expansion and stress induced birefringence.

These effects are especially important now with the development of diode pumped solid state lasers. In the last 4 years diode power available from a single device has increased more than 10 fold from 40W diode bars up to the latest kilowatt stacks. With these powers comes the need to extract more heat than ever before.

1.5.1 Thermal lensing and distortions

Thermal lensing effects in end [40] [41] [42] and side [43] [44] [45] pumped solid state lasers have been studied extensively. When a laser medium is pumped, heat is deposited via the quantum defect and a range of spectroscopic processes. If the medium is cooled then a steady temperature

distribution will be reached.

Heating of a laser medium causes the refractive index to change via two processes: Firstly, the linear thermally induced refractive index change and secondly through any stress induced refractive changes [40]. The combination of these effects and the ”bulging” or curvature of the mediums end faces form a lens. The strength of this lens depends on the thermal loading and material properties of the laser medium.

The focal length of a thermal lens is generally found to be inversely proportional to the power of the pump beam [42] [45]. The quality of the lens is dependent on the pump beam profile.

For a uniform or top hat pump distribution a parabolic variation in temperature and therefore refractive index profile is formed [43] (only within the pumped region in the case of the top hat distribution). This profile gives a lens with no higher order terms and as such shouldn't aberrate any beam passing through it [46].

In a real laser system it is more common for the pump beam to have a Gaussian (or near Gaussian) profile. In this case a more complex refractive index profile is produced. The resultant lens will contain higher order phase terms which act to distort any beam that passes through it. In order to calculate the effect that these highly complex lenses have on the beam quality generally only the quartic phase aberrations are considered [42]. Seigman's analysis [46] of the effect of quartic phase aberration due to a spherical lens gives the increase in the beam quality factor (M^2) as

$$M^2 = \frac{8\pi C_4 w^4}{\lambda\sqrt{2}} \tag{1.13}$$

where w is the beam radius and C_4 the quartic phase aberration coefficient.

1.5.1.1 Methods of cooling

Solid state laser crystals are generally conduction cooled through their side faces. Conduction cooling is achieved by placing the laser crystal in good thermal contact with water cooled copper heatsinks. In order to achieve good thermal contact between crystal and heatsink heat paste, indium foil or wax are used. In low power lasers systems Peltier air cooling can replace the water cooling.

In side pumped schemes this is through the top and bottom faces (Figure 1.13a). In end pumped schemes cooling is preformed through the edge faces of the rod (Figure 1.13b). Rods are generally used in end pumped systems in order to achieve symmetry in the heat distribution.

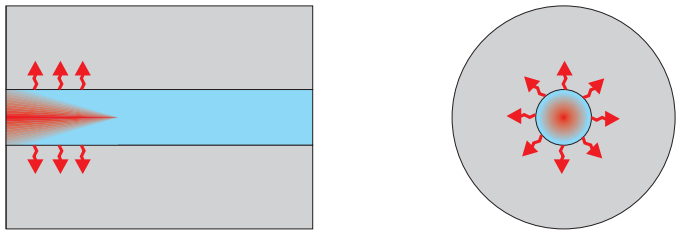

Figure 1.13: Cooling in, a, side pumped, and b, end pumped, laser crystals.

1.5.2 Existing power scaling solutions

1.5.2.1 MOPA systems

Master oscillator power amplifier (MOPA) systems (Figure 1.14) are currently used to generate high power single (spatial and longitudinal) mode lasers. Generally a stable low power laser (the master oscillator) is built with a diffraction-limited, single frequency output. The beam generated by the master oscillator is passed through a Faraday isolator to prevent any feedback, then through the amplifier (or amplifier chain).

In a MOPA system the problems of achieving a single (spatial and longitu-

dinal) mode beam are de-coupled from the problems of power scaling the beam. This property allows high power lasers to be designed and built in such a way that their output power can be scaled by simply adding more amplifiers.

The powers available from MOPA systems under single mode operation are limited by the thermally induced distorting effects in the amplifiers. With out these effects you could theoretically just keep adding more and more amplifier modules to your laser and keep scaling in power indefinitely (as long as any parasitic lasing processes were being suppressed.). The presence of thermally induced distortions such as the quartic phase aberration means that even for the best amplifier designs beam quality will still suffer.

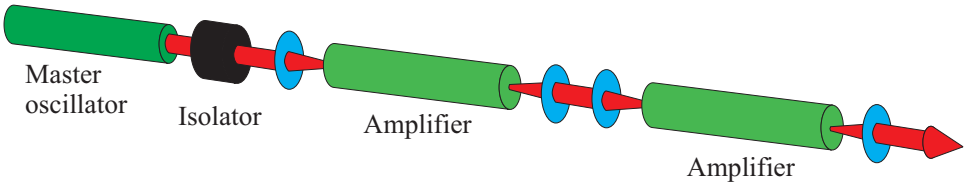

Figure 1.14: A MOPA system.

1.5.2.2 Double clad fibre amplifiers

Another method of avoiding thermal effects is the use of a waveguide geometry, specifically double clad fibre amplifiers. In a double clad fibre amplifier (Figure 1.15) the signal beam is confined to a single mode core whilst the pump beam is transmitted through the (multi mode) cladding. This maintains the beam quality of the signal beam whilst allowing a multimode pump beam to be coupled to it. Fibre lasers of this sort pumped with beam shaped diode stacks have recently reached kilowatt power levels whilst maintaining single mode output.

The thermal effect found in conventional solid state systems are reduced in double clad systems by controlling the pump absorption length. The absorption length is increased from that of a standard core pumped fibre

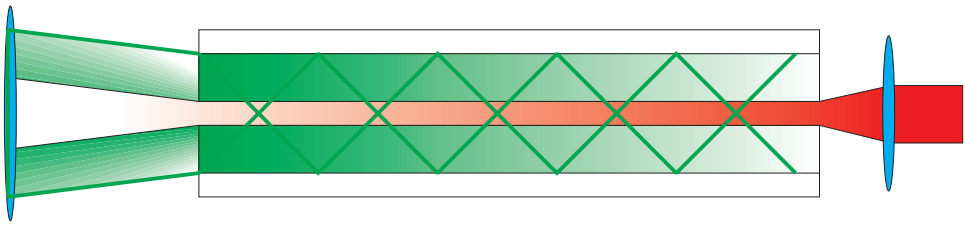

Figure 1.15: Double clad fibre laser/amplifier.

by the ratio of the cladding area to the core area. The absorption length can be increased still further if required by using low dopant concentration fibres. The long absorption length reduces the thermal power deposited per meter to a level that can be easily dissipated.

High fibre lasers and amplifiers do however suffer from problems due to the vast intensities reached in their cores. These intensities can lead to problems with feedback due to nonlinear effects such as Brillouin and Raman scattering. Recent developments of large mode area fibres have helped to combat this [47]. Large mode area fibres have a very small difference in refractive index between the core and cladding. This allows larger core area to be used (Thus increasing the power threshold of any intensity dependent non-linear processes) whilst maintaining confinement on one spatial mode.

1.5.3 Phase conjugate MOPA systems

The ability of phase conjugate systems to dynamically compensate for distortions in beams makes them ideally suited for work in MOPA systems.

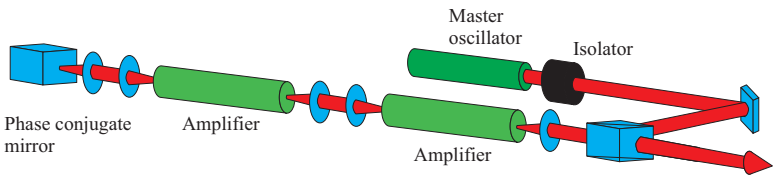

Figure 1.16: Phase conjugate MOPA system.

Figure 1.16 shows a system which was used to produce an output of 520W

average power with M^2=1.2 [48]. The diffraction-limited signal beam was generated by a low power master oscillator (approximately 1W) passed through an optical isolator then into the amplifier chain. On passing through the first amplifier the beam quality had deteriorated to $M^2 \simeq 5$. The distorted beam was reflected by the phase conjugate mirror (in this case a multimode silica fibre achieving phase conjugation via SBS) and passed back through the amplifiers. The final beam had a beam quality of M^2= 1.9.

1.6 Thesis overview

The remainder of this thesis deals with the development of continuous wave phase conjugate systems operating via saturable gain gratings.

Chapter 2 covers the nonlinear process of gain saturation. Side pumped slab amplifiers in a grazing incidence (or bounce) geometry are described as a method of achieving high small signal gains. Four-wave mixing is introduced as a method of achieving phase conjugation in terms of a holographic analogy. The process is then modelled using saturable gain gratings to achieve phase conjugation. Experimental data is then presented on the phase conjugate reflectivities. The contributions of the two gratings which aid phase conjugation are also covered.

Chapter 3 covers the development of a simple phase conjugate oscillator based on saturable gain four-wave mixing. The output powers and temporal properties are modelled and determined experimentally. The development of this into a monolithic system is also discussed.

Chapter 4 describes the operation of a stable holographic resonator based on saturable gain gratings. A non-reciprocal transmission element is inserted into the resonator to enable single longitudinal mode operation and increased output powers. The ability of the resonator to compensate for intra-cavity phase distortions is also demonstrated.

Chapter 5 covers the development of the holographic resonator into a phase conjugate MOPA system. The system is modelled, then realised experimentally and its limiting factors discussed.

Chapter 6 describes the attempts made to achieve phase conjugation via saturable gain gratings in a multimode fibre. The concepts involved in four-wave mixing in fibres along with the various methods of achieving this are covered. Experimental attempts are made to try and observe phase conjugation, and the failure of these experiments is then explained.

1.7 References

[1] B. Ya. Zel'dovich, V.I. Popovichev, V.V. Ragul'skii, F.S. Faizullov, and P.N. Lebedev. Connection between the wave-fronts of the reflected and excited light in stimulated Mandel'shtam-Brillouin scattering. *Soviet Journal JEPT Letters*, 15(3):160–164, 1972.

[2] H. Kogelnik. Holographic image projection through inhomogeneous media. *The Bell System Technical Journal*, 44:2451, 1965.

[3] W.P. Cathey. Holographic simulation of compensation for atmospheric wavefront distortions. *Proceedings of the IEEE*, 56:340, 1968.

[4] T Bearden. *Aids:Biological warfare*. Tesla Book Company, 1988.

[5] A. Yariv. *Optical electronics*, pages 670–684. Saunders College Publishing, fourth edition, 1991.

[6] B. Ya. Zel'dovich, N.F. Pilipetskii, and V.V. Shuknov. *Principles of phase conjugation*, pages 25–65. Springer Verlag, first edition, 1985.

[7] B. Ya. Zel'dovich, N.F. Pilipetskii, and V.V. Shuknov. Experimental investigation of wave-front reversal under stimulated scattering. In R.A. Fisher, editor, *Optical Phase Conjugation*, pages 135–167. Academic Press, London, 1983.

[8] A. Heuer and R Menzel. Principles of phase conjugating Brillouin mirrors. In A. Brignon and J.P. Huignard, editors, *Phase Conjugate Laser Optics*, pages 19–62. John Wiley & Sons, Hoboken, 2004.

[9] G. J. Crofts, M. J. Damzen, and R.A. Lamb. Experimental and theoretical investigation of 2-cell stimulated-Brillouin-scattering systems. *Journal of the Optical Society of America B-Optical Physics*, 18(11):2282–2288, 1991.

[10] H.J. Eichler, A. Mocofanescu, T. Riesbeck, and D. Risse, E. Bedau. Stimulated Brillouin scattering in multimode fibers for optical phase conjugation. *Optics Communications*, 15(4-6):427–431, 2002.

[11] M. Sjöberg, M.L. Quiroga-Teixeiro, S. Galt, and S. Hård. Dependence of stimulated Brillouin scattering in multimode fibers on beam quality, pulse duration, and coherence length. *Journal of the Optical Society of America B-Optical Physics*, 20(3):434–442, 2003.

[12] R.A. Fisher. *Optical Phase Conjugation*. Academic Press, London, 1983.

[13] A. Yariv and D. M. Pepper. Amplified reflection, phase conjugation, and oscillation in degenerate four-wave mixing. *Optics Letters*, 1(1):16–18, 1977.

[14] J.P. Huignard, J.P. Herriau, P. Auborg, and E. Spitz. Phase-conjugate wavefront generation via real-time holography. *Optics Letters*, 4:21, 1979.

[15] D. Fekete, J. AuYeung, and A. Yariv. Phase-conjugate reflection by degenerate four-wave mixing in a nematic liquid crystal in the isotropic phase. *Optics letters*, 5(2):51–53, 1980.

[16] R. L. Abrams and R. C. Lind. Degenerate four-wave mixing in absorbing media. *Optics Letters*, 2(4):94–96, 1978.

[17] J. Reintjes and L. J. Palumbo. Phase conjugation in saturable amplifiers by degenerate frequency mixing. *IEEE Journal of Quantum Electronics*, 18(11):1934–1940, 1982.

[18] A. Yariv. *Optical electronics*, pages 637–669. Saunders College Publishing, fourth edition, 1991.

[19] J Feinberg. Optical phase conjugation in photorefractive materials. In R.A. Fisher, editor, *Optical Phase Conjugation*, pages 417–443. Academic Press, London, 1983.

[20] J.O. White, M. Cronin-Golumb, B. Fischer, and A. Yariv. Coherent oscillation by self-induced gratings in photorefractive crystals. *Applied Physics Letters*, 40:450, 1982.

[21] A. Yariv. *Optical electronics*, page 642. Saunders College Publishing, fourth edition, 1991.

[22] J Feinberg. Self-pumped, continuous-wave phase conjugator using internal reflection. *Optics Letters*, 7(10):486–804, 1982.

[23] R. Tyson. *Principles of adaptive optics*. San Diego Academic Publishing, San Diego, 1991.

[24] O. Graydon. US team breaks power density record, 2004. IOP publishing, http:\\www.Physicsweb.org.

[25] T. Maiman. Stimulated optical radiation in ruby. *Nature*, 187:493–494, 1960.

[26] R.J. Keyes and T.M. Quist. Injection luminescent pumping of CaF_2:U^{3+} with GaAs diode lasers. *Applied Physics Letters*, 4(3):50–52, 1964.

[27] J. Sebastian, F. Bugge, F. Buhrandt, G. Erbert, H.G. Hansel, R. Hulsewede, A. Knauer, W. Pittroff, R. Staske, M. Schroder, H. Wenzel, M. Weyers, and G. Trankle. High-power 810nm GaAsP-AlGaAs

diode lasers with narrow beam divergence. *IEEE Journal on Selected Topics in Quantum Electronics*, 7(2):334338, 2001.

[28] A. Al-Muhanna, L.J. Mawst, D. Botez, D.Z. Garbuzov, R.U. Martinelli, and J.C. Connolly. High-power ($>$ 10W) continuous-wave operation from 100-μm -aperture 0.97-μm -emitting Al-free diode lasers. *Applied Physics Letters*, 73(9):11821184, 1998.

[29] Thales. Laser diode bars, 2004. http:\\www.thales-laser-diodes.com.

[30] Coherent. Diode lasers, 2004. http:\\www.coherentinc.com.

[31] W. Koechner. *Solid-State Laser Engineering*, page 37. Springer-Verlag, forth edition, 1996.

[32] J.R. O'Connor. Unusual crystal-field energy levels and efficient laser properties of YVO_4:Nd. *Applied Physics Letters*, 9(11):407–409, 1966.

[33] R. A. Fields, M. Birnbaum, and C. C. Fincher. Highly efficient Nd:YVO_4 diode-laser end-pumped laser. *Applied Physics B-Lasers and Optics*, 51(23):1885–1886, 1987.

[34] A.W. Tucker, M. Birnbaum, C.L. Fincher, and J.W. Erler. Stimulated-emission cross section at 1064 and 1342nm in Nd:YVO_4 . *Journal of Applied Physics*, 48(12):4907–4911, 1977.

[35] W. Koechner. *Solid-State Laser Engineering*, pages 63–65. Springer-Verlag, forth edition, 1996.

[36] Y. Guyot, H. Manaa, J.Y. Rivoire, R. Moncorge, N. Garnier, E. Descroix, M. Bon, and P. Laporte. Excited-state-absorption and upconversion studies of Nd^{3+} -doped single crystals $Y_3Al_5O_{12}$, $YLiF_4$ and $LaMgAl_{11}O_{19}$. *Physical Review B*, 51:784–799, 1995.

[37] S. Guy, C.L. Bonner, D.P. Shepherd, D.C. Hanna, A.C. Tropper, and B. Ferrand. High-inversion densities in Nd:YAG: Upconversion and bleaching. *IEEE Journal of Quantum Electronics*, 34(5):900–909, 1998.

[38] Y.F. Chen, C.C. Liao, Y.P. Lan, and S.C. Wang. Determination of the Auger upconversion rate in fiber-coupled diode end-pumped Nd:YAG and Nd:YVO_4 crystals. *Applied physics B-Lasers and Optics*, 70(7):487490, 2000.

[39] L. Fornasiero, S. Kuck, T. Jensen, G. Huber, and B.H.T. Chai. Excited state absorption and stimulated emission of Nd^{3+} in crystals. part 2: YVO_4, $GdVO_4$ and $Sr_5(PO_4)_3F$. *Applied Physics B-Lasers and Optics*, 67:449–553, 1998.

[40] W. Koechner. *Solid-State Laser Engineering*, pages 406–468. Springer-Verlag, forth edition, 1996.

[41] J.K. Jabcyński, K. Kopczyński, and A. Szczęśniak. Thermal lensing and thermal aberration investigations in diode-pumped lasers. *Optical Engineering*, 35(12):3572–3578, 1996.

[42] W. A. Clarkson. Thermal effects and their mitigation in end-pumped solid-state lasers. *Journal of Physics D-Applied Physics*, 34(16):2381–2395, 2001.

[43] T.J. Kane, J.M. Egglestone, and R.L. Byer. The slab geometry laser- : Part 2 thermal effects in a finite slab. *IEEE Journal of Quantum Electronics*, 21(8):1195–1210, 1985.

[44] P. Hello, E. Durand, P. K. Fritschel, and C. N. Man. Thermal effects in Nd-YAG slabs 3d modeling and comparison with experiments. *Journal of Modern Optics*, 41(7):1371–1390, 1994.

[45] J.C. Bermudez, V.J. Pinto-Robledo, A.V. Kir'yanov, and M.J. Damzen. The thermo-lensing effect in a grazing incidence diode-side-pumped Nd:YVO_4 laser. *Optics Communications*, 210(1-2):75–82, 2002.

[46] A.E. Seigman. Analysis of laser beam quality degradation caused by quartic phase aberrations. *Applied Optics*, 32(30):5893–5901, 1993.

[47] N.G.R. Broderick, H.L. Offerhaus, D.J. Richardson, R.A. Sammut, J. Caplen, and L. Dong. Large mode area fibers for high power applications. *Optical Fiber Technology*, 5(2):185–196, 1999.

[48] H. J. Eichler and O. Mehl. Phase conjugate mirrors. *Journal of Nonlinear Optical Physics and Materials*, 10(1):43–52, 2001.

Chapter 2

Four-wave mixing in a saturable gain medium

2.1 Introduction

In this chapter four-wave mixing via saturable gain gratings will be introduced as a method of achieving phase conjugation. Gain saturation will be described and the saturated form of the amplifier gain equations derived. Proximity and lensed coupling will be introduced as methods of side pumping Nd:YVO_4 slabs with diode bars. The population inversion and temperature distribution due to side pumping will be modelled for later use.

The side pumped slab will then be used as an amplifier by passing a signal beam through the slab and reflecting it off the pumped face at a grazing incidence (A bounce geometry). This amplifier will be modelled for proximity and lensed coupled pumps and the gains achieved by the two methods will be compared.

The concept of gain gratings will be described from the effect of an interference pattern in a saturable gain medium leading up to the induced nonlinear polarisation. The effect of a gain grating on a Bragg matched probe

field will be derived leading up to a model of the diffraction efficiency of the gratings, and the relative efficiency of transmission and reflection gain gratings will be compared experimentally.

Four-wave mixing will be introduced in terms of a holographic analogy and will subsequently be described analytically and modelled numerically. Experimental data will be presented showing phase conjugate reflectivities approaching 100 times.

2.2 Gain saturation

2.2.1 Gain saturation theory

The gain seen by a small signal (low power) probe beam passing through a four-level optical amplifier depends on the length of the amplifier, its population inversion and the stimulated emission cross section of the laser ion. The gain can be calculated from

$$\frac{dI(z)}{dz} = \alpha_0 I(z) \tag{2.1}$$

where $I(z)$ is the probe beam intensity and α_0 the small signal gain (ssg) coefficient which is given by

$$\alpha_0 = N.\sigma_{se} \tag{2.2}$$

where σ_{se} is the stimulated emission cross section and N the upper state population density [1].

Equation 2.1 can be solved for a probe beam of initial intensity I_0 to give

[1] In a four level system it can be assumed that the the population of the upper laser level (N_2) is far greater than that of the lower level(N_1). Hence we can approximate that $N_2 \sim N_2$-N_1.

$$I(z) = I_0 e^{\alpha_0 z} \tag{2.3}$$

In a real laser medium the gain that can be achieved also depends on the intensity of the probe beam.

When a probe beam is present in an optical amplifier it induces stimulated emission from the excited ions. This reduces the population inversion in the medium and causes the gain to decrease. In a homogeneous medium this effect can be quantified by modifying the gain coefficient to the form shown in equation 2.4 [1].

$$\alpha = \frac{\alpha_0}{1 + \frac{I(z)}{I_{sat}}} \tag{2.4}$$

where α is the gain coefficient and I_{sat} the saturation intensity. The saturation intensity is defined as the signal intensity needed to reduce the gain coefficient to half of its small signal value. The saturation intensity is calculated from

$$I_{sat} = \frac{h\nu}{\sigma_{se}\tau} \tag{2.5}$$

where h is Planck's constant, ν the frequency of the seed beam and τ the fluorescence lifetime.

The saturated gain coefficient (Equation 2.4) can now be used to modify the small signal gain equation (Equation 2.1) to give the saturable gain equation

$$\frac{dI(z)}{dz} = \alpha_0 \frac{I(z)}{1 + \frac{I(z)}{I_{sat}}} \tag{2.6}$$

Equation 2.6 is solved analytically for a single input beam of initial intensity I_0 to give

$$\ln\left(\frac{I(z)}{I_0}\right) + \frac{I(z) - I_0}{I_{sat}} = \alpha_0 z \tag{2.7}$$

The effects of gain saturation on an amplifier can be seen in figure 2.1. Here a probe beam is passed through an amplifier with a small signal gain of 10. The green dotted line shows the gain seen without gain saturation taken into account, while the blue solid line shows the effect of gain saturation.

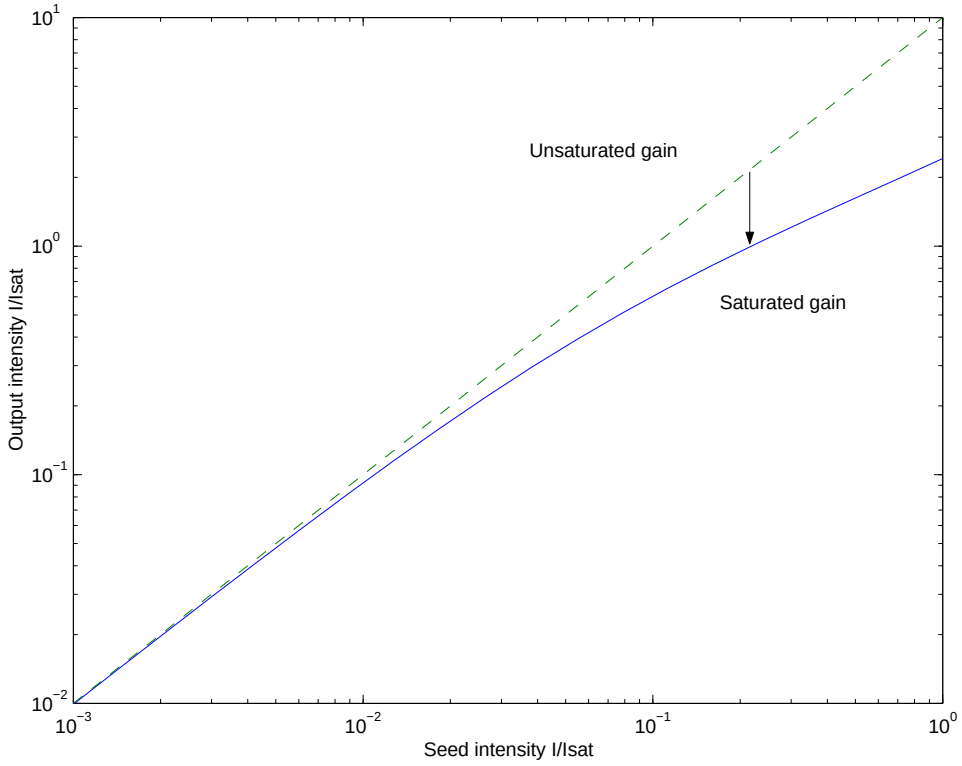

Figure 2.1: A comparison of gains from saturated and unsaturated amplifiers.

2.2.2 Gain saturation in Nd:YVO_4

Nd:YVO_4 is a uniaxial crystal and as such has different stimulated emission cross sections along its c and a/b axes. This asymmetry causes the pump absorption, saturation intensity and gain coefficient to be polarisation dependent.

The stimulated emission cross sections along the a and b axis (see table A.1) are a factor of ∼3.5 less than that along the c-axis. The small signal gain coefficients (equation 2.2) and the saturation intensities (equation 2.5) differ by the same factor.

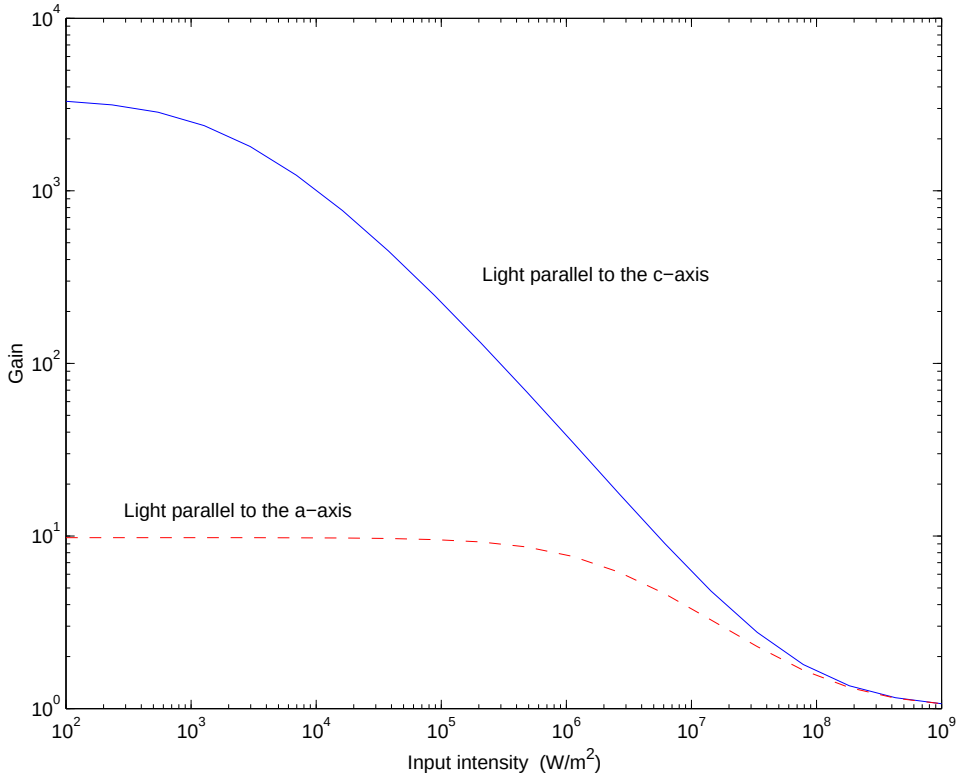

Figure 2.2: The gain profile of beams polarised parallel to the a and c crystal axes.

The higher stimulated emission cross section seen by light polarised parallel to the crystal's c-axis causes the gain to be far higher than that for light polarised perpendicular to it. Figure 2.2 shows a comparison of the gain profiles for beams of both polarisations passing through the same amplifier. Here it can be seen that the beam polarised parallel to the c-axis sees a small signal gain that is a factor of ∼300 greater than that for a beam polarised parallel to the a-axis.

2.3 Side pumping with laser diode bars

2.3.1 Methods of side pumping with diode bars

Laser diode bars are arrays of many closely packed single emitter laser diodes. The combined output of these emitters gives an elliptical beam ideal for side pumping slab amplifiers.

In the vertical direction (y) the bars aperture is roughly the same width as the wavelength of the light that it emits (The aperture is $\sim$1μm compared with a emission wavelength of 0.8μm). In this direction the beam is near diffraction limited with a large divergence angle (see figure 2.3b).

In the horizontal direction (z) the diode bar consists of many near diffraction limited lasers placed next to each other. When these beams are combined the effect is roughly the same as a highly multimode beam (M^2s of thousands) being emitted from a 1cm aperture. This causes the beam to be emitted with a small diverge angle (see figure 2.3c).

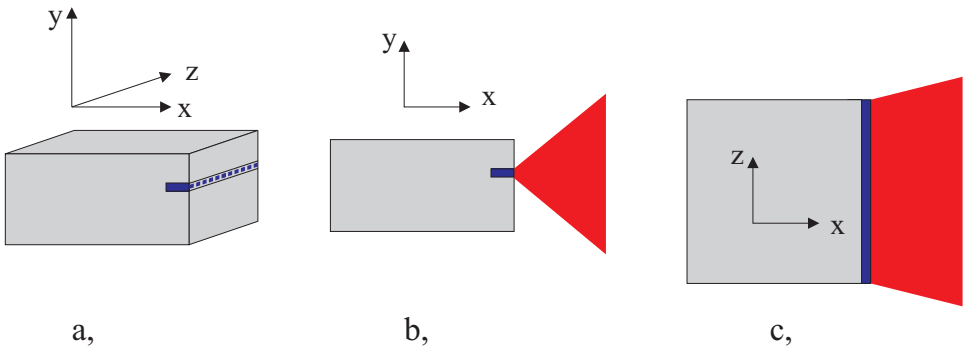

Figure 2.3: a, A diode bar. b, Output diverges rapidly in the vertical (y) direction. c, Output diverges slowly in the horizontal (z) direction

Two methods of side pumping will be described here, namely proximity coupling and lensed coupling.

2.3.1.1 Lensed coupling

Figure 2.4 shows the pump light from a diode bar being collimated by a fibre lens then focused onto the face of a laser crystal with a cylindrical lens. By adjusting the distance from the lens to the crystal the size of the pumped region can be controlled.

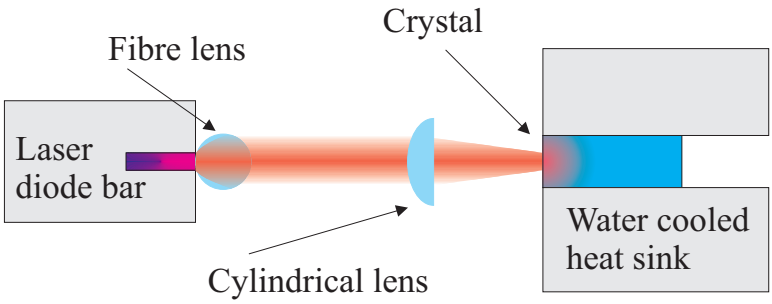

Figure 2.4: Side pumping with a lens-coupled diode-bar pump system.

2.3.1.2 Proximity coupling

Proximity coupling a diode bar to a crystal involves placing the diode bar next to the crystal and directly coupling in the light, as shown in figure 2.5.

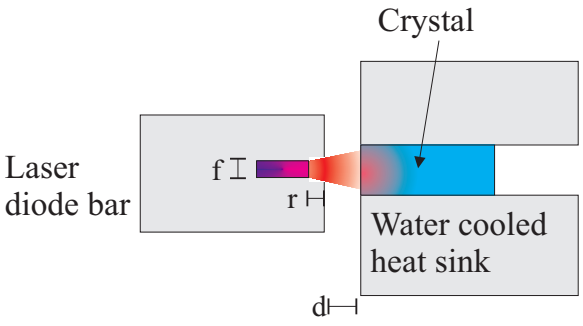

Figure 2.5: Side pumping with a proximity coupled diode bar system.

Proximity coupling has the advantage of being the much simpler system. There are no focusing components needed, resulting in lower losses and therefore more efficient pumping than the lensed system. The spot size is limited by the diode's facet height, beam divergence and recess. Whilst

the facet height has little effect, the recess of the emitters into the bar can be up to 200µm , severely limiting the potential spot size.

The vertical pump spot size (w_{py})at the crystal face can be calculated from the (FWHM) divergence angle of the diode (θ_{div}) which is typically around 35° , the facet height (f), recess (r) and distance from the diode bar to crystal face (d).

$$w_{p_y} = \frac{f + 2(d + r)\tan(\theta_{div})}{2} \tag{2.8}$$

2.3.2 Side pumping Nd:YVO_4 crystal slabs

The amplifiers used in the majority of the bulk work found in this thesis are 1.1%at doped a cut Nd:YVO_4 slabs. These slabs are described in detail in appendix A. They are (unless otherwise stated) all 1mm by 5mm by 20mm with a 3 degree wedge to prevent parasitic lasing. The front b-face (1mm by 20mm) is AR (anti reflection) coated for 808nm and the two side a-faces are AR coated for 1064nm. The crystals are water cooled through copper heat sinks on the top and bottom c-faces (5mm by 20mm).

2.3.2.1 Modelling the pump distribution

The pump distribution through the amplifier is dependent on the pump absorption length, spot size at the crystal face and beam divergence. The absorption coefficient (α_p) at 808nm for pump light polarised parallel to the crystal c-axis in 1.1%at doped Nd:YVO_4 is 31.2 cm^{-1} (9.2 cm^{-1} for light polarised parallel to the a-axis). The short absorption length means that 99% of the pump light is absorbed in the first 1.5mm of the crystal.

The vertical beam quality of the pump beam from the diode bars used in these experiments was M_y^2 = 5.5 for the 60W fibre lensed Coherent bars

and M_y^2 = 5 for the 40W IMC bars. When these are focused with a 6.3mm focal length lens a ∼30µm spot size is achieved.

$$Z_r = \frac{\pi w_0^2 n}{M^2 \lambda} \tag{2.9}$$

The Rayleigh range (Z_r) of the pump beam is ∼900 µm (calculated from equation 2.9)which is significantly less than the absorption length ($1/e^2$∼300µm). This means that it is justified to assume that the radius of the pump beam does not change across the pumped region, and as such any divergence of the pump beam can be ignored.

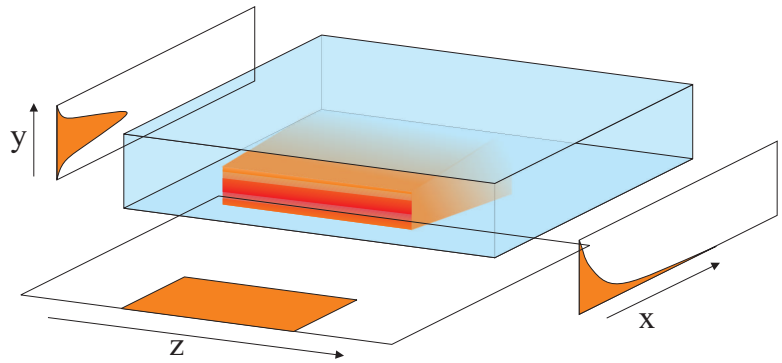

Figure 2.6: The pump distribution in a side-pumped crystal.

Figure 2.6 shows a schematic of the pump distribution in a side-pumped Nd:YVO_4 crystal. The intensity of the pump beam through the crystal is given by (using the coordinate set defined in figure A.2)

$$I(x,y,z) = \begin{cases} I\left(\frac{-x_0}{2},0,0\right) e^{\frac{-2y^2}{w_{p_y}^2}} e^{-\alpha_p\left(x-\frac{-x_0}{2}\right)} & \text{if } |z| < w_{p_z} \\ 0 & \text{if } |z| > w_{p_z} \end{cases} \tag{2.10}$$

assuming a Gaussian distribution of power in y and a top hat distribution in z. w_{p_y} is the pump beam vertical spot size (∼30µm) and w_{p_z} the pump beam width (remaining approximately constant at 1cm).

The power incident on the pump face can now be calculated as:

$$\begin{aligned} P_{incident} &= \int_{area} I_p\left(\frac{-x_0}{2}, y, z\right) dA \\ &= \int_{y=-\infty}^{y=\infty}\int_{z=\frac{-z_0}{2}}^{z=\frac{-z_0}{2}} I_p\left(\frac{-x_0}{2}, y, z\right) dy.dz \\ &= I_p(\frac{-x_0}{2}, 0, 0) w_{p_z} \int_{y=-\infty}^{y=\infty} e^{\frac{-2y^2}{w_{p_y}^2}} dy \\ &= I_p\left(\frac{-x_0}{2}, 0, 0\right) w_{p_y} w_{p_z} \sqrt{\frac{\pi}{2}} \end{aligned} \tag{2.11}$$

Rearranging equation 2.11 for $I_p\left(\frac{-x_0}{2}, 0, 0\right)$ and substituting it into equation 2.10 gives

$$I_p(x, y, z) = \begin{cases} \frac{P_{incident}}{w_{p_y} w_{p_z} \sqrt{\pi/2}} e^{\frac{-2y^2}{w_{p_y}^2}} e^{-\alpha_p\left(x - \frac{-x_0}{2}\right)} & \text{if } |z| < w_{p_z} \\ 0 & \text{if } |z| > w_{p_z} \end{cases} \tag{2.12}$$

2.3.2.2 Population inversion

The steady state population inversion of a laser medium can be calculated from the pump rate and fluorescence lifetime.

The pump rate (R) is given as the number of excited ions created per second per unit volume (assuming no ground state depletion or competing spectroscopic processes) . The pump beam is travelling in the x-direction so the depletion along this axis is used to find the number of ions created.

$$R(x, y, z) = -\frac{d}{dx} I_p(x, y, z) \frac{1}{h\nu} \tag{2.13}$$

$$R(x, y, z) = \frac{\alpha_p I_p(x, y, z)}{h\nu} \tag{2.14}$$

which gives the population inversion at all points in the crystal of

$$N(x,y,z) = \frac{\alpha_p I_p(x,y,z)\tau_f}{h\nu} \tag{2.15}$$

2.3.3 Thermal effects in side-pumped amplifiers

When any laser medium is pumped, heat is deposited. In Nd:YVO_4 this is via the quantum defect [2] and spectroscopic effects such as energy transfer upconversion [3], which are discussed in detail in Koechner [4].

2.3.3.1 Temperature distribution

The temperature distributions for side-pumped slabs in single bounce and zigzag geometries have been studied for a range of materials (see references [5] , [6] and [7] for examples). More recently the steady state thermal load on a side-pumped Nd:YVO_4 crystal slab with cooling from the top and bottom (the c-faces) has been calculated by Bermudez et al [8]. His solution is derived from a superposition of the solution to the homogeneous heat equation and the particular solution for the boundary conditions [7] and can be found in appendix B. The boundary conditions and materials used in Bermudez's solution to the heat equation are exactly the same as those used in the experiments in Nd:YVO_4 in this thesis and his model for the temperature distribution will therefore be used.

Figures 2.7, 2.8 and 2.9 show the calculated temperature distribution for pumping at a range of powers focused to a 100μm by 10mm spot in the centre of the pump face.

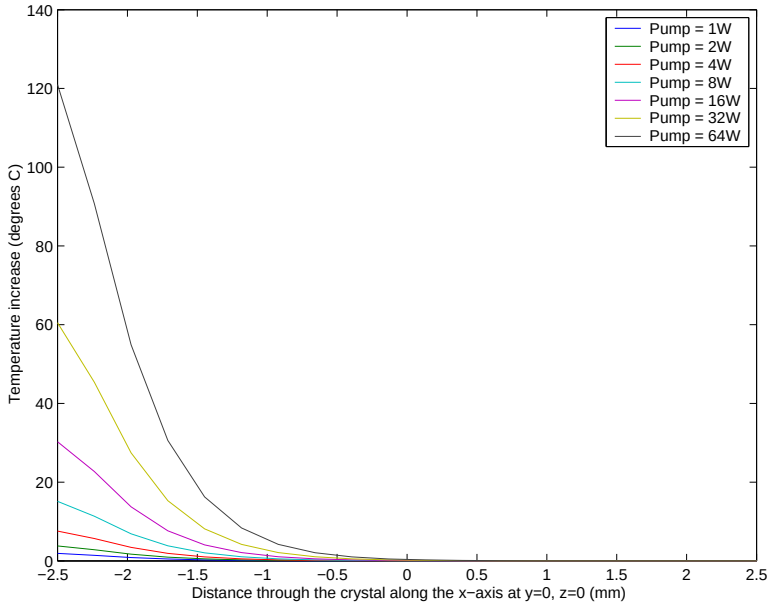

Figure 2.7: The temperature distribution through a side-pumped Nd:YVO_4 slab as a function of distance through the crystal along the x-axis at y=0, z=0 (mm).

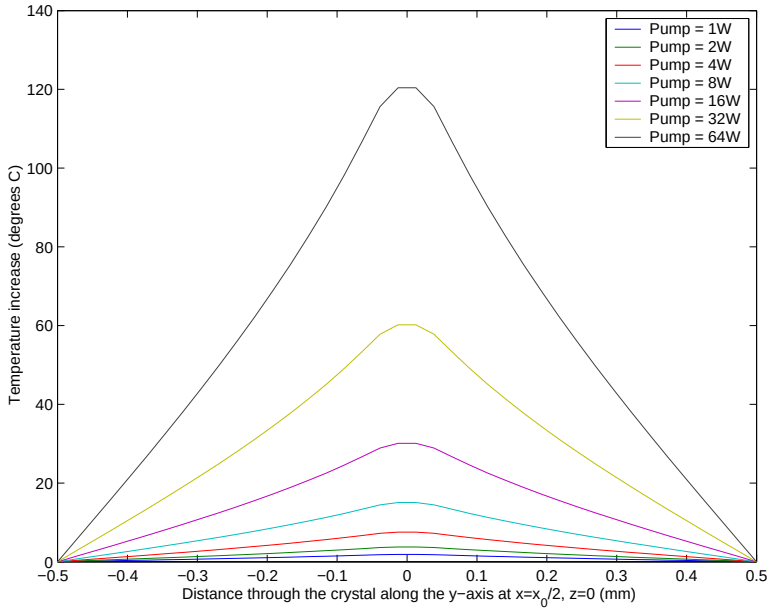

Figure 2.8: The temperature distribution through a side-pumped Nd:YVO_4 slab as a function of distance through the crystal along the y-axis at $x=x_0/2$, z=0 (mm).

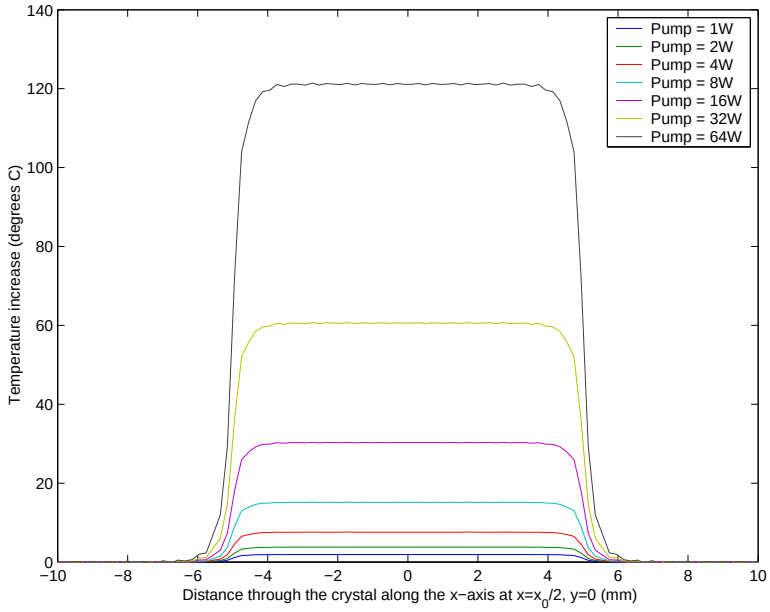

Figure 2.9: The temperature distribution through a side-pumped Nd:YVO_4 slab as a function of distance through the crystal along the z-axis at x=$x_0/2$, y=0 (mm).

2.3.3.2 Refractive index distribution

The refractive index change due to the thermal load in a pumped crystal can be calculated from the sum of the effective temperature-induced refractive index changes and the thermally induced stress.

$$\Delta n_i(x,y,z) = \left(\frac{dn}{dT}\right)_{eff} T(x,y,z) - B_{eff}\sigma_{ii} \tag{2.16}$$

Where T is the temperature increase, $(dn/dT)_{eff}$ is the effective temperature dependent refractive index coefficient and B_{eff} is the stress optical coefficient (both of these terms are dependent on the polarisation of the light passing through the crystal). σ_{ii} is the stress in direction i where $i = x, y, z$ [5]

Bermudez [8] shows that in side-pumped slabs of Nd:YVO_4 with a bounce geometry with a small angle of incidence (a grazing incidence geometry [9]) the stress optical effect is far weaker (roughly 1/30th) than the directly

temperature dependent term. Under this assumption equation 2.16 can be simplified to

$$\Delta n_i(x, y, z) = \frac{dn}{dT} T(x, y, z) \tag{2.17}$$

where the incident beam is polarised parallel to the c-axis of the crystal.

2.4 Side-pumped, bounce geometry amplifiers

2.4.1 The bounce geometry

The bounce geometry amplifier was developed by Bernard and Alcock for use in laser [9] and amplifier [10] configurations. In this geometry a slab amplifier is side-pumped with a diode bar. A signal beam is passed though the amplifier and reflected off the pumped face of the slab at a grazing incidence as shown in figure 2.10.

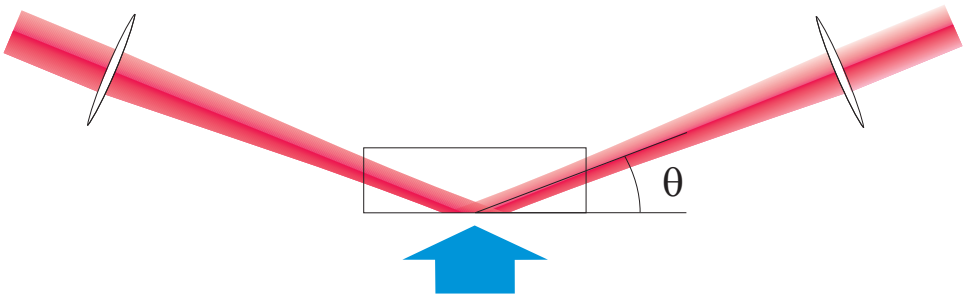

Figure 2.10: The bounce geometry.

Maximum overlap between the signal and pump beams is achieved by ensuring that the vertical diameter of the pump beam matches that of the focused spot of the seed beam. The angle that the seed beam is launched is chosen such that the overlap with the pumped region is maximised whilst avoiding diffraction effects from the edge of the crystal.

The bounce geometry is particulary suited for work with Nd:YVO_4 due

to its short absorption length ($\sim$300μm). Other side pumping geometries present difficulties accessing the region of highest gain. The bounce geometry gives a horizontally symmetric gain across the signal beam removing the need for the two bar pumping commonly used in multi-pass and zigzag amplifiers.

2.4.2 Modelling single pass gains

The side-pumped amplifier can be modelled using the population inversion calculated in equation 2.15. A focused beam is passed through the crystal, bouncing off the pumped face and the saturated gain calculated by integrating equation 2.1 along the path of the beam. Special attention must be paid to the region close to the pumped face of the crystal, where the signal beam overlaps with itself, complicating the gain calculations.

In this model the effects of energy transfer upconversion (ETU, see section 1.4.2.1) and amplified spontaneous emission (ASE) have been ignored. At the levels of pump intensity reached here ETU does not significantly effect the gain available for the laser beam. ASE will however act to reduce the extremely high small signal gains modelled here. In the regions in which we are experimentally interested however ASE is a negligible effect and as such has not been included in the model.

2.4.2.1 Deriving the model

The population inversion in a Nd:YVO_4 slab amplifier is calculated using equation 2.15 for an 808nm pump beam of 35W focused into a spot of 1cm $\times$ 30μm and aligned to overlap with the signal.

A diffraction-limited 1064nm signal beam is passed through the pumped Nd:YVO_4 amplifier in a bounce geometry with an internal incidence angle, θ, of 4° . The beam is focused to a 30μm spot at the pumped face of the amplifier. The Rayleigh range of the signal beam inside the crystal

is 11.4mm, which means that the beam can be approximated as having a constant radius whilst passing through the pumped region of the crystal.

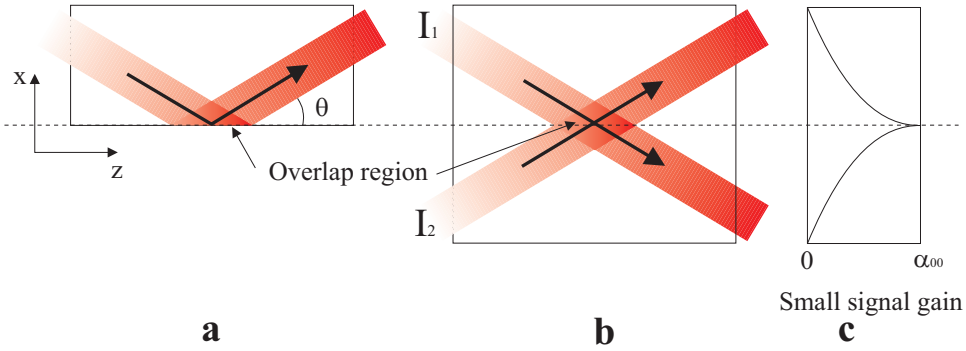

Figure 2.11: a, The bounce geometry. b,Two beams passing through a mirrored crystal replicating the bounce. c, The small signal gain coefficient of the mirrored crystal analogy.

The bounce geometry (shown in figure 2.11a) will be treated as two identical intersecting beams passing through a single crystal (figure 2.11b) with the small signal gain coefficient varying as shown in figure 2.11c. The crystal modelled here is effectively two of the real pumped crystals stuck together at their pumped faces. When the beams pass through the crystals they intersect at the region of highest gain replicating the overlap seen in the bounce geometry. The total intensity of the beams (needed to calculate the saturated gain equation) can be found by simply adding the intensities of the two beams at any point (Neglecting interference). The following coupled gain equations are produced

$$\frac{dI_1}{dp} = \alpha_0(x,y,z)\frac{I_1}{1+\frac{I_1+I_2}{I_{sat}}} \tag{2.18}$$

$$\frac{dI_2}{dp} = \alpha_0(x,y,z)\frac{I_2}{1+\frac{I_1+I_2}{I_{sat}}} \tag{2.19}$$

These are solved numerically by simultaneously tracing the two beams through the crystal and calculating the saturated gain at each point. Figure 2.12 shows a plot of the total seed intensity in the y=0 plane as two

beams pass through the system. The dashed line shows where the reflection occurs in the bounce geometry.

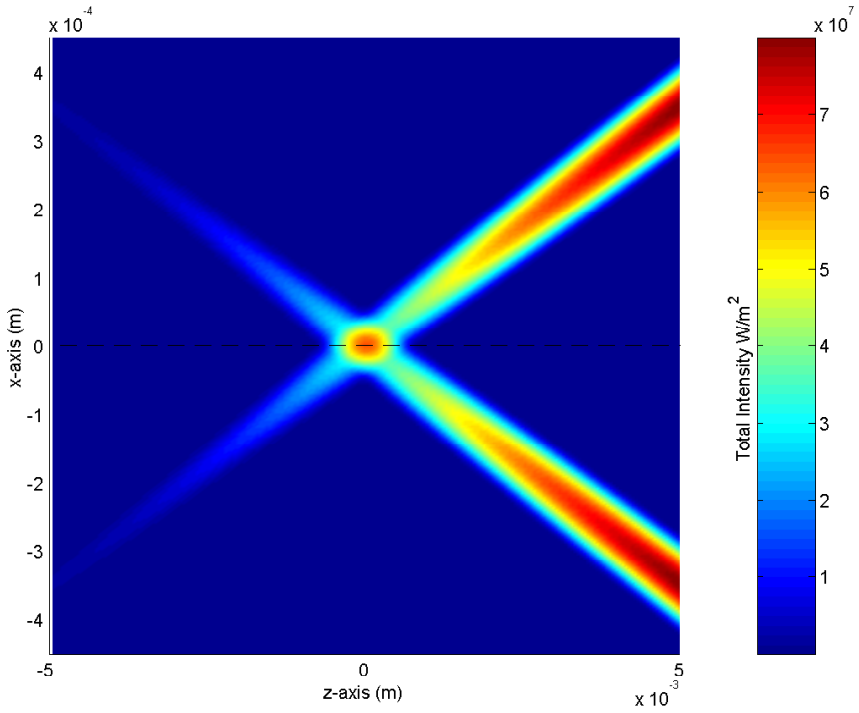

Figure 2.12: Two beams passing through the symmetrical gain region described in figure 2.11c.

2.4.2.2 Beam expansion

One of the disadvantages of the bounce geometry amplifier is that the amplified beam is expanded asymmetrically. This is due to the asymmetry in the shape of the gain region. The total unsaturated gain seen along the path of the beam has a gaussian distribution in the y-direction and a (roughly) flat distribution in the x-direction.

In the y-direction the shape of the intensity profile of the beam is unaffected by amplification as the Gaussian shape of the gain region matches that of the signal beam. At the centre of the beam the high intensity causes the gain to saturate where as in the wings the gain remains unsaturated. This causes the amplification to be roughly constant across the beam.

In the x-direction however the flat gain profile means that the wings will see more gain than the middle of the beam causing the beam to broaden. This has the effect that when a signal beam with a circular intensity profile (figure 2.13a) is passed through the amplifier it is emitted with an elliptical profile (figure 2.13b).

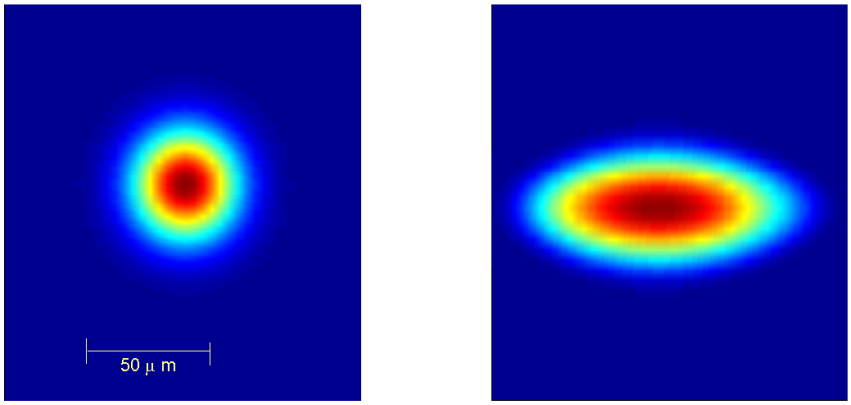

Figure 2.13: a, Beam on entry to the amplifier. b, Beam expands asymmetrically as it is passed through the amplifier. Intensities are normalised to allow the beams to be compared.

2.4.2.3 Modelling results varying the launch angle

Figure 2.14 shows the change in gain as a function of internal bounce angle. The small signal gain increases as the incidence angle is reduced. In a real crystal where the beam has a finite size, if the angle that it makes with the pumped face is too small diffraction effects from the edge of the crystal will cause it to scatter. This is an effect known as clipping.

2.4.2.4 Modelling results for a constant size signal beam

Figure 2.15 shows the change in gain with varying pump spot sizes for a constant radius seed beam (30μm). The small signal gain rapidly decreases with increasing pump spot size, as the overlap between the beams is reduced and the extraction efficiency (and therefore the gain) falls.

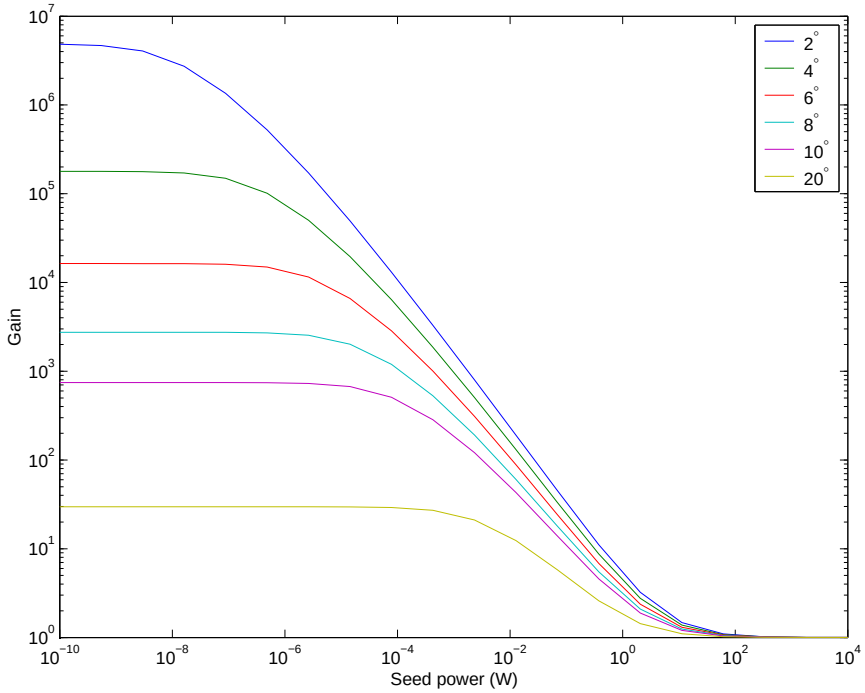

Figure 2.14: Gain profiles for a bounce geometry amplifier as a function of internal bounce angle.

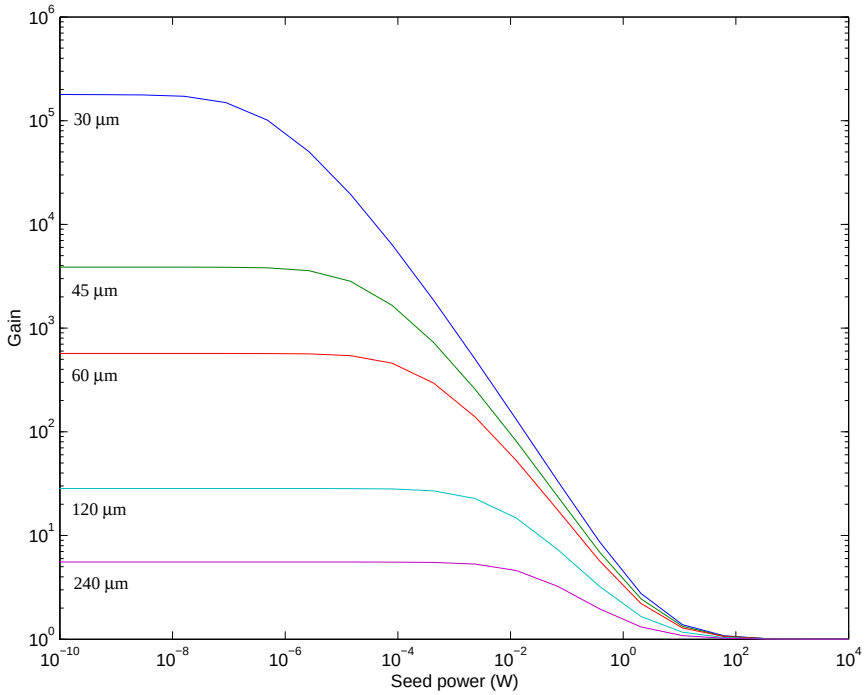

Figure 2.15: Gain profiles for a bounce geometry amplifier as a function of the pump beam spot size (for a seed beam of a fixed radius of 30µm) .

2.4.2.5 Modelling results with pump/signal overlap kept constant

Figure 2.16 shows the gain profiles where the spot size of the signal beam and the vertical spot size of the pump beam are equal over a range of spot sizes. Reducing the spot size of the beams causes the small signal gain to increase. This is to be expected as the population inversion will be increased so the small signal gain coefficient will increase.

For higher signal powers the opposite becomes true (see the enlarged section of figure 2.16). When the spot sizes are increased the intensity of the signal beam decreases. This results in saturation occurring at higher powers for larger beams.

This shows that in order to achieve high small signal gains tightly focused beams are needed. To achieve greater gains at high powers however a larger area beam is preferable.

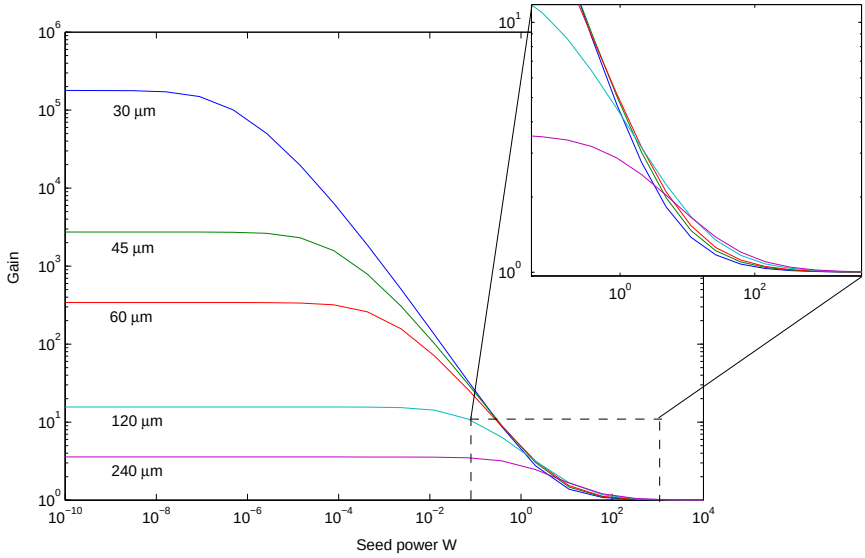

Figure 2.16: Gain profiles for a bounce geometry as a function of spot size where the pump and signal beams are the same size.

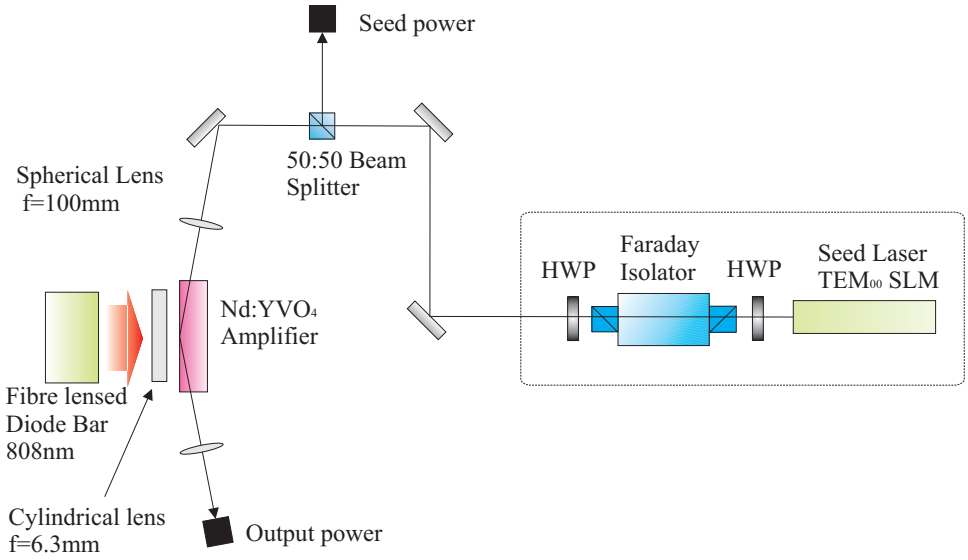

Figure 2.17: Experimental setup for measuring the gain achieved by the side-pumped bounce geometry amplifier

2.4.3 Single pass gain experimental

Figure 2.17 shows the apparatus used to measure the single pass gains achieved from a side-pumped amplifier in a bounce geometry. Experiments were performed using both lensed and proximity coupled pumping (Figure 2.17 shows the lensed case only). The amplifier used in these experiments is a 1.1%at doped a-cut Nd:YVO_4 crystal described in appendix A.

2.4.3.1 Amplifier setup

The seed beam is produced by a SLM (single longitudinal mode), TEM_{00} laser (from Crystalaser) emitting a 300mW, 1064nm beam with a 1mm spot size. The seed beam is initially passed through a half-wave plate (HWP) then a Faraday isolator. The combination of the HWP and the first polariser of the Faraday isolator act as a variable attenuator.

The beam is then passed through a second half-wave plate which is used to adjust the polarisation for maximum gain. The beam is passed through

a 50:50 beam splitter (so that the seed power can be observed without disturbing the experiment) and is then focused into the Nd:YVO_4 crystal with a 100mm focal length spherical lens. The beam is reflected off the pumped face of the crystal and re-collimated by a second 100mm focal length spherical lens.

2.4.3.2 Lensed coupled pumping

In the lensed coupling experiments the amplifier is pumped with a 40W TM polarised 808nm diode bar. The pump beam is collimated at the facet of the diode bar with a fiber lens. It is then focused onto the centre of the front b-face of the amplifier with a 6.3mm focal length cylindrical lens. The overlap between the pump and signal beams is controlled by defocusing the 6.3mm lens.

2.4.3.3 Proximity coupled pumping

In the proximity coupling experiments a 40W TM polarised 808nm diode bar is placed next to the amplifier as shown in figure 2.5. The overlap between the pump and signal beams is controlled by varying the distance between the crystal and diode bar.

2.4.4 Single pass amplification results

2.4.4.1 Lensed coupling results

Figure 2.18 shows the gain profiles for the side-pumped amplifier with a $\sim 7^\circ$ external angle ($\sim 3^\circ$ internal). The blue squares show the gain profile when the pump beam is optimally overlapped with the signal beam. It also shows the reduced gains achieved with a de-focused pump beam (the red diamonds and green triangles).

The solid lines are modelled data produced using a pump power of 40W focused to pump sizes of 30µm (the blue line), 60µm (the red line) and 90µm (the green line).

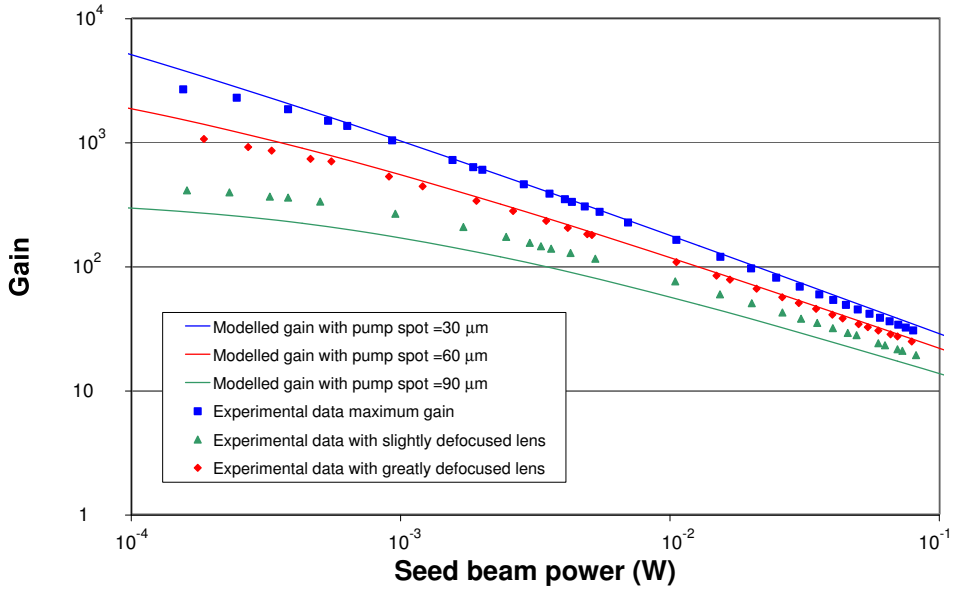

Figure 2.18: Gain profiles for the lensed coupled side-pumped bounce geometry amplifier with reducing overlap between pump and signal beams.

2.4.4.2 Proximity-coupling results

Figure 2.19 shows the gain seen by a 0.5mW probe beam as a function of the separation between the diode bar and amplifier. When the diode bar and crystal are brought closer the gain seen by the probe beam increases as expected (the pump spot size is related to the separation distance by equation 2.8) . When the separation reaches $\sim$ 50µm the gain profile flattens out.

Figure 2.20 shows the best small signal gain profile achieved with the proximity coupled pumping. The recess of the diode emitters into the bar such that the true distance between the face of the crystal and the waist of the beam is $\sim$200 µm greater than that measured (the theoretical line shown in figure 2.20 is equivalent to a 192µm separation between diode facet and crystal face.). This means that the small pump spot sizes needed to achieve

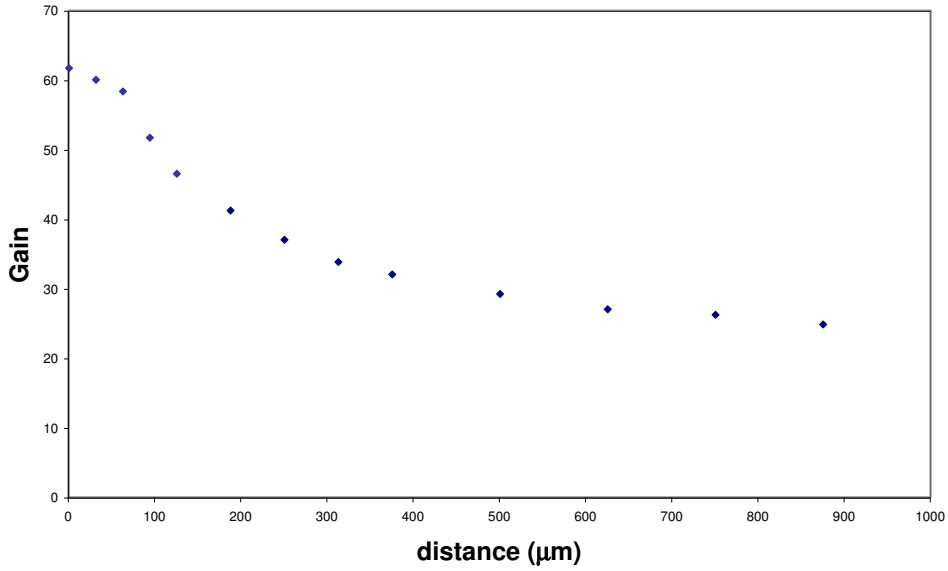

Figure 2.19: Gain as a function of diode-crystal separation for the proximity-coupled side-pumped bounce geometry amplifier.

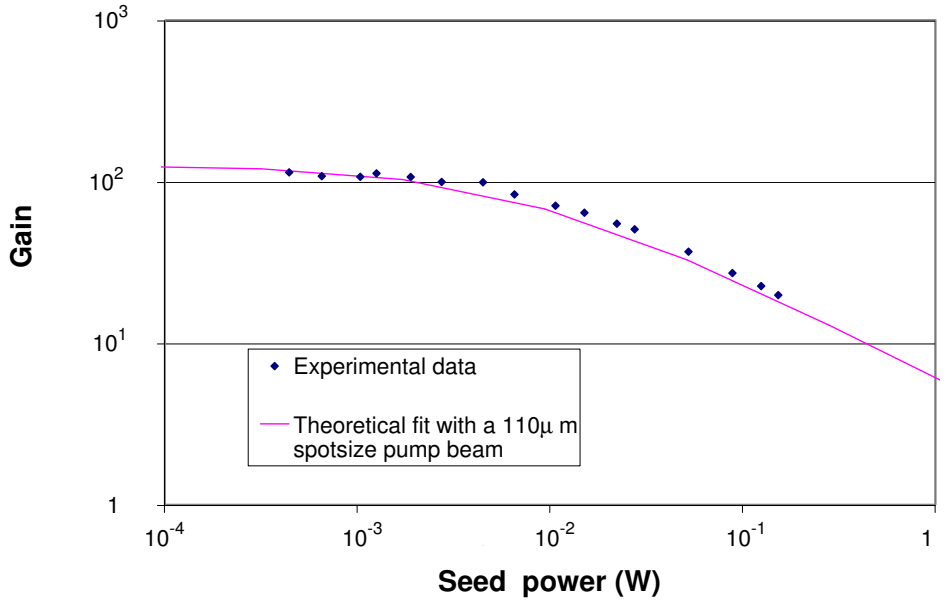

Figure 2.20: Gain profile for the proximity coupled side-pumped bounce geometry amplifier with a theoretical fit for a 110μm pump spot size.

high small signal gains are unobtainable. Further attempts to improve the efficiency of the proximity coupled system resulted in damage to both the diode bar and crystal.

2.4.5 Modelling the amplifier with multiple signal beams

When many signal beams are present in the same gain medium calculating the amplification characteristics become more complicated. In the following model it will be assumed that all beams are counter or co-propagating, have the same spot size and occupy the same region of space. In the majority of experiments in this thesis this is true, where the beams are not exactly counter or co-propagating they still overlap almost completely in the regions of highest gain.

The assumption that the beams share the same space and directionality means that all of the beams propagating in the same direction can be considered to be one beam with a power equal to sum of its constituent parts.

Consider two sets of beams counter-propagating through a gain medium.

$$B_{Left} = [I_{1L}, I_{2L}, I_{3L}...] \tag{2.20}$$

$$B_{Right} = [I_{1R}, I_{2R}, I_{3R}...] \tag{2.21}$$

The total intensity passing in each direction is the sum of each of these sets.

$$I_L = \sum_i I_{iL} \tag{2.22}$$

$$I_R = \sum_i I_{iR} \tag{2.23}$$

Once the system has been simplified to a two signal beam situation it can be described as a pair of coupled differential equations.

$$\frac{dI_L(z)}{dz} = \alpha_0(x,y,z)\frac{I_L(z)}{1+\frac{I_L(z)+I_R(z)}{I_{sat}}} \quad (2.24)$$

$$\frac{dI_R(z)}{dz} = \alpha_0(x,y,z)\frac{I_R(z)}{1+\frac{I_L(z)+I_R(z)}{I_{sat}}} \quad (2.25)$$

Figure 2.21 shows an example of an amplifier with two beams counter-propagating through it with initial intensities of $I_L = 0.12I_{sat}$ and $I_R = 0.06I_{sat}$. Initial estimates of the gains seen by the two beams are made by passing each of them through the gain medium and calculating the gain they see (the dashed lines in figure 2.21). The saturated gain coefficient is calculated from the sum of the intensities of the beams at each point in space. A relaxation is then performed to find the gain seen by each beam (the solid lines in figure 2.21).

The model derived here is used as the basis for much of the subsequent theoretical work in this thesis.

2.5 Four-wave mixing theory

Four-wave mixing is a method of achieving phase conjugation and is analogous to dynamic holography. Three beams intersect in a nonlinear material generating a fourth which is the phase conjugate of one of the beams. In these experiments four-wave mixing is achieved via gain saturation.

2.5.1 The holographic analogy

Four-wave mixing can be most easily visualised by first considering simple static holography. In order to write a hologram an interference pattern

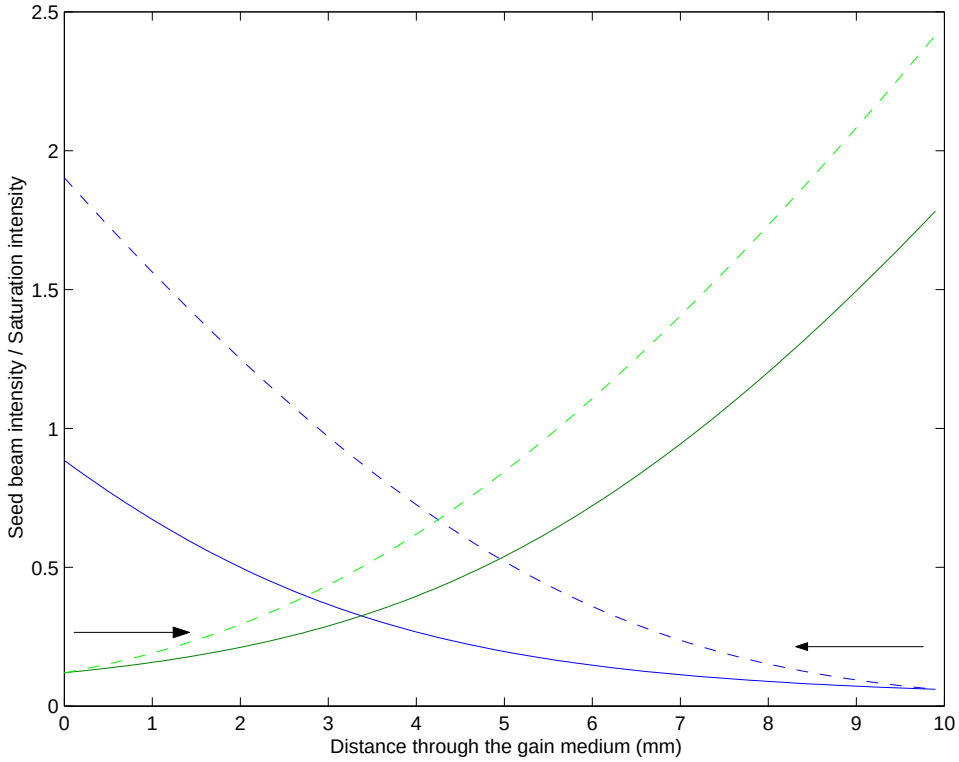

Figure 2.21: Two counter-propagating beams passing through the same gain medium. The dashed lines are beams passing through the medium independently. The solid lines are the case where the saturation is calculated taking into account the presence of both beams.

is formed between an image and reference beam on (or in) a piece of holographic material (such as a photographic plate) as shown in figure 2.22. The writing beams are then extinguished and the hologram developed.

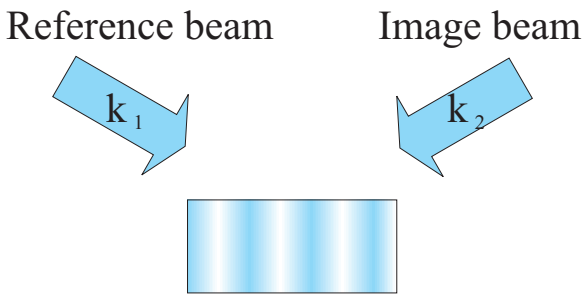

Figure 2.22: Writing a simple hologram.

The image and reference beams are defined as

$$\begin{aligned} \varepsilon_{reference} &= E_1 e^{ik_1 \cdot r + \omega t} + c.c. \\ \varepsilon_{image} &= E_2 e^{ik_2 \cdot r + \omega t} + c.c. \end{aligned} \tag{2.26}$$

which, when they interfere give

$$I = |E_1|^2 + |E_2|^2 + 2E_1 E_2 \cos((k_1 - k_2) \cdot r) \tag{2.27}$$

A replica of the reference beam is then used to illuminate the hologram (figure 2.23).

Assuming that the transmittance (τ) of the hologram is proportional to I then the amplitude of the holographic output will be the product of the transmission and the incident beam.

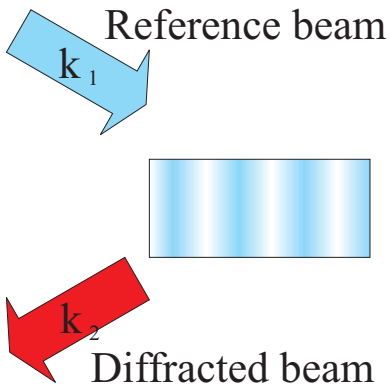

Figure 2.23: Reading a simple hologram with the reference beam.

$$\tau E_1 e^{-ik_1 r} = E_1^2 E_1 e^{-ik_1 r} + E_2^2 E_1 e^{-ik_1 r} + E_1 E_2 E_1 e^{i(k_2 - 2k_1)\cdot r} + E_1 E_2 E_1 e^{-ik_2 \cdot r} \tag{2.28}$$

Here the first two terms are light transmitted in the same direction as the incident beam. The third term is scattered off and can be ignored. The fourth term of the equation is transmitted in the same direction as the signal beam as a replica of its wavefront.

2.5.1.1 Achieving phase conjugation through holography

If the grating is instead illuminated with a replica of the reference beam travelling in the opposite direction, the transmitted intensity is

$$\tau E_1 e^{ik_1 r} = E_1^2 E_1 e^{ik_1 r} + E_2^2 E_1 e^{ik_1 r} + E_1 E_2 E_1 e^{-i(k_2 - 2k_1)\cdot r} + E_1 E_2 E_1 e^{ik_2 \cdot r} \tag{2.29}$$

Again the first two terms are in the direction of the incident beam and the third term is scattered off and can be ignored. The fourth term of the equation travels along k_2 but with the opposite sign k-vector. The transmitted beam is travelling back along the path of the signal beam, effectively as its

phase conjugate.

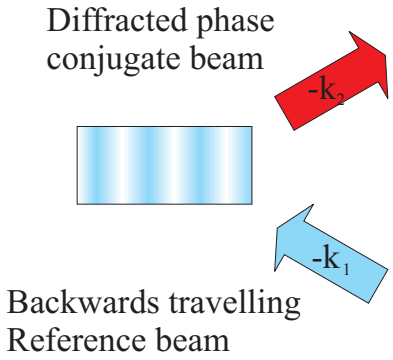

Figure 2.24: The reading of a simple hologram with a reference beam travelling in the opposite direction to the writing beam. A phase conjugate of the signal is generated.

2.5.2 Writing a gain grating

When two coherent beams of the same polarisation intersect they interfere to form a standing wave. If this occurs in an excited saturable gain medium a gain grating will be formed.

Figure 2.25 shows two beams intersecting and forming an interference pattern in an excited gain medium. At the nodes there will be a region of low intensity so the population is unaffected. At the antinodes the intensity is high causing the population to be depleted. This process is known as spatial hole burning. The modulation in the population inversion will cause the gain coefficient to vary forming a gain grating, and this gain grating formed is π out of phase with the interference pattern.

This process can be described analytically by taking two plane waves

$$\mathscr{E}_{left} = A_1.e^{(ik_1 \cdot r + wt)} + cc \quad (2.30)$$

$$\mathscr{E}_{right} = A_2.e^{(ik_2 \cdot r + wt)} + cc \quad (2.31)$$

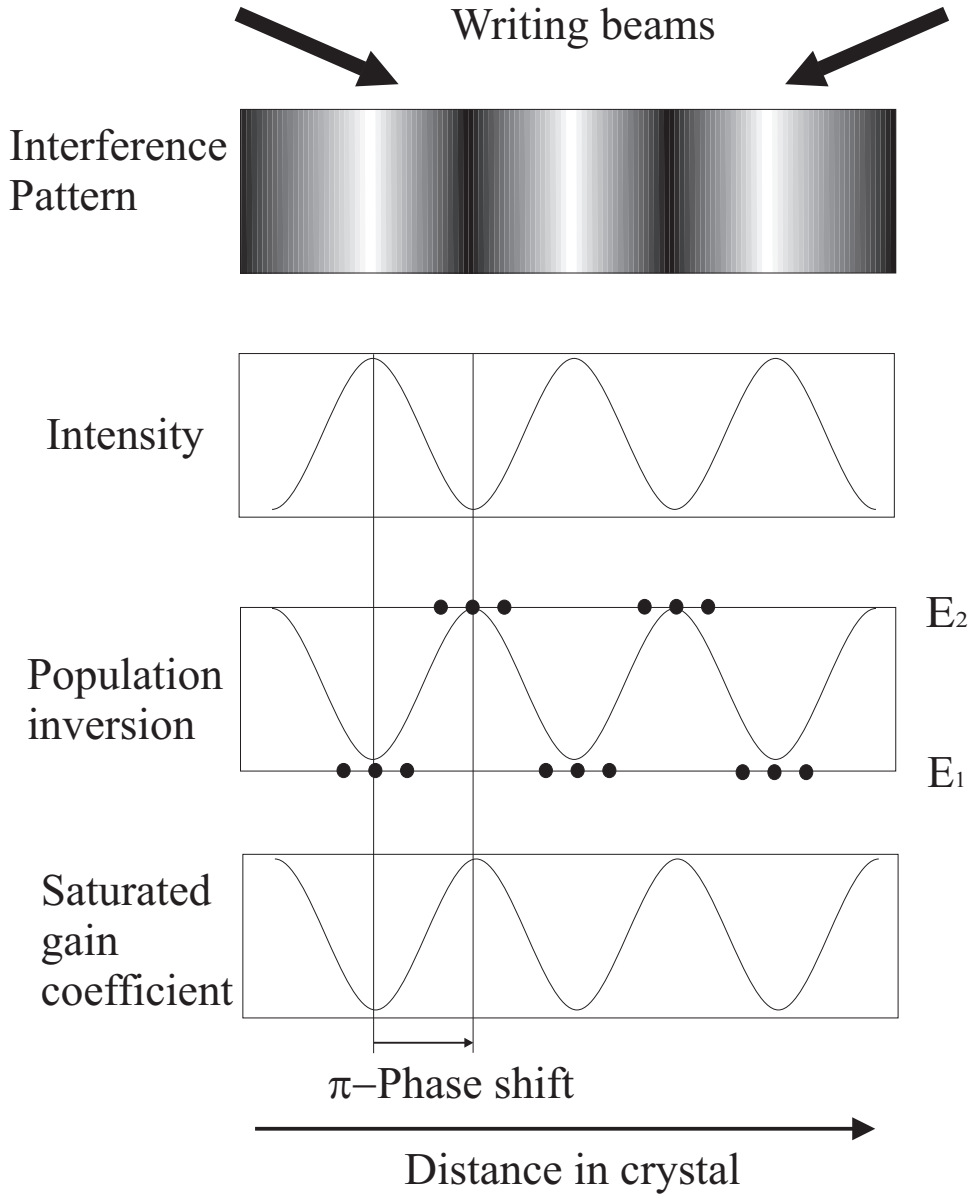

Figure 2.25: The formation of a gain grating by an interference pattern in an excited saturable gain medium.

and interfering them

$$\begin{aligned} E_T.E_T^* &= (\mathscr{E}_{left} + \mathscr{E}_{right})(\mathscr{E}_{left} + \mathscr{E}_{right})^* \\ &= \left(A_1 e^{(ik_1\cdot r+wt)} + A_2 e^{(ik_2\cdot r+wt)}\right)\left(A_1 e^{-i(k_2\cdot r+wt)} + A_2 e^{-i(k_2\cdot r+wt)}\right) \\ &= A_1A_1^* + A_2A_2^* + A_1A_2^* e^{i(k_1-k_2)\cdot r} + A_1^*A_2 e^{i(k_2-k_1)\cdot r} \\ E_T.E_T^* &= A_1^2 + A_2^2 + 2A_1A_2\cos\left((k_1-k_2)\cdot r\right) \end{aligned} \tag{2.32}$$

Using

$$I = \frac{1}{2} nc\varepsilon_0 EE^* \tag{2.33}$$

the total time averaged intensity is then given by

$$I_{av} = I_1 + I_2 + 2\sqrt{I_1 I_2}\cos\left((k_1-k_2)\cdot r\right) \tag{2.34}$$

When this occurs in an excited laser medium the gain coefficient is modulated by the intensity of the standing wave.

$$\alpha = \frac{\alpha_0}{1 + \frac{I_{av}}{I_{sat}}} \tag{2.35}$$

Equation 2.35 can now be expanded and simplified to give

$$\alpha = \frac{\alpha_0}{1 + \frac{I_1+I_2+2\sqrt{I_1 I_2}\cos((k_1-k_2)\cdot r)}{I_{sat}}} \tag{2.36}$$

$$\alpha = \Upsilon \frac{1}{1+\Omega\cos(\theta)} \tag{2.37}$$

where

$$\begin{aligned} \Upsilon &= \frac{\alpha_0}{1+\frac{I_1+I_2}{I_{sat}}} \\ \Omega &= \frac{2\sqrt{I_1 I_2}}{I_{sat}+I_1+I_2} \\ \theta &= (k_1-k_2)z \end{aligned} \tag{2.38}$$

assuming that the grating k-vector lies only in the z-direction and any other components cancel.

For two beams of intensity I= $I_{sat}/10$, counter-propagating through an amplifier with a small signal gain of 1000, (figure 2.26a), the resultant gain gratings can be seen in figure 2.26b.

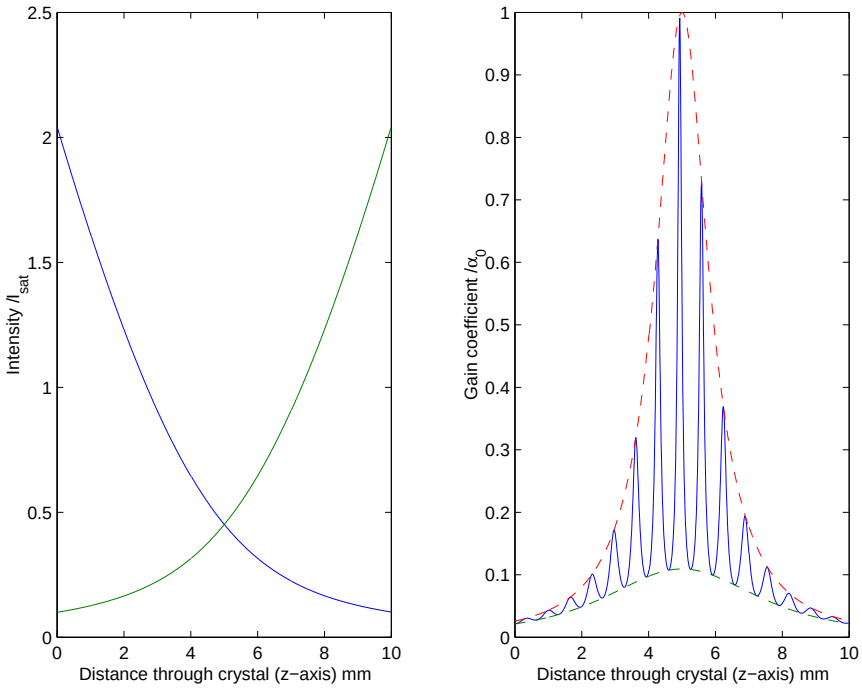

Figure 2.26: a and b Two beams counter-propagating through an amplifier (ssg=1000) interfere to write gain gratings.

The dashed lines are the maximum and minimum values of the gain coefficient at each point. The grating shown here has an arbitrarily large period for clarity (The true period is $\lambda_0/2n$ = 245nm)

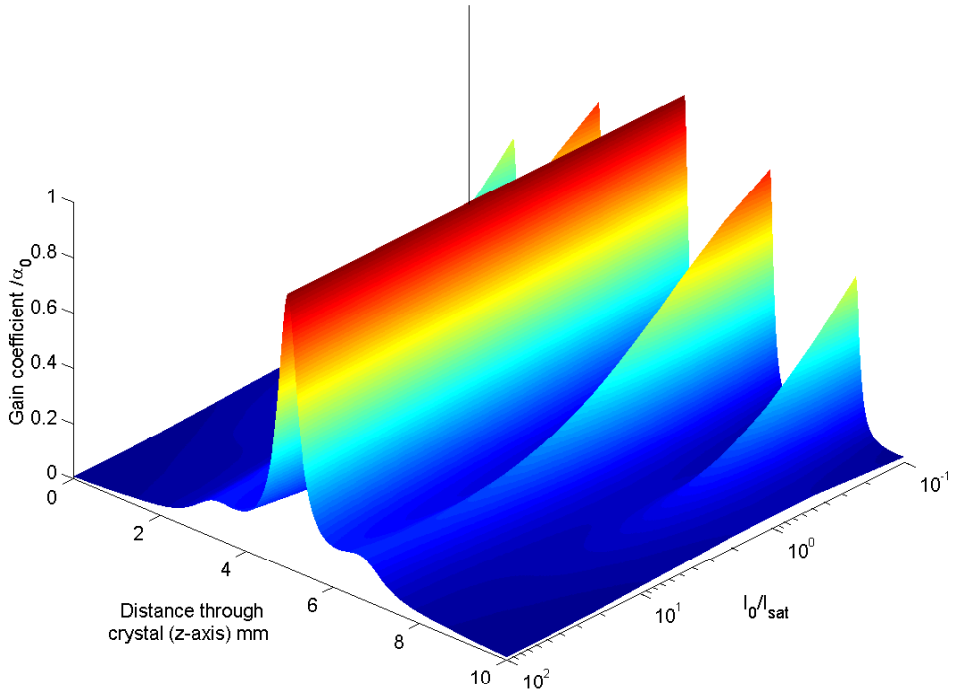

Figure 2.27: Gain gratings formed for a range of initial writing beam intensities.

Figure 2.27 shows the strength of the gain gratings as a function of the writing beams initial intensity. Increasing the intensity of the beams causes the contrast ratio of the grating to increase which will improve its diffraction efficiency [11].

2.5.3 Diffraction from a gain grating

In order to find the effect that a gain grating has on an incident optical field (degenerate but not coherent with the writing fields) the nonlinear polarisation induced by the gain grating must be found [12]. This is then substituted into the nonlinear Maxwell wave equation to find the effect on the probe field.

2.5.3.1 The nonlinear polarisation due to a gain grating

The nonlinear polarisation caused by gain saturation is given by [2]

$$\wp^{at}(r,t) = \mathbf{P}^{at}e^{i\omega t} + cc \tag{2.39}$$

where the complex polarisation amplitude ($\mathbf{P}^{at}$)is given by

$$\mathbf{P}^{at} = \epsilon_0 \chi^{at} \mathbf{E}_{total} \tag{2.40}$$

and the atomic susceptibility due to a homogeneously broadened transition due to gain saturation is [13]

$$\chi^{at} = i\frac{2\alpha}{k} \tag{2.41}$$

Substituting in the gain coefficient calculated in equation 2.35 gives a total atomic susceptibility of

$$\chi^{at} = \frac{2i}{k}\frac{\alpha_0}{1+\frac{I_1+I_2+2\sqrt{I_1 I_2}\cos((k_1-k_2)\cdot r)}{I_{sat}}} \tag{2.42}$$

or simplified using equation 2.37 and the substitutions from equations 2.38

$$\chi^{at} = \frac{2i}{k}\Upsilon\frac{1}{1+\Omega\cos(\theta)} \tag{2.43}$$

This can now be expanded via a Fourier cosine series of the form

$$\chi^{at} = \frac{2i}{k}\sum_{n=0}^{\infty}\alpha_g^{(n)}(z)\cos(n\theta)$$

[2] This derivation adapted from Syed et al [12].

$$= \frac{1}{2}\frac{2i}{k}\sum_{n=0}^{\infty}\alpha_g^{(n)}(z)\left(e^{in\theta}+e^{-in\theta}\right) \tag{2.44}$$

with harmonic coefficients given by

$$\alpha_g^{(0)} = \frac{\Upsilon}{\sqrt{1-\Omega^2}} \tag{2.45}$$

$$\alpha_g^{(n)} = (-1)^n\frac{2\Upsilon}{\sqrt{1-\Omega^2}}\left(\frac{1-\sqrt{1-\Omega^2}}{\Omega}\right)^n \tag{2.46}$$

2.5.3.2 The wave equations

The polarisation calculated above is now substituted into the nonlinear Maxwell wave equation (Equation 2.47). An optical field (degenerate but incoherent with the writing fields) is then applied and the diffracted field found.

$$\nabla^2\mathbf{E} = \frac{n^2}{c^2}\frac{\partial^2\mathbf{E}}{\partial t^2} + \mu_0\frac{\partial^2\wp}{\partial t^2} \tag{2.47}$$

This can be simplified using the slowly varying envelope approximation [14]

$$\begin{aligned} |k^2\mathbf{A}| &\gg |k\frac{\partial\mathbf{A}}{\partial z}| \gg |\frac{\partial^2\mathbf{A}}{\partial z^2}| \\ |\omega^2\mathbf{A}| &\gg |\omega\frac{\partial\mathbf{A}}{\partial t}| \gg |\frac{\partial^2\mathbf{A}}{\partial t^2}| \end{aligned} \tag{2.48}$$

and assuming plane waves (the paraxial approximation)

$$\frac{\partial\varepsilon}{\partial x} = \frac{\partial\varepsilon}{\partial y} = 0 \tag{2.49}$$

to give

$$\left(\frac{\partial}{\partial z}+\frac{n}{c}\frac{\partial}{\partial t}\right)\varepsilon_T=-\frac{i\mu_o\omega^2}{2k}\wp \tag{2.50}$$

where ε_T is the total electric field incident on the gain grating averaged over one optical period and $\wp$ is the complex amplitude of the nonlinear polarisation.

Assuming the degenerate case the incident electric field consists of two components, the incident field and the diffracted field.

$$\begin{aligned}\varepsilon_T &= \varepsilon_i+\varepsilon_d &(2.51)\\ \varepsilon_T &= E_ie^{i(k_i\cdot r+\omega t)}+E_de^{i(k_d\cdot r+\omega t)} &(2.52)\end{aligned}$$

In order to diffract off the grating the probe field must be Bragg-matched to the grating. Degenerate reading beams must counter (or co-) propagate with the writing beams. In the counter-propagation case $k_i\cdot r=-k_1z$ and $k_d\cdot r=-k_2z$.

The nonlinear polarisation due to this incident field and the Fourier expansion form of the gain grating (equation 2.44) is given by

$$\begin{aligned}\mathbf{P}_{NL} = \frac{i\epsilon_0}{k}\Big(&\alpha_g^{(0)}\left(E_ie^{-ik_1z}+E_de^{-ik_2z}\right)+\\ &+\alpha_g^{(1)}e^{i(k_1-k_2)z}\left(E_ie^{-ik_1z}+E_de^{-ik_2z}\right)+\\ &+\alpha_g^{(1)}e^{-i(k_1-k_2)z}\left(E_ie^{-ik_1z}+E_de^{-ik_2z}\right)+\\ &+\alpha_g^{(2)}\ldots\Big)\end{aligned} \tag{2.53}$$

Equation 2.50 can now be applied to each field individually where $\mathbf{P}_j$ is

the part of the nonlinear polarisation that contributes to the jth incident field. This contribution can be found by selecting the phase-matched components of the nonlinear polarisation.

$$\left(\frac{\partial}{\partial z}+\frac{n}{c}\frac{\partial}{\partial t}\right)\varepsilon_j=-\frac{i\mu_o\omega^2}{2k}\mathbf{P}_j \tag{2.54}$$

The following coupled differential equations are produced by selecting the phase-matched terms for each probe field.

$$+\frac{dE_i}{dz}=\gamma E_i+\kappa E_d \tag{2.55}$$

$$-\frac{dE_d}{dz}=\gamma E_d+\kappa E_i \tag{2.56}$$

where

$$\gamma = \alpha_g^{(0)} \tag{2.57}$$

$$\kappa = \alpha_g^{(1)} \tag{2.58}$$

2.5.3.3 Numerical modelling

The coupled differential equations (Equations 2.55 and 2.56) can be used to give a great insight into diffraction from a gain grating. The equations describe the growth of each of the probe field terms as they pass through the gain grating. The first term describes how each field is amplified through the self-coupling coefficient γ. The second term describes how each field is amplified (or attenuated) by diffraction of the other field from the gain grating.

The coupled differential equations are solved numerically using relaxation techniques. Figure 2.28 shows the reflectivity of the gain gratings as a function of the writing beams intensity for a fixed intensity seed beam. The

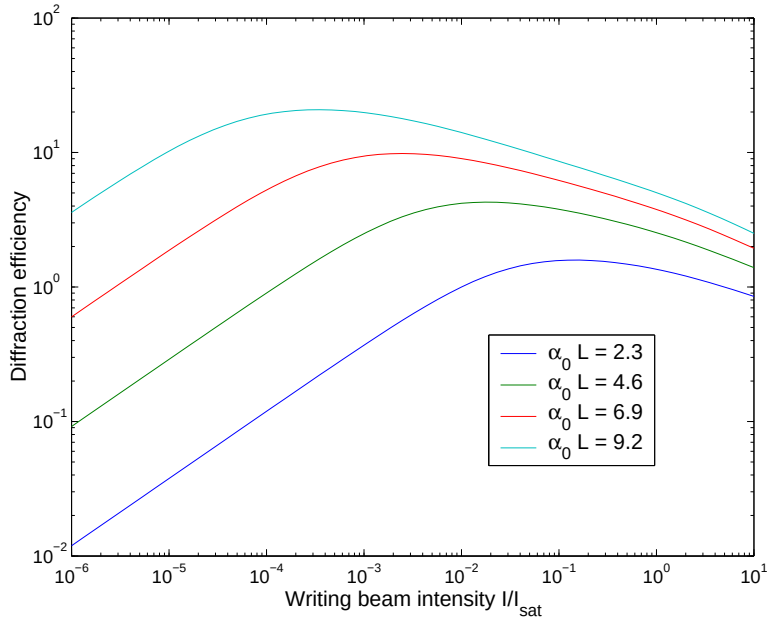

Figure 2.28: Diffraction efficiency of a gain grating as a function of writing beam intensities.

diffraction efficiency initially rises steeply as the gain gratings are formed and their diffraction efficiency increases. The efficiency peaks at the saturation intensity then decreases as the writing beams extract more of the gain from the system.

2.5.4 Degenerate four-wave mixing

In degenerate four-wave mixing all of the beams are present all of the time. If these beams are coherent and of the same polarisation then they will all interfere with each other forming many gratings. In the degenerate case in order to achieve Bragg-matching between the gratings the beams need to counter-propagate. The gratings formed are shown in figure 2.29.

This derivation is adapted from a derivation by Crofts and Damzen, our collaborators on this project at Imperial College London and a full version can be found in appendix C. Consider a material illuminated simultaneously with four optical fields, where E_T is the total complex electric field amplitude.

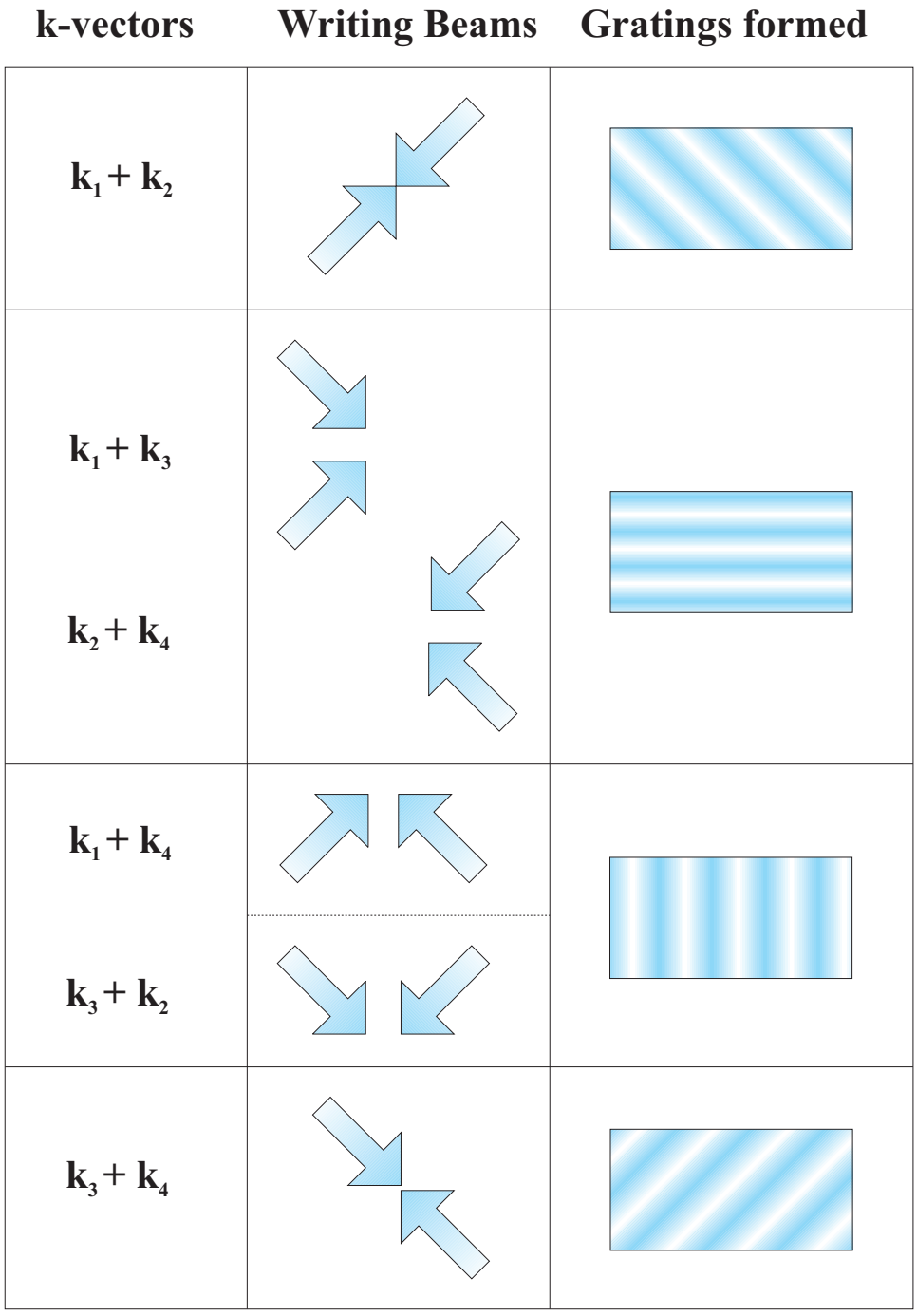

Figure 2.29: Interference patterns formed with two sets of counter-propagating beams interfering with each other.

$$E_T = A_1 e^{-ik_1 \cdot r} + A_2 e^{-ik_2 \cdot r} + A_3 e^{-ik_3 \cdot r} + A_4 e^{-ik_4 \cdot r} \tag{2.59}$$

where the slowly varying amplitude, A_j describes the amplitude, phase and polarisation state of the jth electric field, and k_j is the wave vector.

Fields A_1 and A_2 counter-propagate along the z_1 axis while fields A_3 and A_4 counter-propagate along the z_2 axis as shown in figure 2.30 where θ is the small angle between the two k-vectors.

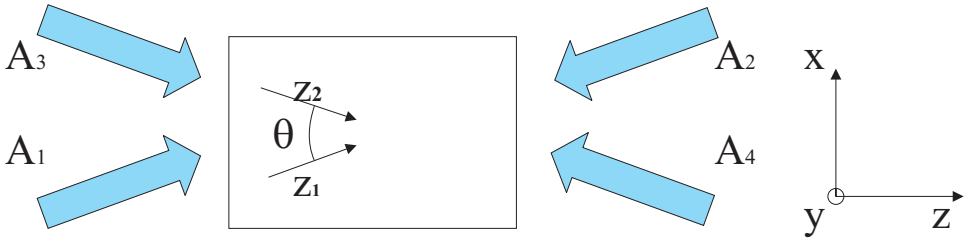

Figure 2.30: Four optical fields (A_1 A_2 A_3 and A_4) intersect in a crystal. A_1 and A_2 counter-propagate along z_1, A_3 and A_4 counter-propagate along z_2.

The k vectors of the four beams can be defined in terms of the angle subtended by the fields relative to the z-axis.

$$k_{1,2} = \pm k\hat{z}_1 = \pm k\left(\hat{x}\sin(\theta/2) + \hat{z}\cos(\theta/2)\right) \tag{2.60}$$

$$k_{3,4} = \pm k\hat{z}_2 = \pm k\left(-\hat{x}\sin(\theta/2) + \hat{z}\cos(\theta/2)\right) \tag{2.61}$$

where the '+' terms are k_1 and k_3 and the '-' terms are k_2 and k_4 and $\hat{x}, \hat{y}, \hat{z}_1$ and $\hat{z}_2$ are the unit vectors in their respective directions.

The total time-averaged intensity in the medium is calculated from equation 2.33 to give

$$\frac{I_T}{I_{sat}} = \sigma + |\tau|\cos\left(K_\tau x - \phi_\tau(z)\right) + |\rho|\cos\left(K_\rho z - \phi_\rho(z)\right) \tag{2.62}$$

where

$$K_\tau = k(z_1 - z_2) \qquad K_\rho = k(z_1 + z_2) \tag{2.63}$$

$$\sigma = \frac{1}{A_s}\sum_{j=1}^{4} A_j(z,t)A_j^*(z,t) \tag{2.64}$$

$$\tau = |\tau|e^{i\phi_\tau} = \frac{2}{A_s^2}\left(A_1A_3^* + A_2^*A_4\right) \tag{2.65}$$

$$\rho = |\rho|e^{i\phi_\rho} = \frac{2}{A_s^2}\left(A_1A_4^* + A_2^*A_3\right) \tag{2.66}$$

and the interactions between A_1 and A_2, and A_3 and A_4 are ignored.

The effect of the gain grating on the optical fields is then found by inserting the Fourier expansion of the modulated gain (equation 2.62) into the non-linear Maxwell wave equation and applying the slowly varying envelope and plane wave approximations.

The following set of coupled differential equations are then produced describing the steady state interactions with the transmission grating

$$+\frac{dA_1}{dz} = \gamma_\tau A_1 + \kappa_\tau A_3 \tag{2.67}$$

$$-\frac{dA_2}{dz} = \gamma_\tau A_2 + \kappa_\tau^* A_4 \tag{2.68}$$

$$+\frac{dA_3}{dz} = \gamma_\tau A_3 + \kappa_\tau^* A_1 \tag{2.69}$$

$$-\frac{dA_4}{dz} = \gamma_\tau A_4 + \kappa_\tau A_2 \tag{2.70}$$

and the reflection grating;

$$+\frac{dA_1}{dz} = \gamma_\rho A_1 + \kappa_\rho A_4 \tag{2.71}$$

$$-\frac{dA_2}{dz} = \gamma_\rho A_2 + \kappa_\rho^* A_3 \tag{2.72}$$

$$+\frac{dA_3}{dz} = \gamma_\rho A_3 + \kappa_\rho A_2 \quad (2.73)$$

$$-\frac{dA_4}{dz} = \gamma_\rho A_4 + \kappa_\rho^* A_1 \quad (2.74)$$

where the coupling terms are found from the Fourier transform of the gain grating and given by.

$$\gamma_g(z) = \alpha_g^{(0)}(z) \quad (2.75)$$

$$\kappa_g z = \frac{1}{2}\alpha_g^{(1)} \quad (2.76)$$

2.5.5 Numerical modelling

The coupled differential equations (Equations 2.74) have been previously solved by Crofts and Damzen [15] and more recently their solution expanded by Dr. Jason Hendricks (a co-student on this project) and these solutions will be shown here for completeness.

Figure 2.31 shows the phase conjugate reflectivities as a function of writing beam power for the reflection grating (blue lines) and transmission grating (red lines).

When the writing beam powers are initially increased the gain grating contrast ratio increases. This causes the diffraction efficiency to rise and the phase conjugate output to increase. This increase in output begins to decrease as the writing beams start to saturate the amplifier. The output then falls as the power available from the amplifier is extracted by the writing beams.

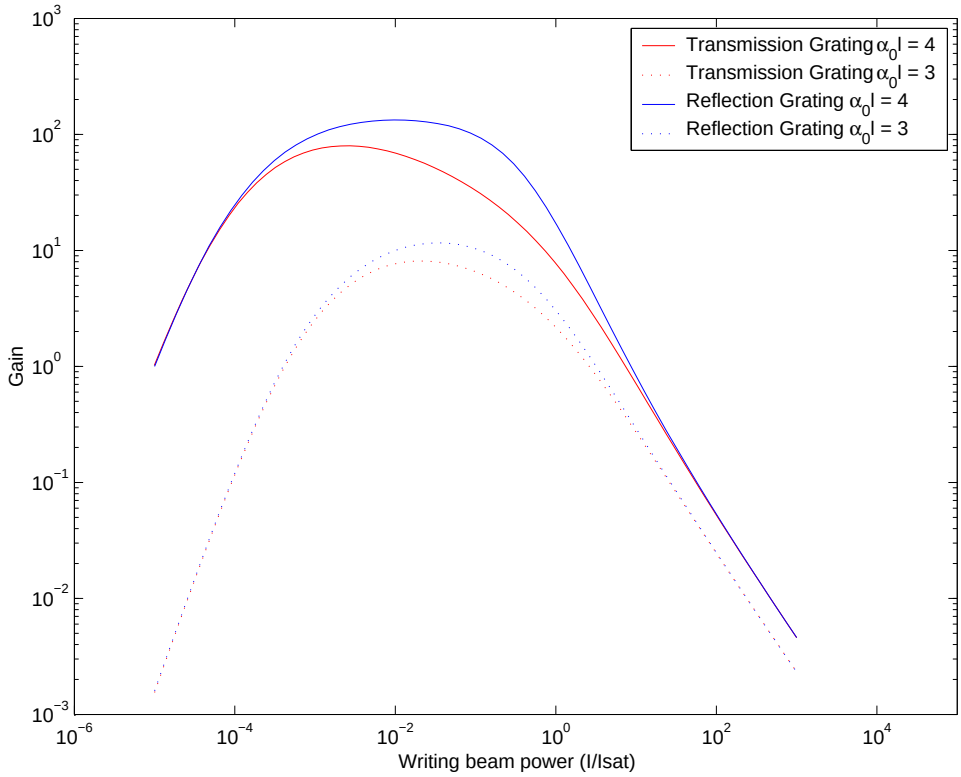

Figure 2.31: Diffraction efficiency for transmission and reflection gratings as a function of grating writing beam powers for small signal gains of ∼50 (solid lines) and ∼20 (dashed lines).

2.6 Degenerate four-wave mixing: experimental work

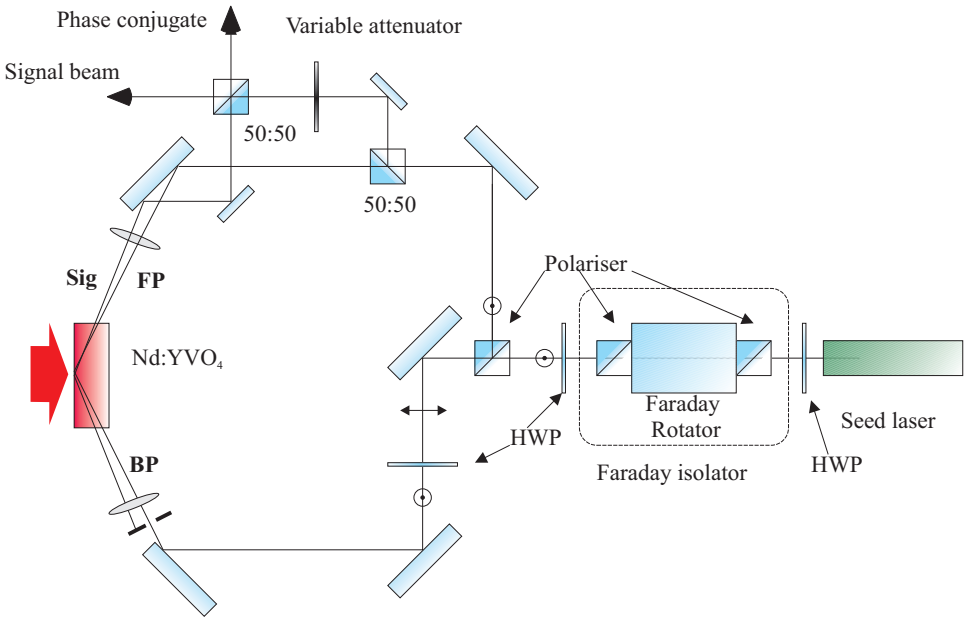

Figure 2.32: Experimental setup for the degenerate four-wave mixing experiments.

Figure 2.32 shows the experimental setup used to achieve degenerate four-wave mixing. The seed beam (300mW, TEM_{00}, SLM, 1064nm) is first passed through a half-wave plate then a Faraday isolator. The combination of the half-wave plate and the first polariser of the Faraday isolator act as a variable attenuator which allow the total seed power to be controlled. The Faraday isolator additionally prevents any feedback into the seed laser.

The beam then passes through a second half-wave plate and a polariser. Adjusting the angle of the half-wave plate allows the ratio of beam powers transmitted through either side of the polariser to be controlled. The horizontally polarised beam is re-aligned to the vertical by a third half-wave plate. This mechanism provides control over the ratio of the writing beams in the four-wave mixing amplifier, and is effectively an *optical valve* (and will be referred to as such from here on).

The top beam (in figure 2.32) is split with a 50:50 beam splitter into the

forward pump (FP) and signal beams (Sig). A second 50:50 beam splitter is used to observe the signal and phase conjugate output powers. The signal beam power is selected with a variable attenuator between the two beam splitters.

The beams are then launched into a Nd:YVO_4 amplifier with a pair of 100mm focal length cylindrical lenses. The forward pump and signal beams are aligned to be parallel before the lens in order to intersect at the focus. The forward and backward pump beams are aligned such that they counter-propagate so that each beam will Bragg match with the grating written by the other two beams.

The Nd:YVO_4 amplifier is the same as that used in the side-pumped amplifier experiments and described in appendix A. The crystal is pumped with a fibre lensed 60W 808nm TE polarised Coherent diode bar running at 40W. (At higher powers ASE becomes a severe problem competing for gain with the phase conjugate mode). The pump beam is focused onto the front face of the crystal with a 6.3mm focal length cylindrical lens as shown in figure 2.4.

2.6.1 Results

2.6.1.1 Reflectivity as a function of signal beam power

Figure 2.33 shows the reflectivity of the degenerate four-wave mixing system as a function of the signal beam power. The forward and backward pump beams were of powers 10.7mW and 133mW respectively, and were chosen to produce the maximum phase conjugate output power from the system.

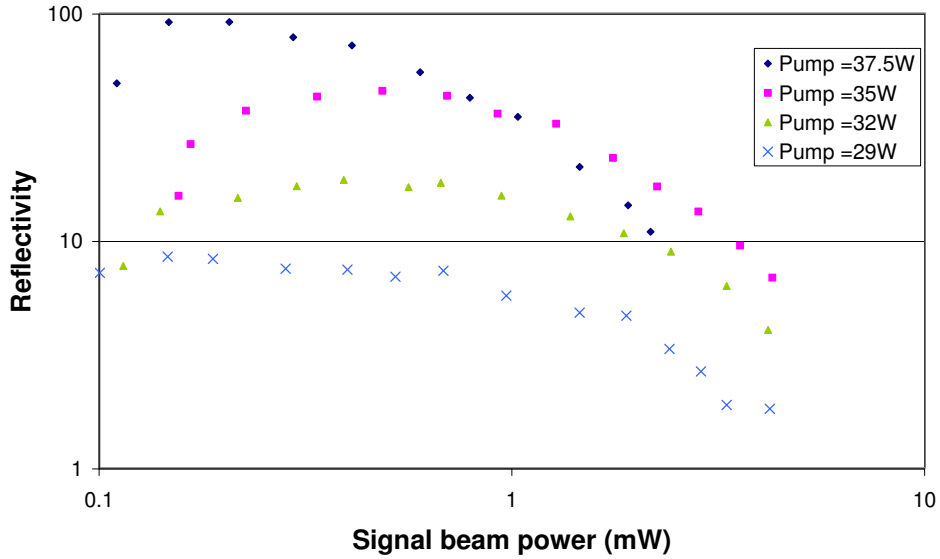

Figure 2.33: Four-wave mixing reflectivity as a function of power from the signal beam.

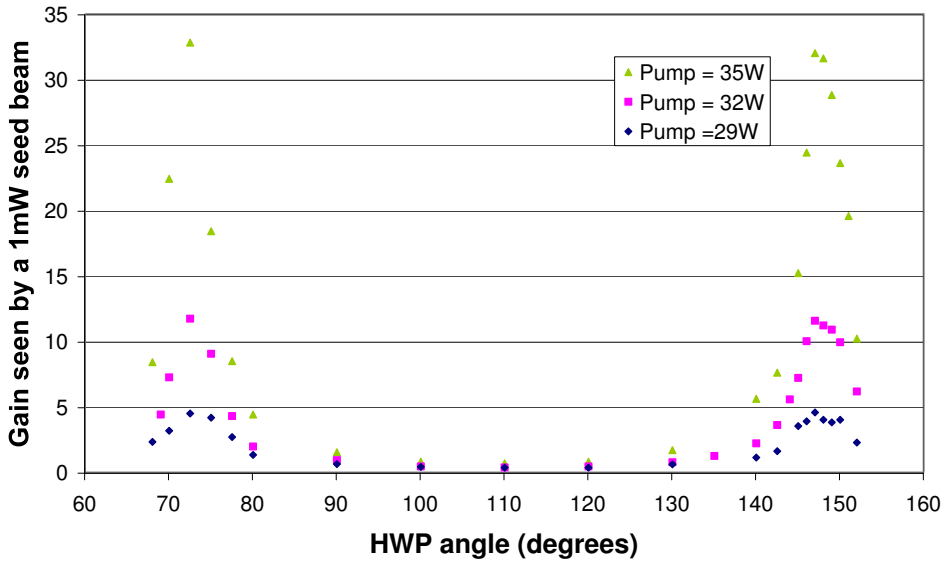

Figure 2.34: Four-wave mixing reflectivity for a fixed signal beam power of 1mW as a function of half-wave plate angle.

2.6.1.2 Reflectivity as a function of relative pump beam intensities

The phase conjugate reflectivity was measured as a function of the ratio of powers of the forward and backward pump beams. In order to keep the total power of the pump beams constant a 50:50 beam splitter was inserted into the path of the backward pump beam. Figure 2.34 shows the phase conjugate reflectivity seen by a 1mW signal beam as a function of the half-wave plate angle in the *optical valve*. The signal beam power was kept at a constant value by adjusting the variable attenuator.

2.6.1.3 Beam profiles of the phase conjugated beam

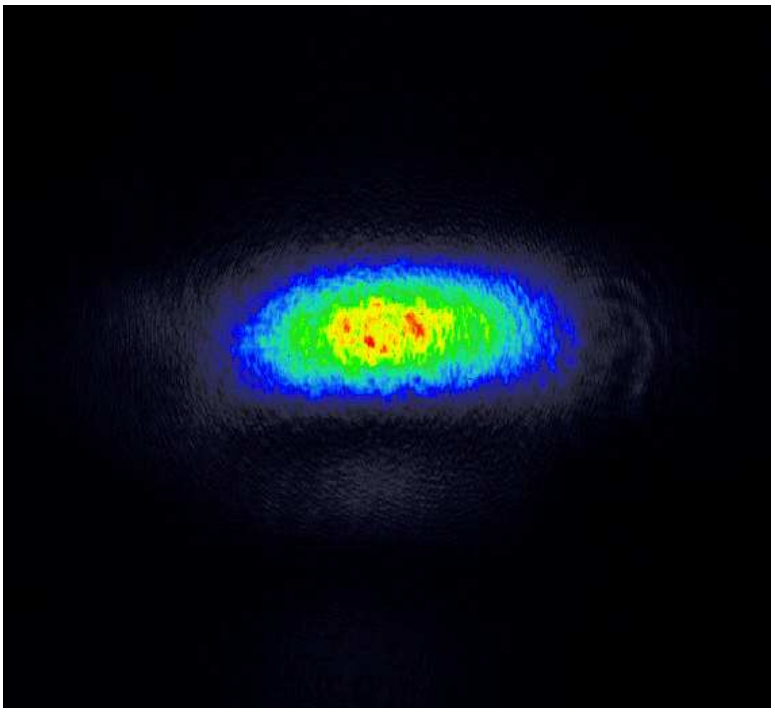

Figure 2.35: The beam profile of the phase conjugate beam from the degenerate four-wave mixing system.

The spatial profile of the phase conjugate beam is shown in figure 2.35. The profile was unchanged when a phase distorter (a glass slide etched in hydrofluoric acid) was placed in the path of the signal beam. The elliptical shape of the beam is due to the asymmetry in the gain region of the

amplifier.

2.7 The effect of individual gain gratings

In degenerate four-wave mixing the effect of two gratings combine to form the phase conjugate output (as noted previously, other gratings are also present but these do not contribute to phase conjugation.). This section details experiments carried out on each of the gratings individually. In each case a grating is written between two coherent laser beams (split from the same original beam) and read by a second beam, incoherent with the writing beams.

The reading beam is generated by a second seed laser which is identical in all respects to the first (they are both from the same make and model). The second laser is not coherent with the first so shouldn't form a stable interference pattern according to the third Fresnel-Arago law [16].

2.7.1 Transmission gratings

Figure 2.36 shows the experimental setup used to measure the diffraction efficiency of a transmission grating. This is a modified version of the degenerate four-wave mixing setup used in the previous section (figure 2.32). The half-wave plate and polariser previously used to select the power ratio of the four-wave mixing beams is set to transmit only to the vertically polarised direction . The two beams from this laser intersect in the pumped crystal as before and write a transmission grating.

The grating is read by a beam from a second seed laser. The reading beam is aligned such that it counter-propagates with one of the writing beams.

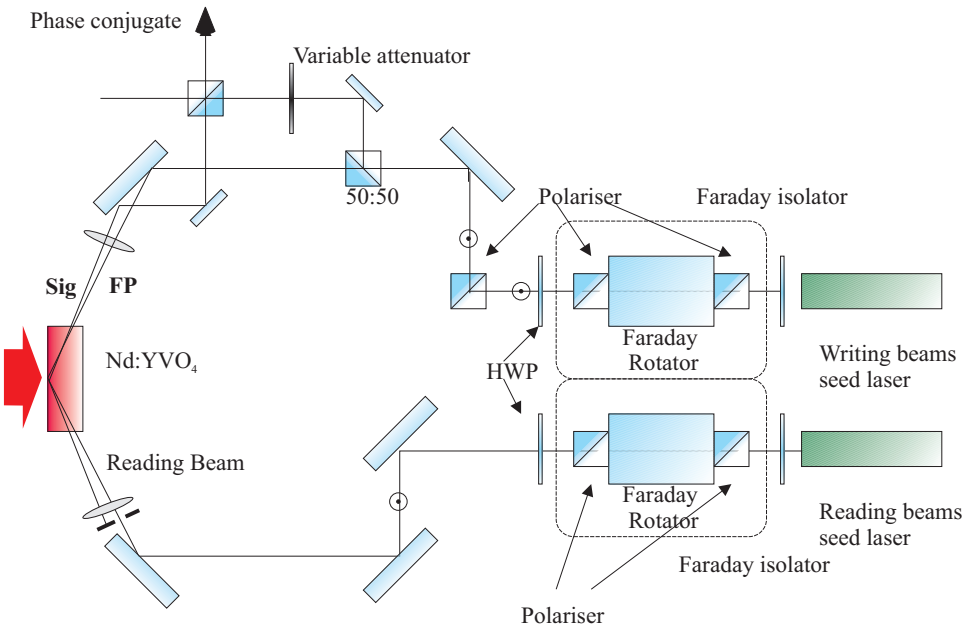

Figure 2.36: Experimental setup for the transmission grating experiments.

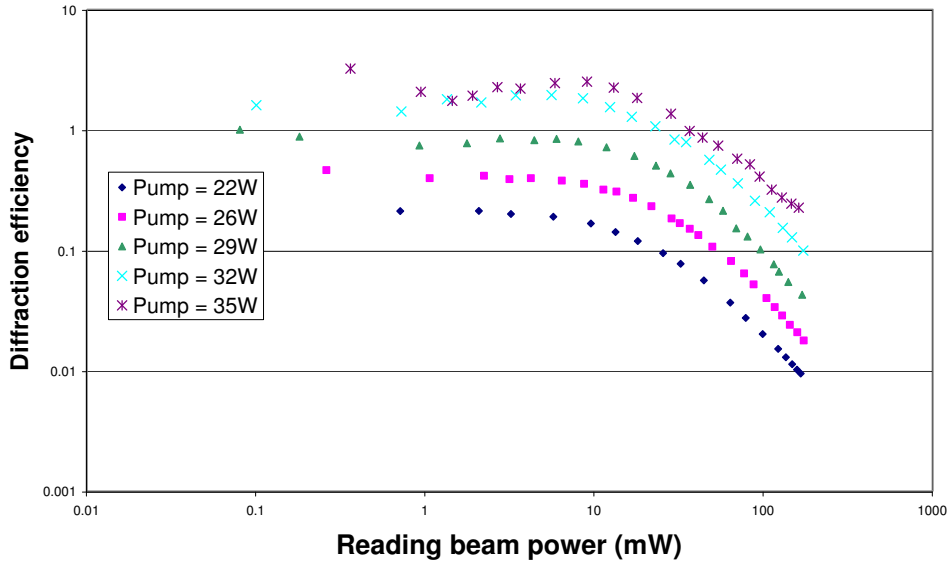

Figure 2.37: Diffraction efficiency of the transmission grating as a function of the reading beams intensity.

2.7.1.1 Reflectivities as a function of reading beam power

Figure 2.37 shows the diffraction efficiency of the transmission grating as a function of the intensity of the reading beam. The diffraction efficiency is constant for low reading beam powers then falls as the beams increase the saturation of the gain of the amplifier. Increasing the pump power increases the reflectivity by increasing the gain available to the beams.

2.7.1.2 Reflectivities as a function of total writing beam power

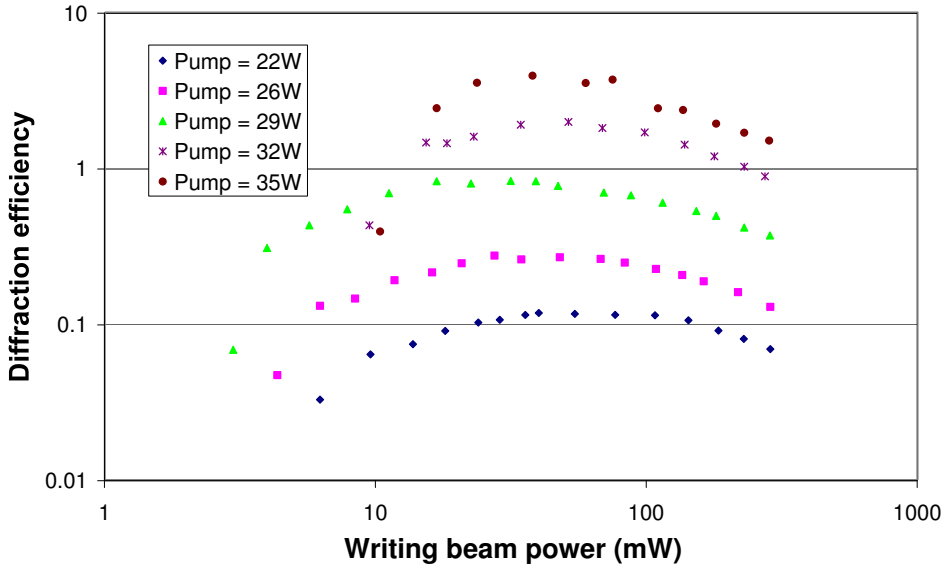

Figure 2.38: Diffraction efficiency of the transmission grating as a function of writing beam power.

Increasing the intensity of the writing beams causes the modulation of the grating to increase. This increased modulation in turn causes the diffraction efficiency to improve and hence the gain to rise. The increase in the modulation of the grating also reduces the gain available to the reading beam. This reduction in gain then causes the diffraction efficiency to fall.

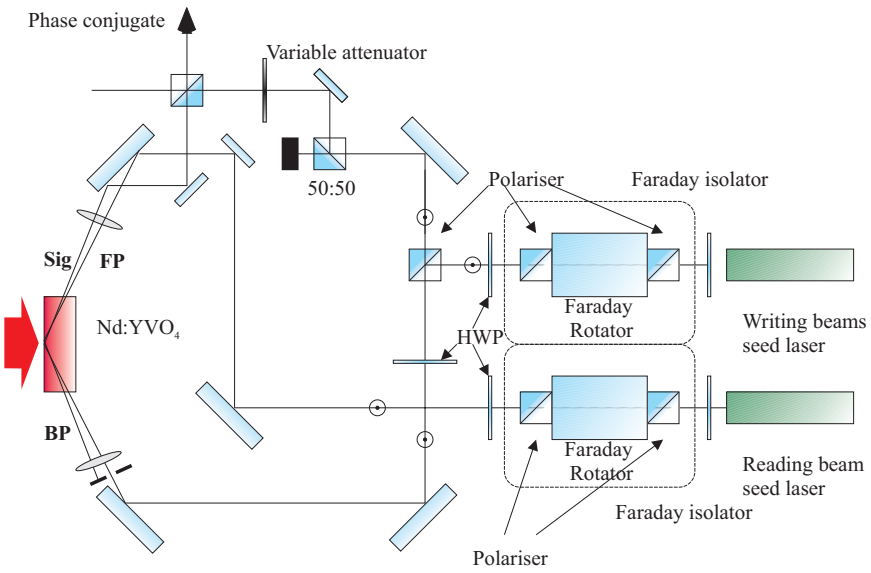

Figure 2.39: Experimental setup for the reflection grating experiments.

2.7.2 Reflection gratings

Figure 2.39 shows the experimental setup used to measure the diffraction efficiency of a reflection grating. This setup is a modified version of the apparatus used in the degenerate four-wave mixing experiment. Here the original backward pump beam is blocked and replaced with one generated by a second seed laser. The new reading beam is aligned such that it counter-propagates with the former forward pump beam. A reflection grating is written by the beams split from one of the seed lasers and is read by a beam generated by the second seed laser.

2.7.2.1 Reflectivities as a function of signal power

Figure 2.40 shows the diffraction efficiency of the reflection grating as a function of the power of the reading beam. At low reading beam powers the diffraction efficiency is constant. When the reading beam power is raised the saturation of the amplifier is increased and the gain available to the reading and writing beam decreases. This saturation in the gain causes the diffraction efficiency to fall.

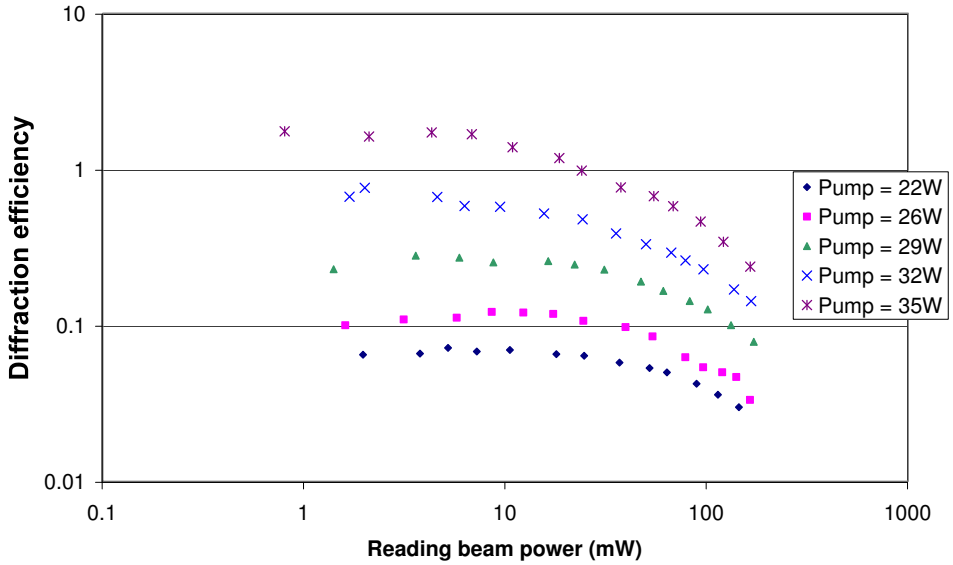

Figure 2.40: Diffraction efficiency of the reflection grating as a function of reading beam power.

2.7.2.2 Reflectivities as a function of total writing beam power

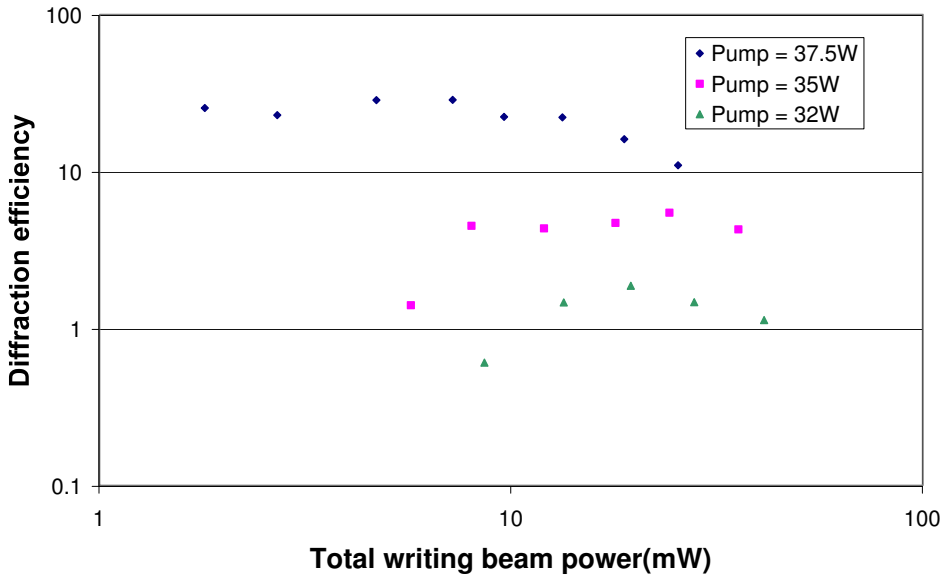

Figure 2.41: Diffraction efficiency of a reflection grating as a function of writing beam power.

Figure 2.41 shows the diffraction efficiency of a reflection grating as a function of the total power to the grating writing beams.The signal beam has a fixed power of 100mW, and the writing beams have equal powers. In-

creasing the power to the writing beams causes the modulation of the gain gratings to increase. This in turn causes the diffraction efficiency to improve. At higher powers the diffraction efficiency falls as the gratings start to saturate and less gain becomes available to the diffracted beam (and the writing beams).

2.7.2.3 Beam profile of the diffracted beam.

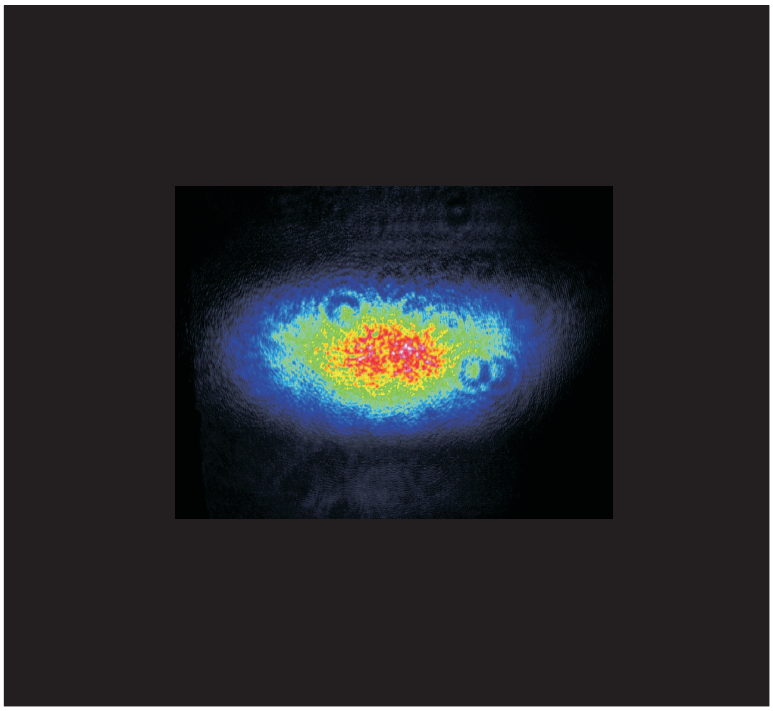

Figure 2.42: Beam profile of a beam diffracted from a reflection grating.

Figure 2.42 shows the beam profile of the diffracted beam. The beam's elliptical shape is due to the asymmetry of the gain region. The beam is near diffraction-limited and remained so when a phase distorter was placed in the path of the signal beam between the pick off beam splitter and crystal.

2.8 Cross polarisation experiments

The first Fresnel-Arago law [16] states that in order for two beams to interfere they must be polarised parallel to each other (or at least have components that are). If this condition is not met, the beams are orthogonally polarised and no interference will be observed. In these experiments a gain grating will be written by two vertically polarised beams then read out by an orthogonally polarised beam. This has been achieved before in non-birefringent materials such as Nd:YAG [12] but is the first time in a birefringent material to our knowledge.

In order to diffract off a grating the probe beam must be Bragg-matched to the grating. In the non-birefringent case this can be easily achieved by making the read beam and one of the writing beams counter-propagate: in a birefringent medium however complications arise.

2.8.0.4 Alignment issues in a birefringent medium

The wavelength of light in a medium of refractive index n is given by

$$\lambda = \frac{\lambda_0}{n} \tag{2.77}$$

In a birefringent medium the refractive index is different for each non-symmetric crystal axis. In the case of Nd:YVO_4 vertically polarised light (parallel to the c-axis) has a refractive index of 2.17 and horizontally polarised n = 1.96. Which gives the writing beams a wavelength of 490nm and the reading beam 543nm inside the crystal.

Figure 2.43 shows the path of the reading beams when diffracted off gratings written by light of a shorter wavelength. The angle which the reading beams deviate from the writing can be found using the Bragg condition.

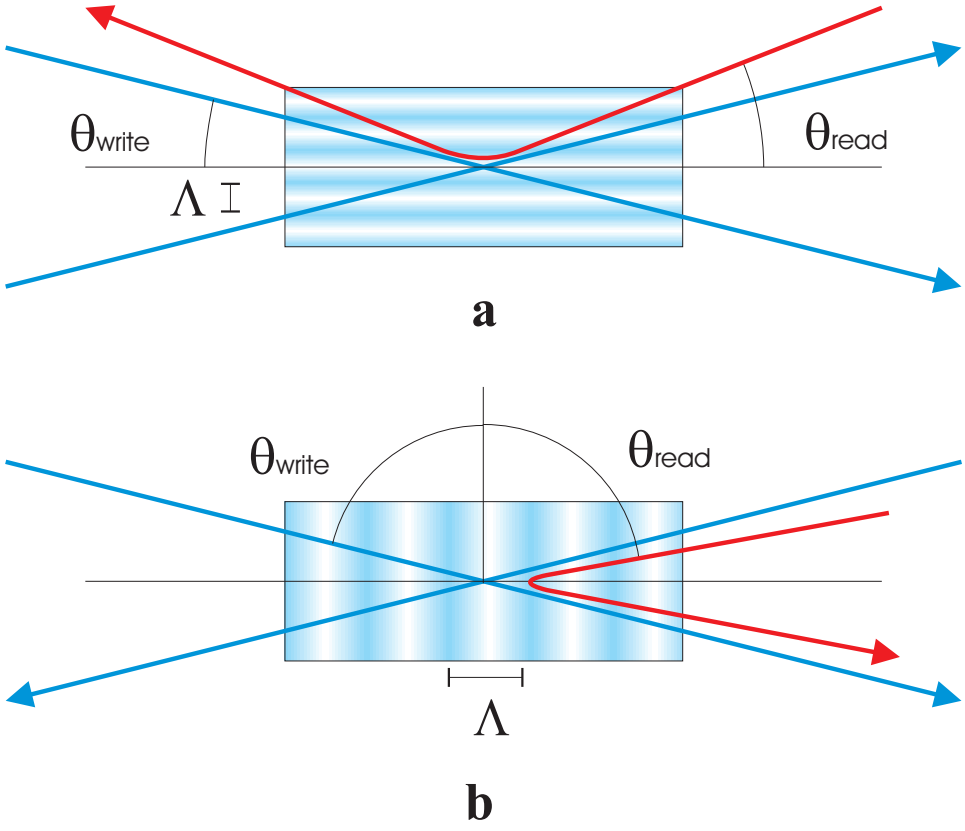

Figure 2.43: a, A transmission grating read by a beam with a longer wavelength than the writing beam. b, A reflection grating read by a beam with a longer wavelength than the writing beam.

$$\Lambda = \frac{\lambda_0}{(2n_{write}\sin(\theta_{write})} \tag{2.78}$$

$$\Lambda = \frac{\lambda_0}{(2n_{read}\sin(\theta_{read})} \tag{2.79}$$

which are equal and can be rearranged to give

$$n_{read}\sin(\theta_{read}) = n_{write}\sin(\theta_{write}) \tag{2.80}$$

which can in turn be plotted to give the read angle as a function of the writing beam's angle (as defined in figure 2.43).

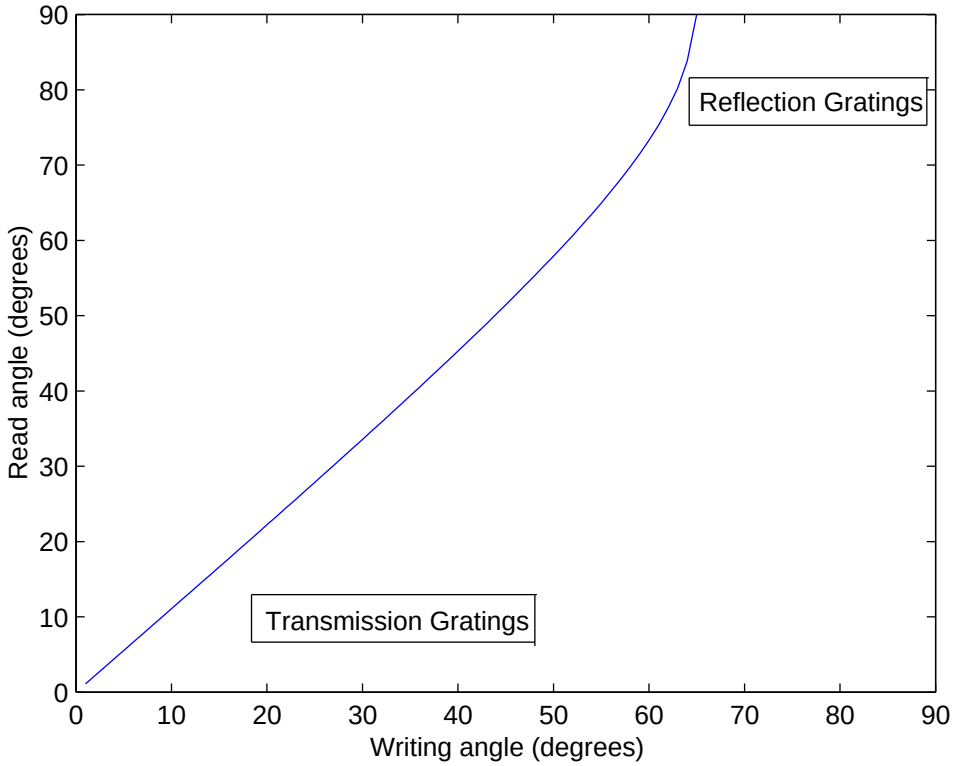

Figure 2.44: Read beam angle as a function of the writing beams angle.

Figure 2.44 shows that when the angle between the writing beams and the normal is small (the grating formed in this situation is generally referred to as a transmission grating) the read angle is also small (and, in fact sim-

ilar). When the angle between the beams is large (a reflection grating) the read angle becomes imaginary and therefore it is not possible to read the grating.

Further complications in aligning the birefringent system are caused by the interface between the crystal and air where the beam is launched into the amplifier. Refraction of the beam at the edge of the crystal is different for each polarisation. This problem is solved using Snell's law. A ray trace of the launch of the reading and writing beams into the crystal is shown in figure 2.45.

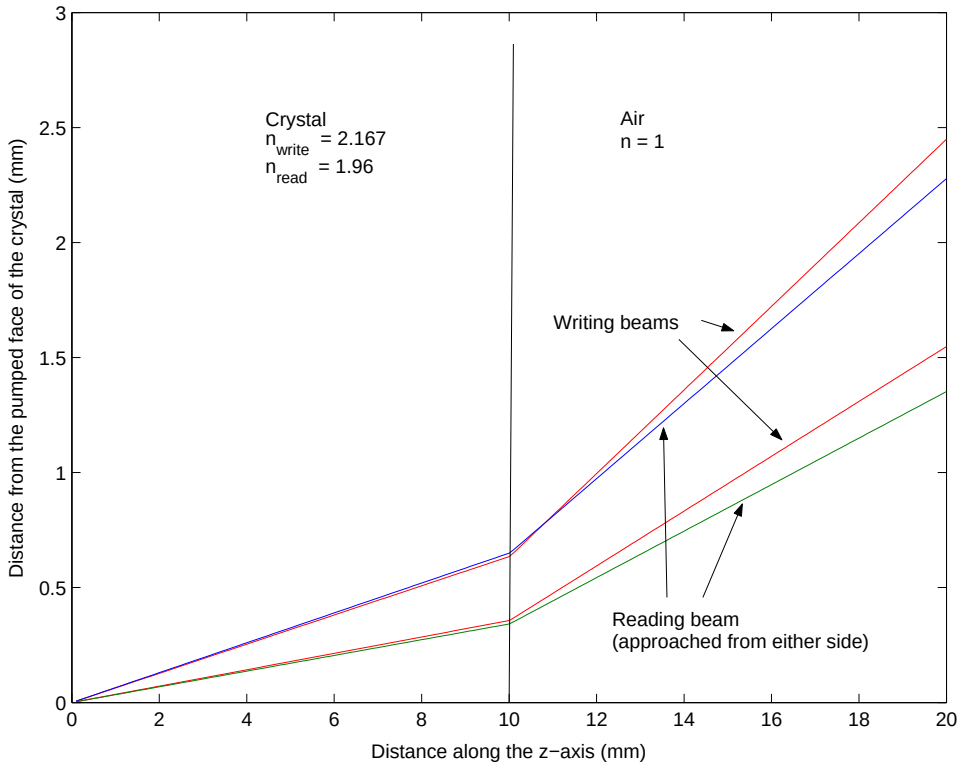

Figure 2.45: A grating is written with vertically polarised beams at 7 and 10 degrees external angle (red lines). The grating is then read either from the top (blue line) or the bottom (green line).

It is interesting to note that refraction of the top read beam (blue line) causes its angle to change such that it intersects with the top writing beam outside the amplifier. This gives launch conditions which are counter intuitive to those based solely on consideration of the grating.

2.8.1 Experimental

A similar setup was used in these experiments as in the degenerate four-wave mixing experiments but with several differences (figure 2.46). The polarisation of the backward pump beam was rotated by 90° by removing the half-wave plate that had previously been used to make it vertically polarised. The backward pump beam was then realigned such that it would Bragg match with the gain grating (as shown in figures 2.43 and 2.45).

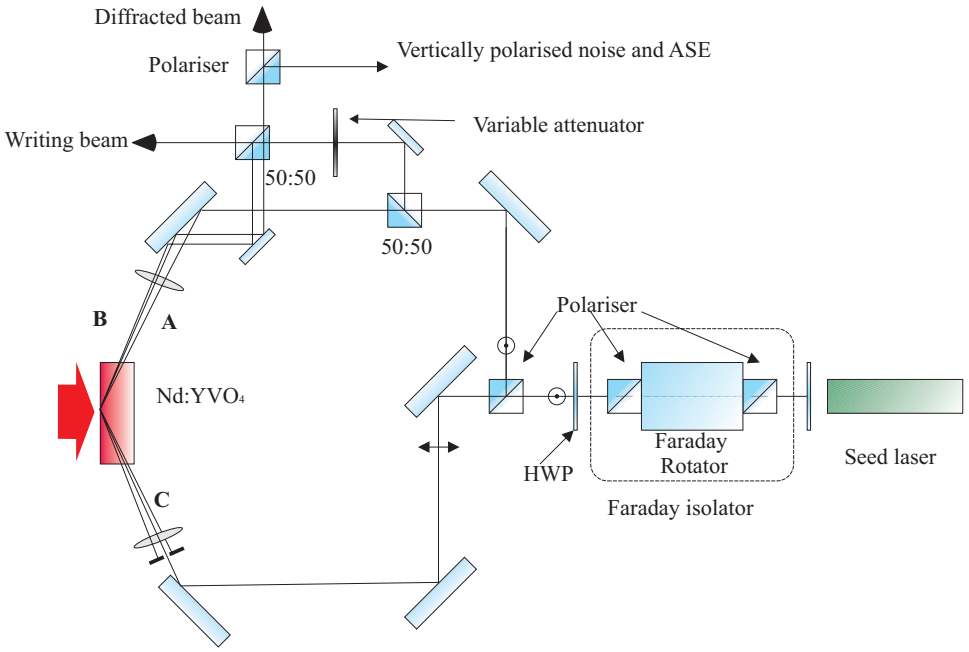

Figure 2.46: Experimental setup for the crossed polarisation grating experiments.

The output was polarisation filtered in order to remove any noise or scattered light (ASE emitted by Nd:YVO_4 is predominantly vertically polarised).

2.8.1.1 Reflectivities as a function of probe beam power

Figure 2.47 shows the gain seen by a horizontally polarised reading beam as a function of its intensity for a range of pump powers. The powers of signal and forward pump beam were selected to achieve maximum diffraction efficiency.

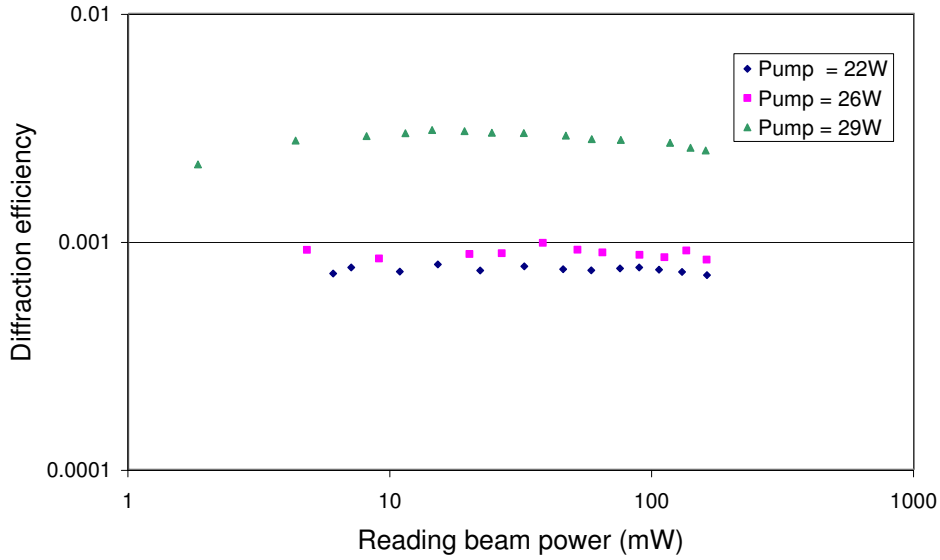

Figure 2.47: Diffraction efficiency seen by a horizontally polarised beam from a gain grating written with vertically polarised beams.

The diffraction efficiency of the grating remained constant for probe powers of 0.1 to 150mW. The gain coefficient available to the horizontally polarised beam means that it extracted a tiny proportion of the power from the amplifier compared with the vertically polarised writing beams. The small power extraction by the probe beam caused only a minimal effect on the gain gratings leading to a constant diffraction efficiency.

2.8.1.2 Reflectivities as a function of total writing beam power

The effect on the diffraction efficiency of the gain gratings as a function of the total power of the writing beams is shown in figure 2.48. As before initially the gain increases with signal power as the diffraction efficiency improves. The output peaks at ~50mW then falls as the gratings become over saturated.

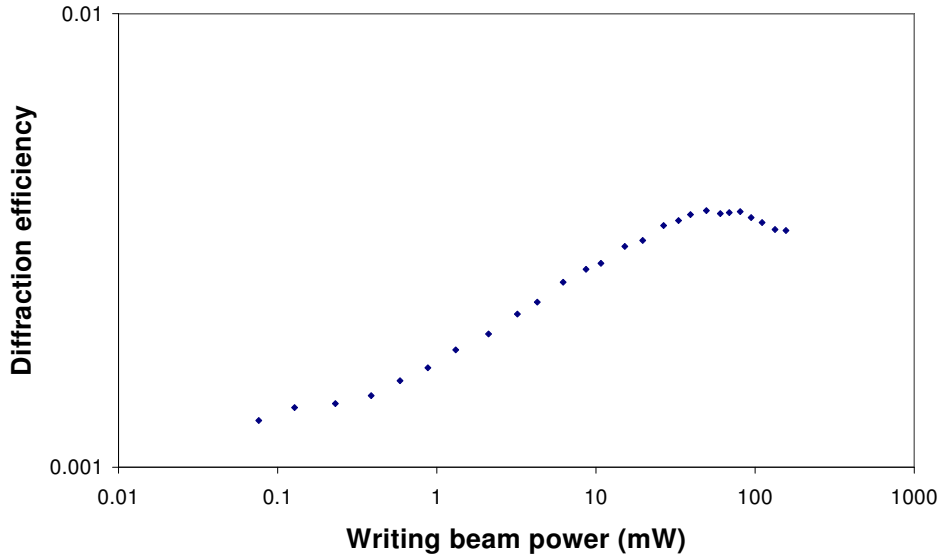

Figure 2.48: Diffraction efficiency seen by a horizontally polarised signal beam as a function of the total power of the gain grating writing beams. The amplifier had a 26W pump.

2.9 Discussion

Experiments and modelling have been performed to compare proximity and lensed coupled pumping schemes in a side-pumped bounce geometry amplifier. Whilst proximity coupling has the advantages of lower losses and a more simplistic experimental setup lensed coupling is clearly preferable. The recess on a diode bar is needed to protect the diode from any accidental damage, and this recess prevents proximity coupled systems from achieving the spot sizes (and therefore small signal gains) available from a lensed system.

The relative effects of transmission and reflection gain gratings were observed is sections 2.7.1 and 2.7.2 respectively. In both cases significantly lower gains were seen than from the degenerate four-wave mixing experiments. This was probably due to a mismatch in beam diameters between the two seed lasers and minor misalignments.

2.10 Conclusions

In these experiments phase conjugation via four-wave mixing has been achived through saturable gain gratings. Reflectivities of nearly 10000% have been achieved in degenerate four-wave mixing. Greater than unity gains have been observed from both reflection and transmission gratings.

The process has been modelled, the effect of a gain grating on a probe beam studied and the relative effects of the constituent gain gratings examined.

Side-pumped Nd:YVO_4 bounce geometry amplifiers have been modelled extensively. Proximity and lensed coupled pumping schemes have been compared with lensed coupling proving to be the most useful.

2.11 References

[1] A.E. Seigman. *Lasers*, pages 292–303. University Science Books, 1986.

[2] R. A. Fields, M. Birnbaum, and C. C. Fincher. Highly efficient Nd:YVO_4 diode-laser end-pumped laser. *Applied Physics B-Lasers and Optics*, 51(23):1885–1886, 1987.

[3] I.O. Musgrave, W.A. Clarkson, and M.J. Yarrow. Energy-transfer upconversion in Nd:YVO_4 and its effect on laser performance. *Awaiting publication*, 2004.

[4] W. Koechner. *Solid-State Laser Engineering*, pages 406–468. Springer-Verlag, forth edition, 1996.

[5] J.M. Egglestone, T.J. Kane, K. Kuhn, J. Unternahrer, and R.L. Byer. The slab geometry laser- : Part 1 theory. *IEEE Journal of Quantum Electronics*, 20(3):289–301, 1984.

[6] T.J. Kane, J.M. Egglestone, and R.L. Byer. The slab geometry laser- : Part 2 thermal effects in a finite slab. *IEEE Journal of Quantum Electronics*, 21(8):1195–1210, 1985.

[7] P. Hello, E. Durand, P. K. Fritschel, and C. N. Man. Thermal effects in Nd-YAG slabs 3d modeling and comparison with experiments. *Journal of Modern Optics*, 41(7):1371–1390, 1994.

[8] J.C. Bermudez, V.J. Pinto-Robledo, A.V. Kir'yanov, and M.J. Damzen. The thermo-lensing effect in a grazing incidence diode-side-pumped Nd:YVO_4 laser. *Optics Communications*, 210(1-2):75–82, 2002.

[9] J. E. Bernard and A. J. Alcock. High-efficiency diode-pumped Nd:YVO_4 slab laser. *Optics Letters*, 18(12):968–970, 1993.

[10] J. E. Bernard, E. McCullough, and A. J. Alcock. High-gain, diode-pumped Nd:YVO_4 slab amplifier. *Optics Communications*, 109(1-2):109–114, 1994.

[11] H. Kogelnik. Coupled wave theory for thick hologram gratings. *The bell system technical journal*, 48(9):2909–2947, 1969.

[12] K. S. Syed, G. J. Crofts, R.P.M. Green, and M. J. Damzen. Vectorial phase conjugation via four-wave mixing in isotropic saturable-gain media. *Journal of the Optical Society of America B-Optical Physics*, 14(8):2067–2078, 1997.

[13] J.C. Diels, I.C. McMichael, and H. Vanherzeele. Degenerate four-wave mixing of picosecond pulses in the saturable amplification of a dye laser. *IEEE Journal of Quantum Electronics*, QE-20:630–636, 1984.

[14] A. Yariv and R.A. Fisher. Optical phase conjugation. In R.A. Fisher, editor, *Optical Phase Conjugation*, pages 9–11. Academic Press, London, 1983.

[15] G. J. Crofts and M. J. Damzen. Numerical modelling of continuous-wave holographic laser oscillators. *Optics Communications*, 175(4-6):397–408, 2000.

[16] E. Hecht. *Optics*, pages 388–389. Addison-Wesley, 1987.

Chapter 3

Towards a monolithic phase conjugator

3.1 Introduction

The aim of this chapter is to develop a phase conjugator operating via gain gratings for development into a monolithic system. In the previous chapter a phase conjugator with a reflectivity of greater than unity was described. This will be used in a self intersecting geometry to produce a seeded phase conjugate oscillator. The oscillator will be modelled, characterised and results giving phase conjugate output powers of $\sim$1W will be presented. Possible methods of increasing the output power and incorporation into a monolithic system will then be discussed.

3.2 Phase conjugate oscillator theory

3.2.1 Fundamental operation

We will first consider four-wave mixing via a reflection grating. Figure 3.1 shows the formation and reading of the gain grating. Here the forward and backward pump beams (FP and BP respectively) write the grating which is then read by the signal beam (sig) producing a phase conjugate of the backward pump beam (PC).

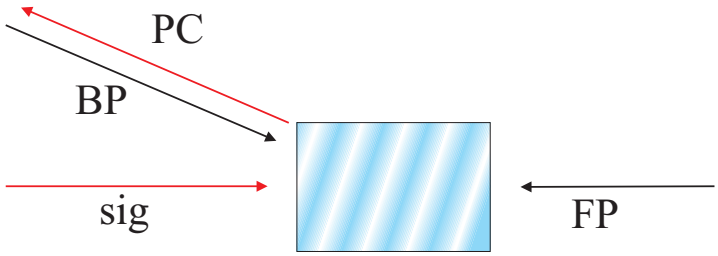

Figure 3.1: Writing a reflection grating with the forward pump (FP) and backward pump (BP) with diffraction of a signal beam (sig) generating a phase conjugate (PC) of the backward pump.

The reflection grating can be written by passing a beam through the gain medium twice such that it intersects with itself (as shown in figure 3.2). At the point of intersection the beams interfere forming a gain grating. This grating is encoded with information about any phase distortions that the beam sees from passing through the crystal.

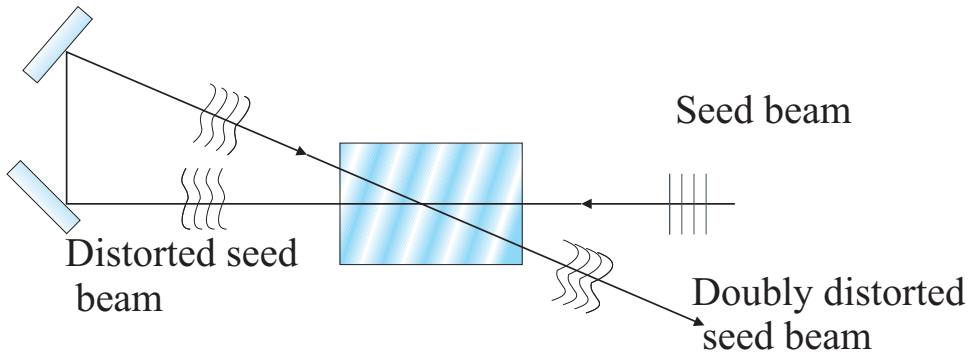

Figure 3.2: Writing a gain grating between a seed beam and a distorted version of the seed beam.

Fluorescence from the amplifier will then scatter off the grating. When the fluorescence scatters it Bragg matches with the grating, counter and co-propagating with the writing beams as shown in figure 3.3.

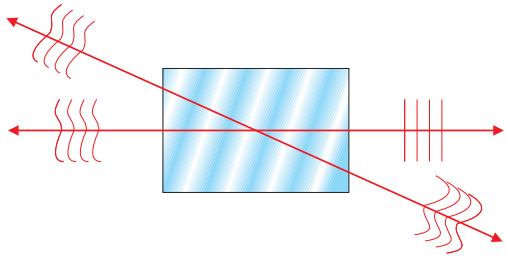

Figure 3.3: Fluorescence scattering off the grating.

The scatter that propagates along the path of each beam will have the same wavefront as that beam. The scattered light that counter-propagates along the path of the beams will have a wavefront which is the reverse of that beam, in other words its phase conjugate.

Scattered fluorescence will propagate around the loop in the opposite direction to the initial writing beam (following the path of the backward pump). When it reaches the amplifier again a portion will scatter off the grating back along the path of the backward pump again (figure 3.4).

If more of the beam is scattered than is incident on the grating (this is possible due to the gain seen in the medium) then the power in the loop will build until threshold is reached (the gain is equal to the losses) and it reaches a stable oscillation. The wavefront of this beam is defined by the spatial information encoded in the gain grating and is, as previously stated, the phase conjugate of the backward pump.

The portion of the oscillating beam that is not scattered by the grating will leave the crystal re-tracing the path of the seed beam as its amplified phase conjugate (Figure 3.5).

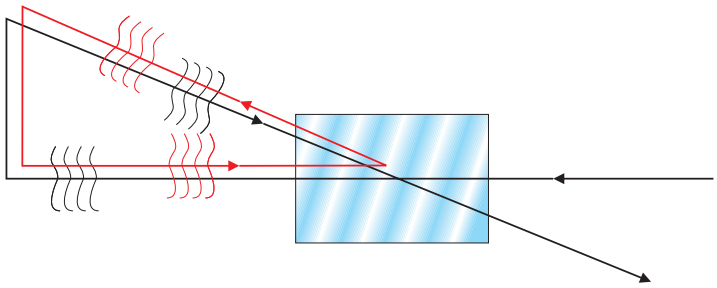

Figure 3.4: Build up of fluorescence into a steady state oscillation.

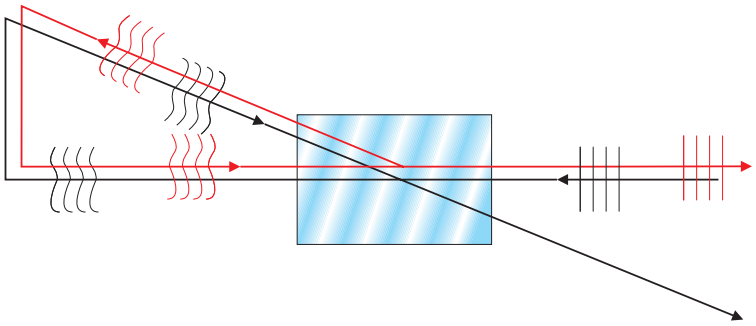

Figure 3.5: The phase conjugate oscillator emitting a phase conjugate of the signal beam.

3.2.2 Longitudinal modal structure

In the previous chapter the formation of gain gratings in a laser medium was described. Figure 2.25 showed that a gain grating is formed with a π phase shift relative to the interference pattern. This phase shift can be used to describe the longitudinal modal structure of the oscillation [1].

3.2.2.1 Writing the grating

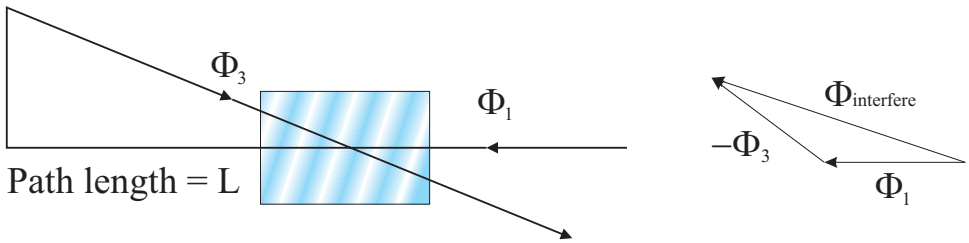

Figure 3.6: The phase diagram of the interference pattern formed whilst writing a reflection gain grating

The phase of a gain grating can be calculated from the phase of its writing beams. Figure 3.6 shows the writing of a gain grating using a self intersecting geometry. Here the seed beam has an instantaneous phase of Φ_1 and a wave vector k_1. When this is passed around the loop and back into the amplifier it has a phase Φ_3 given by

$$\Phi_3 = \Phi_1 + k_1 L + \Phi_{other} \tag{3.1}$$

where L is the length of the loop and Φ_{other} accounts for any other phase effects present in the loop.

The interference pattern at the intersection of the two beams will have a phase of $\Phi_{interfere}$ which can be calculated from

$$\begin{aligned} \Phi_{interfere} &= \Phi_1 - \Phi_3 & (3.2)\\ &= \Phi_1 - (\Phi_1 + k_1 L + \Phi_{other}) & (3.3)\\ \Phi_{interfere} &= -(k_1 L + \Phi_{other}) & (3.4) \end{aligned}$$

The phase of the gain grating can now be calculated by adding a π phase shift to the phase of the interference pattern

$$\begin{aligned} \Phi_{grating} &= \Phi_{interfere} + \pi & (3.5)\\ \Phi_{grating} &= \pi - (k_1 L + \Phi_{other}) & (3.6) \end{aligned}$$

3.2.2.2 Reading the gain grating

The gain grating is then read by scattered ASE which has built up to form a stable resonant loop. A stable beam is produced passing around the loop anticlockwise and reflecting off the gain grating as shown in figure 3.7.

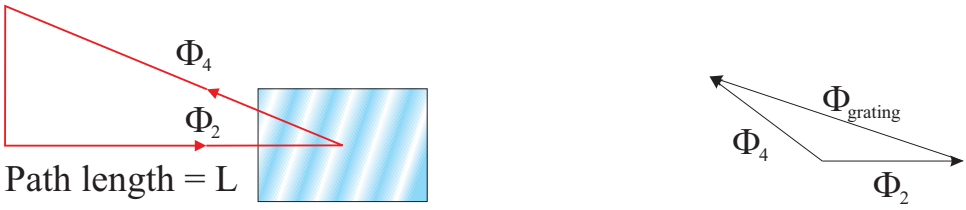

Figure 3.7: The phase diagram for reading a gain grating

In the reading process beam 2 (with phase Φ_2 at the grating) enters the amplifier with wave vector k_2. It diffracts off the gain grating to produce beam 4 which has a phase Φ_4.

$$\Phi_4 = \Phi_2 + \Phi_{grating} \tag{3.7}$$

$$\Phi_4 = \Phi_2 + \pi - (k_1 L + \Phi_{other}) \tag{3.8}$$

Beam 4 then passes around the loop re-entering the amplifier as beam 2^* (With phase Φ_2^*).

$$\Phi_2^* = \Phi_4 + k_2 L + \Phi_{other} \tag{3.9}$$

$$\Phi_2^* = \Phi_2 + (k_2 - k_1)L + \pi \tag{3.10}$$

If the grating writing beam has the same wavelength as the reading beams ($k_1 = k_2$) then $\Phi_2^* = \Phi_2 + \pi$. This will cause destructive interference to occur between the two beams leading to an unstable laser mode.

In order to maintain a stable oscillation constructive interference is needed. This can be achieved by setting $\Phi_2^* = \Phi_2 + 2n\pi$. Hence

$$(k_2 - k_1)L = (2n - 1)\pi \tag{3.11}$$

where n is any integer.

This allows the phase conjugator to oscillate over a range of frequencies given by

$$\Delta\nu = \frac{\left(n + \frac{1}{2}\right) c}{L} \tag{3.12}$$

For a loop length of 1 metre a frequency shift of $\Delta\nu = 0.15$ GHz from the writing beam is needed, which is well within the 254 GHz gain bandwidth of Nd:YVO_4 [2].

Lasing will then occur on the frequencies which see the highest gain. Emission on two longitudinal modes either side of the writing beam's frequency has been observed in pulsed experiments in Nd:YAG [3]. Emission over multiple wavelengths is possible if each mode can see enough gain to resonate.

3.3 Phase conjugate oscillator modelling

The phase conjugate oscillator operates under the same basic principles as the degenerate four-wave mixing phase conjugator described in the previous chapter. The operation of the oscillator is described by the same coupled differential equations (Equations C.27) but with boundary conditions defined by the loop nature of the oscillator.

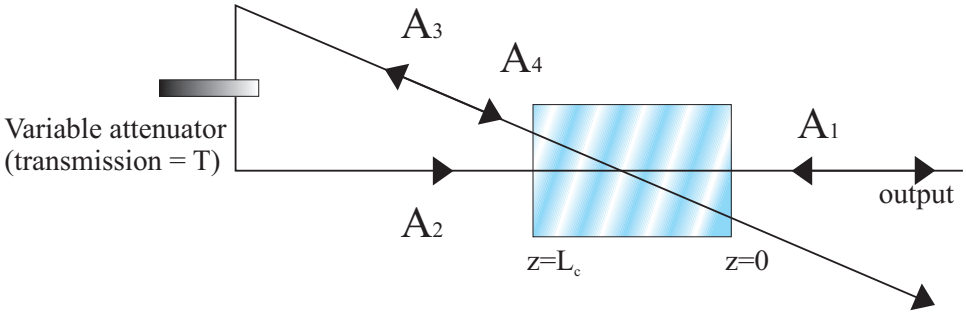

Figure 3.8: Schematic of the reflection grating phase conjugate oscillator with a variable attenuator inserted into the loop.

The boundary conditions for the reflection grating geometry are

$$A_4(L_c) = tA_1(L_c) \tag{3.13}$$

$$A_2(L_c) = tA_3(L_c) \tag{3.14}$$

$$A_3(0) = 0 \tag{3.15}$$

using the notation from appendix C and where t is the amplitude transmission of the variable attenuator ($t^2 = T$ the intensity transmission).

The ratio of powers of the writing beams is controlled by a variable attenuator inserted into the loop of the oscillator. The variable attenuator used in this model consists of two polarisers with a half-wave plate in between. By varying the angle of the half-wave plate (θ_{HWP}) the attenuator's transmission can be selected using

$$T(\theta_{HWP}) = \cos^2(2\theta_{HWP}) \tag{3.16}$$

The oscillator can be modelled numerically by applying these boundary conditions to the FWM model derived in chapter 2 and appendix C.

Figure 3.9 shows the modelled phase conjugate output power as a function of the angle of the half-wave plate in the variable attenuator for a range of small signal gains. The seed intensity is fixed at a value equal to the saturation intensity of the amplifier.

The output power is greatest when the loop transmission is maximised and a high output power is maintained over about 35 degrees either side of the maximum. After this point the transmission becomes too low to allow a mode to form and the output drops off rapidly.

In the phase conjugate oscillator two competing effects lead to high output powers: The diffraction efficiency of the grating and the gain seen by the oscillating beam.

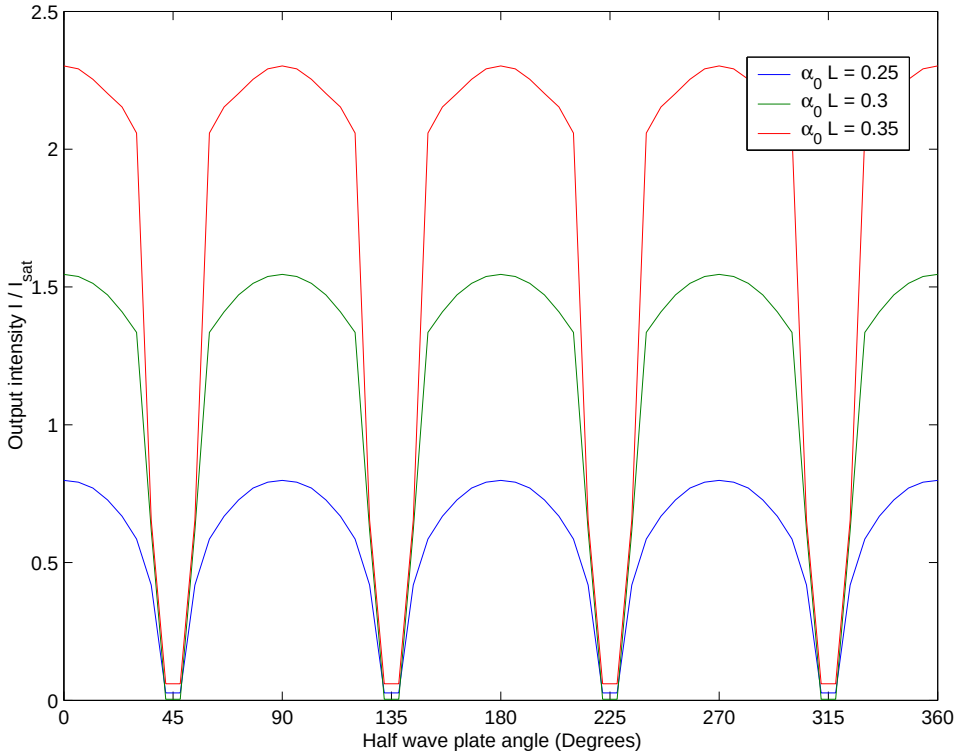

Figure 3.9: Output intensity as a function of the half-wave plate angle in the variable attenuator.

The diffraction efficiency of the grating is maximised when the writing beams powers are equal. In order to achieve this a low transmission through the variable attenuator is needed.

The output power is maximised when the phase conjugate beam sees the most gain. However in order to maximise the gain seen by the oscillating beam the loop transmission is needed to be high.

The model shows that of these two effects the gain seen by the phase conjugate beam is the dominant process. It seems that even with a low diffraction efficiency as long as the gain seen is great enough the system will oscillate.

Figure 3.10 shows the phase conjugate output intensity as a function of the signal beam intensity with a fixed loop transmission of 1 (The variable attenuator is set to allow the beam to pass through unimpeded).

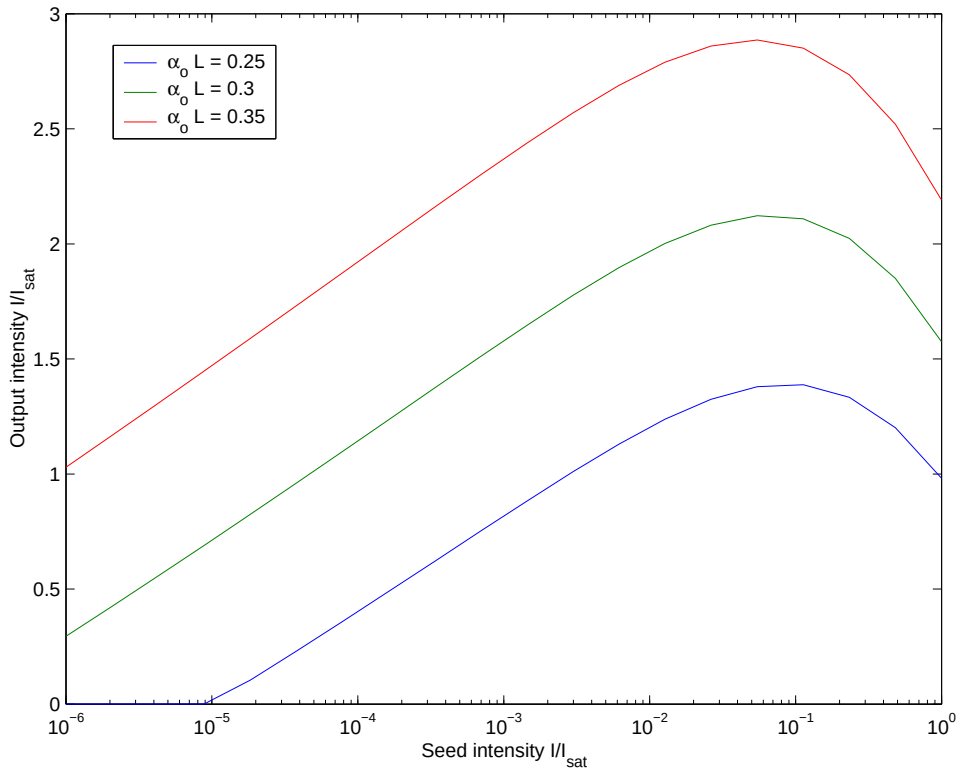

Figure 3.10: Output intensity as a function of seed beam intensity for fixed loop transmission of 1.

At low seed powers the diffraction efficiency is low due to the imbalance in powers between the two writing beams causing the grating to have a low contrast ratio. The seed power is then increased and the amplifier begins to saturate. This decreases the gain seen by the seed beam causing the ratio of writing beam powers to decrease. Eventually the majority of the power from the system will be taken by the writing beams leaving little left for the phase conjugate and causing the output power to fall.

3.4 Experimental

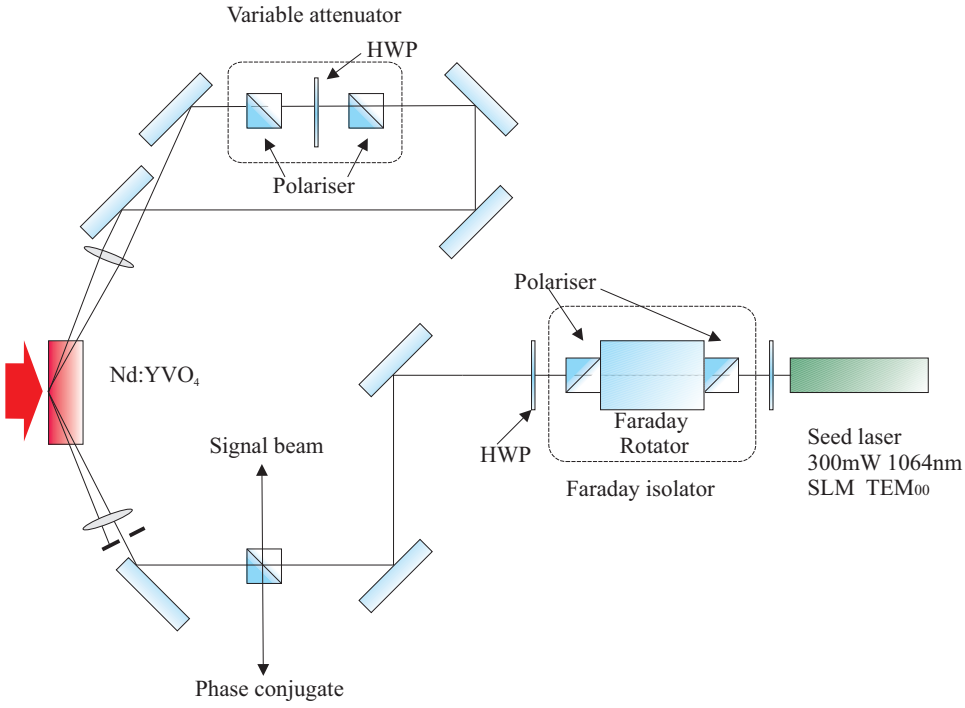

Figure 3.11: A schematic of the experimental setup used in the phase conjugate oscillator experiments.

Figure 3.11 shows a schematic of the setup used in these experiments. A seed beam is passed through a side-pumped Nd:YVO_4 amplifier in a bounce geometry as described in section 2.4.3.

The amplified beam is then passed through a variable attenuator consisting of two cube polarisers with a half-wave plate between them. This is

used to vary the ratio of intensities of the grating writing beams. The second polariser is needed to ensure that the writing beams have the same polarisation and therefore will interfere with the maximum possible contrast ratio.

The amplified and attenuated beam is launched back into the amplifier through the second 100mm focal length lens such that it intersects with the initial beam at the pumped face of the crystal.

The phase conjugate output and signal beams are measured at the 50:50 beam splitter in the input/output arm of the resonator.

3.5 Results

3.5.1 Output powers as a function of seed beam power

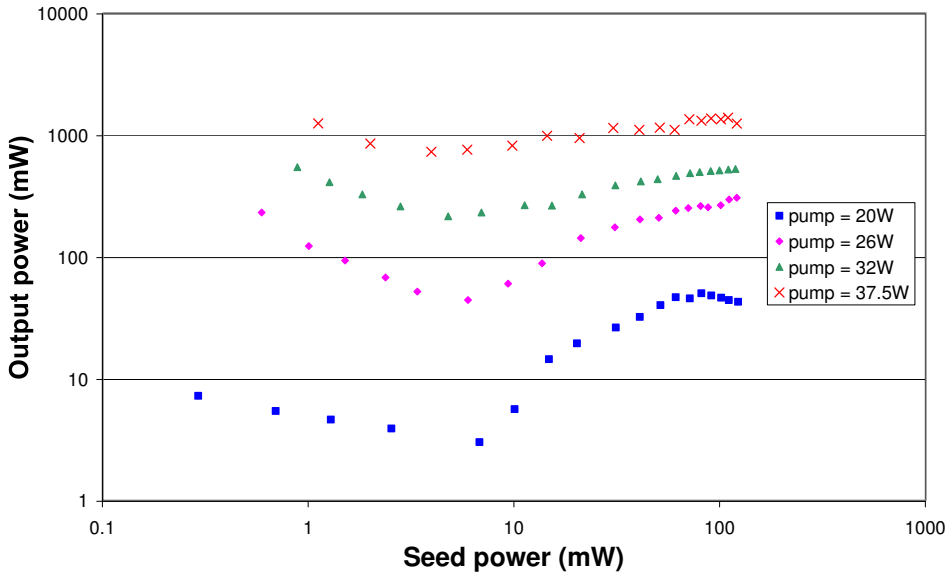

Figure 3.12: Output power as a function of seed power for a range of pump powers.

Figure 3.12 shows the output power achieved by the system as a function of seed power. With no seed beam present double pass ASE is generated along the paths of the seed/output beam and the doubly amplified beam.

The output has a spatial structure defined by the size of the pumped region of the crystal and the aperturing effect of the loop, which may make it appear similar to a lasing mode. There is however, no temporal structure to this output indicating that it is ASE rather than any form of phase conjugate.

When the seed power is increased from zero the ASE is suppressed causing the total output power to decrease. Increasing the power still further causes the ASE to die away completely and the gain gratings to form. The oscillating mode scattering off the gain gratings builds up, and as the seed power increases so does the output power. In each of these experiments the variable attenuator in the loop is set to achieve the strongest output.

3.5.2 Output powers as a function of transmission

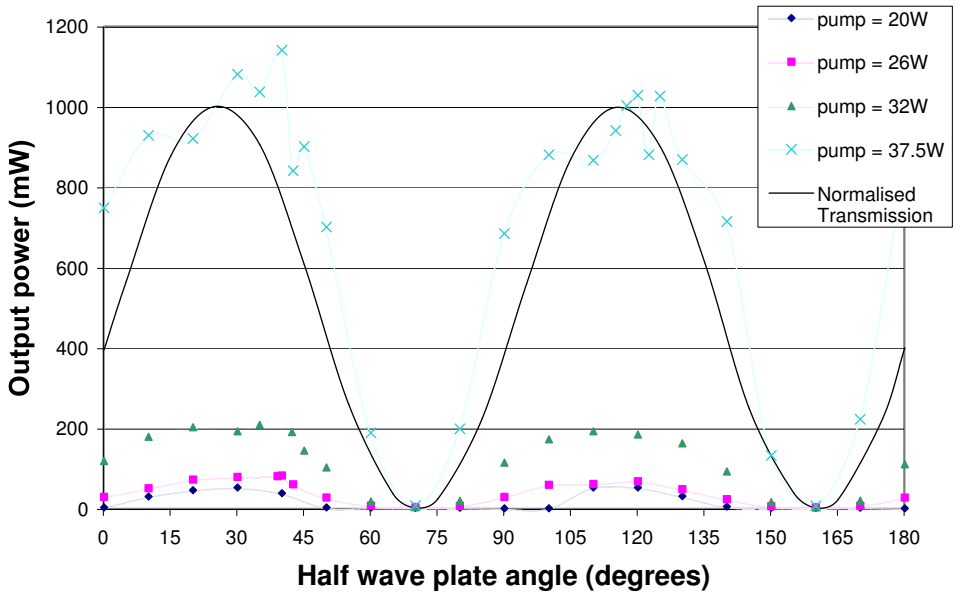

Figure 3.13: Output power as a function of the angle of the half-wave plate in the variable attenuator (the solid line is the intensity transmission of the variable attenuator).

Figure 3.13 shows the phase conjugate output power as a function of the half-wave plate's angle in the variable attenuator for a range of pump

powers. The solid line is the normalised transmission of the variable attenuator. The seed beams power was fixed at 100mW.

In section 3.3 it was explained that there are two coupled processes which control the output power of the phase conjugate oscillator: the diffraction efficiency of the grating and the gain seen by the oscillating phase conjugate beam.

The conditions required to optimise these processes are unfortunately mutually incompatible. In order to maximise the diffraction efficiency the variable attenuator needs to be set to almost its maximum transmission. However, the oscillating beam wants to see as little loss as possible, and as such needs the attenuation in the loop to be as low as possible.

The conflict between these two processes helps to explain the low efficiency of the system. At all of the possible loop attenuations either oscillating power is lost (a high loop attenuation) or the diffraction efficiency of the gain gratings suffers (a low loop attenuation). As such, high efficiencies and therefore output powers are impossible to achieve with this system.

From figure 3.13 it can be seen that the greatest output powers occur when the transmission of the variable attenuator is at its maximum. At the point of minimum transmission the output powers are at their lowest. This indicates that the gain experienced by the oscillating phase conjugate beam is the dominant factor in determining the output of the system.

3.5.2.1 Output power as a function of pump power

Figure 3.14 shows the phase conjugate output power as a function of pump power for a fixed seed power of 150mW and a loop transmission of 100%. The slope efficiency ($\sim$5.5%) is low due to the inefficiencies in the gain grating formation and loss of power to the doubly amplifier seed beam.

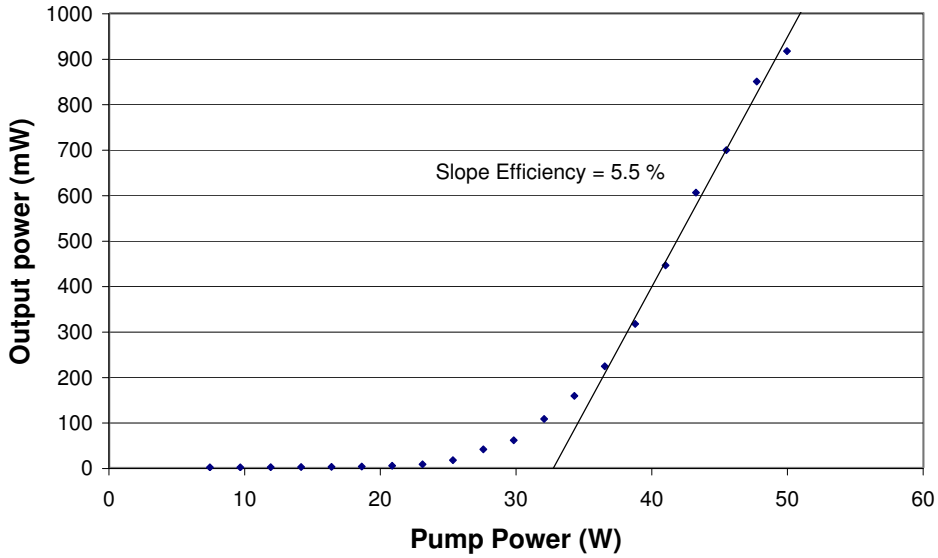

Figure 3.14: Phase conjugate output power as a function of pump power for a fixed seed power of 150 mW.

3.5.3 Beam quality measurements

3.5.3.1 Longitudinal modes

The frequency spectrum of the oscillator was measured using a confocal Fabry-Perot interferometer. The output beam exhibited ”mode hopping” behaviour fluctuating rapidly between single (Figure 3.15) and multi-mode (Figure 3.16) emission.

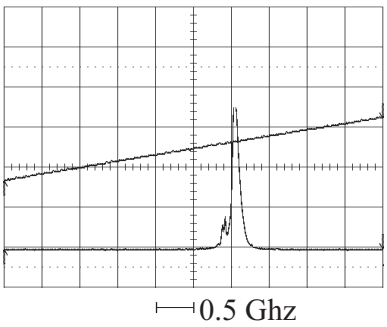

Figure 3.15: Single longitudinal mode emission from the phase conjugate oscillator.

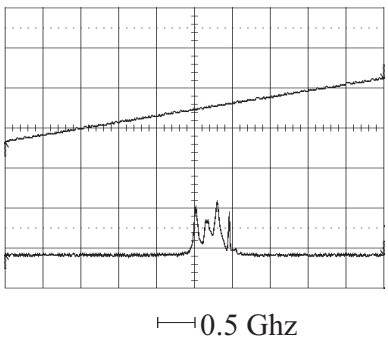

Figure 3.16: Multiple longitudinal mode emission from the phase conjugate oscillator.

These measurements show that the oscillator is lasing (and not just double pass ASE) but does not maintain a stable output. The single mode emission (figure 3.15) has a linewidth of 0.2Ghz. When the oscillator emits on multiple frequencies the modes have a separation of $\sim$0.15GHz .

Measurements taken with the seed laser turned off reveal no coherence in the output. This indicates that the output in this regime is just double pass ASE.

3.5.3.2 Spatial beam quality

Figure 3.17 shows the evolution of the phase conjugate mode with increasing signal beam power.

Initially double pass ASE is emitted from the system, its spatial structure being defined by the size of the pumped region of the crystal and the aperturing effect of the loop. When the signal beam power is increased, the output decreases in intensity as the gain is saturated by the signal beam. Gain gratings then begin to form and the phase conjugate mode is emitted. The output power of the phase conjugate mode increases with the power of the signal beam.

The beam quality of the phase conjugate output was measured to be M_x^2 = M_y^2 = 1.4 . A phase distortion (an etched glass slide) was inserted into the loop of the oscillator, and this had no effect on the beam quality (and only a negligible effect on the power) of the output, indicating the ability of the system to compensate for intracavity distortions.

The elliptical profile of the beam is due to the asymmetry in the gain seen by a beam passing through the bounce geometry amplifier (as shown in section 2.4.2.2).

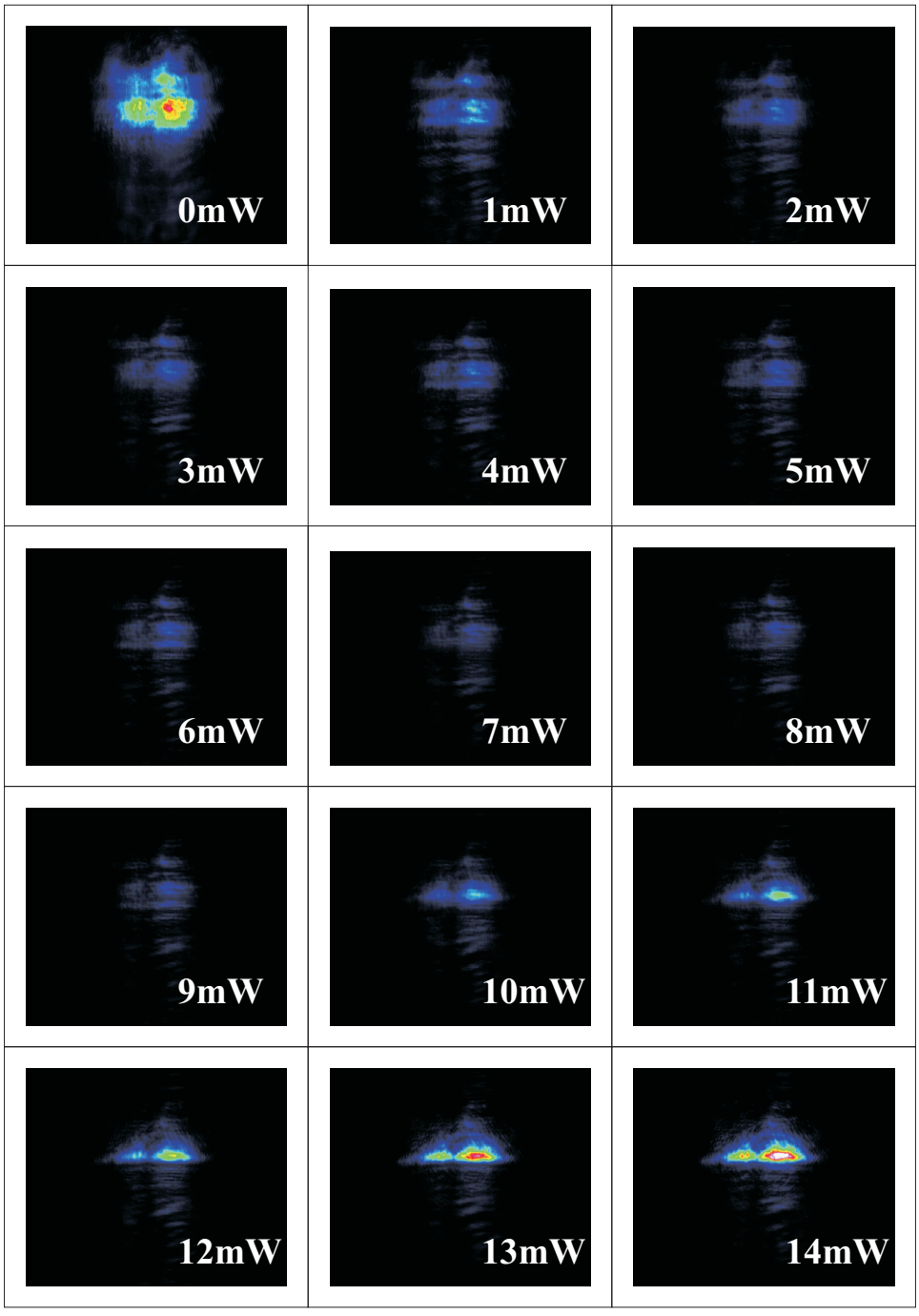

Figure 3.17: The formation of the phase conjugate mode. Signal beam power is increased from 0 to 14 mW in 1mW steps. The weaker spot to the left of the image is due to a reflection from the wedge used to pick off the image.

3.6 Future work

3.6.1 Methods of increasing the output power

In section 3.3 it was explained that two coupled processes control the output power of the phase conjugate oscillator: the diffraction efficiency of the grating and the gain seen by the phase conjugate beam.

These conditions needed to optimise these processes are unfortunately mutually incompatible as the variable attenuator needs to be set to its maximum transmission in one direction and to near its minimum in the other. What is needed is some nonlinear loss mechanism in the loop which will allow a low power beam to pass in one direction whilst attenuating a higher power beam travelling in the other direction.

One solution to this problem is a non-reciprocal transmission device using a ”leaky” Faraday isolator. This is unsuitable for use in a monolithic system but will be discussed further and its implementation described in the next chapter.

3.6.1.1 Controlling the transmission with an aperture

Another possible solution to this problem is the insertion of an aperture into the loop.

When a finite-sized beam is apertured its power is reduced. If this attenuated beam is then reflected by a phase conjugate mirror (PCM). The reflected phase conjugate will pass back through the aperture unattenuated. By varying the diameter of the aperture the power of the writing beam can be controlled whilst maintaining 100% transmission in the opposite direction.

Unfortunately the aperture method of controlling the power ratio has several major disadvantages. If a real Gaussian beam is passed through an

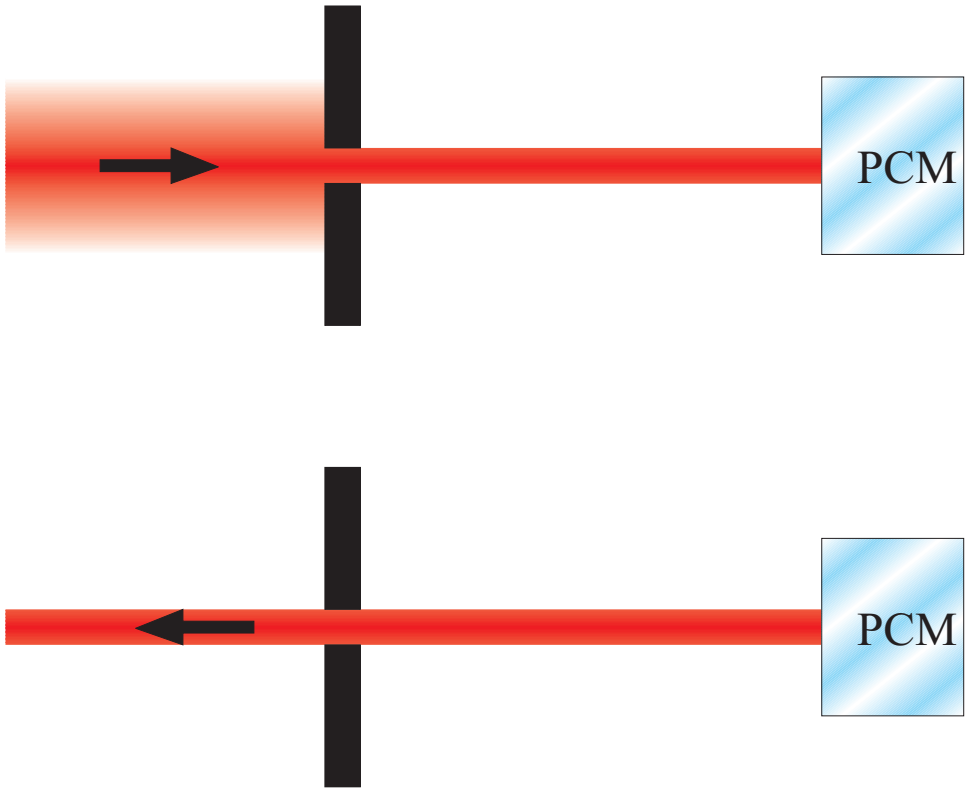

Figure 3.18: Inserting an aperture into a beam which is then phase conjugated.

aperture diffraction effects will act to distort the beam. This will result in a loss of information at the phase conjugate mirror and therefore a distorted reflection.

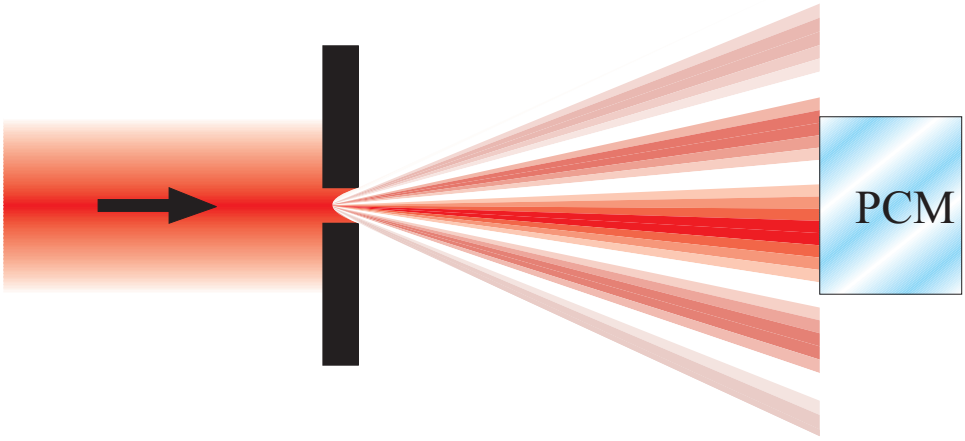

Figure 3.19: Diffractive effects from an aperture limit the ideal phase conjugate behaviour.

Beam steerage due to the thermal load in the amplifier is another issue to be contended with (this will be covered more fully in chapter 5). When the amplifier is pumped the refractive index changes by an amount proportional to its temperature. In a side-pumped geometry this causes the beam's path to deviate by an amount proportional to the pump power. The beam can easily become misaligned with respect to the aperture causing the transmission to vary.

3.6.2 A monolithic resonator

The experiments performed in this chapter show that a (all be it unstable and multi frequency) self intersecting phase conjugator operating via gain gratings with minimal optics can be built. This has the potential for development into a monolithic phase conjugator of a similar design to photo refractive phase conjugators.

A possible schematic of a monolithic phase conjugator is shown in figure 3.20. Here a seed beam is launched into a side-pumped crystal and re-

flected off the pumped face. The beam is then reflected off a corner of the crystal such that it intersects with itself in the region of highest gain. The angle that the seed beam meets the reflective faces would be selected such that their reflectivities would optimise the transmission of the loop and therefore the diffraction efficiency of the gain gratings.

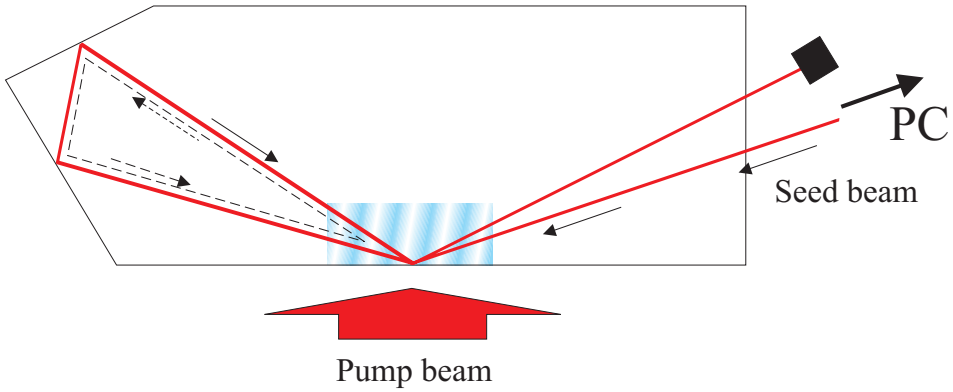

Figure 3.20: A possible schematic for a monolithic phase conjugator.

In order to achieve phase conjugation in the CW regime very high gains are needed. The drawback with high gains is the possibility of power loss through parasitic lasing. The reflective surfaces needed to steer the beam greatly increase the risk of parasitics and multiple pass ASE. This whole topic will be discussed in more detail in chapter 6.

3.7 Conclusions

The oscillator generates a phase conjugate of its seed beam adapting to phase distortions inserted into its cavity. An output power of ~1W is achieved with a slope efficiency of ~5.5%. The output power and longitudinal modal structure fluctuate rapidly. These fluctuations are due to the phase shift between the gain grating and its interference pattern. Several temporal modes are constantly competing for gain suppressing and supporting each other seemingly at random. This complex system results in the power fluctuations that we see in the output.

3.8 References

[1] J.M. Hendricks. *Holographic laser resonators*. PhD thesis, School of Physics, Faculty of Science, University of Southampton, 2002.

[2] Casix. Neodymium doped yttrium orthovanadate (Nd:YVO_4) crystal, 2001. http:\\ www.casix.com.

[3] O. Wittler, D. Udaiyan, G. J. Crofts, K. S. Syed, and M. J. Damzen. Characterization of a distortion-corrected Nd:YAG laser with a self-conjugating loop geometry. *IEEE Journal of Quantum Electronics*, 35(4):656–664, 1999.

Chapter 4

The holographic resonator

4.1 Introduction

In this chapter the phase conjugate oscillator (described in the previous chapter) will be developed into a stable laser system. A non-reciprocal transmission element (NRTE) is inserted into the loop of the oscillator, which acts to improve the efficiency of the system and enable single frequency operation by removing the phase shift between the grating reading and writing beams. The oscillator will be built in both side loop and ring geometries, and it will then be modelled and characterised. A self-starting version of the oscillator will also be built and again modelled and characterised.

4.2 Phase conjugate resonator theory

Solid state phase conjugate oscillators operating via gain gratings have previously been constructed under several pulsed regimes including flash-lamp pumped Nd:YAG [1], diode pumped Nd:YVO_4 [2], laser-pumped Ti:sapphire [3] and more recently Nd:YLF [4]. The development of high power (tens of Watts) laser diodes in conjunction with the high gain laser

crystal Nd:YVO_4 have allowed for the development of continuous-wave devices [5] [6], which will be investigated here.

4.2.1 Operation of the resonator

The resonator described in this chapter operates in fundamentally the same manner as the resonator described in the previous chapter.

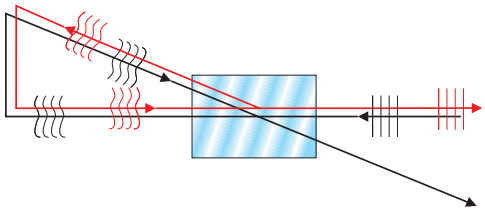

Figure 4.1: Operation of the side loop resonator.

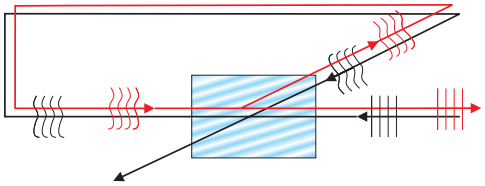

Figure 4.2: Operation of the ring resonator.

Figures 4.1 and 4.2 show schematics of the operation of the holographic resonator in both the side loop and ring geometries. In both geometries the grating is written by a seed beam (the black line) which intersects with itself in a saturable amplifier. Fluorescence then scatters off the gratings, counter and co-propagating along the paths of the writing beams. The fluorescence propagating around the loop anticlockwise builds up to form stable oscillation (the red lines), and the fraction of this oscillating power which is not diffracted by the gain grating is emitted as a phase conjugate output.

4.2.2 The non-reciprocal transmission element

A non-reciprocal transmission element (NRTE) is used to control the power flow around the loop of the resonator. It acts as a leaky optical diode allowing a beam to pass in one direction with high transmission but severely attenuating any transmission in the reverse direction.

The NRTE consists of a polariser followed by a 45° Faraday rotator, a half-wave plate and finally another polariser (aligned in the same orientation as the first polariser) [7].

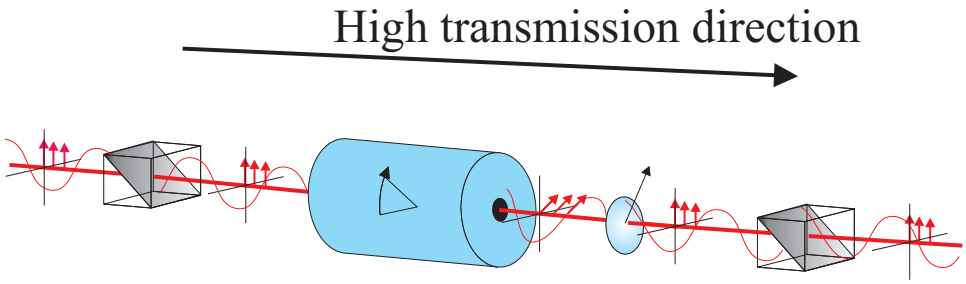

Figure 4.3: A beam passing through an NRTE left to right (t_+).

Figure 4.3 shows the effect on a vertically polarised beam as it passes through a NRTE set to its maximum extinction efficiency for light incident in the reverse direction. The beam first passes through a polariser then the Faraday rotator, which rotates the polarisation of the beam by 45° clockwise as seen looking back to the source of the beam. The beam then passes through a half-wave plate which rotates the polarisation back to vertical (45° anticlockwise). Finally the beam passes through a second polariser leaving the NRTE unattenuated.

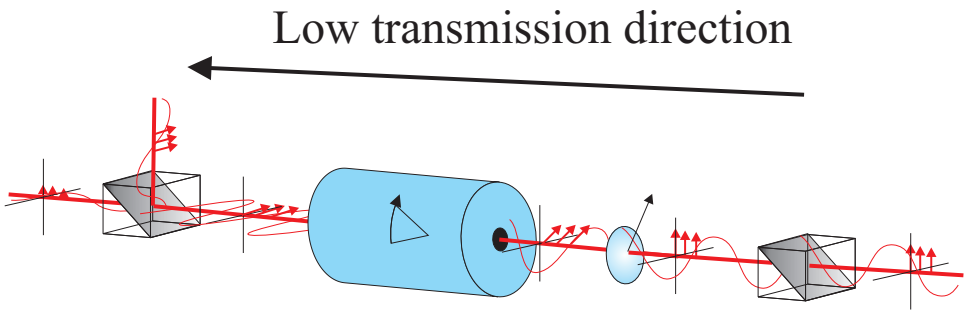

Figure 4.4: A beam passing through an NRTE right to left (t_-).

If a vertically polarised beam is passed through the NRTE in the opposite direction (Figure 4.4) it will be severely attenuated. The beam first passes through the polariser then the half-wave plate. At the half-wave plate its polarisation will be rotated by 45° anticlockwise (again as seen looking back at the source of the beam). The beam then passes through the Faraday

rotator which will rotate the polarisation by a further 45° anticlockwise. The beam, now horizontally polarised, is rejected by the final polariser.

By varying the angle of the half-wave plate the transmission of the NRTE can be controlled. With the half-wave plate rotated such that its optic axis is set to an angle of 22.5° [1] to the vertical the NRTE will act as an optical diode permitting high transmission in one direction but inhibiting it in the other. If the half-wave plate is rotated slightly the extinction ratio (the ratio of incident power to transmitted power) will fall permitting some transmission in the previously blocked direction and slightly attenuating the transmission in the other.

4.2.2.1 A Jones matrix model of the NRTE

The transmission of the NRTE as a function of the angle of its half-wave plate can be calculated by using a Jones matrix approach [8].

The Jones matrix of a beam polarised parallel to an arbitrary y-axis (by convention vertically polarised) is given by

$$\mathbf{V} = \begin{pmatrix} 0 \\ 1 \end{pmatrix} \tag{4.1}$$

with its intensity calculable from

$$\mathbf{I} = \mathbf{V} \cdot \mathbf{V}^* \tag{4.2}$$

The Jones matrices given in table 4.1 can be used to find the transmission in each direction through the NRTE. Firstly a beam travelling left to right (t_+) through the NRTE as shown in figure 4.3 will be described by:

[1] The polarisation shift induced by a half-wave plate is equal to twice the angle that its axis makes with the polarisation of the incident beam. Hence a half-wave plate angle of 22.5° results in a 45° polarisation rotation.

Component	Orientation	Jones matrix
Polariser	Transmission axis is vertical	$\mathbf{P} = \begin{pmatrix} 0 & 0 \\ 0 & 1 \end{pmatrix}$
Half-wave plate	Crystal axis is at an angle θ_{hwp} to the vertical	$\mathbf{H} = i \begin{pmatrix} \cos(2\theta_{hwp}) & \sin(2\theta_{hwp}) \\ \sin(2\theta_{hwp}) & -\cos(2\theta_{hwp}) \end{pmatrix}$
Faraday rotator	Rotation set to θ_{rot}	$\mathbf{R} = \begin{pmatrix} \cos(\theta_{rot}) & -\sin(\theta_{rot}) \\ \sin(\theta_{rot}) & -\cos(\theta_{rot}) \end{pmatrix}$

Table 4.1: Jones matrices for the optical components of an NRTE [8]

$$\begin{aligned} t_+ &= \mathbf{P} \cdot \mathbf{H} \cdot \mathbf{R} \cdot \mathbf{P} \cdot \mathbf{V} \\ &= i \sin(\theta_{rot}) \sin(2\theta_{hwp}) - i \cos(\theta_{rot}) \cos(2\theta_{hwp}) \end{aligned} \tag{4.3}$$

With a $\theta_{rot} = 45°$ the transmission intensity is given by

$$T_+ = \cos^2(\frac{\pi}{4} - 2\theta_{hwp}) \tag{4.4}$$

and right to left (t_-) as in figure 4.4

$$\begin{aligned} t_- &= \mathbf{P} \cdot \mathbf{R} \cdot \mathbf{H} \cdot \mathbf{P} \cdot \mathbf{V} \\ &= -i \sin(\theta_{rot}) \sin(2\theta_{hwp}) - i \cos(\theta_{rot}) \cos(2\theta_{hwp}) \end{aligned} \tag{4.5}$$

giving an intensity transmission of

$$T_- = \cos^2(\frac{\pi}{4} + 2\theta_{hwp}) \tag{4.6}$$

The theoretically calculated transmissions are shown along with the experimental values in figure 4.5.

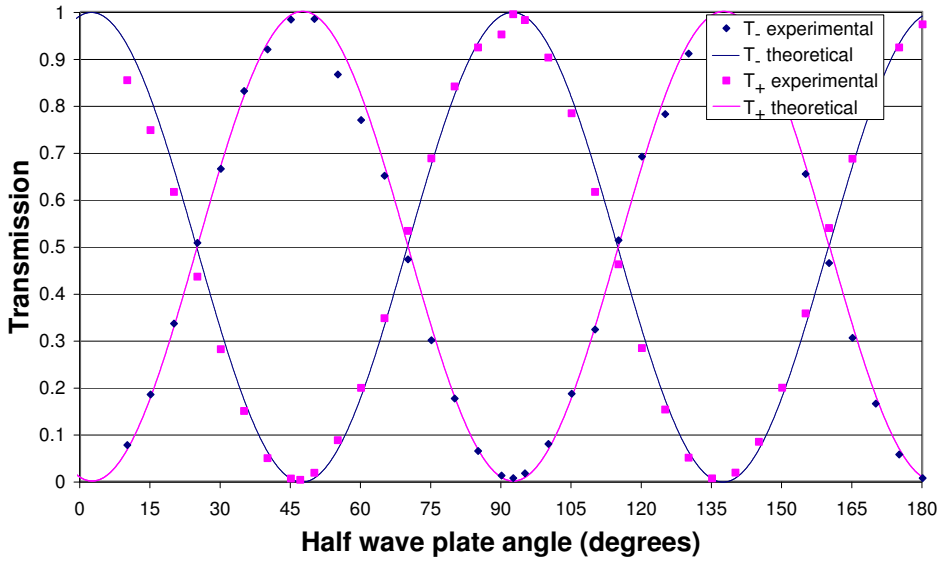

Figure 4.5: Transmission of the NRTE as a function of its half-wave plate angle.

4.2.3 Temporal properties

Figure 4.6 shows the amplitude transmission of the NRTE. It can be seen that over a range of half-wave plate angles (22.5 to 67.5° and 112.5 to 157.5°) there is a phase difference between the beams transmitted in either direction. This non-reciprocal (π) phase shift between the transmission in either direction has a very useful consequence.

In section 3.2.2 the temporal structure of a resonator without an NRTE was examined. It was found that oscillation on the resonator's seed wavelength was not possible due to the phase shift between the gain grating and its interference pattern. By inserting an NRTE into the loop, the π phase shift caused by the gain gratings is cancelled out allowing the resonator to operate on a single frequency.

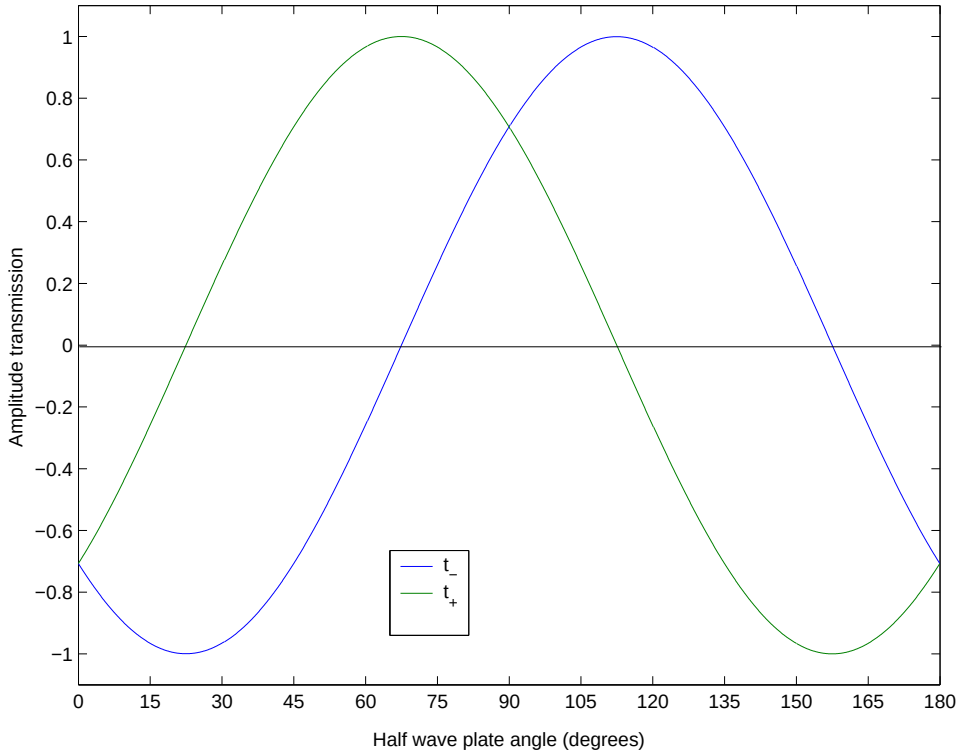

Figure 4.6: Amplitude transmission of the NRTE as a function of its half-wave plate angle.

4.3 Modelling the phase conjugate resonator

The resonator functions (as did the oscillator described in the previous chapter) under the same basic principles as the degenerate four-wave mixing phase conjugator described in chapter 3. The operation of the resonator is described by the same coupled differential equations (Equations C.27 for the side arm loop geometry and C.22 for the ring geometry) but with boundary conditions defined by the loop nature of the resonator [9].

4.3.1 Boundary conditions

4.3.1.1 Side loop resonator

The boundary conditions for the side loop resonator are

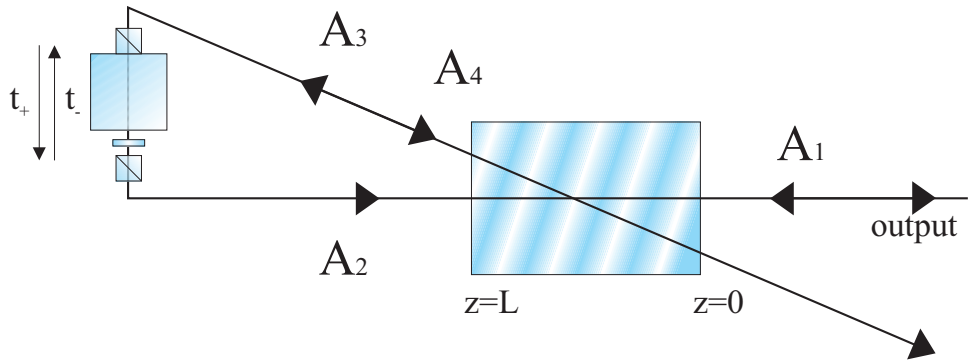

Figure 4.7: A schematic of the phase conjugate resonator in a side loop geometry with an NRTE inserted into the loop.

$$A_4(L) = t_- A_1(L) \tag{4.7}$$

$$A_2(L) = t_+ A_3(L) \tag{4.8}$$

$$A_3(0) = 0 \tag{4.9}$$

where t_+ and t_- are the amplitude transmissions of the NRTE in each direction as shown in figure 4.7.

4.3.1.2 Ring resonator

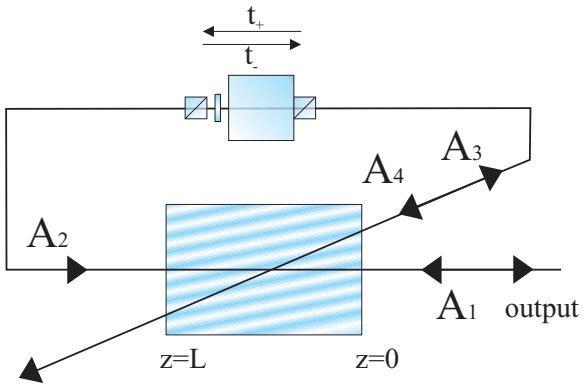

Figure 4.8: A schematic of the phase conjugate resonator in a ring geometry with an NRTE inserted into the loop.

The boundary conditions for the ring resonator are

$$A_4(0) = t_- A_1(L) \quad (4.10)$$

$$A_2(L) = t_+ A_3(0) \quad (4.11)$$

$$A_3(L) = 0 \quad (4.12)$$

where the beams and NRTE transmissions are labelled as shown in figure 4.8

4.3.1.3 Self-starting resonator

In the case of a self-starting resonator the seed beam is replaced by an output coupler generating the additional boundary condition

$$A_1(0) = rA_2(0) \quad (4.13)$$

where r, the amplitude reflectivity of the output coupler, $= \sqrt{R}$ where R is the intensity reflectivity.

4.3.2 Numerical modelling of output powers

The output power characteristics of the resonators are calculated by solving the coupled differential equations governing the four-wave mixing process (Equations C.22 and C.27) under the boundary conditions defined by each geometry. The equations are solved numerically in Matlab using a program developed by my predecessor on this project Dr Jason Hendricks. I have since expanded his program, changing the method in which it solved the differential equations to improve its accuracy and adapted it to the specific situations detailed here.

4.3.2.1 Modelled output powers as a function of seed power

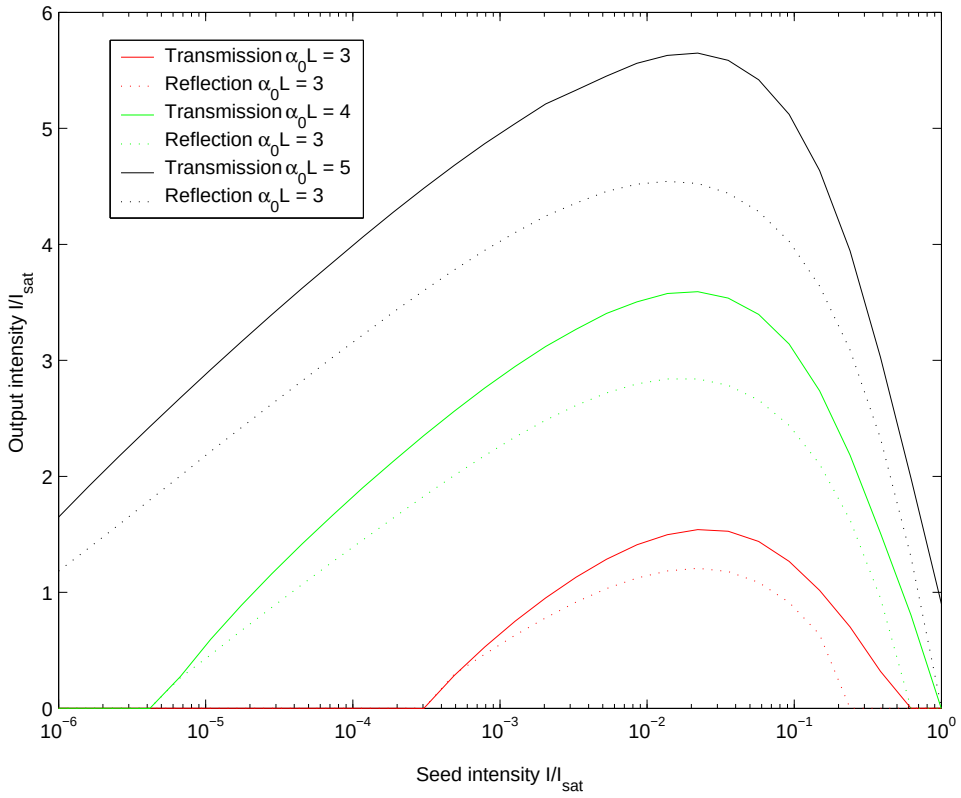

Figure 4.9: Modelled output power as a function of seed power.

Figure 4.9 shows the modelled output power of the resonator as a function of its seed power for a range of amplifier gains. At low seed beam intensities the gain gratings formed are with the gain unsaturated at the nodes of the interference pattern. This leads to a low diffraction efficiency and therefore low output powers. The diffracted beam at this point will however see strong gain.

The output intensity increases as the seed power is increased due to the increase in diffraction efficiency of the gain gratings. Whilst this is happening however the gain available to the diffracted beam is being depleted by the seed beam.

The output power reaches a peak then falls as the gain extracted by the seed beam depletes that available to the phase conjugate. Eventually so

much power will be extracted that the reflectivity of the gain gratings will fall below unity making the resonating beam unsustainable and lasing will cease.

4.3.2.2 Modelled output powers as a function of loop transmission

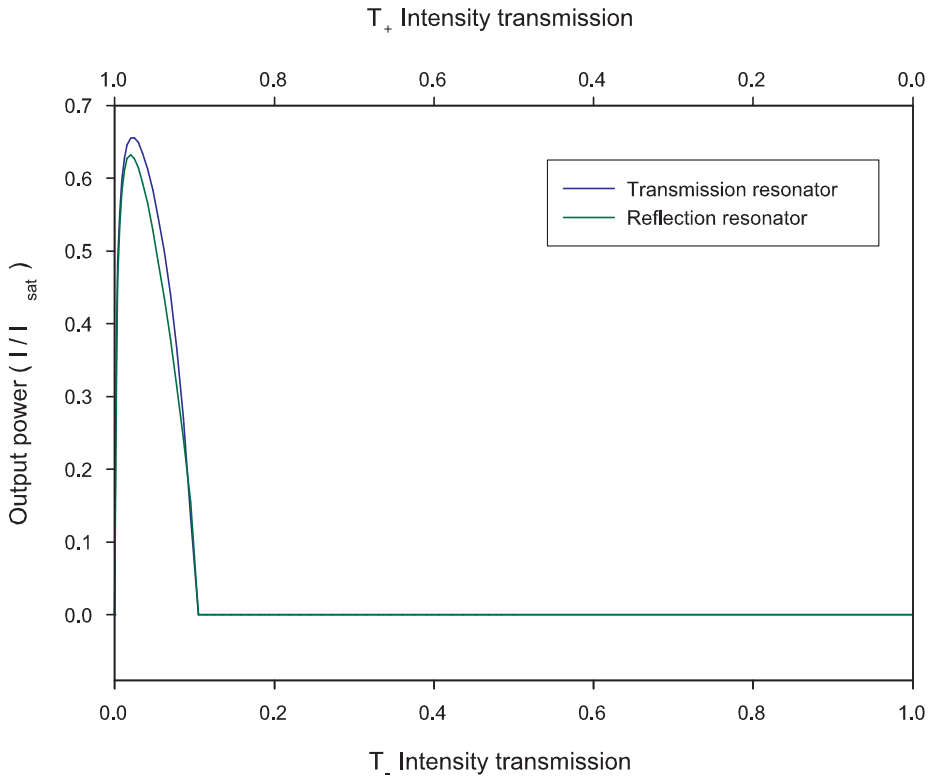

Figure 4.10: Phase conjugate output power as a function of loop transmission.

Figure 4.10 shows the modelled output power as a function of loop transmission in both directions. The balance between the transmissions in either direction around the loop govern the operation of the resonator.

This model shows that the lasing threshold is reached at roughly the same point for both resonator geometries. The threshold is at a transmission of $T_- = 0.1$ (clockwise) and $T_+ = 0.9$ (anticlockwise). This is equivalent to a half-wave plate angle of 58° to the vertical in the NRTE.

Once threshold has been reached increasing the anticlockwise transmis-

sion (T^+) will lower the losses seen by the resonating beam. The resultant decrease in the clockwise transmission (T^-) will cause the grating writing beams to equalise, increasing the diffraction efficiency and therefore the output power.

The output power peaks at a transmission of $T_- = 0.02$ (Equivalent to a half-wave plate angle of 63°). Here the writing beams have equal intensities so the contrast ratio and hence the diffraction efficiency of the grating will be maximised.

Increasing the anticlockwise transmission still further (and subsequently decreasing the clockwise transmission) causes the output power to fall. This decrease is due to the imbalance between the grating writing beams (the intensity of the amplified beam falls below that of the seed beam), which causes the contrast ratio and hence the diffraction efficiency of the gain grating to be reduced.

4.3.2.3 Intracavity flux modelling

The power build up in the resonator is dependent on the diffraction efficiency of the gain gratings and the gain seen by the resonating beam. Figure 4.11 shows the resonating intensity as a function of the seed intensity for a range of amplifications. The contrast ratio of the gain grating increases with the rising seed power causing the intracavity flux to increase. Whilst this is happening the gain available to the resonating flux falls as more is taken by the seed beam.

4.3.2.4 Resonator threshold calculations

In order to achieve phase conjugate output the reflectivity of the gain gratings needs to be greater than unity. Figure 4.12 shows the output power of the resonator as a function of the gain coefficient-length product. Threshold is reached at $\alpha_0 L = 2$ which is equivalent to a small signal single pass

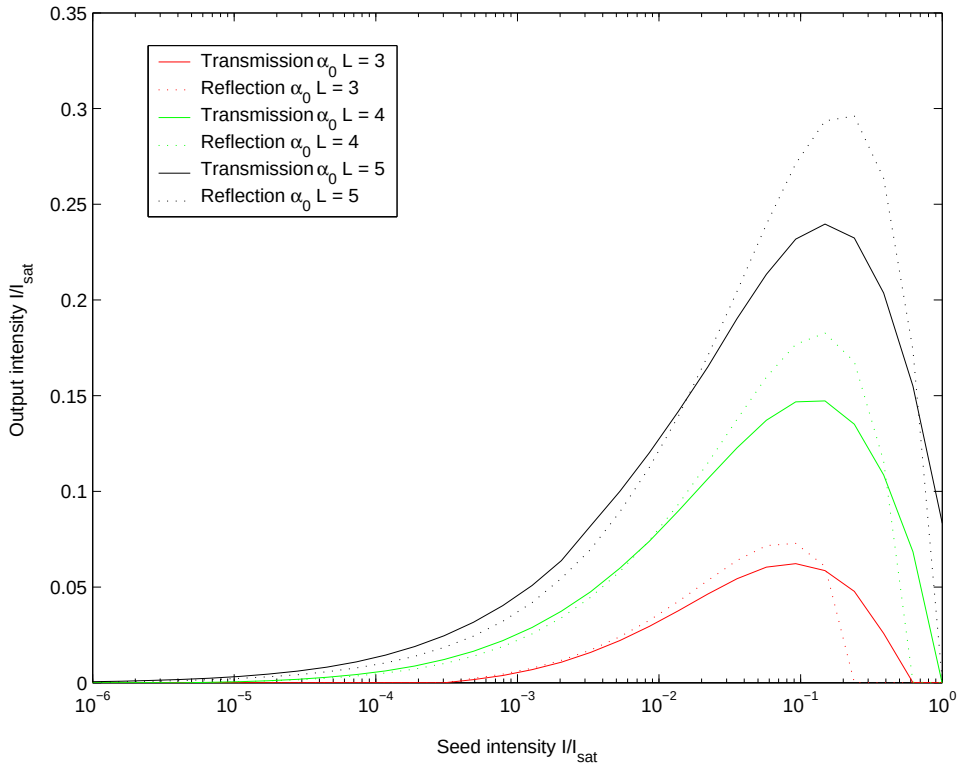

Figure 4.11: Intracavity flux in the loop of the resonator.

gain (SSSPG) of 55.

4.4 Experimental

4.4.1 Side loop resonator setup

Figure 4.13 shows the experimental setup used to investigate the properties of the holographic resonator in a side loop geometry. A seed beam is passed through a side-pumped Nd:YVO_4 amplifier in a bounce geometry as described in section 2.4.3. The seed beam is focused to a $\sim$30µm spot at the pumped face.

The amplified beam is passed through an NRTE then launched back into the crystal through the face that it left with the second 100mm focal length spherical lens. The beam is aligned such that it will intersect with itself

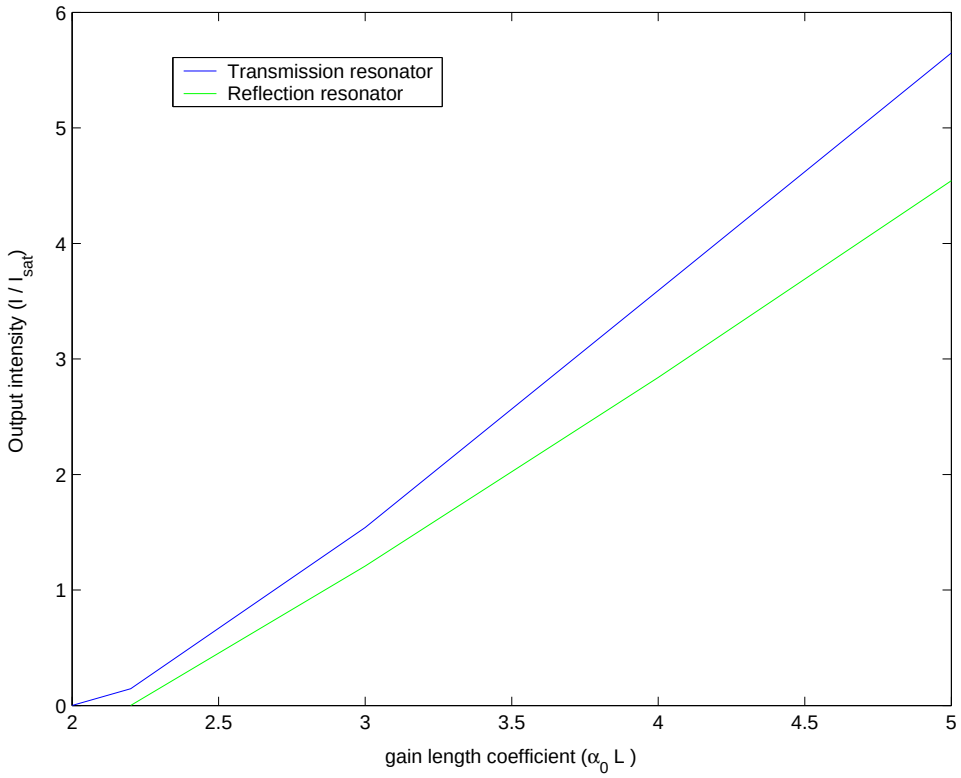

Figure 4.12: Threshold calculations for the ring resonator.

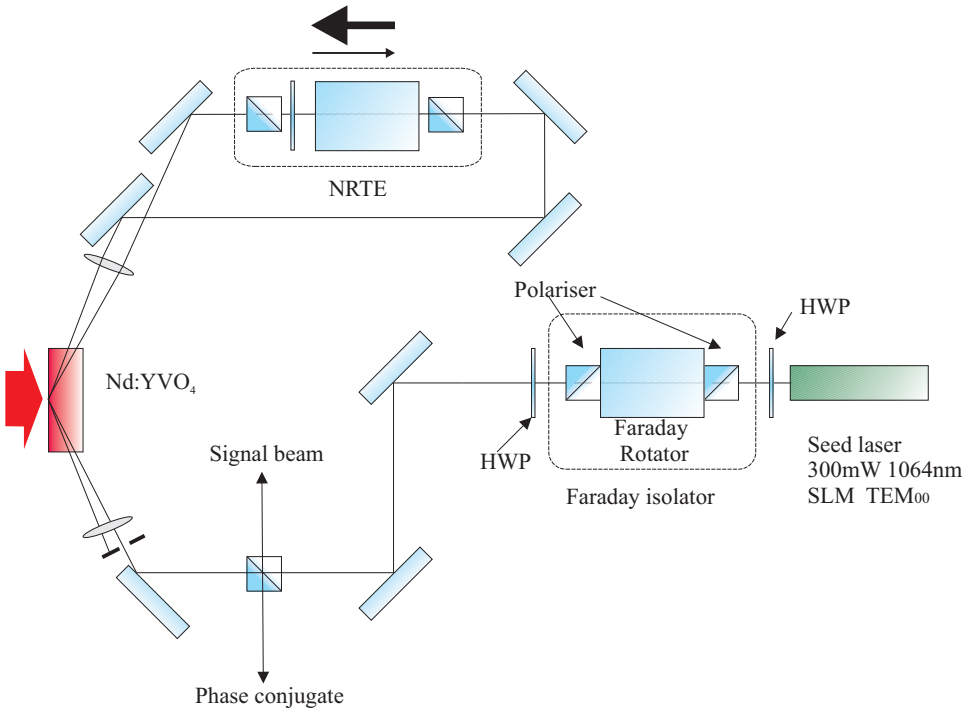

Figure 4.13: A schematic of the phase conjugate resonator in a side loop geometry.

at the pumped face of the amplifier. Any phase conjugate generated is measured at a 50:50 beam splitter inserted into the arm of the resonator.

The amplifier is side pumped with a 40W 808nm TM polarised diode bar. The pump beam is initially collimated with a fibre lens then focused into the amplifier with a 6.3mm focal length cylindrical lens.

4.4.2 Ring resonator setup

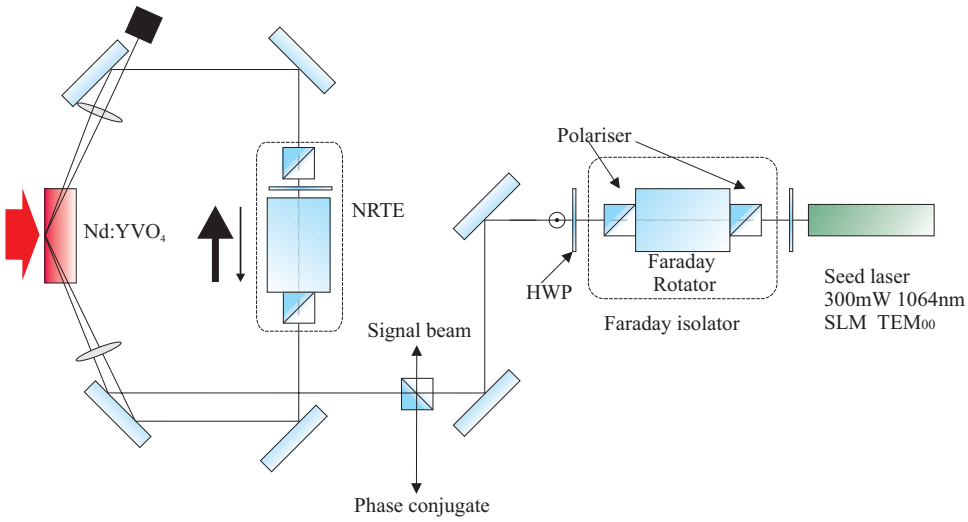

Figure 4.14: A schematic of the phase conjugate resonator in a ring geometry.

Figure 4.14 shows the setup used in the ring geometry resonator experiments. All of the parameters in this setup are the same as for the side loop geometry, the only difference being that once the beam has passed through the NRTE it is launched back into the amplifier through the same face that the seed beam was launched.

A self starting version of the ring resonator was constructed by replacing the seed laser with a 4% reflectivity output coupler and inserting a 2mm diameter aperture into the input/output arm.

4.5 Results

4.5.1 Output powers as a function of seed beam power

4.5.1.1 Ring resonator results

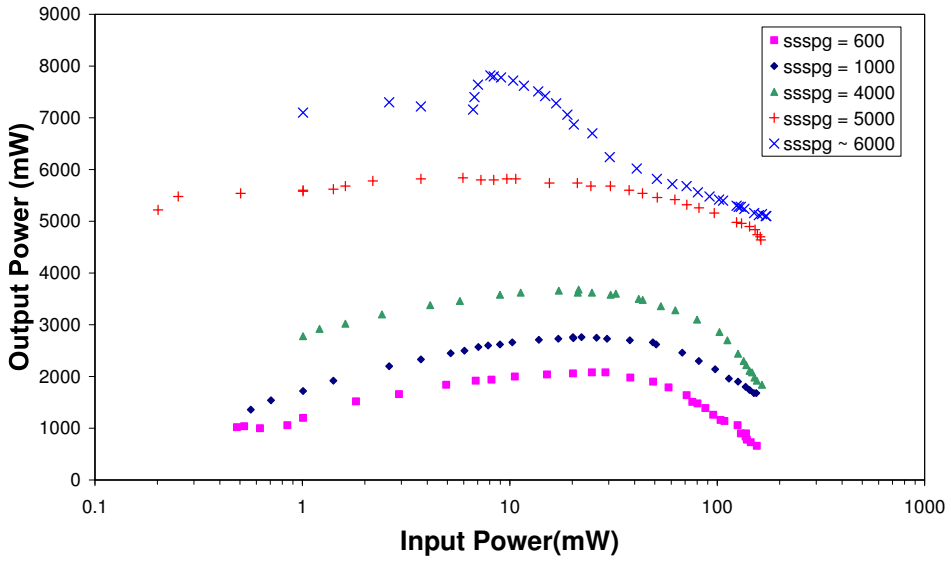

Figure 4.15: Phase conjugate output power as a function of seed power.

Figure 4.15 shows the phase conjugate output power produced by the ring resonator as a function of its seed power for a range of measured small signal single pass gains. The NRTE transmission is chosen to obtain the maximum phase conjugate output power.

At low seed powers the gain gratings formed have a low contrast ratio resulting in a low diffraction efficiency. As the seed power is raised the contrast ratio of the grating increases causing the diffraction efficiency to rise. When the seed power is increased still further the diffraction efficiency keeps rising, however the high seed power causes the gain to decrease lowering the output power. Increasing the seed power still further causes the amplifier to be completely saturated and resonator operation to cease.

4.5.1.2 Side loop resonator results

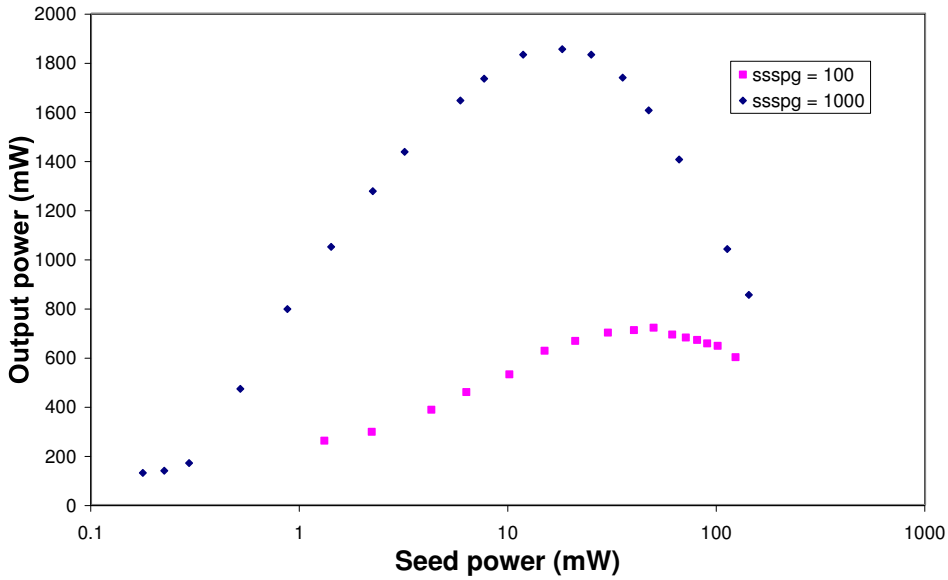

Figure 4.16: Phase conjugate output power as a function of seed power.

Figure 4.16 shows the phase conjugate output power produced by the side loop resonator as a function of seed power. The NRTE transmission is chosen to obtain the greatest phase conjugate output power. This resonator operates in the same manner as the ring resonator.

4.5.2 Output powers as a function of loop transmission

4.5.2.1 Ring resonator results

Figure 4.17 shows the phase conjugate output power produced by the ring resonator as a function of the half-wave plate angle of the NRTE. The transmission in each direction for the NRTE can be found in figure 4.5.

Starting at a half-wave plate angle of 22.5° where the clockwise transmission around the loop is at its maximum and the anticlockwise its minimum. The transmission seen by the scattered fluorescence is so low that lasing threshold is not reached and no phase conjugate is generated. The half-wave plate angle is then increased to ∼45° where the anticlockwise

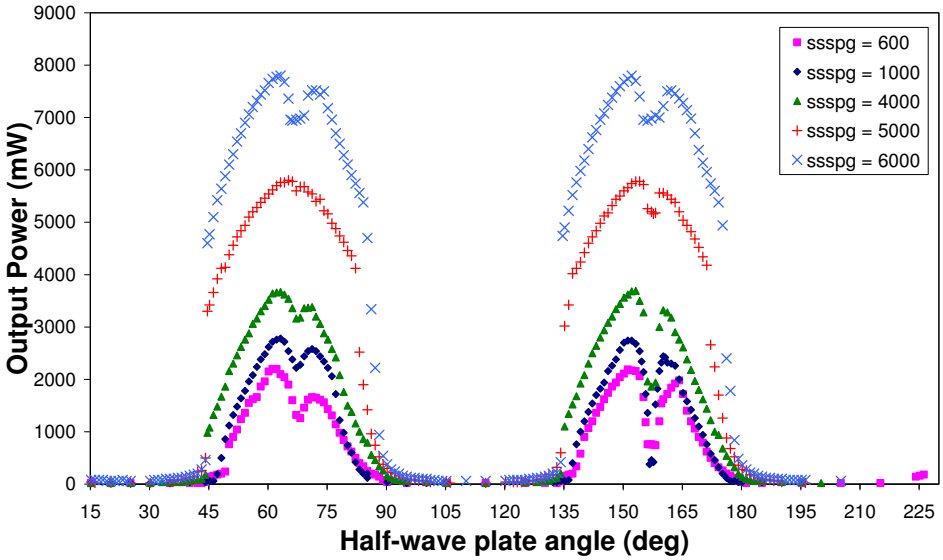

Figure 4.17: Phase conjugate output power as a function of the angle of the half-wave plate in the NRTE with respect to the vertical.

transmission rises enough for the lasing threshold to be met and a phase conjugate output produced.

The half-wave plate angle is increased still further causing the clockwise transmission to fall and the powers of the grating writing beams to equalise, increasing the diffraction efficiency of the grating. The anticlockwise transmission also increases which results in a lower attenuation of the resonating beam. The output power is maximised at $\sim 65^\circ$.

At $\sim 70^\circ$ the clockwise transmission is so small that the amplified writing beam has a lower intensity than the seed beam. This causes the diffraction efficiency of the gain grating to fall and with it the output power. The output reaches a minimum at $\sim 68^\circ$ after which the intensity of the amplified beam increases raising the diffraction efficiency of the grating and with it the output power.

Beyond $\sim 70^\circ$ the output power falls again as the grating diffraction efficiency decreases and the transmission of the loop falls. This behaviour is repeated every time the half-wave plate is rotated by a further 90° .

4.5.2.2 Side loop resonator results

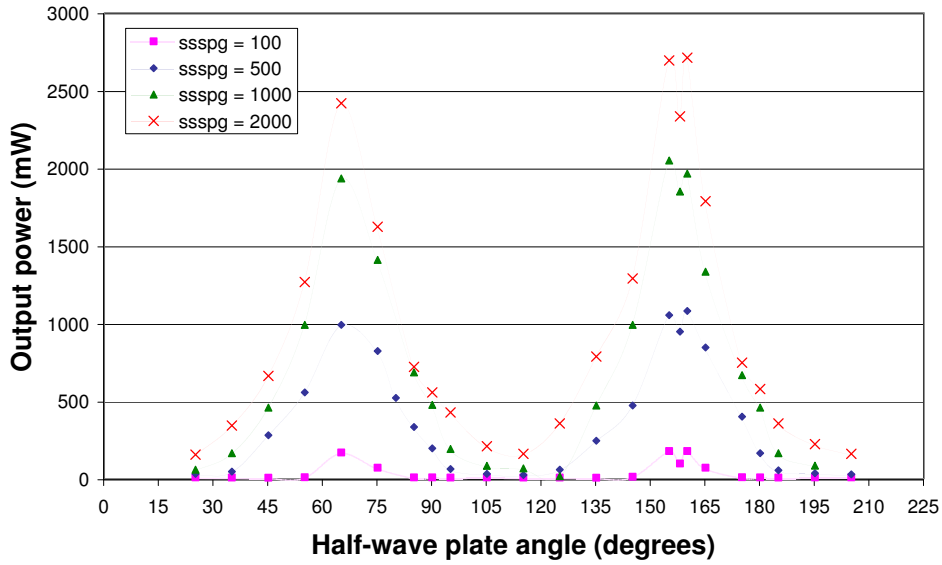

Figure 4.18: Phase conjugate output power as a function of the angle of the half-wave plate in the NRTE.

Figure 4.18 shows the phase conjugate output power of a side-loop resonator as a function of the half-wave plate angle of the NRTE. Its characteristics are fundamentally the same as those for the ring resonator with only minor differences.

4.5.3 Ring resonator intracavity flux measurements

The intracavity oscillating power in a ring resonator was measured by inserting a wedge into the loop between the NRTE and crystal. In this experiment the NRTE was set to achieve maximum output power.

Figure 4.19 shows the power of the oscillating beam as a function of seed beam power. Initially the oscillating power rises slowly as the gain gratings form and their diffraction efficiency increases. The oscillating power keeps increasing reaching a maximum at a seed power of ~70mW (at a ssspg of 4000) after which it falls sharply.

It should be noted that the resonators intracavity power is low compared

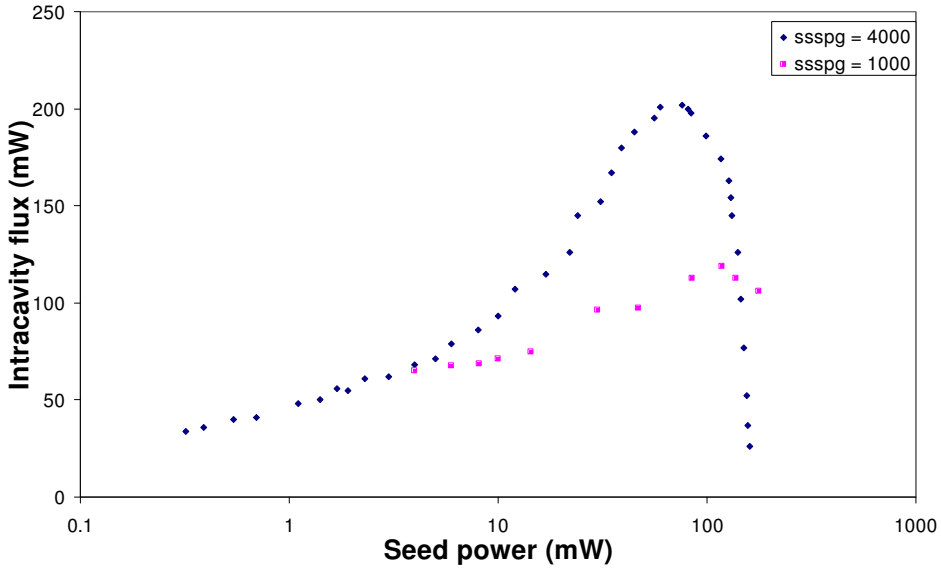

Figure 4.19: Intracavity flux in the loop of a ring resonator as a function of seed power.

with its output power. This gives some insight into the operation of the holographic resonator.

If we look at the ssspg=4000 data set, then for an intracavity flux of 120mW (Reached at a seed power of ∼20mW) we get an output of ∼4W. This is equivalent to the beam seeing a gain of 33 which is roughly the same as that experienced by a 120mW beam passed through an amplifier with a ssspg=4000 (See the modelling and experimental single pass gain work in chapter 2).

This shows that only a small portion of the oscillating beam is diffracted from the gain grating (The product of the gain seen on passing through the amplifier and the reflectivity of the grating is one). The majority of the beam passes back through amplifier seeing gain and is emitted as the phase conjugate of the seed beam.

4.5.4 Frequency Spectrum

The frequency spectrum of the holographic resonators was measured using a plane-plane Fabry-Perot interferometer. Figure 4.20 shows the longitudinal modal structure of the ring resonator and figure 4.21 for the side loop resonator. In both cases SLM operation is achieved with instrument limited linewidths of ∼0.2 GHz.

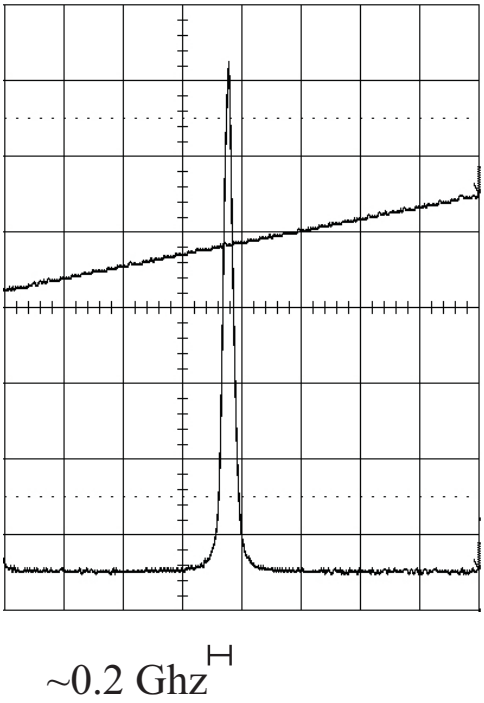

Figure 4.20: Fabry-Perot trace from the ring resonator.

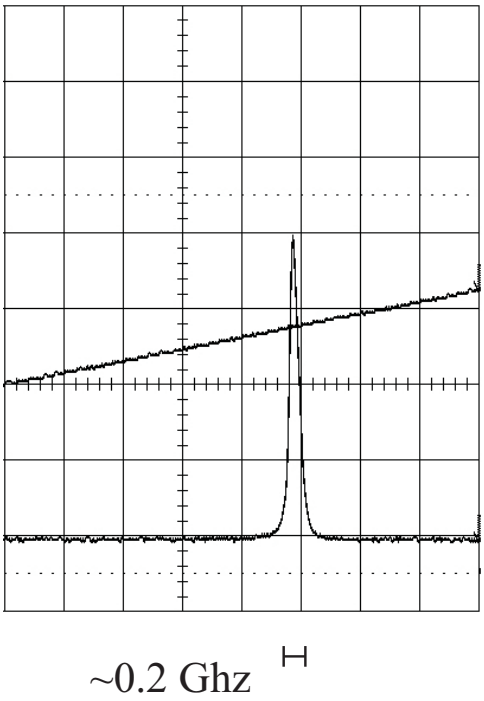

Figure 4.21: Fabry-Perot trace from the side-loop resonator.

4.5.5 Spatial beam quality

The spatial output of the ring resonator was viewed and captured by a Coherent BeamView Analyzer. The spatial output for a ring resonator with a SSSPG = 4000 is shown in figure 4.22. Figure 4.23 shows the effect on the output caused by the insertion of a phase distorter (an etched glass slide) into the cavity of the resonator. Figure 4.24 shows the effect that the distortion has on a single (spatial) mode beam. The output (both with and

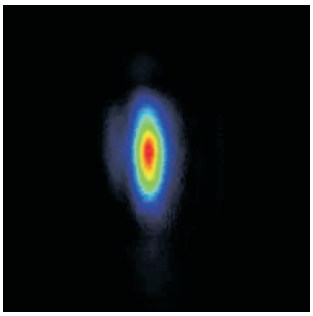

Figure 4.22: Spatial profile of the output beam from the ring resonator.

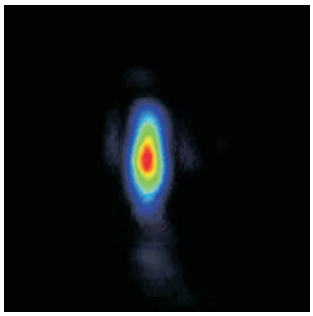

Figure 4.23: Spatial profile of the output beam from the ring resonator with intra cavity distortion.

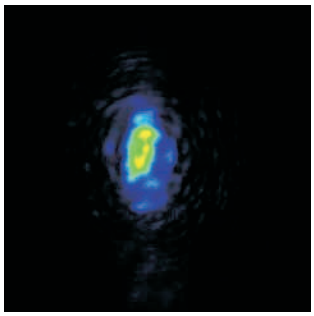

Figure 4.24: The effect of the distorting element on a single mode beam.

without the additional intracavity distortion) was found to have a beam quality of $M_x^2 \simeq 1.3$ and $M_y^2 \simeq 1.2$ with a diffraction-limited seed beam.

In some experiments the insertion of the phase distorter caused the output power of the laser to increase. It did this by suppressing any parasitic processes, while the resonator on the other hand could just adapt to the distortion.

The beam shape is elliptical due to the asymmetry in the gain region of the amplifier as shown in section 2.4.2.2. A circular beam can be formed by the use of cylindrical optics to focus the initial beam into the amplifier. This has been realised experimentally by our collaborators at Imperial College London [10].

4.5.6 Self-starting experiments results

In these experiments the ring resonator was modified by replacing the seed laser with an output coupler with a 4% intensity reflectivity and the insertion of an aperture into the input/output arm of the resonator.

Figure 4.25 shows the phase conjugate output power as a function of the the NRTE half-wave plate angle. The output power varies with the half-wave plate angle in a similar manner to the seeded ring resonator. There

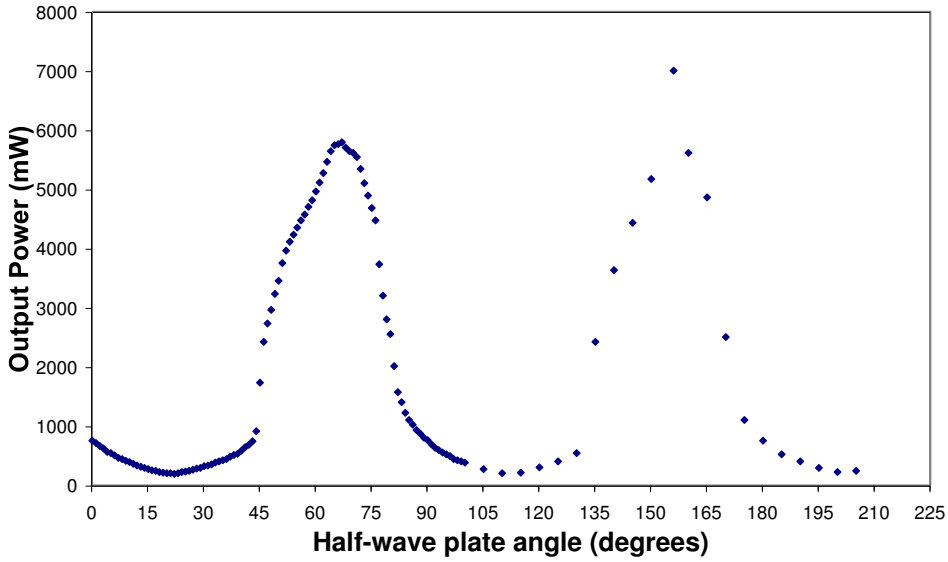

Figure 4.25: Phase conjugate output power as a function of the angle of the half-wave plate in the NRTE. Here the seed laser has been replaced by a 4% reflectivity output coupler.

is however no dip at the point of minimum transmission. This can be explained by considering the adaptive nature of the resonator.

If a beam is sent through the NRTE at a slight angle then the maximum achievable attenuation is reduced. In the self starting resonator the spatial mode can take a range of paths around the loop as long as it intersects with itself inside the region of high gain . By shifting in angle slightly the mode will increase its transmission and therefore keep lasing even at the point of maximum attenuation.

The insertion of the aperture in the arm of the self-starting ring resonator was performed in order to define the transverse mode structure of the output. Single transverse mode operation was achieved with beam qualities of M_x^2 = 1.5 and M_y^2 = 1.4. These beam qualities (and the output power) were unaffected by the insertion of an etched glass slide into the loop of the resonator.

4.6 Discussion

4.6.1 Operation of the resonator

The output power of the resonator is determined by two things, the diffraction efficiency of the gain gratings and the gain seen by the resonating phase conjugate. The use of the NRTE vastly improves the efficiency of the resonator by allowing the grating beams to have equal strength whilst allowing the phase conjugate to resonate unimpeded.

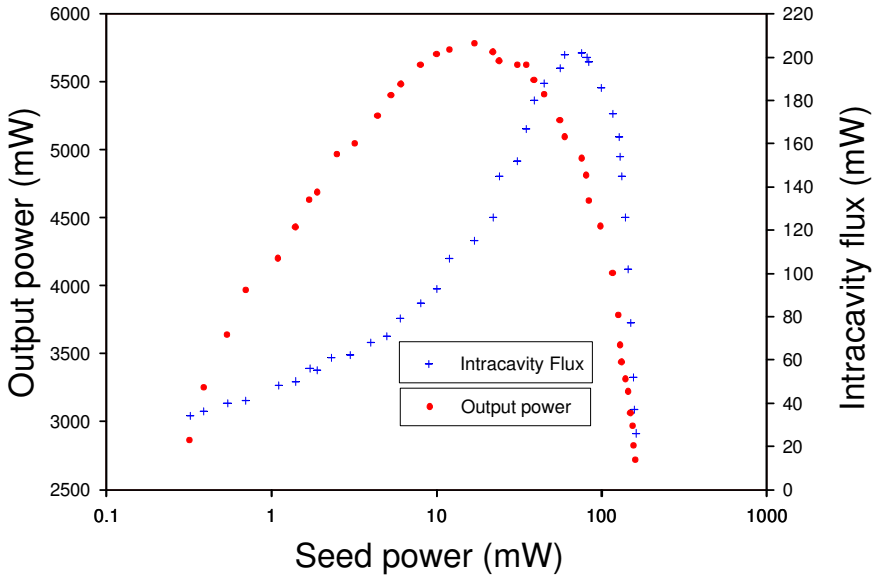

Figure 4.26: Phase conjugate output power and intracavity flux as a function of seed beam power.

Figure 4.26 shows the intracavity flux and output power on the same graph. It is initially surprising that the peak output power does not occur at the same seed power as the peak in the resonating flux. This does match what the modelling predicts (figure 4.27) and shows that whilst intracavity intensity is at its greatest enough power has been extracted from the amplifier to cause the final beam to see lower than optimal gain. This also helps to demonstrate the many factors that have to be balanced in the resonator

in order to achieve the greatest output.

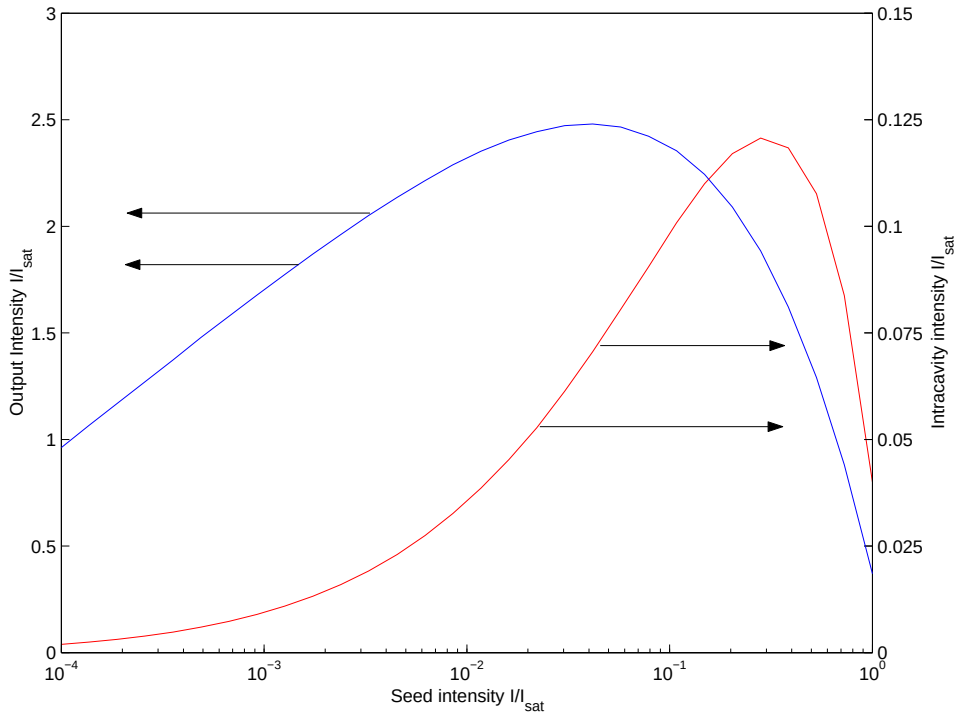

Figure 4.27: Modelled output power and intracavity flux as a function of seed beam power of an amplifier gain of $\alpha_0 L = 4$.

4.6.2 Comparing the geometries

Theoretically there is little difference between the ring and side loop geometries. Experimentally however the ring geometry proved to be more useful. Every time the seed beam is passed through the amplifier it becomes distorted. In the ring resonator the doubly distorted (and amplified) seed beam is directed away from the input/output arm and does not affect it.

In the side loop resonator however the doubly distorted beam is emitted from the same side of the resonator as the output. This can result in an overlap between the seed beam and the distorted beam, making it hard to isolate the phase conjugate. Whilst the problem can be reduced by increasing the angular separation of the beams this causes a reduction in overlap

between the writing beams (and therefore shorter gain gratings) and lowers the gain seen by the resonating beam. The combination of these effects reduces the power that can usefully be extracted from the resonator and hence lowers its efficiency. When the pump power is increased the doubly distorted beam is expanded still further exasperating the problem. These effects make any experimentally realisable side loop resonator noticeably less efficient than the equivalent ring resonator.

4.7 Conclusions

The holographic resonator with a non-reciprocal transmission element has been investigated in both side-loop and ring geometries. Output powers of up to 8W in a ring resonator and 2.5W in a side loop resonator have been achieved with single longitudinal and spatial mode operation. A self-starting version of the ring resonator achieved output powers of $\sim$7W. The resonator has been shown to adapt to intracavity phase distortions with no loss of beam quality.

4.8 References

[1] M. J. Damzen, R. P. M. Green, and K. S. Syed. Self-adaptive solid-state laser-oscillator formed by dynamic gain-grating holograms. *Optics Letters*, 20(16):1704–1706, 1995.

[2] A. Brignon and J. P. Huignard. Continuous-wave operation of saturable-gain degenerate 4-wave- mixing in a Nd:YVO_4 amplifier. *Optics Letters*, 20(20):2096–2098, 1995.

[3] A. Minassian, G. J. Crofts, and M. J. Damzen. Self starting Ti sapphire holographic laser oscillator. *Optics Letters*, 22:697–699, 1997.

[4] S. Y. Lam and M. J. Damzen. Self-adaptive Nd:YLF holographic laser with selectable wavelength operation. *Applied Physics-B Lasers and Optics*, 76:237–240, 2002.

[5] M. Trew, G. J. Crofts, M. J. Damzen, J. Hendricks, S. Mailis, D. P. Shepherd, A. C. Tropper, and R. W. Eason. Multiwatt continuous-wave adaptive laser resonator. *Optics Letters*, 25(18):1346–1348, 2000.

[6] A. Brignon, L. Loiseau, C. Larat, J. P. Huignard, and J. P. Pocholle. Phase conjugation in a continuous-wave diode-pumped Nd:YVO_4 laser. *Applied Physics B-Lasers and Optics*, 69(2):159–162, 1999.

[7] A.E. Seigman. *Lasers*, pages 535–536. University Science Books, 1986.

[8] A. Yariv. *Optical electronics*, pages 17–29. Saunders College Publishing, fourth edition, 1991.

[9] G. J. Crofts and M. J. Damzen. Numerical modelling of continuous-wave holographic laser oscillators. *Optics Communications*, 175(4-6):397–408, 2000.

[10] B.A. Thompson, A. Minassian, and M.J. Damzen. Operation of a 33-W continuous-wave, self-adaptive, solid-state laser oscillator. *Journal of the Optical Society of America B-Optical Physics*, 20(5):857–862, 2003.

Chapter 5

Power-scaling holographic resonators

5.1 Introduction

The holographic resonator described in chapter 4 produces an amplified phase conjugate of the injected seed beam and its design compensates for any distortions present within the loop of the resonator. If the single spatial mode seed beam is passed through a distorting medium before it enters the resonator the output will be the phase conjugate of the distorted beam. When this is passed back through the distorting medium, the aberrations are healed and a replica of the original beam is produced. This ability suggests the use of the holographic resonator as a phase conjugate MOPA (master oscillator power-amplifier), where any distortions created by additional amplifiers can also be compensated for, allowing a high power diffraction-limited beam to be produced.

This chapter covers the integration of an optical amplifier into the holographic resonator. The system is examined to discover the optimal position for the insertion of an amplifier in order to achieve maximum power extraction. For the chosen position the system is modelled and the ex-

pected output powers calculated. The ability of the phase conjugator to operate with a less than diffraction-limited seed beam will be discussed along with its ability to cope with a displaced seed beam. Initial results of the power scaling of the holographic resonator are then presented showing an output of 11.6W with a single spatial and longitudinal mode [1]. Methods for improving the efficiency of the power-scaled holographic resonator are then discussed.

5.2 Modelling the amplified resonator

5.2.1 The positioning of a power amplifier

There are three possible positions for the insertion of a power amplifier into the holographic resonator (shown in figure 5.1.): In the loop between the FWM amplifier and the NRTE (position 1), after the NRTE but before the beam has re-entered the FWM amplifier (position 2), or in the arm of the resonator (position 3).

5.2.1.1 The amplifier in position 1

In this arrangement the seed beam initially passes through the FWM crystal where it is amplified and then passes through the power amplifier where it is amplified still further. The beam is then attenuated by the NRTE such that the beams are balanced in the four-wave mixer. The scattered beam generated in the FWM amplifier then passes back through the NRTE, this time in the high transmission direction comparatively unattenuated. The scattered beam passes back through the power amplifier and finally four-wave mixer being amplified by both, in turn.

The intracavity flux measurements in the previous chapter (section 4.5.3) show that at this point the clockwise flux is far greater than the anticlock-

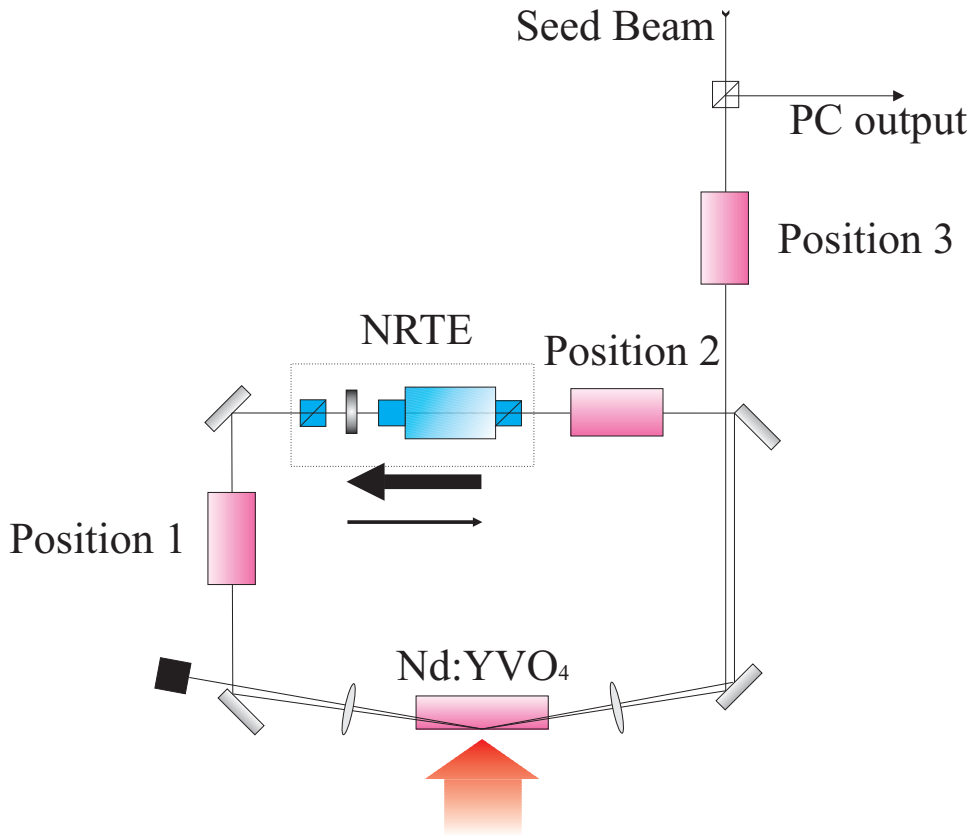

Figure 5.1: The possible positions for the insertion of an amplifier into the holographic resonator

wise. As such most of the power from the amplifier is transferred to the clockwise beam and hence the clockwise beam needs to be severely attenuated by the NRTE in order to achieve efficient FWM so any additional gain seen by the clockwise beam will be lost. The scattered beam travelling anticlockwise now passes through a depleted amplifier with little gain available. Hence placing an amplifier at position one will lead to a very inefficient process.

5.2.1.2 The amplifier in position 2

The seed beam passes through the four-wave mixing amplifier followed by the NRTE where it is attenuated. This attenuated beam passes though the power amplifier and then back into the four-wave mixing amplifier. The scattered beam passes back through the power amplifier, the NRTE (in the high transmission direction), through the four-wave mixing crystal and out of the system.

In order to achieve high reflectivities from the gain gratings the writing beam powers must be balanced, and hence the amplified attenuated clockwise beam needs to be of a similar power to the seed beam. To achieve this the NRTE will have to be set to an extremely high attenuation.

The scattered anticlockwise beam from the four-wave mixer passes through the amplifier then the NRTE (un-attenuated) and through the four-wave mixer again. In this case both of the beams that pass through the power amplifier are of comparatively low power. This will result in high gains being seen by both beams but a low extraction efficiency from the power amplifier leading to an inefficient amplification process. The low level of extraction will give rise to high levels of ASE which will raise the threshold of the system and lower its efficiency.

5.2.1.3 The amplifier in position 3

When the amplifier is placed in position 3 the seed beam is amplified before it enters the resonator. Once the beam enters the resonator it passes around the loop normally producing an amplified phase-conjugate output. The phase conjugate beam is then further amplified to become the output beam. In this position none of the additional power from the amplifier is ″thrown away″ by the NRTE as the initial amplification of the seed beam will simply shift the peak output power to a lower seed power. The high power output from the holographic resonator should allow for good extraction from the amplifier and an efficient amplification process.

5.2.2 Using the holographic resonator as a MOPA system

The previous section showed that insertion of an amplifier into the output arm of the resonator (position 3 in figure 5.1) was the most efficient method of power-scaling the system. For this arrangement the operation of the resonator should be unaffected by the amplifier, apart from the amplification of the seed and output beams. In effect it will act as a phase conjugate MOPA.

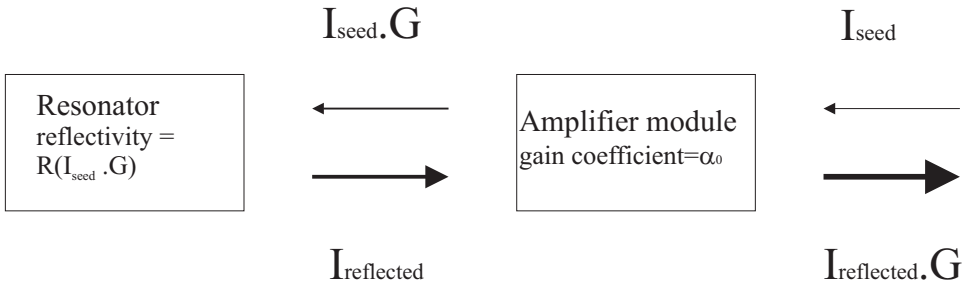

Figure 5.2: Schematic of the amplifier system boundary conditions.

The amplified resonator is now modelled by considering a double-pass saturable amplifier with a variable reflectivity mirror. Here the holographic resonator is treated as the variable reflector where its reflectivity is a function of the seed power. The resonator incorporated into the double-pass

amplifier is shown schematically in figure 5.2. Here a beam of intensity I_{seed} is passed through an amplifier where it sees an intensity gain of G (G is the effective gain of the amplifier when the presence of both beams is taken in to account). The amplified beam is then reflected by the phase conjugate resonator (now having an intensity of $I_{reflected}$) and is passed back through the amplifier, seeing the same intensity gain (G) as on its first pass. The resultant beam has an intensity of $I_{reflected}.G$. The reflectivity from the resonator is calculated empirically from data in chapter 4

The amplifier produces the following coupled differential equations for the beams travelling to the left (I_L) and right(I_R) respectively.

$$\frac{dI_L}{dz} = \alpha_0 \frac{I_L}{1 + \frac{I_L + I_R}{I_{sat}}} \tag{5.1}$$

$$\frac{dI_R}{dz} = \alpha_0 \frac{I_R}{1 + \frac{I_L + I_R}{I_{sat}}} \tag{5.2}$$

where α_0 is the unsaturated gain coefficient and I_{sat} the saturation intensity.

The following boundary conditions are applied to the amplifier. I_{seed} is the initial intensity of I_L and $I_{seed}G$ its final value. $I_{reflected}$ is the initial value of I_R and $I_{reflected}G$ its final value, where G is the saturated gain from the amplifier.

$I_{seed}G$ and $I_{reflected}$ are related by the reflectivity of the holographic resonator to give

$$I_{reflected} = I_{seed} \times G \times R\,(I_{seed} \times G) \tag{5.3}$$

This system is solved numerically using a relaxation model for small signal single pass gains (ssspg) of 1,5 and 10 with the result shown in figure 5.3

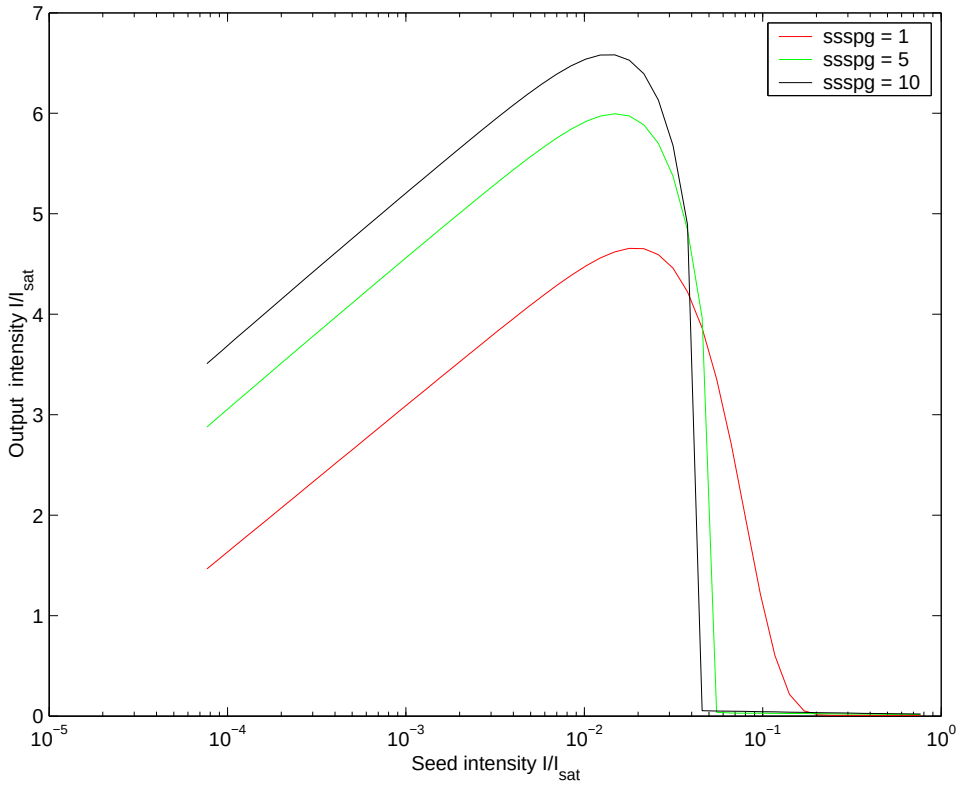

Figure 5.3: The modelled input/output power curves for a fixed holographic resonator with varying levels of additional amplification.

5.2.3 The limitations of the phase conjugator

The holographic resonator will compensate for most aberrations and distortions within its seed beam. This distortion correcting ability depends on the FWM beams achieving a good overlap with each other and with the pump beam. If this overlap is reduced the reflectivity and fidelity of wavefront replication will fall. Effects that can reduce the beam overlap are beam steering (where the beams are deviated from their optimal path for some reason) and changes in spot size. The addition of an amplifier to the arm of the resonator will cause a reduction in beam quality and thermal lensing effects leading to changes in spot size and beam steering.

5.2.3.1 Beam steering effects

In chapter 2 the thermal load and subsequent refractive index changes in side pumped amplifiers were studied using the work by Bermudez et al [2] and Hello et al [3]. Those models are developed further here in order to calculate the deviations on the path of a seed beam caused by the change in refractive index in the amplifier due to pumping. The seed beam is passed through the amplifier in a bounce geometry and, for simplicity is assumed to be infinitely narrow.

For Nd:YVO_4 the thermally induced variation of refractive index is directly proportional to the temperature and a stress induced birefringent component [2]. For this model the stress-optical effect will be ignored as it is far weaker [2] than the temperature dependent refractive index effect. This gives a refractive index variation of

$$\Delta n\left(x,y,z\right)=\left(\frac{dn}{dT}\right)T(x,y,z) \tag{5.4}$$

where the rate of change in refractive index parallel to the c-axis is given by $\frac{dn_c}{dT}=3.9\times10^{-6}\mathrm{C}^{-1}$ [2]

Substituting the temperature profile found in equations B.1 into equation 5.4 generates the refractive index for any point in the crystal for light polarised parallel to the crystal c-axis. (By substitution of the values for light polarised parallel to the a-axis the alternative polarisation can be studied.)

From the temperature (and hence refractive index) distribution described in appendix B it can be seen that the variation of refractive index in the z-direction of the crystal is minimal in the region that the beam passes through. As such we can approximate that the refractive index only varies in the x-direction.The crystal is then treated as if it consisted of many layers of material each with a slightly different refractive index. A ray can then be traced through these layers applying Snell's law at each interface.

$$n_1 \sin\theta_1 = n_2 \sin\theta_2 \tag{5.5}$$

$$n\left(x,y,z\right)\sin\theta\left(x,y,z\right) = n_1 \sin\theta_1 \tag{5.6}$$

treating $n_1 \sin\theta_1$ as a conserved quantity and converting to a differential equation (equation 5.6) as shown in figure 5.4.

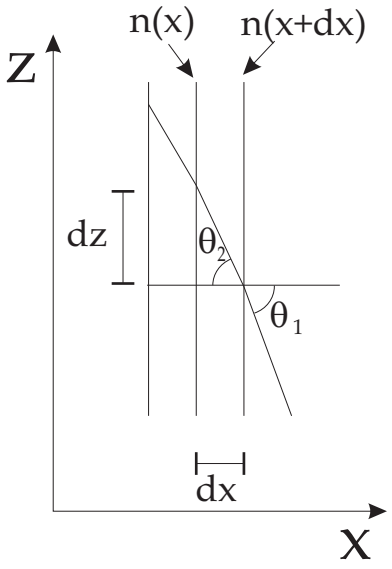

Figure 5.4: Tracing a ray through a variable refractive index.

$$\sin\left(\theta\left(x\right)\right) = \frac{dz}{\left(dx^2 + dz^2\right)^{1/2}} \tag{5.7}$$

$$\sin\left(\theta\left(x\right)\right) = \left(\frac{dx^2}{dz^2} + 1\right)^{-1/2} \tag{5.8}$$

Equation 5.8 can then be substituted into equation 5.6 for $\sin(\theta(x, y, z))$ to give

$$dz = dx\left(\left(\frac{n(x)}{n_1 \sin\theta_1}\right)^2 - 1\right)^{-1/2} \tag{5.9}$$

which is integrated numerically through the previously calculated refractive index profile.

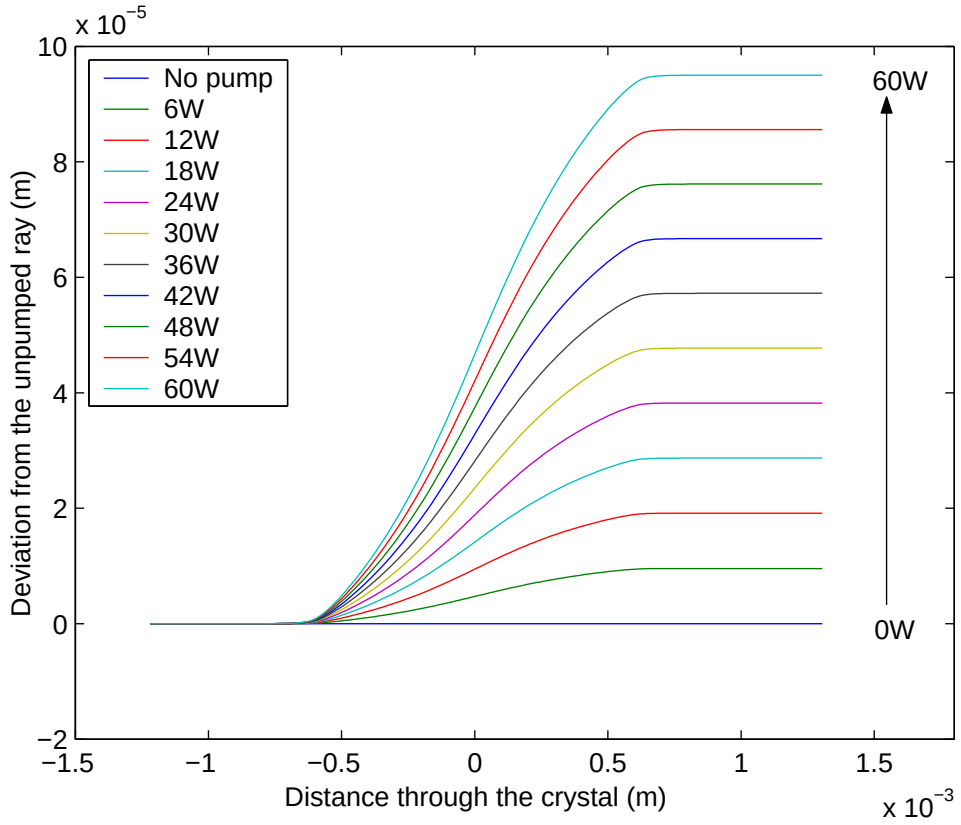

Figure 5.5: Deviation of a ray from the normal path when passed through a pumped crystal as a function of pump power.

Figure 5.5 shows the calculated deviation from the normal path as a ray passes through the crystal as a function of pump power (for a 100µm by 10mm full width rectangular pump spot) where the normal path is that for a ray passing through the crystal in a bounce geometry with a 7° (to the pumped face of the amplifier) incident angle. The change in angle of the beam is small (less than 10^{-6} of a degree) due to the symmetry of the bounce geometry. (The angle of the beam is changed by roughly the same amount on each side of the bounce). The spatial deviation however is such that when extrapolated throughout the loop of the resonator a misalignment of the four-wave mixing beams could occur. This misalignment will lead to a reduction and ultimately breakdown of phase conjugation.

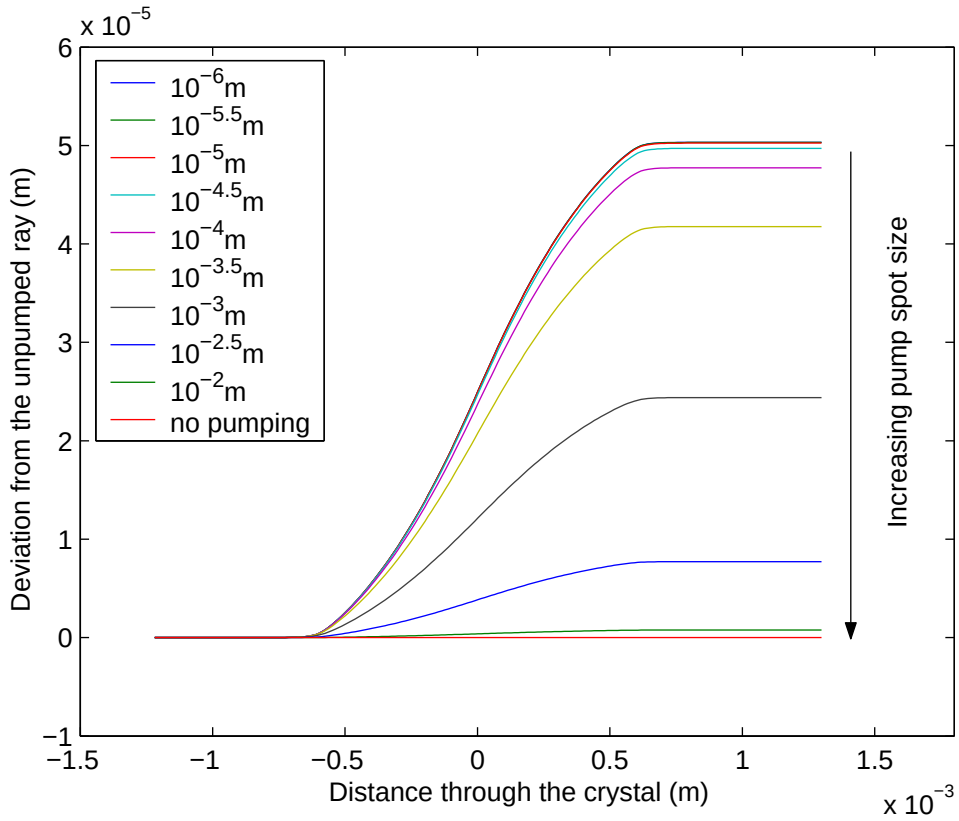

Figure 5.6: Deviation of a ray from the normal path when passed through a pumped crystal as a function of pump spot width.

Figure 5.6 shows the deviation from the normal path as a function of pump spot width from 10µm to 10mm. By varying the pump spot width the gain available to the beam passing through the amplifier can be controlled. This

method of changing the power is used in the experiments detailed in this chapter in order to remove the need to compensate for the wavelength shift in the pump diode[1].

5.2.3.2 Thermally induced distortions

When a diffraction-limited beam is passed through an amplifier its beam quality will degrade due to thermally induced distortions. By looking at the cumulative effect of several of these distortions on a probe beam the resultant changes in beam quality and spot size can be found.

The cumulative effect of several aberration in series is given by

$$M^2_{total} = \sqrt{\left(M^2_{initial}\right)^2 + \sum_i \left(M^2_i\right)^2} \tag{5.10}$$

where $M^2_{initial}$ is the $M^2$of the initial beam and M^2_i is the beam quality degradation factor of the ith element in the series.

For the holographic resonator with a power amplifier in its arm (position 1) the beam first passes through the power amplifier, the FWM amplifier, around the loop and back into the FWM amplifier as shown in figure 5.7.

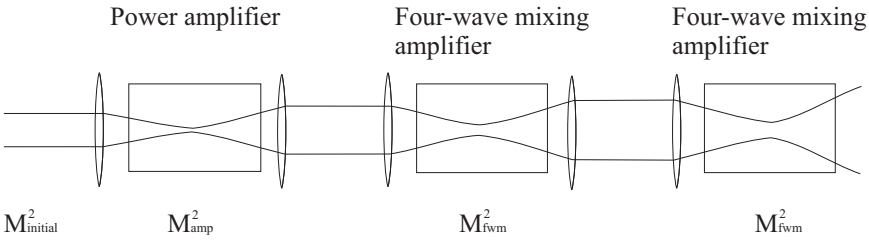

Figure 5.7: A schematic to show beam quality changes through the system.

After the beams have interacted in the FWM amplifier a phase conjugate is produced which will retrace the beam's path back through the system

[1]The wavelength emitted by laser diode bars varies with temperature by ∼0.2 nm/degree.

undoing the aberrations that it has acquired. Assuming that the initial beam is diffraction-limited the beam quality of the forward pump at the FWM amplifier will be

$$M^2_{total} = \sqrt{1 + \left(M^2_{amp}\right)^2 + \left(M^2_{fwm}\right)^2} \tag{5.11}$$

As the amplification is increased the beam quality will decrease leading to an expansion in the spot sizes within the FWM amplifier.

The holographic resonator used in these experiments was built to produce a stable 6W output which was achieved by increasing the spot size of the pump beam such that the gain coefficient was reduced. The large pump spot size reduces the impact of any expansion of the FWM beams caused by a decrease in beam quality.

5.3 Experimental

5.3.1 The amplified holographic resonator

A schematic of the setup is shown in figure 5.8. Here a power amplifier is inserted into the output arm of the holographic resonator described in chapter 4. As before a 300mW, single longitudinal mode, TEM_{00}, 1064nm Nd:YVO_4 seed laser was used to define the phase conjugate mode. The beam from the seed laser was launched through the power amplifier into the resonator. An amplified phase conjugate beam was generated by the resonator which then passed back through the power amplifier to produce an amplified output.

The power amplifier uses the same bounce geometry as the resonator with some minor differences. The amplifier crystal is a 1.1at% doped Nd:YVO_4 a-cut slab with dimensions $20 \times 5 \times 1$mm with a 3° wedge to prevent parasitic lasing. The 5×1mm a-faces are AR coated for 1064nm and the

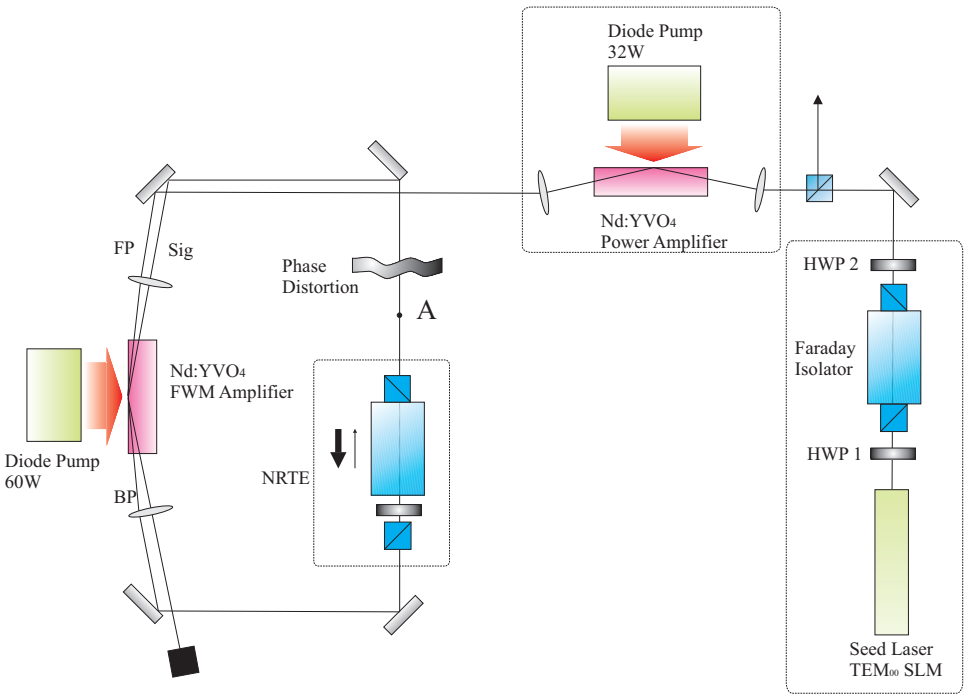

Figure 5.8: Schematic for the holographic resonator with a power amplifier in its arm.

1×20mm faces AR coated for the diode pump at 808nm. The pump source used is a TE polarised 32W CW diode bar whose polarisation is rotated 90° by a half-wave plate to be parallel with the c-axis of the crystal. The pump beam is initially collimated by a Doric lens attached to the facet of the diode bar, and is then focused into the crystal with a 12.7mm focal length cylindrical lens. A pair of 100mm focal length spherical lenses are used to focus the seed beam into the amplifier with a spot size of $\sim$30µm and re-collimated it afterwards.

The gain of the power amplifier was controlled by moving the 12.7mm cylindrical lens which focused the pump light.

The holographic resonator used in these experiments differs from that described in the previous chapter. Here the resonator was built to enable a greater degree of mobility in the seed beam. To allow for this a larger four-wave mixing amplifier crystal was used ($20 \times 5 \times 3$mm) in order to reduce the risk of "clipping" when the doubly aberrated beam was re-launched into the four-wave mixing amplifier. The FWM beams were also

less tightly focused in order to achieve a better modal overlap, which resulted in a lower than optimal peak power of 6W but a far more robust system.

5.4 Results

5.4.1 Lasing results from the amplified holographic resonator

Figure 5.9 shows the phase conjugate output power generated by the amplified resonator as a function of the seed laser input power.

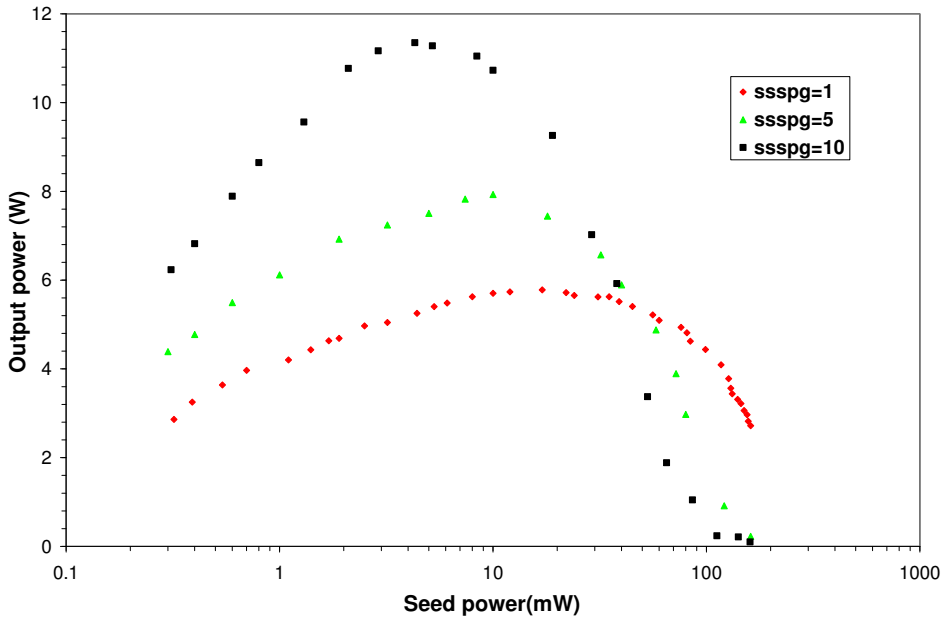

Figure 5.9: The phase conjugate output power of the MOPA system as a function of seed power for various small signal gains.

Here the first curve (the red diamonds) represents the output power when the power amplifier has a small signal single pass gain of one (the power amplifier is switched off). As the seed power is increased from 0.3mW to ~20mW the PC output power increases as the contrast ratio of the gain gratings rises. At a signal power of 20mW the maximum output power of 6W is reached. As the signal power is increased beyond 20mW the FWM

amplifier becomes over saturated, which causes the diffraction efficiency to fall and less power to be available to the output beam. This process is studied in more detail in chapter 4.

The second curve (green triangles) shows the results for the system with the power amplifier switched on and the pump beam de-focused. A large pump spot size compared with the seed beam is used in order to lower the gain which gives the amplifier a small signal gain of 5. Here the amplification of the seed beam causes the peak output of the system to be seen at around 10mW. The maximum output power of the system however is now around 8W

The third curve (the black squares) shows the PC output when the power amplifier has a ssspg of ~ 10. The seed input for maximum output occurs at ~ 4.3mW giving a peak power output of ~ 11.5W.

5.4.2 Output as a function of NRTE HWP angle

The effect of the NRTE on the output power of the un-amplified resonator was described in detail in section 4.5.2. The phase shift caused by the NRTE is needed to achieve stable oscillation and its properties as a variable transmission element enable the diffraction efficiency of the gain gratings to be controlled and therefore the output power to be optimised.

Figure 5.10 shows the output power of the amplified resonator as a function of the angle of the HWP in the NRTE. The seed power is chosen to provide the maximum output from the system. In these experiments the relationship between the HWP angle and output power is similar to that described in section 4.5.2 for the standard resonator. From $\sim 25^\circ$ to $\sim 65^\circ$ the output from the system is minimal. In this region the transmission through the NRTE in a clockwise direction is high. This causes the signal and forward pump beams to have hugely different powers and so the gratings that they write are weak. Any phase conjugate that did try to

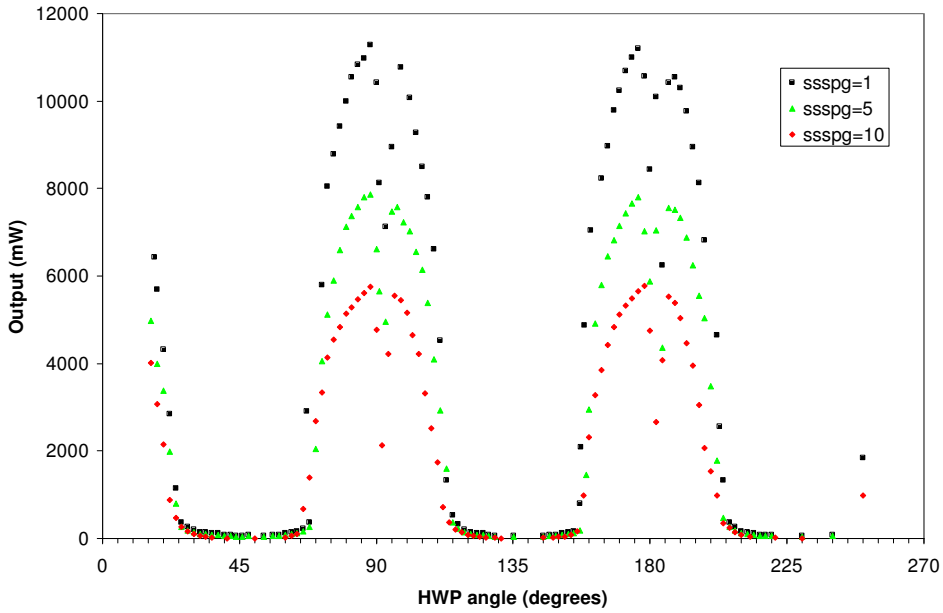

Figure 5.10: The effect of varying the angle of the HWP in the NRTE for various amplifications

build up in the anti-clockwise direction would be severely attenuated by the NRTE.

At $\sim 65^\circ$ the powers of the signal and forward pump begin to equalise causing the gain gratings to become more pronounced and their diffraction efficiency to increase. The attenuation in the anti-clockwise direction also decreases allowing a phase-conjugate mode to build up.

The output power continues to increase until the HWP reaches 90° . At this point the signal and forward pumps are equalised so the diffraction efficiency of the gain gratings is at its greatest. As the NRTE passes through its point of maximum attenuation the output power falls as the beams become unbalanced (here the beam which has just passed through the NRTE is weaker than the resonators seed beam.). The HWP angle is then increased and the output power increases back to its maximum value as the beams equalise. Beyond this point the power falls as the beams once again become unbalanced.

Increasing the amplification from the power amplifier causes the output

power to rise but does not change the effect that the NRTE has on the operation of the resonator.

5.4.3 Intracavity flux

The intracavity flux was measured by placing a 4% wedge in the beam at point A (see figure 5.8) and sampling a small amount of the circulating power without disturbing the beam.

Figure 5.11 shows the intracavity flux measured in an anti-clockwise direction in the loop of the resonator as a function of seed power for various levels of amplification. As the amplification is increased there is little change in the shape of the curves. The amplification of the seed beam by the power amplifier causes the curves to shift to lower seed powers.

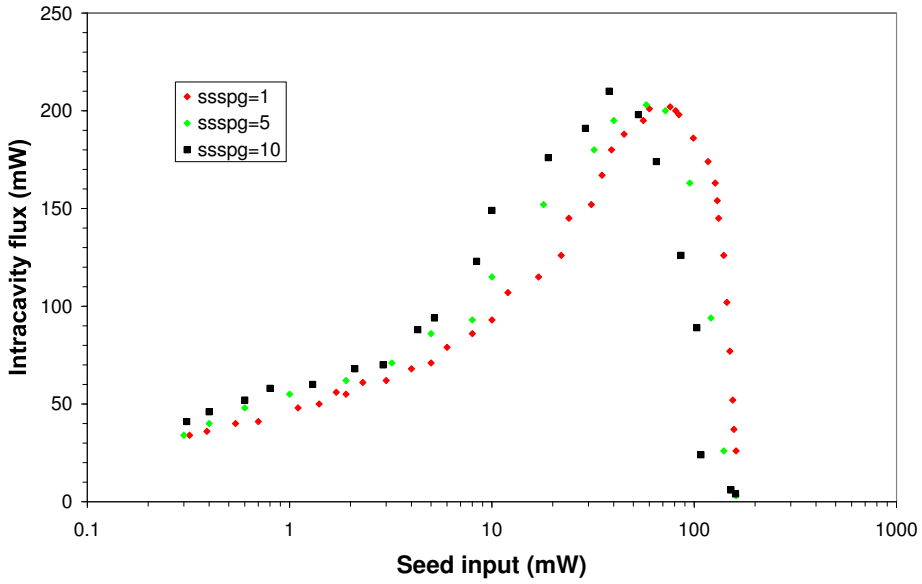

Figure 5.11: Intracavity flux (measured in the clockwise direction at point A in figure 5.8) as a function of seed input power

5.4.4 Beam quality measurements for the MOPA system

The spatial output of the resonator was viewed and captured by a Coherent BeamView Analyzer. The spatial output with the power amplifier turned off (SSSPG=1) is shown in figure 5.12. The output power is ~ 6W and it operates on a near diffraction-limited mode. The beam is elliptical due to the asymmetry in the gain region of the FWM amplifier. The output was found to have a beam quality of M_x^2 =1.3 and M_y^2 =1.2.

Figure 5.13 shows the spatial profile when the amplification was increased the to give an output of ~ 8W (SSSPG=5) and the beam quality in both directions remained essentially unchanged. The amplification was then increased to produce an output of $\sim 12W$ (SSSPG=10) with the spatial profile shown in figure 5.14. The $M^2$of this beam increases slightly in the horizontal direction to M_x^2 =1.4 but remains unchanged in the vertical direction.

The longitudinal modes of the resonator were examined with a plane-plane Fabry-Perot interferometer . The resonator was found to generate a single longitudinal mode at the same frequency as the seed laser with a linewidth of $\nu \sim 0.2$GHz. The output remained both spatially and longitudinally single mode with the insertion of a phase distortion (a glass slide etched in HF) in to the loop of the resonator. The insertion of the slide had a negligible effect on the output power of the resonator.

5.5 Discussion

The results presented in this chapter describe the initial investigation into the possibility of amplifying the output from the holographic resonator. It is important to note that throughout these experiments the holographic resonator was not adjusted to optimise the output power or beam quality of the system. The results have been obtained by increasing the amplifica-

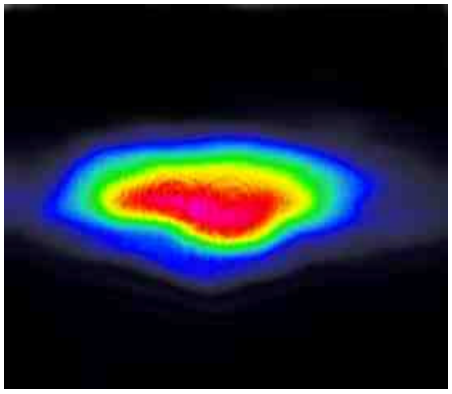

Figure 5.14: Beam profile of the amplified resonator with a sspg=10 from the power amplifier

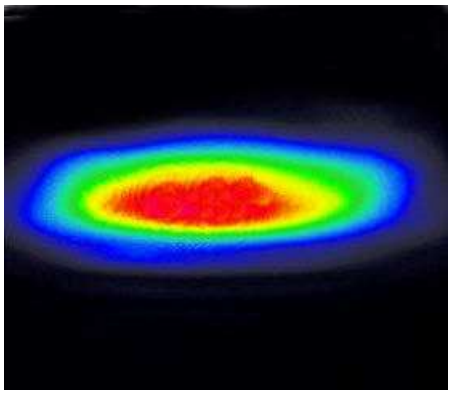

Figure 5.13: Beam profile of the amplified resonator with a sspg=5 from the power amplifier

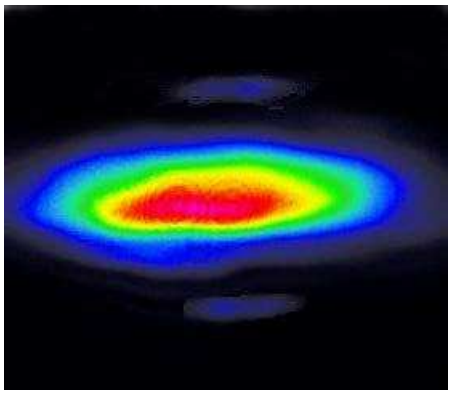

Figure 5.12: Beam profile of the amplified resonator with the amplifier turned off

tion from the power amplifier alone. Had the resonator/amplifier system been optimised the insight into the intrinsic operation and efficiency of the resonator would have been lost.

The output power of the resonator with the power amplifier turned off was set to 6W by defocusing the pump beam in the FWM region. This made the FWM region less sensitive to movement of the interacting beams which allowed for some beam steering and lensing from the power amplifier to be compensated for. When the power to the FWM amplifier was increased, the interacting beams no longer mode matched with the pump beam causing the threshold to be raised and lasing to cease.

Increasing the power and improving the pump/signal mode overlap of the power amplifier was also investigated. As well as the beam steerage and lensing issues caused by the increased thermal load on the amplifier ASE also became a problem. With a tighter focus of the pump in the power amplifier the gain increases and consequently causes the ASE power to rise. This ASE could then travel to the FWM amplifier where it would extract gain from the resonator, raising the threshold and reducing the efficiency of the laser.

When a signal beam is passed through a bounce geometry (or indeed any geometry) amplifier its beam quality will be degraded by thermally induced distortions. The main source of these is quartic phase aberration due to the less than perfect thermal lens.

Degradation of the beam quality of a signal beam by a bounce geometry amplifier was observed by our collaborators at Imperial college [4]. They passed a 16.5W diffraction limited beam (A self starting holographic ring resonator) through an amplifier pumped with 50W of diode power. The resultant beam was 36W $M^2 > 2$. This can be compared with a similar experiment where they placed an additional amplifier inside the input/output arm of the self starting resonator. In this case they achieved an output power of 33W with a near diffraction limited beam.

Further work has since been carried out based on these experiments by our collaborators at Imperial College London [4]. In their experiments both the amplifier and resonator have been optimised to take account of the beam steering and thermal lensing issues. Their use of cylindrical optics increased the mode overlap of the signal and pump beams which led to greater pump extraction and therefore output powers. Using these techniques they achieved output powers of 33W with 103W of diode pump power in a system optimised for high power operation. By compensating for the thermal lensing and beam steering issues present at the higher output powers the efficiency was increased but the adaptability of the system was lost. In the laser described here the output power could be ”ramped up” in power from 6 to 11.5W with no adjustment whereas the optimised system from Imperial College would only function efficiently over a small power range.

5.6 Conclusion

These experiments show that the seeded holographic resonator can be power-scaled by the insertion of a power amplifier into its output arm.

Intracavity flux and loop transmission measurements (figures 5.10 and 5.11) were taken showing that the operation of the resonator is unaffected by the insertion of the power amplifier.

Using a seeded holographic resonator with an output power of 6W output powers of up to 11.5W have been achieved. Further amplification caused misalignment between the beams in the FWM gain region and hence the phase-conjugate oscillator to cease operation.

The insertion of the amplifier does not detract from its ability to adapt to additional phase distortions and maintain single mode (both spatial and longitudinal) operation.

The operation of the holographic resonator with the amplifier in the arm was modelled and an increase in output power consistent with the experimental data produced.

5.7 References

[1] J.M. Hendricks, D.I. Hillier, S.J. Barrington, D. P. Shepherd, R. W. Eason, M. J. Damzen, A. Minassian, and B Thompson. Power scaling of continuous-wave adaptive gain-grating laser resonators. *Optics Communications*, 205(1-3):197–205, 2002.

[2] J.C. Bermudez, V.J. Pinto-Robledo, A.V. Kir'yanov, and M.J. Damzen. The thermo-lensing effect in a grazing incidence diode-side-pumped Nd:YVO_4 laser. *Optics Communications*, 210(1-2):75–82, 2002.

[3] P. Hello, E. Durand, P. K. Fritschel, and C. N. Man. Thermal effects in Nd-YAG slabs 3d modeling and comparison with experiments. *Journal of Modern Optics*, 41(7):1371–1390, 1994.

[4] B.A. Thompson, A. Minassian, and M.J. Damzen. Operation of a 33-W continuous-wave, self-adaptive, solid-state laser oscillator. *Journal of the Optical Society of America B-Optical Physics*, 20(5):857–862, 2003.

Chapter 6

Four-wave mixing and holographic resonators in waveguides

6.1 Introduction

The output power available from near diffraction-limited fibre lasers has increased from tens of Watts to kilowatts [1] in the last four years. Output powers are still limited by nonlinear effects, heating and optical damage (The CW optical damage threshold of silica is $\sim$1kW/μm ^{2}) generated at the intensities reached inside these lasers. Recent developments in large mode area fibres [2] [3] have reduced these effects but they are still an issue. The ability to generate a single (spatial) mode output from a multi-mode fibre would enable these fibre lasers to be power-scaled still further. Currently single-mode output is achieved by using bend loss [4] or fibre tapers [5] to strip out higher order modes of the fibre. Developing a fibre based holographic resonator would be another method however of achieving these goals.

This chapter will describe the progress made towards developing a fibre

based phase conjugator operating via saturable gain gratings. Four-wave mixing in fibres will be introduced in a qualitative way and the various arrangements for achieving it described. Fibre amplification will then be briefly covered along with the formation of gain gratings in end-pumped systems. A possible arrangement for a resonator based on four-wave mixing will be presented and discussed. Experimental attempts to achieve four-wave mixing via gain gratings in fibres will be described and the failure of these experiments explained.

6.2 Four-wave mixing in a fibre

Applying four-wave mixing to a multimode waveguide geometry can be most easily visualised from a ray tracing perspective. Three beams are launched into a fibre, two counter-propagating "pump beams" and one signal beam. The signal beam is launched in the same end as, but at an angle to, the forward pump beams. Each time the signal beam and the forward pump beam intersect an interference pattern is formed. If this occurs in a pumped saturable amplifier then many gain gratings will be written. The backward pump beam will then "see" these gain gratings and diffract off it as a phase conjugate of the signal beam. The cumulative effects of these interactions along the length of the fibre should then add up to generate the phase conjugate output. A schematic of this process can be seen in figure 6.1. The same effect will occur with the gratings written by interference between the signal and the backward pump beam which are scattered off by the forward pump beam.

6.2.1 Two beam four-wave mixing

Phase conjugation via parametric four-wave mixing in a multimode waveguide has been observed [6] and analysed [7] using the same beam for both the signal and forward pump beams. Four-wave mixing is achieved by

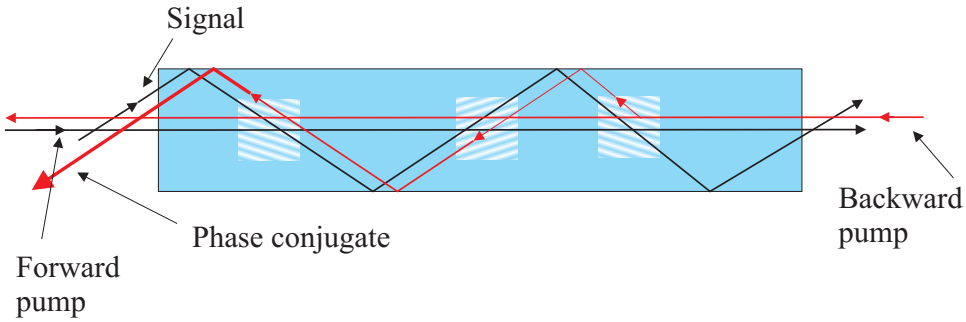

Figure 6.1: Diffraction off many gratings along the fibre.

two modes from one of the beams interacting with a mode from the other beam. As long as two of the modes present counter-propagate four-wave mixing can occur. Figure 6.2 shows a ray tracing view of this process. The forward pump beam splits into several rays which propagate along the fibre intersecting at regular intervals, and where they intersect gratings are written. If a component of the backward pump beam counter-propagates with one of the components of the forward beam then the three beams will meet in a four-wave mixing geometry. The backward pump beam will scatter off the grating written by the two components of the forward pump as the phase conjugate of the beam that it doesn't counter-propagate with. The same effect should occur throughout the fibre every time two counter-propagating modes and another mode intersect (i.e. every time three modes interact in a four-wave mixing geometry). The cumulative effect of these interactions should therefore produce a phase conjugate output.

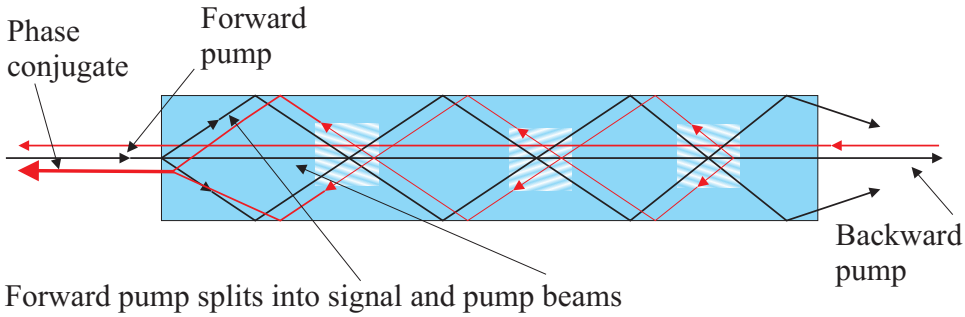

Figure 6.2: 'Two beam' four-wave mixing.

6.2.2 Double-clad geometries

In a double-clad fibre geometry it is possible to use a variation of the four-wave mixing arrangement previously described. Here the forward and backward pump beams are launched into the core of the fibre, whilst the signal beam is launched into the cladding (as shown in figure 6.3). Where the cladding launched beam intersects with the core it will interfere with the pump beams in a four-wave mixing geometry. This will generate a phase conjugate of the signal beam propagating through the cladding.

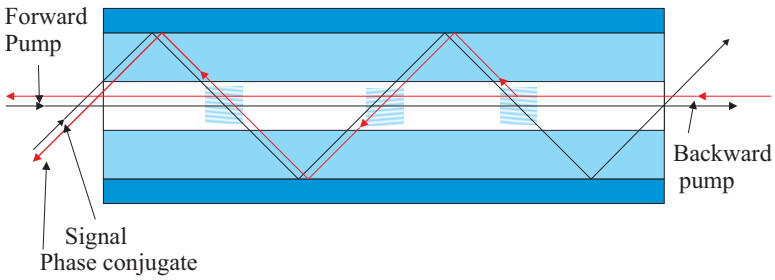

Figure 6.3: Forward and backward pump beams launched into the core, with signal into the cladding.

The advantage of this method is that the signal beam can be launched from outside the output cone of the amplified pump beam (Figure 6.4) and this should make it easier to detect any phase conjugate generated as it will not overlap with the amplified backward pump beam. A similar geometry was used by Stegeman [8] to achieve four-wave mixing using planar guided pump beams with an incident free-space signal beam.

6.2.3 Fibre based resonator

Once a phase conjugate reflectivity of greater than unity is achieved a fibre based resonator system can be developed. This resonator would operate under the same principles as the resonator described in chapter 4.

A schematic of a possible arrangement for a multimode fibre based system is shown in figure 6.5. Here a single mode (spatial and longitudi-

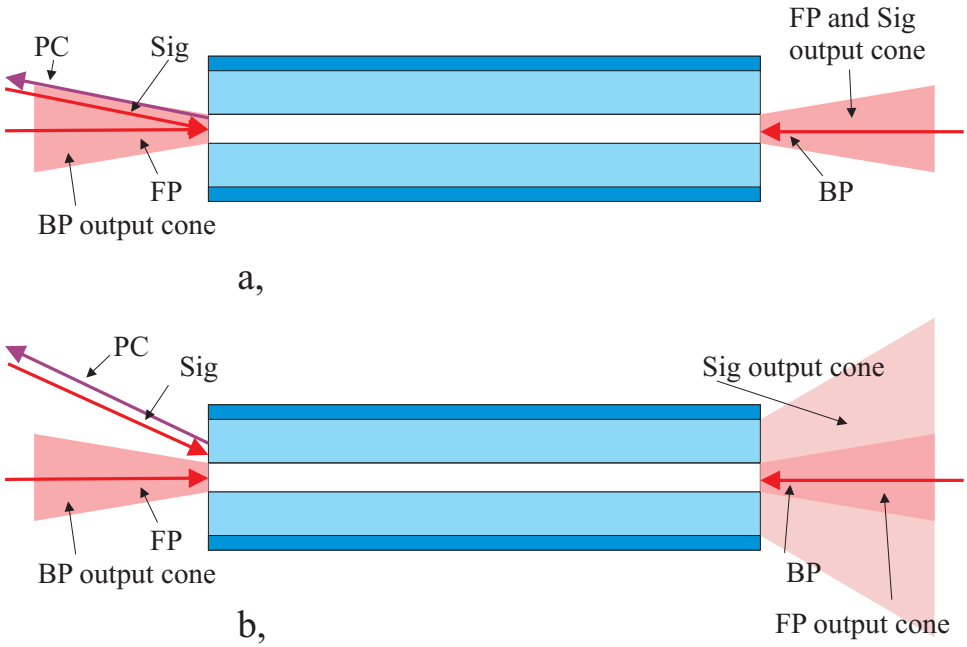

Figure 6.4: a, All beams in the core. b, Pump beams in the core signal and phase conjugate launched into the cladding.

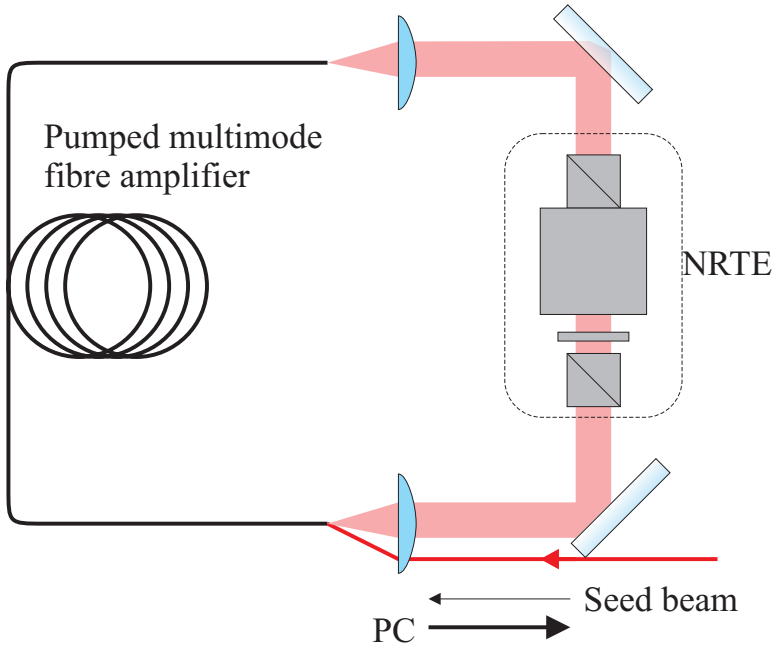

Figure 6.5: A possible fibre based holographic resonator.

nal) seed beam is launched into the fibre as the forward pump beam. The beam is transmitted through the fibre where it is amplified and expands to fill all of the supported modes. The amplified, multimode beam is then passed through an NRTE where its intensity is reduced and launched back into the fibre as the signal beam. Interference between the signal and forward pump beams writes gain gratings along the fibre. ASE scatters off these gratings passing back through the NRTE and into the fibre as the phase conjugate of the signal beam. The scattered beam will then pass back through the fibre scattering off the gratings and building up into a steady oscillation. This oscillating beam will function as the backward pump beam. The portion of the oscillating beam which does not scatter off the gratings will leave the system as an amplified phase conjugate of the seed beam.

The NRTE is needed to control the power ratio of the four-wave mixing beams and compensate for the π phase shift caused by the formation of the gain grating (See section 4.2.3). An alternative, fibre based NRTE was suggested for use in this resonator [9], a schematic of which is shown in figure 6.6.

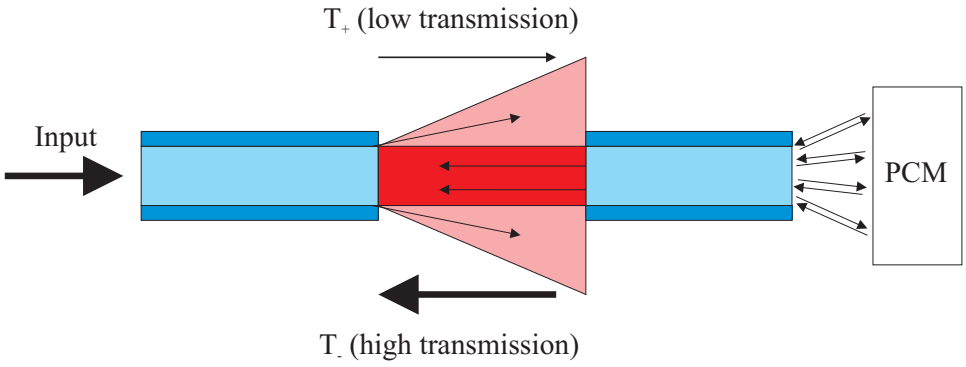

Figure 6.6: Non-reciprocal transmission through a break in a fibre.

When a single (spatial) mode beam is passed through a multimode fibre it becomes modally scrambled. If this scrambled pattern is reflected by a phase conjugate mirror on transmission back through the fibre a replica of the original beam will be produced [10]. If a break in the fibre is introduced

the transmission in the input direction T_+ (left to right in figure 6.6) will fall by an amount related to the length of the break and the misalignment of the two sections of fibre. The transmission in the other direction (T_-) will be determined solely by the phase conjugate nature of the reflected beam. The phase conjugated beam will exactly re-trace its path through the fibre and pass through the break without attenuation. This device can be applied to the fibre based holographic resonator for use as an NRTE.

The same effect can be realised by misaligning the launch of the modally scrambled signal beam in the fibre resonator. By adjusting the launch efficiency of this beam the transmission in the clockwise direction can be controlled. Any phase conjugate which is generated and propagates in the opposite direction will exactly retrace the path of the beam which generated it resulting in a theoretical 100% transmission efficiency. This NRTE does have the disadvantage however that it does not insert a non-reciprocal phase change into the loop.

6.3 Gain gratings in fibre amplifiers

Gain gratings in single mode erbium doped fibre amplifiers [11] [12] have been studied for uses in optical filtering [13], imposing single frequency laser operation [14] and a range of other applications. The pump scheme used in fibre amplifiers causes the gain coefficient of the amplifier to vary exponentially along its length, this results in the formation of a more complex gain grating than those seen in side pumped systems.

6.3.1 Gain saturation fibre amplifiers

When laser ions are sited in a glass they are distributed in a combination of crystalline-like (homogeneous) and glass-like (inhomogeneous) states [15]. This combination of states causes gain saturation to occur via both

homogeneous and inhomogeneous broadenings. In the strongly pumped regime gain saturation is generally approximated to be homogeneous [16] [17].

6.3.2 Gain available from a fibre amplifier

For a double clad Nd^{3+} doped fibre amplifier pumped from one end (z=0) the pump power in the fibre is given by

$$P(z) = P_0 e^{-\alpha_p z \Gamma} \tag{6.1}$$

where Γ is the ratio of the core to cladding areas, α_p is the pump absorption coefficient and P_0 is the incident pump power.

Assuming negligible ground-state depletion this will produce a population inversion given by

$$N(z) = \frac{\alpha_p \tau_f P_0}{h\nu A} e^{-\alpha_p z \Gamma} \tag{6.2}$$

where A is the area of the core of the fibre. This will result in an unsaturated gain coefficient of

$$\alpha_0(z) = \frac{\alpha_p \tau_f \sigma P_0}{h\nu A} e^{-\alpha_p z \Gamma} \tag{6.3}$$

This gain coefficient can then be substituted into the saturated gain equation (Equation 2.6).

$$\frac{dI(z)}{dz} = \alpha_0(z) \frac{I(z)}{1 + \frac{I(z)}{I_{sat}}} \tag{6.4}$$

which can then be solved for a known fibre.

6.3.3 Gain gratings in end-pumped fibres

Using the gain coefficient given in equation 6.3 the amplification of two beams counter-propagating through a fibre can be calculated in a similar manner to that in section 2.5.2. and the resultant gain grating can then be found. Figure 6.7 shows the gain grating written by two counter-propagating beams in a Nd^{3+} doped amplifier (assuming no variation of pump or signal power across the fibre's core). The fibre modelled here is a single clad fibre with a 100µm radius and is 5 times longer than its pump absorption length. The fibre is pumped with 1W and contains two signal beams each having an initial intensity of $I_{sat}/1000$.

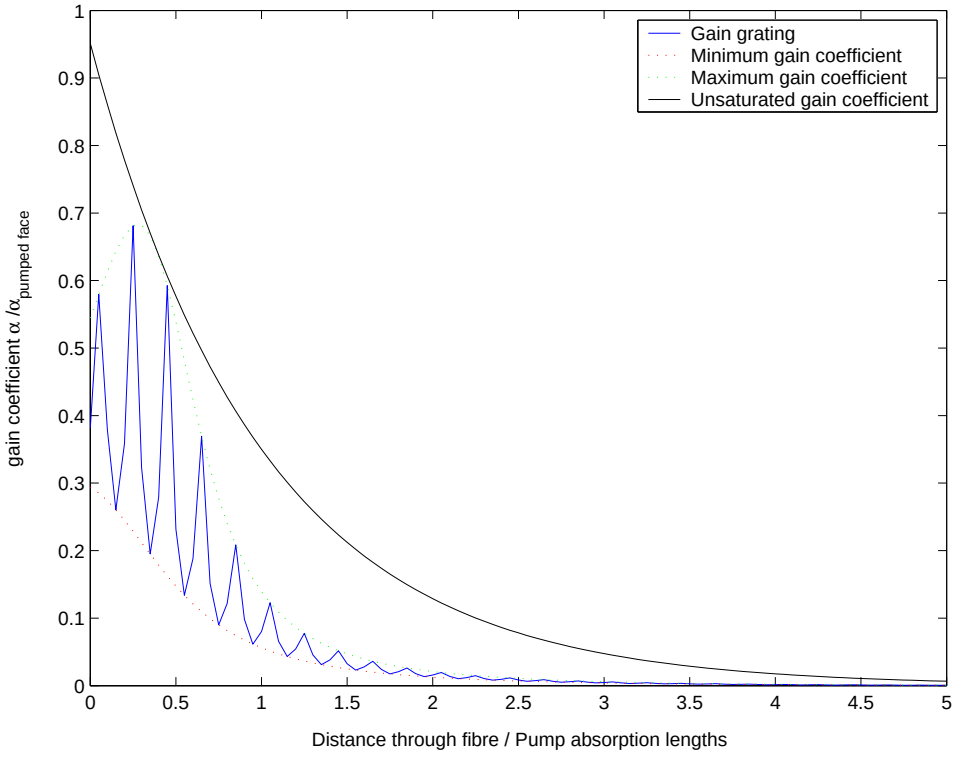

Figure 6.7: Gain grating formation in an end-pumped fibre (the period of this grating is much longer than in reality.).

The contrast ratio of the grating reaches its maximum value a short distance from the pumped end of the fibre, which is where the two counter-propagating beams are of equal intensity. Beyond this point the contrast ratio dies away as the intensities of the beams diverge.

6.3.4 Diffraction efficiency of an end pumped gain grating

The diffraction efficiency of a gain grating can be found by following the procedure used in section 2.5.3 in which the nonlinear polarisation induced by the gain grating is calculated. This is then substituted in to the SVEA form of the nonlinear Maxwell wave equation which is solved for an incident probe beam.

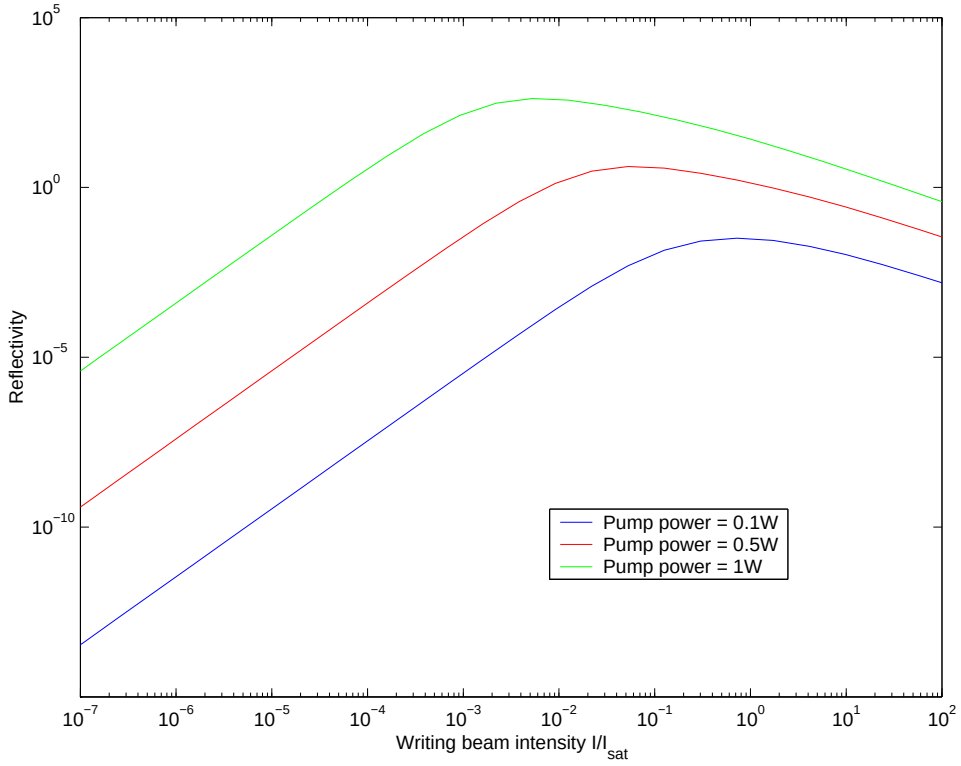

Figure 6.8: Reflectivity of an end pumped fibre.

Figure 6.8 shows the modelled reflectivity of the gain grating formed in the end pumped fibre for a range of writing beam powers and pump powers. The modelled reflectivities show that for comparatively low pump powers a high phase conjugate reflectivity should be expected. This high reflectivity is due to the length of the gain gratings and the high gains achievable in fibre amplifiers.

6.4 Experimental techniques

A range of techniques were used in these experiments to try and increase the visibility of any phase conjugate generated in the fibre. These include methods of suppressing parasitic lasing, coupling light into multimode fibres and the identification of any phase conjugate output.

6.4.1 Suppression of parasitic lasing

Fibre amplifiers have long been used to produce very high gains at low signal powers and these huge gains make lasing very easy to achieve. In order to form and use gain gratings however we need to prevent lasing from occurring. In a conventional laser, gain is capped at threshold given by [18]

$$r_1 r_2 e^{2\alpha L} = 1 \tag{6.5}$$

where r_1 and r_2 are the amplitude reflectivities of the output mirrors and $e^{2\alpha L}$ the amplitude gain. The reflectivity from the end face of a fibre can be calculated from the Fresnel equations, which at an incident angle of 0° reduce to

$$r = \frac{n_{fibre} - n_{air}}{n_{fibre} + n_{air}} \tag{6.6}$$

The silica:air interface gives an amplitude reflectivity of 0.2, equivalent to an intensity reflectivity of 4%. In a pumped fibre this reflectivity from the end faces which will cause the intensity gain to be capped at 625.

In order to control the high gains needed to write gratings lasing must be suppressed such that threshold is not reached till a much higher gain. In order to suppress lasing, the reflectivity from the end face of the fibre

must be reduced, which is achieved either by changing the angle of the end faces or the use of end caps.

6.4.1.1 Angling the fibre ends

By angling the end of a fibre the reflected part of the transmitted beam will no longer be confined by the core of the fibre (Figure 6.9). Introducing even a slight angle to the end of the fibre can result in sufficient loss to raise the threshold significantly.

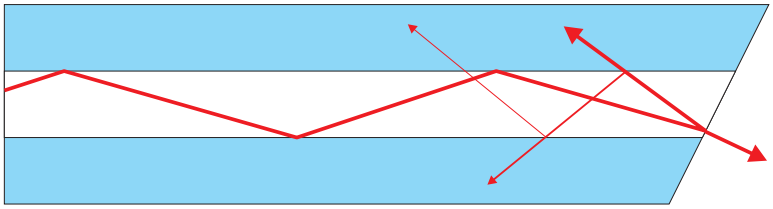

Figure 6.9: An angled fibre end.

Angling the end of the fibre is achieved by either angle polishing or angle cleaving, which may be performed by twisting the fibre whilst it is being cleaved. This puts a torsion on the fibre such that when it is cleaved the line of least resistance is at an angle to the normal.

6.4.1.2 Fibre end caps

A more extreme method of suppressing lasing is the use of end caps, an example of which can be seen in figure 6.10. These consist of a glass tube with a glass slide attached at an angle to the end. This tube is then filled with index matching fluid. The fibre is supported in the middle of the tube with its facet a short distance from (but not touching) the glass plate.

No reflection occurs at either of the glass:fluid interfaces as they have the same refractive index, while at the glass:air interface a reflection will occur. The angle of this interface is chosen such that the reflection misses the end

of the fibre and none of the reflected light is therefore coupled back into the fibre.

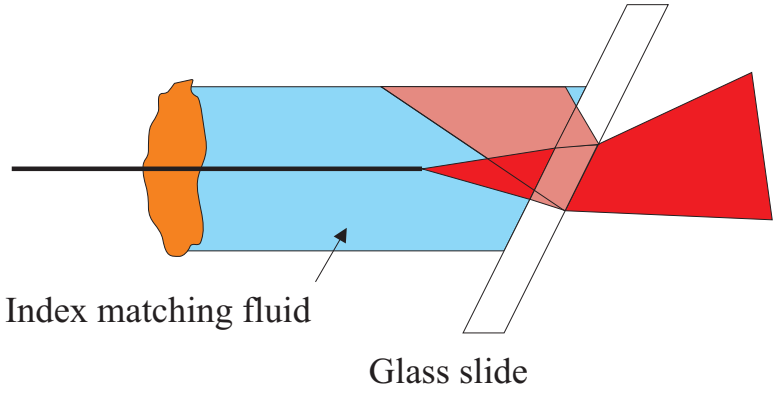

Figure 6.10: End cap to reduce back reflection and suppress lasing.

6.4.2 Coupling light into multimode fibres

In order to efficiently couple a beam into a fibre the beam must be capable of being focused to a spot smaller than the core of the fibre whilst remaining inside the fibre's numerical aperture [19]. One way of calculating this is to compare the V-number of the fibre with the product of the divergence and spot size of the beam. The V-number is related to the number of modes that the fibre can support and is given by

$$V = \frac{2\pi a NA}{\lambda} \tag{6.7}$$

where a is the radius of the fibre, NA the fibres numerical aperture given by $NA = \sqrt{n_{core}^2 - n_{clad}^2} = \sin\theta_c$ where θ_c is the external maximum launch angle. The number of modes supported by a fibre can be approximated using

$$N \simeq \frac{V^2}{2} \tag{6.8}$$

When a collimated Gaussian beam is focused its spot size is given by

$$r = \frac{\lambda f M^2}{\pi R} \tag{6.9}$$

where f is the focal length of the lens, r the radius of the focused spot and R the beams radius at the lens. The divergence of the beam can be defined as $D = R/f$

The conditions for launching a Gaussian beam into a fibre are given by comparing equations 6.7 and 6.9 to derive the inequalities

$$M^2 < \frac{V^2}{2} \qquad \text{where} \qquad NA > D \tag{6.10}$$

This process can be visualised more easily by considering a typical multimode fibre of core radius 20μm and a numerical aperture of 0.2. This fibre will have a V number of 23.62 when transmitting a 1064nm beam. The fibre will accept a beam with an $M^2$of up to 6. However if a diffraction-limited beam is launched into the fibre filling the whole cone of acceptance it can be focused down to a spot with a 3μm radius or filling the core of the fibre with a divergence (D) of 0.034. This can be seen more clearly in figure 6.11

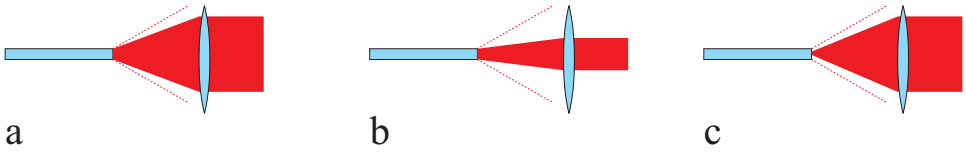

Figure 6.11: a, A beam with M^2=6 fills the fibre core and acceptance cone. b, A diffraction-limited beam fills the core but not the acceptance cone. c, A diffraction-limited beam fills the acceptance cone but not the core.

6.4.3 Identification of phase conjugate output

The process described in the previous section is also used to aid identification of any phase conjugate generated in a multimode fibre. A single mode beam launched such that it fills the core of the fibre will have a solid angle

which is small compared with the output cone of the fibre (Figure 6.12). When this beam is phase conjugated it should be comparatively easy to see against any other noise coming out of the fibre.

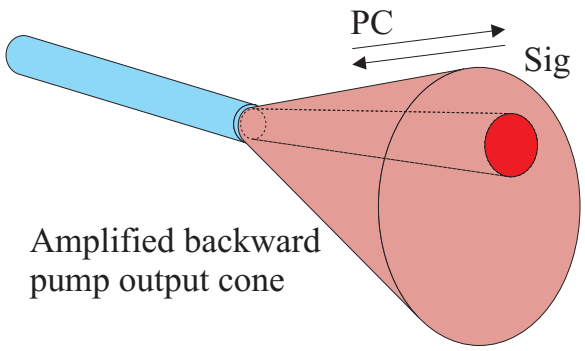

Figure 6.12: Phase conjugate beam in the output cone

Where the phase conjugate beam is not immediately obvious comparisons of beam images are taken with and without the signal beam present. The differences between these images are then found using computer based image processing techniques. Any phase conjugate should then be far easier to see.

Another method of identifying any phase conjugate is performed by pulsing the signal beam (this was done by inserting a chopper into the path of the signal beam) then looking for a spatially dependent variation of the fibre's output at this pulsing frequency. The spatial dependence is needed to counter any two-wave mixing effects or additional gain saturation caused by the presence of the signal beam.

6.5 Experimental

In this section experiments performed to try and observe four-wave mixing in a fibre/waveguide geometry are described. A range of fibres and four-wave mixing geometries were used and are detailed here.

6.5.1 Fibres used in these experiments

Fibre number HD649: Single clad Nd^{3+} doped fibre with a dopant concentration of 100 dB/km/ppm. The fibre had a 30µm core and an NA of 0.01.

Fibre number F183-LF52: Single clad Nd^{3+} doped fibre with a dopant concentration of 60dB/km/ppm. The fibre had a 120 µm core and an NA of 0.2.

Fibre number HD586-01 : Double clad Nd^{3+} doped fibre with a dopant concentration of ∼100dB/km/ppm. The fibre had a 60µm core with an NA of 0.1 and a 650µm clad and an NA of 0.43.

6.5.2 Single clad fibre experiments

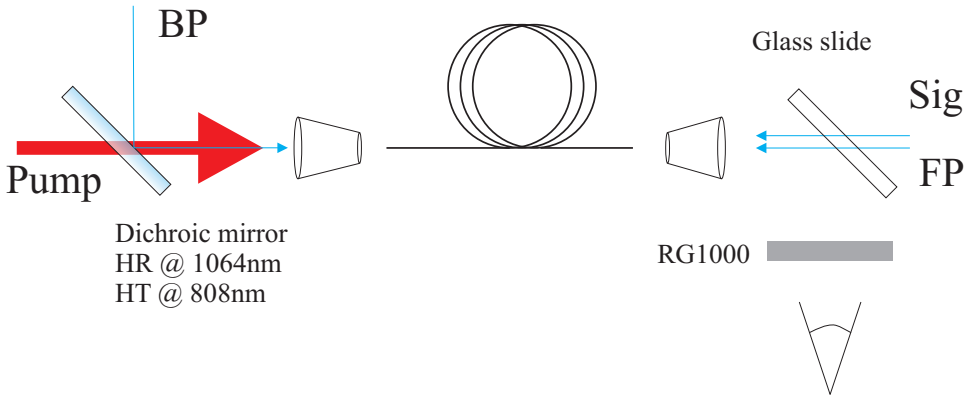

Figure 6.13: Single clad fibre four-wave mixing experimental setup.

Two experiments were performed using the setup shown in figure 6.13: Firstly 1 metre of fibre HD649 was core pumped with a Ti:sapphire laser emitting 1W at 808nm. In the second experiment 4 m of fibre F183-LF52 was core pumped with an 808nm, 8W fibre-coupled laser diode system.

In both cases the forward pump, backward pump, and signal beams were split from the same 300mW, 1064nm, TEM_{00} , SLM, seed laser and launched into the fibre. The backward pump beam was launched into the same

end of the fibre as the 808nm pump, while the signal and forward pump beams were launched into the other end. The beams were focused to a spot size equal to the core of the fibre. The forward and backward pump beams were launched along the axis of the fibre, while the signal beam was launched at an angle (generally a few degrees) to the forward pump beam.

Any phase conjugate was observed by inserting a glass slide into the path of the signal and forward pump beams. The reflected part of the fibre's output was then passed through an RG1000 filter to remove any remaining pump and into a CCD camera.

6.5.2.1 Results

Fibre HD649 supported several spatial modes at 1064nm and lased at very low pump powers. Lasing was suppressed with end caps in order to achieve gains of $\sim$1000 with 1W of pump power.

Fibre F183-LF52 was observed to support thousands of spatial modes emitting a speckle pattern. Lasing was suppressed by angle polishing the ends of the fibre achieving gains of $\sim$100 with 8W of pump power.

Evidence of phase conjugation was investigated by studying the spatial profile of the output from the fibre. Figure 6.14a shows a typical spatial output from fibre number F183-LF52 with all four-wave mixing beams present. This can be compared with figure 6.14b where the signal beam has been blocked.

The difference between the two spatial outputs was found using computer based image subtraction techniques resulting in the profile shown in figure 6.14c. These techniques were performed for a range of four-wave mixing beam and pump power configurations with no evidence of any phase conjugate output detected.

Experiments were performed modulating the intensity of the signal beam

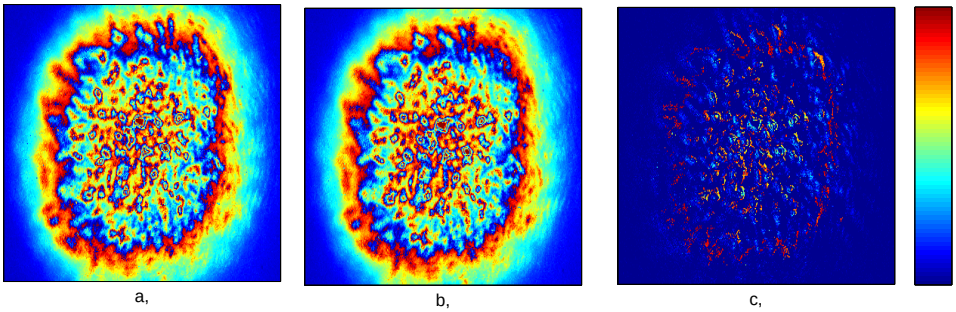

Figure 6.14: Typical spatial outputs from the end of the fibre a, All beams present. b, Signal beam removed. c, The difference between a and b.

whilst looking for intensity variations in the beam where the phase conjugate was expected to appear. Whilst the intensity of the speckle pattern changed slightly there was again no noticeable variation across the pattern.

These experiments were also performed using the two beam configuration described in section 6.2.1. Again no evidence of any phase conjugate output was observed.

6.5.3 Double clad fibre experiments

The same setup was used in these experiments as in the single clad fibre experiments with several differences. Fibre number HD586-01 was cladding pumping with an 808nm, 8W fibre coupled laser diode system. Two methods of launching the four-wave mixing beams into the fibre were used; Firstly all beams launched into the core as in the single clad fibre experiments. Secondly, the two pump beams were launched into the core and the signal beam was launched into the cladding (as described section 6.2.2).

6.5.3.1 Results

Gains in the the region of ∼100 were observed in the beams which were launched into the core of the fibre. The beams launched into the cladding whilst these beams were present saw very low, if any gain. These low gains seen by cladding launched beams implied that it had only a low level of interaction with the core. No evidence of any phase conjugation was observed in these experiments.

6.5.4 Crystal fibre experiments

Single crystal fibres of Nd:YAG with a 0.1 %at dopant concentration of lengths ranging from 10mm to 50mm and diameters from 150μm to 420μm were pumped with an 8W fibre coupled diode system at 808nm. The fibres were fabricated using a laser heated pedestal growth technique and were obtained from Digonnet [20] and Laversenne [21].

Early attempts made to clad the fibres in glass with the same thermal expansion coefficients resulted in catastrophic failure when pumped. Subsequent experiments were performed with the fibres "air clad" and coated with a low index polymer commonly used as the outer coating in double clad fibres.

The same setup was used as in the single clad fibre based experiments, with the only major difference being the replacement of the silica fibre with a crystal fibre. The crystal fibres were supported on a cradle (shown in figure 6.15) in order to allow them to act as a waveguide with the air Nd:YAG interface. The crystal fibres were air cooled by a top mounted fan.

The crystal fibre had such a large numerical aperture that not all of the light emitted could be captured by the available lenses. This NA allowed beams to be launched with a very small divergence and still be guided. A

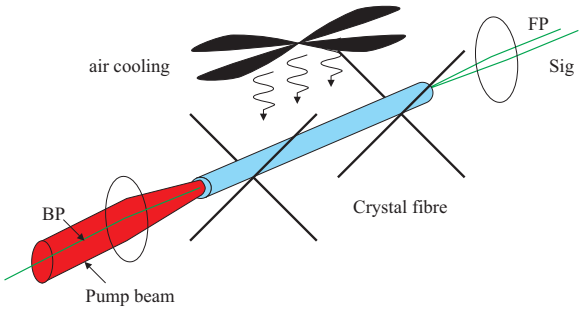

Figure 6.15: Crystal fibre pump scheme.

modified version of the experimental setup is shown in figure 6.16, where the signal beam is launched at an extreme angle into the crystal. This should have made it far easier to discriminate any phase conjugate from the amplified pump beam due to the small divergence of the signal and therefore its phase conjugate.

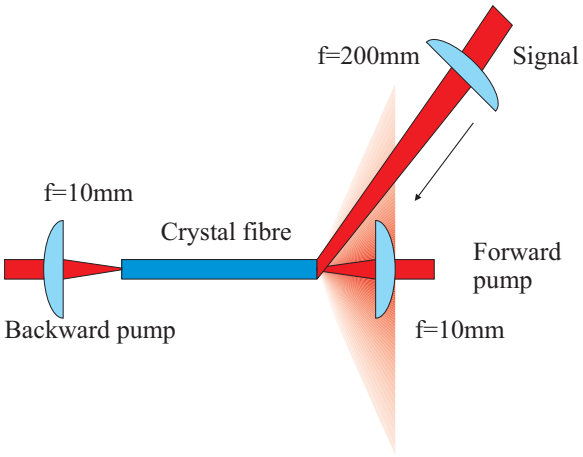

Figure 6.16: Launching the signal beam at an extreme angle.

6.5.4.1 Results

Lasing was suppressed by angle polishing the ends of the fibre which allowed gains of ∼100 to be achieved. No evidence of any phase conjugation was found even with the signal beam was launched at extreme angles.

6.6 Analysis

There are many contributory factors why phase conjugation was not observed in these experiments. These will be explained by comparing parametric and saturable gain four-wave mixing, then looking at other effects that could be hiding or suppressing the generation phase conjugate.

6.6.1 Comparing the Parametric process with gain gratings

The phase conjugate reflectivity achieved by parametric four-wave mixing in a fibre is given by [7]

$$R \sim \beta^2 L^2 \theta_{GH} P_{FP} P_{BP} / S^2 \tag{6.11}$$

where P_{FP} and P_{BP} are the powers of the forward and backward pump beams respectively, S is the cross-sectional area of the guide, L is the length of the guide, θ_{GH} is the overlap factor of the pump beams and β is a coupling term containing the nonlinear susceptibility coefficient.

The reflectivity is dependent on the product of the powers of the two pump beams with no need for equalisation of the beams. The reflectivity also increases quadratically with the length of the fibre.

The reflectivity achievable from a gain grating on the other hand is dependent on the ratio of the pump beam powers, reaching a maximum where they are equal. It is also dependent on the level of gain saturation. The length of the fibre isn't so important as the length of the gain grating which must be controlled by carefully selecting the ratio of pump powers.

In the parametric system any processes which do not contribute to the phase conjugate sum incoherently cancelling each other out. In a gain grating system any scatter or noise is amplified exponentially reducing the gain available to the phase conjugate.

6.6.2 Scattering from other gratings and two-wave mixing

In four-wave mixing six overlapping gratings are formed (see figure 2.29). In bulk experiments the effect of those which do not contribute to the formation of the phase conjugate can be ignored as they can be easily spatially filtered. In a waveguiding geometry however scatter from these other gratings may also be guided. This scatter then sees gain as it propagates along the fibre adding to the speckle field. Whilst it will not build up as the phase conjugate should, the presence of the additional confined waves will reduce the gain seen by the phase conjugate.

Two wave mixing is a well understood effect [22] where two counter-propagating beams interfere to form a gain grating. The beams then see this grating and scatter off it as shown in figure 6.17.

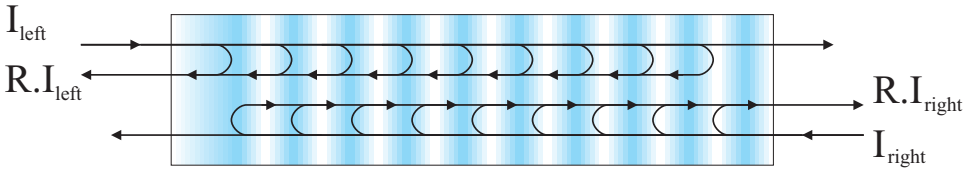

Figure 6.17: Two-wave mixing.

Two-wave mixing has been observed in single mode erbium-doped fibre amplifiers [11] [23] and has been proposed for use in tunable narrow band optical filters and in single frequency fibre lasers. In a multimode fibre two-wave mixing effects work against the generation of a phase conjugate beam. At any point where two (coherent and of the same polarisation) beams intersect they will interfere, and in a gain medium write a gain grating. Each of the beams then scatters off the grating along the path of the other beam. This process does not need the beams to counter-propagate so scatter is generated across the whole output of the fibre.

6.6.3 Overlap with the pump beams

One of the disadvantages of the waveguide geometry is the overlap between the amplified backward pump beam and the phase conjugate. Whilst a good overlap is essential to achieve phase conjugation too much means that the gain seen by any phase conjugate is limited by the presence of the other beams. In the bulk experiments the amplified pump and phase conjugate beams could be easily spatially discriminated. Had they overlapped detection of any phase conjugate would have been near impossible.

In the fibre based system the amplified pump beam produces a speckle field which is so powerful that the phase conjugate cannot be seen (if it exists at all). Experiments performed by modulating the signal beam and looking for localised variations in the speckle pattern were masked by two-wave mixing effects, which caused the whole output speckle pattern to vary when the signal beam was modulated.

6.7 Conclusions

Whilst no evidence of phase conjugation was found in this investigation this area of research should not be neglected. Further work was curtailed due to time constraints, however if methods of suppressing parasitic effects can be found then four-wave mixing via gain saturation in fibres could prove to be a useful method of developing high-power diffraction-limited lasers.

6.8 References

[1] J.K. Jeong, Y.and Sahu, S. Baek, C. Alegria, D.B.S. Soh, C. Codemard, V. Philippov, D.J. Richardson, D.N. Payne, and J. Nilsson. Ytterbium-

doped double-clad large-core fiber lasers with kW-level continuous-wave output power. In *Conference on Lasers and Electro Optics, Technical Digest*, San Francisco, California, 2004. OSA.

[2] D. Taverner, D.J. Richardson, L. Dong, J.E. Caplen, K. Williams, and R.V. Penty. 158-μJ pulses from a single-transverse-mode, large-mode-area erbium-doped fiber amplifier. *Optics Letters*, 22(6):378–380, 1997.

[3] N.G.R. Broderick, H.L. Offerhaus, D.J. Richardson, R.A. Sammut, J. Caplen, and L. Dong. Large mode area fibers for high power applications. *Optical Fiber Technology*, 5(2):185–196, 1999.

[4] J. P. Koplow, D. A. V. Kliner, and L. Goldberg. Single-mode operation of a coiled multimode fiber amplifier. *Optics Letters*, 25(7):442–444, 2000.

[5] J.A. Alvarez-Chavez, A.B. Grudin, J. Nilsson, P.W. Turner, and W.A. Clarkson. Mode selection in high power cladding pumped fibre lasers with tapered section. In *Conference on Lasers and Electro-Optics, Technical Digest*, pages 247–248, Washington, DC, 1999. OSA.

[6] S. M. Jensen and R. W. Hellwarth. Generation of time-reversed waves by nonlinear refraction in a waveguide. *Applied Physics Letters*, 33(5):404–405, 1978.

[7] R. W. Hellwarth. Theory of phase-conjugation by four-wave mixing in a waveguide. *IEEE Journal of Quantum Electronics*, 15(2):101–109, 1979.

[8] G.I. Stegeman, E.M. Wright, and C.T. Seaton. Degenerate four-wave mixing from a waveguide with guided wave pump beams. *Applied Physics Letters*, 64(9):4318–4322, 1988.

[9] J. Hendricks, D. P. Shepherd, H.L. Offerhaus, M. Kaczmarek, R. W. Eason, and M. J. Damzen. Non-reciprocal transmission via phase conjugation in multimode optical fibres. *Optics Letters*, 190:375, 2001.

[10] G. J. Dunning and R.C. Lind. Demonstration of image transmission through fibers by optical phase conjugation. *Optics Letters*, 7(11):558–560, 1982.

[11] B. Fischer, J. L. Zuskind, and D. J. Digiovanni. Nonlinear wave-mixing and induced gratings in erbium-doped fiber amplifiers. *Optics Letters*, 18(24):2108–2110, 1993.

[12] S. A. Boothroyd, A. Skirtach, L. Chan, and A. Akmaloni. Measurement of real-time gain gratings in erbium-doped fiber. *IEEE Journal of Quantum Electronics*, 35(1):39–46, 1999.

[13] B. Zhu, T. Saida, and K. Hotate. Variable optical filter using dynamic grating in Er doped fibre controlled by synthesis of optical coherence function: Proposal and experimental verification. *IECE Trans. Electron.*, E86-C(1):97–99, 1972.

[14] S. A. Havstad, B. Fischer, A. E. Willner, and M. G. Wickham. Loop-mirror filters based on saturable-gain or -absorber gratings. *Optics Letters*, 24(21):1466–1468, 1999.

[15] W. E. Martin and D. Milam. Gain saturation in Nd - doped laser materials. *IEEE Journal of Quantum Electronics*, 18(7):1155–1163, 1982.

[16] A. Hardy and R. Oron. Signal amplification in strongly pumped fibre amplifiers. *IEEE Journal of Quantum Electronics*, 33(3):505–511, 1997.

[17] I. Kelson and A. Hardy. Strongly pumped fibre lasers. *IEEE Journal of Quantum Electronics*, 34(9):1570–1577, 1997.

[18] A.E. Seigman. *Lasers*, page 41. University Science Books, 1986.

[19] G. Best and Ö.M. Sezerman. Shedding light on hybrid optics: A tutorial in coupling. *Optics and Photonics News*, 99(2):30–34, 1999.

[20] M. J. F. Digonnet, C.J. Gaeta, and H.J. Shaw. 1.064- and 1.32-μm Nd:YAG single crystal fiber lasers. *Journal of Lightwave Technology*, 4(4):454–460, 1986.

[21] L. Laversenne. Nd:YAG crystal fibres, 2002. Private communication.

[22] A.E. Seigman. *Lasers*, pages 320–323. University Science Books, 1986.

[23] S.J. Frisken. Transient Bragg reflection gratings in erbium-doped fiber amplifiers. *Optics Letters*, 17(24):1776–1778, 1992.

Chapter 7

Conclusions

7.1 Summary

In this thesis the development of phase conjugate systems operating via saturable gain gratings has been demonstrated. These systems achieve four-wave mixing via saturable gain gratings in side pumped Nd:YVO_4 amplifiers.

7.1.1 Four-wave mixing via saturable gain gratings

In chapter 2 side-pumped slab amplifiers of Nd:YVO_4 were modelled and experimentally analysed. Phase conjugation via four-wave mixing was then performed and modelled using saturable gain gratings as the nonlinear medium. Proximity and lensed coupling were introduced as methods of side pumping Nd:YVO_4 slabs with diode bars. The gains available from a side-pumped amplifier in a bounce geometry were modelled in order to find the optimal amplifier conditions to achieve high small signal gains and also those needed to achieve good extraction efficiencies with higher power signal beams. These amplifiers were then investigated experimentally under both pumping schemes and the results compared.

Four-wave mixing was described using a holographic analogy to show how it can be used as a method of achieving phase conjugation. The concept of a gain grating was introduced and formation of these gratings described. The reflectivities achievable from gain gratings were then modelled using the change in nonlinear polarisation caused by the change in the gain coefficient. Four-wave mixing via saturable gain gratings was then modelled analytically and numerically.

Experiments were then performed to study degenerate four-wave mixing via saturable gain gratings. The system was characterised and phase conjugate reflectivities of up to 100 times were achieved with a system capable of compensating for distortions in the signal beam.

Experiments were also performed to examine the relative contributions of the two gratings which are used to generate the phase conjugate. These experiments were performed by writing a grating between one of the pump beams and the signal beam then measuring the diffraction efficiency with a beam generated by a second seed laser. Diffraction efficiencies of $\sim$30 were observed from the transmission grating and around $\sim$5 from the reflection grating (This was with a lower power pump than the transmission grating experiment).

The diffraction efficiency achieved by diffracting a horizontally polarised beam from a grating written by a pair of vertically polarised beam in a birefringent medium was also investigated. Diffraction efficiencies of around 0.005 were observed which were independent of the intensity of the horizontally polarised beam.

7.1.2 Towards a monolithic phase conjugator

In chapter 3 the phase conjugator was developed into a phase conjugate oscillator. By using a self-intersecting geometry a seed beam forms a gain grating by interfering with itself. This grating is then read by ASE which

builds up to form a stable resonating mode generating a phase conjugate of the seed beam.

A model for the laser's operation was derived and solved by applying appropriate boundary conditions to the four-wave mixing model. The temporal properties of the self-intersecting geometry were studied and showed that single longitudinal mode operation was not possible.

The laser was then built and characterised achieving near diffraction-limited output with powers of up to 2.5W. The laser exhibits mode-hopping behaviour caused by phase shift between the gain grating and the interference pattern that formed it.

7.1.3 The holographic resonator

In this chapter the phase conjugate oscillator previously studied is developed into a stable system. This is achieved by inserting a non-reciprocal transmission element into the loop of the resonator. The NRTE allows the transmission of the loop in either direction to be optimised, and inserts a non-reciprocal phase shift in the transmission.

Two possible geometries for the resonator were proposed, a ring resonator, and a side loop resonator (see figures 4.2 and 4.1 respectively). The two resonators were modelled analytically and numerically and their output characteristics derived.

The resonators were then built and characterised, and both achieved near diffraction-limited output on a single longitudinal mode. Output powers of 8W for the ring resonator and 2.5W for the side loop resonator were achieved. The lower power of the side loop resonator was due to experimental technicalities which made it a less practical configuration.

A self-starting version of the ring resonator was constructed replacing the seed laser with an output coupler. Near diffraction-limited outputs of up

to 7W were achieved from this resonator.

7.1.4 Power scaling the holographic resonator

In chapter 5 the seeded ring resonator described previously was scaled in power by inserting an amplifier into the arm of the resonator. The various possible configurations of the amplified resonator were discussed qualitatively. The amplified resonator was then modelled, by treating it as a MOPA system. The possible limitations of the resonator's ability to phase conjugate were discussed with reference to beam quality and any steering issues from the seed beam.

The amplified resonator was then constructed and characterised. A seeded resonator with a maximum output of 6W was used as the master oscillator and an amplifier module was inserted into its input/output arm. The amplified resonator achieved output powers of 11.5W with a near diffraction-limited output on a single longitudinal mode.

7.1.5 Four-wave mixing and holographic resonators in waveguides

This chapter describes the progress made towards developing a fibre based phase conjugator operating via saturable gain gratings. The theory behind four-wave mixing in fibres is described qualitatively and the various possible methods of achieving it are described. The formation of gain gratings in end-pumped systems is described analytically and then modelled numerically.

Experimental attempts to achieve four-wave mixing via gain gratings in single and double clad fibres and crystal fibres are detailed and the failure of these experiments explained.

7.2 Further work

The output powers of the holographic resonator and amplified resonator described is this thesis have already been scaled further than those described here by our collaborators at Imperial College London. By improving the overlap between the seed beams and the pump area of the amplifiers the holographic resonator the efficiency of the system has been greatly increased. They have achieved outputs of 20W from the holographic resonator which were then power scaled to 33W by the insertion of a power amplifier [1].

7.2.1 A monolithic phase conjugator

Methods of improving the output power of the oscillator described in chapter 3 and of construction a monolithic system have already been discussed in section 3.6.1.1.

7.2.2 Hybrid systems

The work preformed in chapter 5 showed that the holographic resonator could cope with a less than diffraction-limited seed beam but had problems coping with misalignments caused by beam steering issues. This suggests that it may be better used as part of a hybrid system with a fibre amplifier. These systems have been already been developed using photorefractive phase conjugators [2]. The gain grating seeded holographic resonator should (with careful design) be ideally suited to achieving higher power versions of these systems.

7.3 References

[1] B.A. Thompson, A. Minassian, and M.J. Damzen. Operation of a 33-W continuous-wave, self-adaptive, solid-state laser oscillator. *Journal of the Optical Society of America B-Optical Physics*, 20(5):857–862, 2003.

[2] A. Brignon, J. P. Huignard, and E. Lallier. Multimode to single-mode conversion of a Yb-doped fibre amplifier with photorefractive Rh:$BaTiO_3$ crystal. *Applied Physics B-Lasers and Optics*, 72:789–791, 2001.

Appendix A

Properties of the Nd:YVO_4 crystal slab

A.1 Nd:YVO_4 properties

Lasing and physical properties of 1.1% at doped Nd:YVO_4 . Nd:YVO_4 is a uniaxial crystal where the a and b axis are symmetrical.

Crystal axis	a - b	c
Refractive index at 1064nm	n_a = 1.9573	n_c = 2.1652
Refractive index at 808nm	n_a = 1.9721	n_c = 2.1858
Thermo-optical coefficient (dn /dT)	$8.5 \times 10^{-6}/K$	3.9×10^{-6}/K
Stimulated emission cross section (m^2) at 1064nm	7×10^{-23}	25.0×10^{-23}
Saturation intensity W/m^2	29.7×10^6	8.3×10^6
Absorption coefficient cm^{-1}	9.2	31.2
Fluorescence life time μs	90	90

Table A.1: A table of properties for 1.1 at doped Nd:YVO_4 [1] [2] [3] [4]

A.2 Crystal coatings

Unless otherwise stated figure A.1 shows the coating applied to the Nd:YVO_4 crystal.

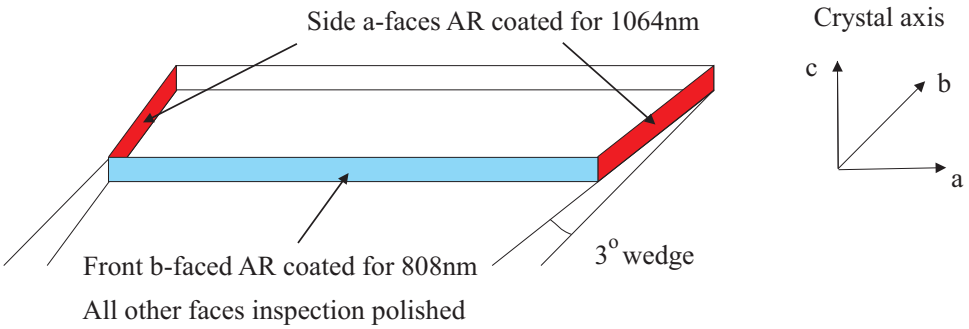

Figure A.1: AR coatings applied to the Nd:YVO_4 slab.

A.3 Crystal dimensions

The axes shown in figure A.2 are used throughout the modelling in this thesis

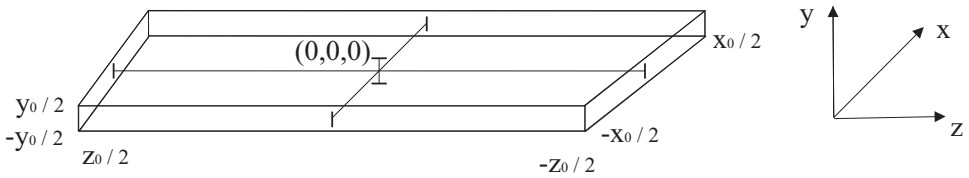

Figure A.2: Crystal axes used in all modelling work.

where in most cases $x_0 = 5$mm , $y_0 = 1$mm and $z_0 = 20$mm

A.4 Crystal cooling and pumping

Figure A.3 shows the cooling and heat deposition on the Nd:YVO_4 slab used in the experiments detailed in this thesis. The top and bottom c-faces are cooled with temperature controlled copper heat sinks. The front b-face

is pumped with a diode bar and all of the heat is deposited close to this face. Lasing (or amplification) occurs along the a-axis with the signal beam 'bouncing' off the pumped face.

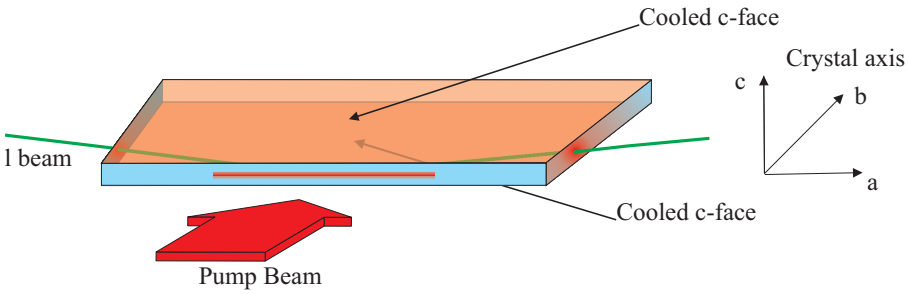

Figure A.3: Crystal pumping and cooling arrangement

A.5 References

[1] W. E. Martin and D. Milam. Gain saturation in Nd - doped laser materials. *IEEE Journal of Quantum Electronics*, 18(7):1155–1163, 1982.

[2] Casix. Neodymium doped yttrium orthovanadate (Nd:YVO_4) crystal, 2001. http:\\ www.casix.com.

[3] A.W. Tucker, M. Birnbaum, C.L. Fincher, and J.W. Erler. Stimulated-emission cross section at 1064 and 1342nm in Nd:YVO_4 . *Journal of Applied Physics*, 48(12):4907–4911, 1977.

[4] A.W. Tucker, M. Birnbaum, and C.L. Fincher. Stimulated emission cross section of Nd:YVO_4 and Nd:$La_2Be_2O_5$ (BeL). *Journal of Applied Physics*, 52(4):3067–3068, 1981.

Appendix B

Temperature distribution in a side pumped Nd:YVO_4 slab

The steady state temperature distribution for a side pumped Nd:YVO_4 crystal slab with edge cooling has been solved by Bermudez et al [1] and is presented here for completeness. This solution has been taken directly from Bermudez's paper and is not my own work.

A full derivation of the solution of the heat equation for side pumped slabs with edge cooling can be found in the paper by Hello et al [2]

B.1 The temperature distribution

$$\begin{aligned} T(x,y,z) &= \sum_{m,n}\left(C^1_{mn}e^{a_{mn}x}+C^2_{mn}e^{-a_{mn}x}-\frac{\alpha}{K}\frac{\Phi_{mn}e^{-\alpha(w/2+x)}}{\alpha^2-a^2_{mn}}\right)\cos(\phi_m y)\cos(\psi_n z) \\ &\quad+\sum_{m,n}\left(C^3_{mn}e^{b_{mn}x}+C^4_{mn}e^{-b_{mn}x}-\frac{\alpha}{K}\frac{\Psi_{mn}e^{-\alpha(w/2+x)}}{\alpha^2-b^2_{mn}}\right)\cos(\phi_m y)\cos(\varphi_n z) \end{aligned} \tag{B.1}$$

where

$$\begin{aligned} a_{mn} &= \pi\left(\frac{(2m+1)^2}{t^2}+\frac{4n^2}{d^2}\right)^{\frac{1}{2}} \\ b_{mn} &= \pi\left(\frac{(2m+1)^2}{t^2}+\frac{(2n+1)^2}{d^2}\right)^{\frac{1}{2}} \end{aligned} \tag{B.2}$$

$$\phi_m = \frac{(2m+1)\pi}{t}, \qquad \psi_n = \frac{2n\pi}{d}, \qquad \varphi_n = \frac{(2n+1)\pi}{d} \tag{B.3}$$

$$\begin{aligned} \Phi_{mn} &= \frac{P_h}{N_{mn}}\text{sinc}\left(\frac{\phi_m w_1}{2}\right)\text{sinc}\left(\frac{\psi_n w_2}{2}\right)\cos(\psi_n z_1) \\ \Psi_{mn} &= \frac{P_h}{M_{mn}}\text{sinc}\left(\frac{\phi_m w_1}{2}\right)\text{sinc}\left(\frac{\varphi_n w_2}{2}\right)\cos(\varphi_n z_1) \end{aligned} \tag{B.4}$$

$$N_{nm} = M_{nm} = \frac{td}{4} \qquad \text{if} \qquad n \neq 0 \qquad \text{and} \qquad N_{m0} = \frac{td}{2} \tag{B.5}$$

C^1, C^2, C^3 and C^4 are defined by the boundary conditions of the slab geometry.

$$\begin{aligned} C^1_{mn} &= \alpha^2\Phi_{mn}e^{-a_{mn}w/2}\frac{e^{-a_{mn}w}-e^{-\alpha w}}{Ka_{mn}(\alpha^2-a_{mn}^2)(1-e^{-2a_{mn}w})} \\ C^2_{mn} &= \alpha^2\Phi_{mn}e^{-a_{mn}w/2}\frac{1-e^{-w(a_{mn}+\alpha)}}{Ka_{mn}(\alpha^2-a_{mn}^2)(1-e^{-2a_{mn}w})} \\ C^3_{mn} &= \alpha^2\Psi_{mn}e^{-b_{mn}w/2}\frac{e^{-b_{mn}w}-e^{-\alpha w}}{Kb_{mn}(\alpha^2-b_{mn}^2)(1-e^{-2b_{mn}w})} \\ C^4_{mn} &= \alpha^2\Psi_{mn}e^{b_{mn}w/2}\frac{1-e^{-w(b_{mn}+\alpha)}}{Kb_{mn}(\alpha^2-b_{mn}^2)(1-e^{-2b_{mn}w})} \end{aligned} \tag{B.6}$$

All of the constants found here have their usual meanings and use the values given in table A.1.

The slab is of size thickness (y-axis) t, length (z-axis) d and width (x-axis) w. It is pumped by a rectangular pump beam with a spot size of w_1 (along the y-axis) by w_2 (along the z-axis) centred at $y = 0$ and $z = z_1$. The total heating power (P_h) is calculated from the quantum defect.

B.2 The temperature distribution in our crystal

The generalised temperature distribution described above can be applied to the Nd:YVO_4 crystals used through out this thesis and described in appendix A using the following values.

Symbol in equation	Description	Value
w	x_0	5mm
t	y_0	1mm
d	z_0	20mm
w_1	Gaussian pump distribution along the y-axis	$\sim$ 30µm to 500µm
w_2	Top hat distribution along the z-axis	10mm

For all of the experiments and modelling performed in this thesis the pump beam is focused into the centre of the crystals b-face hence $z_1 = 0$. This symmetrical situation causes the second summation in equation B.1 to go to zero.

Resulting in the following temperature distribution for a pump beam of power 30W spot size (vertical) of 100µm .

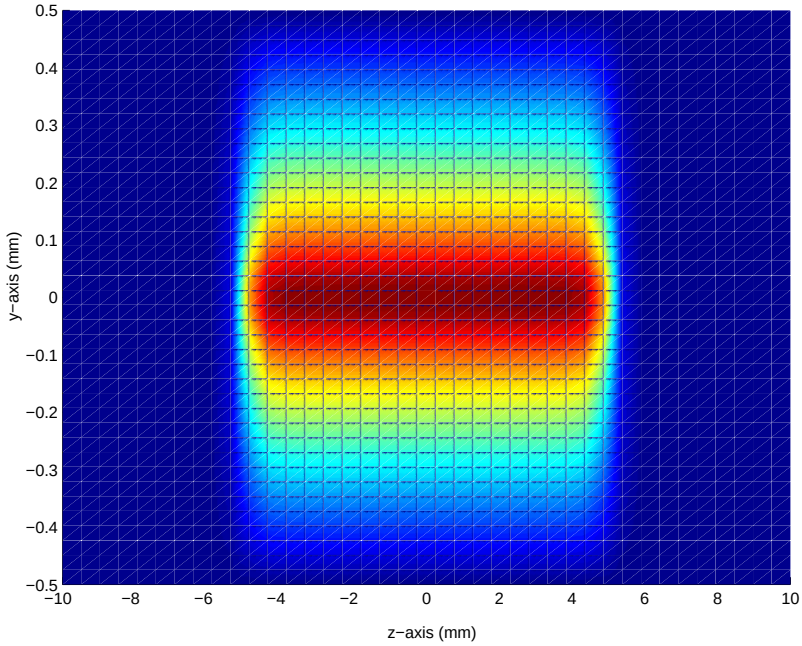

Figure B.1: The temperature distribution through a side pumped Nd:YVO_4 slab as a slice through the x=$x_0/2$ plane.

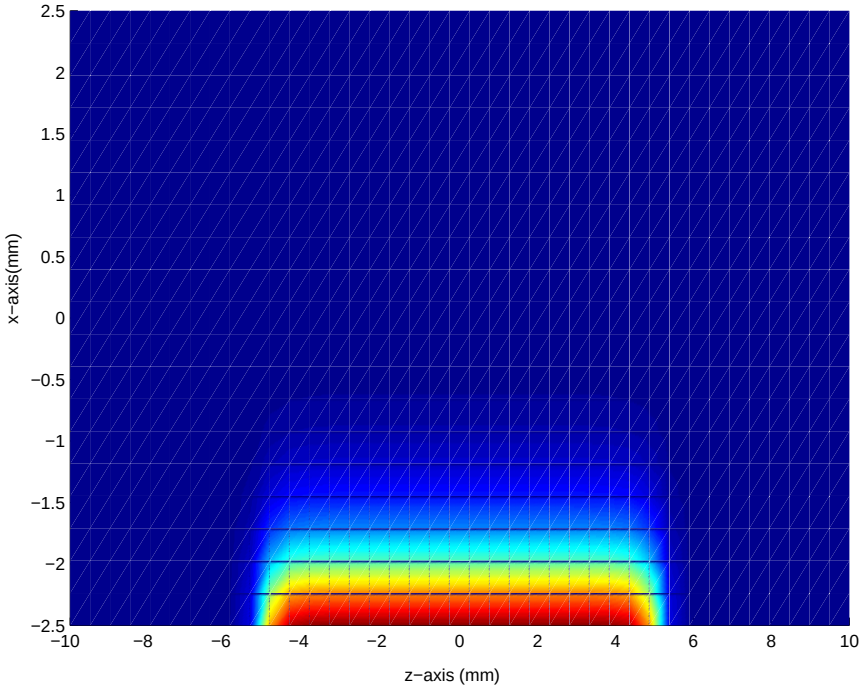

Figure B.2: The temperature distribution through a side pumped Nd:YVO_4 slab as a slice through the y=0 plane.

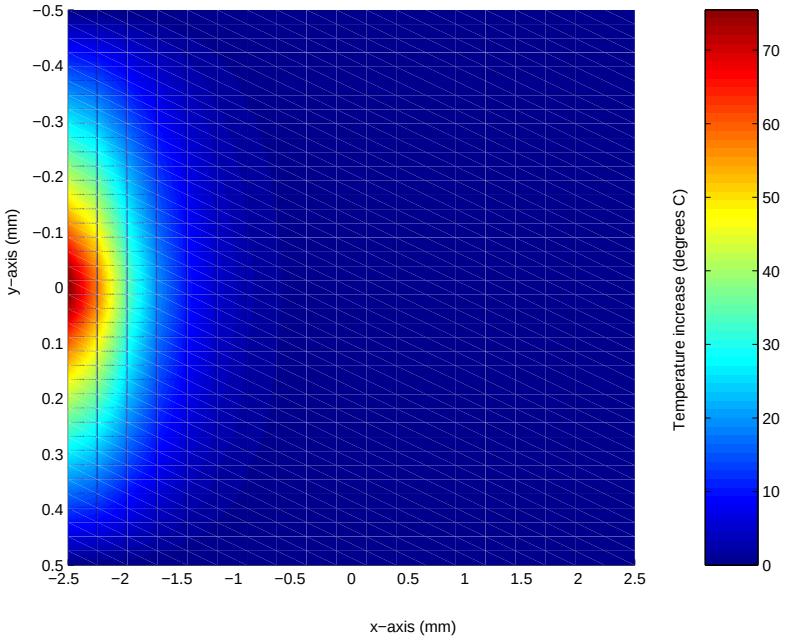

Figure B.3: The temperature distribution through a side pumped Nd:YVO_4 slab as a slice through the z=0 plane.

B.3 The effect of the number of terms in the distribution

The solution to the heat equation (Equation B.1) provided here is a summation figures B.4, B.5 and B.6 show the improvement in accuracy of the summation with the increase in the number of terms.

B.4 References

[1] J.C. Bermudez, V.J. Pinto-Robledo, A.V. Kir'yanov, and M.J. Damzen. The thermo-lensing effect in a grazing incidence diode-side-pumped Nd:YVO_4 laser. *Optics Communications*, 210(1-2):75–82, 2002.

[2] P. Hello, E. Durand, P. K. Fritschel, and C. N. Man. Thermal effects in Nd-YAG slabs 3d modeling and comparison with experiments. *Journal of Modern Optics*, 41(7):1371–1390, 1994.

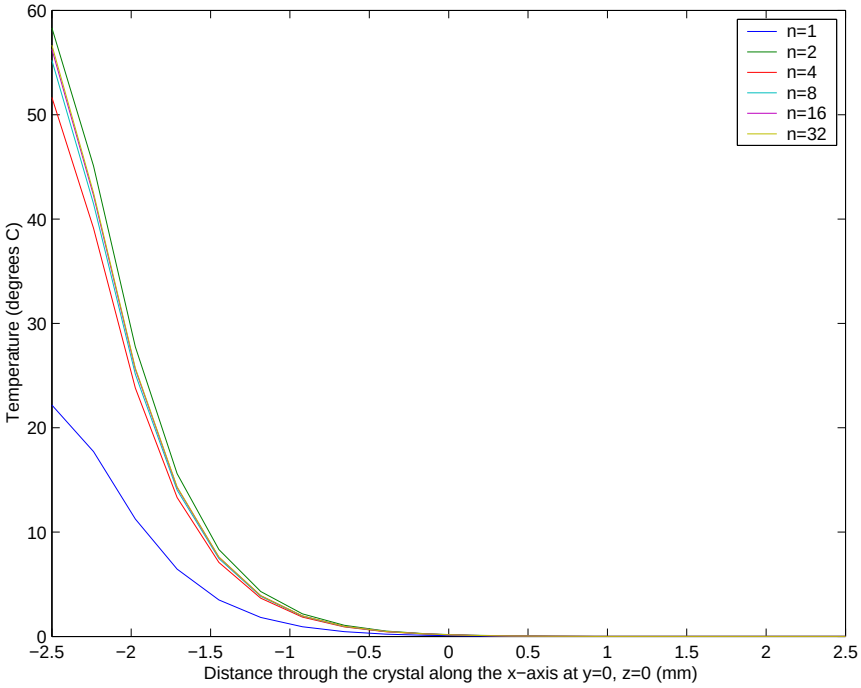

Figure B.4: The temperature distribution along the x-axis as a function of the number of terms included in the summation at y=0, z=0.

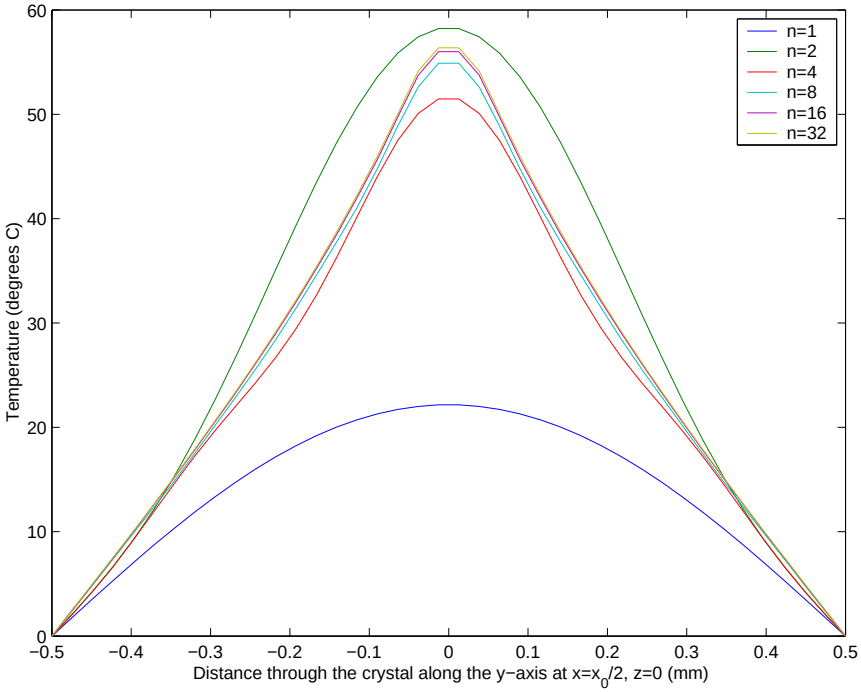

Figure B.5: The temperature distribution along the y-axis as a function of the number of terms included in the summation at x=-$x_0/2$, z=0.

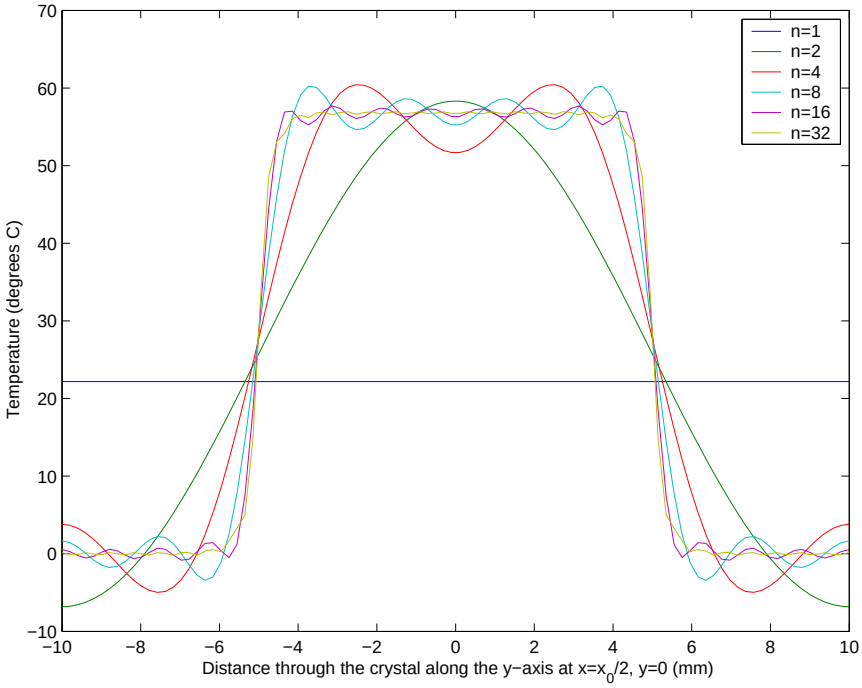

Figure B.6: The temperature distribution along the z-axis as a function of the number of terms included in the summation at x=-$x_0/2$, y=0.

Appendix C

Degenerate four-wave mixing via gain saturation

This derivation is based on one in the numerical modelling paper by Crofts and Damzen [1] our collaborators at Imperial College.

C.1 Theory of gain grating formation and interactions

The interactions between four coherent degenerate beams will be studied here

$$E_T = A_1 e^{-ik_1 \cdot r} + A_2 e^{-ik_2 \cdot r} + A_3 e^{-ik_3 \cdot r} + A_4 e^{-ik_4 \cdot r} \tag{C.1}$$

where the slowly varying amplitude, A_j describes the amplitude, phase and polarisation state of the jth electric field, and k_j is the wave vector.

Fields A_1 and A_2 counter-propagate along the z_1 axis while fields A_3 and A_4 counter-propagate along the z_1 axis as shown in figure 2.30 where θ is the small angle between the two fields.

The k vectors of the four beams can be defined in terms of the angle subtended by the fields relative to the z-axis.

$$k_{1,2} = \pm k\hat{z_1} = \pm k\left(\hat{x}\sin(\theta/2) + \hat{z}\cos(\theta/2)\right) \quad \text{(C.2)}$$

$$k_{3,4} = \pm k\hat{z_2} = \pm k\left(-\hat{x}\sin(\theta/2) + \hat{z}\cos(\theta/2)\right) \quad \text{(C.3)}$$

where the '+' terms are k_1 and k_3 and the '-' terms are k_2 and k_4 and $\hat{x}, \hat{y}, \hat{z_1}$ and $\hat{z_2}$ are the unit vectors in their respective directions.

The total time averaged intensity in the medium is given in equation 2.33 which is then expanded to give

$$\begin{aligned} I_T &= \frac{1}{2}nc\varepsilon_0 E_T E_T^* \\ \frac{I_T}{\frac{1}{2}nc\varepsilon_0} &= A_1A_1^* + A_1A_2^*e^{-i2k_1\cdot r} + A_1A_3^*e^{-i(k_1-k_2)\cdot r} + A_1A_4^*e^{-i(k_1+k_2)\cdot r} + \\ &\quad A_2A_1^*e^{i2k_1\cdot r} + A_2A_2^* + A_2A_3^*e^{i(k_1+k_2)\cdot r} + A_2A_4^*e^{i(k_1-k_2)\cdot r} + \\ &\quad A_3A_1^*e^{i(k_1-k_2)\cdot r} + A_3A_2^*e^{-i(k_1-k_2)\cdot r} + A_3A_3^* + A_3A_4^*e^{-i2k_2\cdot r} + \\ &\quad A_4A_1^*e^{i(k_1+k_2)\cdot r} + A_4A_2^*e^{-i(k_1-k_2)\cdot r} + A_4A_3^*e^{i2k_2\cdot r} + A_4A_4^* \end{aligned} \quad \text{(C.4)}$$

in terms of k_j

By ignoring the interference between the counter-propagating waves equation C.4 can be simplified to

$$\frac{I_T}{I_{sat}} = \sigma + |\tau|\cos\left(K_\tau x - \phi_\tau(z)\right) + |\rho|\cos\left(K_\rho z - \phi_\rho(z)\right) \quad \text{(C.5)}$$

where

$$
\begin{aligned}
K_\tau &= k(z_1 - z_2) \qquad K_\rho = k(z_1 + z_2) \\
\sigma &= \frac{1}{A_s}\sum_{j=1}^{4} A_j(z,t)A_j^*(z,t) && \text{(C.6)} \\
\tau &= |\tau|e^{i\phi_\tau} = \frac{2}{A_s^2}\left(A_1A_3^* + A_2^*A_4\right) && \text{(C.7)} \\
\rho &= |\rho|e^{i\phi_\rho} = \frac{2}{A_s^2}\left(A_1A_4^* + A_2^*A_3\right) && \text{(C.8)}
\end{aligned}
$$

Equation C.5 is inserted into the saturated gain coefficient equation 2.4 and simplified to give

$$
\alpha(x,z) = \frac{\Gamma_0}{1 + M_\tau\cos(\Psi_\tau) + M_\rho\cos(\Psi_\tau)} \tag{C.9}
$$

where

$$
\begin{aligned}
\Psi_\tau(x,z) &= K_\tau x - \phi_\tau(z) && \text{(C.10)} \\
\Psi_\rho(x,z) &= K_\rho z - \phi_\rho(z) && \text{(C.11)} \\
& && \text{(C.12)}
\end{aligned}
$$

are the spatially varying phases of the transmission and reflection gratings, and where

$$
\begin{aligned}
\Gamma_0 &= \frac{\alpha_0}{1 + \sigma_i(z)} && \text{(C.13)} \\
M_\tau(z) &= \frac{|\tau_i(z)|}{1 + \sigma_i(z)} && \text{(C.14)} \\
M_\rho(z) &= \frac{|\rho_i(z)|}{1 + \sigma_i(z)} && \text{(C.15)}
\end{aligned}
$$

are the saturated gain coefficient and the transmission and reflection grating modulation parameters respectively.

For simplicity the contributions from each of the gratings are considered individually either a single transmission grating ($M_\rho = 0$) or a single reflection grating ($M_\tau = 0$). The single grating case allows the gain grating to be expressed as a fourier cosine series.

$$\begin{aligned} \alpha &= \sum_{n=0}^{\infty} \alpha_g^{(n)}(z)\cos(n\Psi_g) \\ &= \sum_{n=0}^{\infty} \alpha_g^{(n)}(z)e^{in\Psi_g} + c.c. \end{aligned} \tag{C.16}$$

with harmonic coefficients given by

$$\alpha_g^{(0)} = \frac{\Gamma_0}{\sqrt{1-M_g^2}} \tag{C.17}$$

$$\alpha_g^{(n)} = (-1)^n \frac{2\Gamma_0}{\sqrt{1-M_g^2}} \left(\frac{1-\sqrt{1-M_g^2}}{M_g} \right)^n \tag{C.18}$$

The effect of the gain grating on the optical fields can be found by substituting the modulated gain into the nonlinear Maxwell wave equation and applying the paraxial and slowly varying envelope approximations (As was done in equations 2.47 to 2.50.

The following sets coupled differential equations are then produced describing the steady state interactions with the transmission grating

$$+\frac{dA_1}{dz} = \gamma_\tau A_1 + \kappa_\tau A_3 \tag{C.19}$$

$$-\frac{dA_2}{dz} = \gamma_\tau A_2 + \kappa_\tau^* A_4 \tag{C.20}$$

$$+\frac{dA_3}{dz} = \gamma_\tau A_3 + \kappa_\tau^* A_1 \quad \text{(C.21)}$$

$$-\frac{dA_4}{dz} = \gamma_\tau A_4 + \kappa_\tau A_2 \quad \text{(C.22)}$$

and reflection grating.

$$+\frac{dA_1}{dz} = \gamma_\rho A_1 + \kappa_\rho A_4 \quad \text{(C.23)}$$

$$-\frac{dA_2}{dz} = \gamma_\rho A_2 + \kappa_\rho^* A_3 \quad \text{(C.24)}$$

$$+\frac{dA_3}{dz} = \gamma_\rho A_3 + \kappa_\rho A_2 \quad \text{(C.25)}$$

$$-\frac{dA_4}{dz} = \gamma_\rho A_4 + \kappa_\rho^* A_1 \quad \text{(C.26)}$$

$$\text{(C.27)}$$

where the coupling terms are found from the fourier transform of the gain grating and given by.

$$\gamma_g(z) = \alpha_g^{(0)}(z) \quad \text{(C.28)}$$

$$\kappa_g z = \frac{1}{2}\alpha_g^{(1)} \quad \text{(C.29)}$$

C.2 References

[1] G. J. Crofts and M. J. Damzen. Numerical modelling of continuous-wave holographic laser oscillators. *Optics Communications*, 175(4-6):397–408, 2000.

Appendix D

Publications

D.1 Journal Publication

J.M. Hendricks, D.I. Hillier, S.J. Barrington, D.P. Shepherd, R.W. Eason, M.J. Damzen, A. Minassian and B. Thompson. Power scaling of continuous-wave adaptive gain-grating laser resonators. *Optics Communications*, Vol.205(**1-3**), pp.197-205, 2002

D.2 Conference Papers

A. Minassian, B. Thompson, M.J. Damzen, R.W. Eason, J.M. Hendricks, D. Hillier, D.P. Shepherd. Lasers with nonlinear optical adaptive mirrors. In *IoP Meeting on Adaptive Optics and Phase Conjugation*, London, 2001.

D.I. Hillier, J.M. Hendricks, S.J. Barrington, D.P. Shepherd, R.W. Eason, M.J. Damzen, A. Minassian, B. Thompson. Power-scaling continuous-wave adaptive laser resonators. In *CLEO 2002*, Long beach, 2002.

B.A. Thompson, A. Minassian, M.J. Damzen, J.M. Hendricks, D.I. Hillier, S.J. Barrington, D.P. Shepherd, R.W. Eason. Efficient adaptive self-starting Nd:YVO_4 gain grating laser oscillator. In *CLEO 2002*, Long beach, 2002.